# Multi-scale Compositional and Optoelectronic Characterisation of Photovoltaic Devices


Yifu Shi

St Catherine's College

University of Oxford

A thesis submitted for the degree of

*Doctor of Philosophy*

Supervisors: Professor Ruy Sebastian Bonilla,
Professor Peter Wilshaw, Professor Michael Moody

Trinity 2025

# *Prologue*

“But a strange thing occurs again and again:
the equations which appear in different fields of
physics, and even in other sciences,
are often almost exactly the same, so that many
phenomena have analogues in these different fields.”

— Richard Feynman*

---

[8] * <*The Feynman Lectures on Physics*>
Volume I, Chapter 21

# Abstract

As the dominant photovoltaic technology, the crystalline silicon solar cell industry has experienced significant technological advancements. Tunnelling Oxide Passivated Contact (TOPCon) has emerged as the mainstream architecture due to its contact selectivity that enables higher energy conversion efficiencies. TOPCon designs benefit from further processing optimisations to further reduce energy losses in current collection and contact recombination. Improving the understanding of the remaining loss mechanisms in TOPCon provides the context for the detailed optoelectronic and compositional characterisation work in this thesis.

An innovative photoluminescence imaging (PL) based characterisation method for evaluating contact recombination in TOPCon structure is presented with advantages of being in-situ and widely applicable. The method leverages the inherent spatial periodicity of the metallisation grid to extract a metal-induced PL variation signal from the spatial frequency spectrum. Numerical device simulations complement this methodology by interpreting the correlation between the periodic PL variation and metal contact recombination. Applying this approach of contact recombination assessment, together with contact resistivity measurements, enables comprehensive evaluation of TOPCon contact selectivity. Industrially fabricated TOPCon samples with structural adaptations and performance variation provide the subject of the characterisation work. Additionally, microstructural analysis through SEM-EDX and volumetric analysis via FIB slicing elucidate microstructural characteristics that correlate to the enhancement or degradation of contact selectivity.

As hydrogen passivation is a key processing in ensuring TOPCon passivation, two complementary chemical characterisation techniques, Elastic Recoil Detection (ERD) and Atom Probe Tomography (APT), are employed to analyse hydrogen distribution in TOPCon. Deuterate (2D) substituted samples are examined to mitigate ambient 1H background interference. The ERD characterisation shows excellent mass separation between D and 1H, but its spatial resolution deteriorates with increasing depth. The APT analysis enables clear depiction of the layered structure but faces ambiguity in quantitative H/D analysis. The H/D signal complications in APT is thoroughly discussed, along with experimental conditions for reducing detection ambiguity. APT results from associate enhanced passivation with increased hydrogen incorporation at the TOPCon tunnelling oxide interface. The combined information

from ERD and APT reveals inaccuracies in the standard H chemical profiling approach using Secondary Ion Mass Spectrometry (SIMS).

Furthermore, an independently developed optoelectronic method, Laser Beam Induced Current (LBIC), is presented, demonstrating sub-micronmetre resolution capability in detecting spatial variations in current collection. The technique is applied on both silicon and perovskite solar cell samples to reveal spatial photocurrent variations linked to structure defects and surface morphology.

Overall, the characterisation work presented in the thesis reveals valuable insights into energy losses primarily at TOPCon interfaces, as well as in other device architectures. The established corrections between structural design and performance provides useful guidance for the future optimisation of solar cell contacts and interfaces.

# Preface

This thesis presents the research undertaken by the author during the course of their DPhil studies in the Department of Materials at the University of Oxford. The author was co-supervised by Professor Sebastian Bonilla, Professor Peter Wilshaw, and Professor Michael Moody.

No part of this thesis has been previously submitted for a degree at this or any other university. The contributions of other researchers and collaborators have been appropriately acknowledged, and full references are provided throughout the text.

During the DPhil programme, the author has led or contributed to the following publications and conference proceedings:

**Shi Y**, DNR Payne, A Fell, et al. Extracting Contact Recombination from FFT-Filtered Photoluminescence Imaging of Half-Metallized Silicon Solar Cells[J]. EES Solar, 2025.

**Shi Y**, Wright M, Sharpe M K, et al. Characterization of solar cell passivating contacts using time-of-flight elastic recoil detection analysis[J]. Applied Physics Letters, 2023, 123(26).

**Shi Y**, Jones M E, Meier M S, et al. Towards accurate atom scale characterisation of hydrogen passivation of interfaces in TOPCon architectures[J]. Solar Energy Materials and Solar Cells, 2022, 246: 111915.

**Shi Y**, Yu M, Goodarzi M, et al. NanoLBIC characterisation of silicon solar cells using a laser pick-up unit[C]//AIP Conference Proceedings. AIP Publishing, 2022, 2487(1).

**Shi Y**, Bonilla R S. Selective laser melting of metal foils for ultrathin patterned contacts in silicon solar cells[C]//AIP Conference Proceedings. AIP Publishing, 2022, 2487(1).

Xiong, Y., Zhou, R., Soeriyadi, A., Liu, Z., Maitra, S., **Shi, Y**, et al. Self-aligned laser opening and stencil metallization for silver-free contacts in silicon solar cells[J]. APL Electronic Devices, 2025, 1(2).

Siniscalchi M, **Shi Y**, Li G, et al. Initiation of dendritic failure of LLZTO via sub-surface lithium deposition[J]. Energy & Environmental Science, 2024, 17(7): 2431-2440.

Yu M, **Shi Y**, Deru J, et al. Assessing the potential of inversion layer solar cells based on highly charged dielectric nanolayers[J]. physica status solidi (RRL)–Rapid Research Letters, 2021, 15(12): 2100129.

Yu M, Wright M, Chen J, **Shi Y**, et al. Towards high efficiency inversion layer cells based on ion-charged dielectrics[C]//Proceedings of the 8th World Conference on Photovoltaic Energy Conversion. WIP GmbH & Co Planungs-KG, 2022: 44-54.

# Acknowledgements

Much has changed since the day I came to oxford. It was a unique and enjoyable journey, one that allowed me to grow personally and professionally. I am lucky to have such excellent friends around throughout this experience.

First and foremost, I would like to first thank Professor Sebastian Bonilla and Professor Michael Moody. Your mentorship has been a constant source of inspiration throughout this incredible scientific journey. Your belief in me kept me motivated during the most challenging times.

I would also like to thank my colleagues and friends—Matt, Xinya, John, Martin, Donghao, Avery, Shona, Soumya, and so many others. Your understanding and support have made our lab a fantastic place for work.

I am grateful to my special friend Shuting for being in my life in Oxford. Your curious mind and rigorous spirit have helped me understand who I am and what I value most in life. While we had our ups and downs, the time we had together has become an integral part of me. I am also deeply thankful to my special college friend, Sally, whose natural kindness is no way from this world.

I look forward to more adventures together in the future.

# Funding

The study was funded by China Scholarship Council – University of Oxford Scholarship award number: 20196880044. Further funding was received in the form or travel grants from St. Catherine's College, Oxford and Department of Materials, Oxford.

# Table of Contents


*1. Introduction ..... 1*

**1.1. Energy and Climate ..... 1**

**1.2. Photovoltaics ..... 2**

**1.3. Silicon solar cell operation ..... 4**

1.3.1. Generation ..... 4

1.3.2. Recombination ..... 6

1.3.3. Transport ..... 11

1.3.4. Device Characteristics ..... 13

**1.4. The TOPCon solar cell architecture ..... 15**

1.4.1. Technology evolution and development of the TOPCon cell ..... 15

1.4.2. Tackling loss mechanisms towards higher cell efficiencies ..... 18

**1.5. Hydrogen Passivation ..... 21**

1.5.1. Overview ..... 21

1.5.2. Hydrogen at silicon defects ..... 22

1.5.3. Hydrogen in TOPCon structure ..... 23

**1.6. Aims and Objectives ..... 24**

**1.7. Structure of the thesis ..... 25**

*2. PL assessment of metal recombination $J0,c$: the Fourier analysis approach . 26*

**2.1. Introduction ..... 26**

**2.2. Experimental Details ..... 28**

**2.3. PL imaging data ..... 29**

**2.4. Fourier analysis of PL data ..... 30**

**2.5. Device simulation for PL experiments ..... 32**

2.5.1. Simulation approach ..... 32

2.5.2. Simulation parameters ..... 33

2.5.3. Simulation results ..... 35

**2.6. Linking simulation results to PL data ..... 38**

**2.7. Case study: contact recombination from different screen-printed Ag pastes ..... 41**

**2.8. Discussion ..... 42**

2.9. Conclusions ..... 45

*3. Linking microstructure to the electrical performance of metallisation technologies in TOPCon solar cells ..... 47*

3.1. Introduction ..... 47

3.2. Sample information and characterisation methods ..... 49

3.3. Device performance results ..... 51

3.4. Contact recombination results ..... 53

3.5. Contact-related resistance results ..... 56

3.6. Microstructural examination of the contact interface ..... 59

3.7. Discussion ..... 64

3.8. Summary ..... 66

*4. Characterisation of TOPCon passivating contact structure via time-of-flight elastic recoil detection analysis ..... 67*

4.1. Introduction ..... 67

4.2. Experimental Details ..... 68

4.3. The coincidence histogram ..... 70

4.4. Depth Profiling ..... 72

4.5. Comparison to SIMS parallel results ..... 75

4.6. Conclusions ..... 76

*5. Characterisation of TOPCon passivating contact structure via atom probe tomography ..... 77*

5.1. Introduction ..... 77

5.2. Experimental method ..... 79

5.3. APT mass spectrum ..... 81

5.4. Effect of laser energy on H background ..... 83

5.5. 3D reconstruction of the TOPCon structure ..... 84

5.6. Overlap solving and depth profiles ..... 86

**5.7. Effect of field strength on H background ..... 89**

**5.8. Comparison of $^{2}$H accumulation at the oxide interface ..... 90**

**5.9. Discussion ..... 92**

**5.10. Conclusions ..... 93**

***6. High-resolution LBIC characterisation of solar cell devices ..... 95***

**6.1. Introduction ..... 95**

**6.2. An LBIC setup with sub-micron resolution ..... 96**

**6.3. Characterisation of silicon solar devices ..... 99**

**6.4. Characterisation of perovskite solar devices ..... 103**

**6.5. Discussion and summary ..... 106**

***7. Conclusions and future work ..... 109***

***8. References ..... 113***

***9. Appendices ..... 146***

**Appendix A. Photoluminescence Imaging ..... 146**

**Appendix B. Secondary Ion Mass Spectrometry ..... 147**

**Appendix C. Atom probe tomography ..... 149**

I. Working principles ..... 149

II. Sample preparation procedure ..... 153

III. APT applications in silicon solar structures ..... 156

IV. Limitations ..... 157

**Appendix D. Elastic recoil detection ..... 159**

**Appendix E. Contact-related resistance measurements ..... 161**

I. TLM Measurements ..... 161

II. Metal Finger Line resistivity measurements ..... 164

**Appendix F. Atomic Force Microscope results ..... 165**

**Appendix G. Photoconductance decay measurement ..... 166**

**Appendix H. FIB sequential slicing ..... 167**

**Appendix I. SEM data for contact microstructure ..... 170**

**Appendix J. Focusing optics for LBIC systems ..... 172**

# 1. Introduction

## 1.1. Energy and Climate

Driven by population growth, economic development and industrialisation, the world today consumes a colossal amount of energy in its daily operations. Figure 1-1 illustrates the steady growth of major energy sources over the past three decades, as reported by the International Energy Agency (IEA) [1]. Currently, fossil fuels such as oil, coal, and natural gas account for over 80% of the global energy supply. This heavy dependence on fossil fuels is closely linked to significant greenhouse gas emissions, which are a primary driver of anthropogenic climate change.

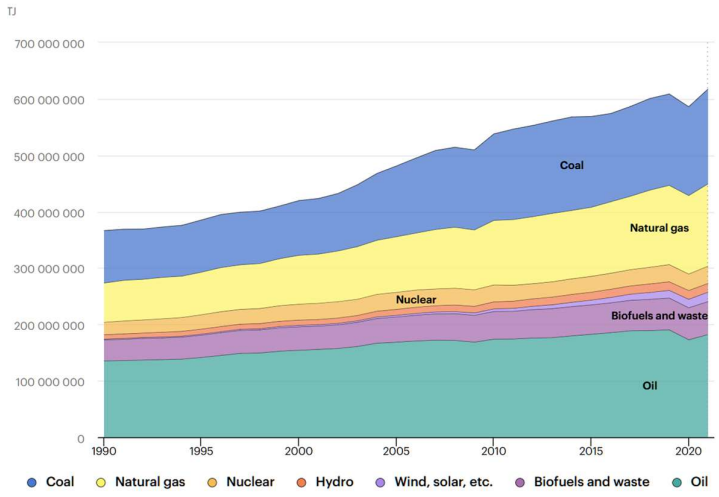


*Figure 1-1 World total energy supply by source 1990-2021, figure by the International Energy Agency (IEA)[1].*

According to the Intergovernmental Panel on Climate Change (IPCC), global surface temperature has increased 1.1°C from 1850-1900 to 2021-2020 [2]. This warming has intensified extreme weather events, rising sea levels, and widespread disruptions in natural systems. Both human societies and ecosystems are under adverse impacts from climate change with varying degrees of vulnerability. In response, the 2015 Paris Agreement set a goal to limit warming to 1.5°C and bring down greenhouse gas emissions to net zero by 2050 [3].

Figure 1-2 illustrates the $CO_2$ emission by sectors, highlighting power, industry and transport as the largest contributors [3]. To achieve the net-zero target, climate adaptation measures are being implemented across all sectors. These measures can be divided into: (a) reducing demand and improving energy efficiency, (b) direct and indirect use of renewable energy and renewable

feedstocks, and (c) carbon removal. Despite some progress, significant gaps remain between current adaptation rates and the requirements of climate goals.

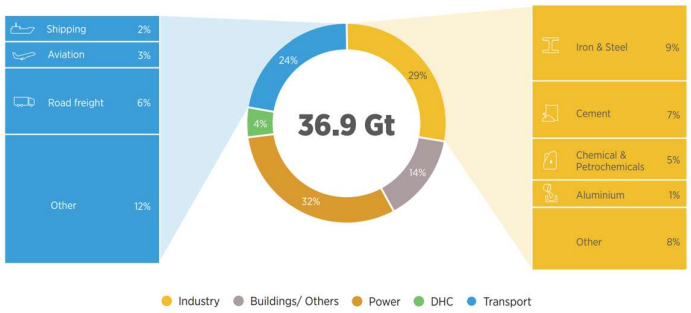


*Figure 1-2 Total $CO_2$ emissions by sector, 2017, figure by the International Renewable Energy Agency [3]*

Renewable energy sources, including solar, wind, and hydropower, are derived from natural processes that can replenish as they are consumed. Renewables produce significantly lower carbon emissions than fossil fuels, making them essential for global decarbonisation efforts. Other benefits of renewables include improved sustainability, reduced pollution and lower health risks [4]. At the 2023 United Nations Climate Change Conference (COP28), countries agreed to triple renewable energy capacity to 11 terawatts by 2030 [5]. Extensive interdisciplinary research efforts on renewables are being made to address complex challenges faced during the deployment of renewables, bringing together the fields of engineering, materials science, environmental sciences, and social sciences.

## 1.2. Photovoltaics

Solar radiation, which is the primary source of nearly all energy types except geothermal and tidal, can be converted directly into electricity through the photovoltaic effect. The first photovoltaic device was constructed in the late 19$^{th}$ century [6]. Later developments by Russel Ohl, Gerald Pearson, and colleagues at Bell Labs in the 1940s and 1950s led to the first practical Si solar cell with concepts still relevant in today's context [6]. Initially finding its application in spacecraft, solar technologies have since come a long way to become a major new addition to the electrical grid worldwide [7], [8]. According to the International Renewable Energy Agency (IRENA), the utility-scale solar cost in weighted-average levelized cost of electricity (LCOE) has seen an 85% reduction between 2010 and 2020 [9]. Thanks to technological advancements and economic upscaling, solar has become an economically competitive energy

source. This is also evident from the steady exponential growth of PV installations, doubling about every three years from 2016-2022 [9].

The key functioning unit in a working PV system is a solar module or panel, which comprises an array of photovoltaic cells. Each cell includes a photon-active absorber material and two collecting electrodes for extracting carriers of opposite polarities. PV technologies can be categorised based on the photoactive material, which broadly includes crystalline silicon and thin film materials such as perovskites, III-V semiconductors, and organic photovoltaics. As shown in Figure 1-3 [10], silicon has dominated PV production since rapid solar power expansion began, accounting for 97% of all products in 2023. It is also clear that monocrystalline material has taken over the previous shares of multicrystalline materials.

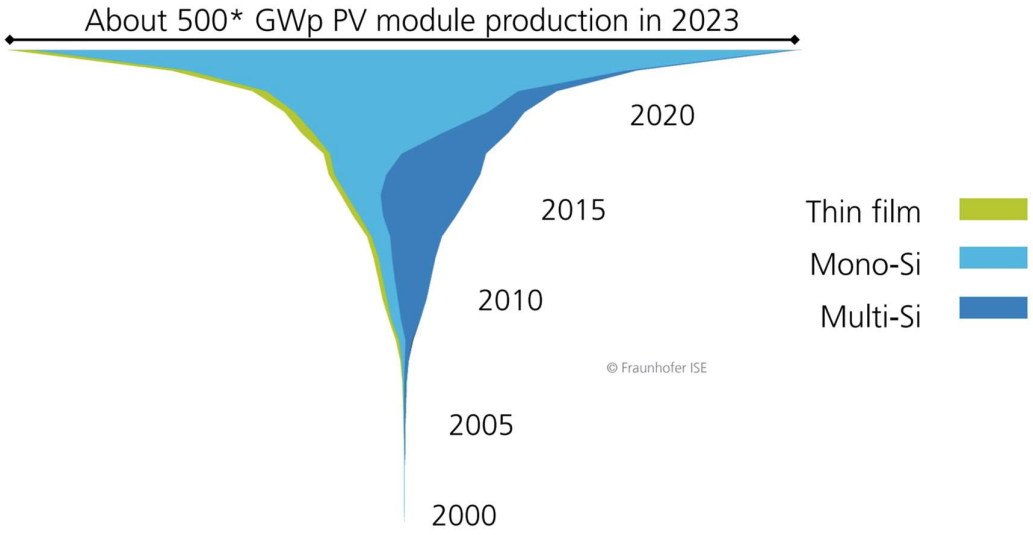


*Figure 1-3 Worldwide annual PV production by technology, figure from Fraunhofer ISE 2024 [10]*

Crystalline silicon has the major advantages of being abundant, stable, non-toxic, and well-characterised as a PV material. However, its indirect bandgap requires a larger thickness (>100 µm) compared to thin films (<1 µm) for effective light absorption. Silicon wafer manufacturing involves energy-intensive thermal processes, reflected by the energy payback time, typically over a year. Nonetheless, large-scale production and optimised industrial processing have led to continuous performance improvements and cost reductions, positioning silicon-based cells ahead in the market for decades [11].

Perovskite solar cells (PSC), introduced in the early 2010s, have rapidly gained attention in both research and industry. The name refers to the perovskite $ABX_3$ crystal structure of the light absorber layer. The most studied compositions use cations A = Methylammonium (MA)

or Formamidinium (FA), B = lead, and anion X = halogen, with multiple variants also explored [12]. PSCs have the performance potential to rival traditional silicon structures with the advantages of less energy-intensive production processes. The main challenge it faces for commercial applications is its material stability and device durability [13], [14], [15].

The power conversion efficiency (PCE) of solar cells is the central indicator for device performance and crucial to the cost of solar electricity. As of 2025, crystalline silicon solar devices have reached a PCE of 27.8% [16], while perovskites have reached 26.9% [17]. Tandem solar structures combining two or more absorbers offer a more practical approach to utilising the solar spectrum. Notably, a perovskite-on-silicon two-terminal tandem has recently reached a record 33.89% PCE [18].

## 1.3. Silicon solar cell operation

This section provides an overview of key concepts in silicon solar devices. The three fundamental physical processes essential to solar cell operation are generation, recombination and carrier transport. These are discussed along with device characteristics and key factors contributing to efficiency losses.

### 1.3.1. Generation

Photovoltaic energy conversion starts with photoexcitation, where a photon is absorbed, resulting in the generation of a pair of charge carriers (usually an electron and a hole). In a homogeneous semiconductor absorber, the absorption under monochromatic illumination with wavelength $\lambda$ is given by:

$$I(\lambda, x) = (1 - R(\lambda))\alpha(\lambda)I_0(\lambda)\exp(-\alpha(\lambda)x) \qquad 1\text{-}1$$

Where $I(\lambda, x)$ is the absorbed light intensity at depth $x$ below surface, $I_0$ is the initial intensity at surface, $R(\lambda)$ is surface reflectivity, and $\alpha(\lambda)$ is the absorption coefficient. The exponential decaying term $\exp(-\alpha x)$ comes from the attenuation of light following the Beer-Lambert law. This equation highlights the importance of the optical parameter $\alpha(\lambda)$ in determining the generation profile within the material.

The absorption coefficient $\alpha$ in a material system is tied to the quantum process of photon energy transfer. Photoexcitation occurs only when the energy of the photon matches the energy difference between two quantum states of the material system, given by:

$$\frac{hc}{\lambda} = E_{\text{final}} - E_{\text{initial}} \qquad 1\text{-}2$$

Where $h$ is Planck's constant, $c$ is the speed of light in vacuum, $\lambda$ is the absorbed photon wavelength, and $E_{\text{final}}, E_{\text{initial}}$ are energy levels difference of quantum states. The availability of these quantum states in the absorber material poses conditions on photon energies that can be effectively absorbed.

Figure 1-4 shows the absorption coefficient $\alpha$ as a function of photon wavelength $\lambda$ across different semiconductor materials. Since photon absorption mostly results in electron transition from the valence band to the conduction band in semiconductors, including silicon, the variations in $\alpha$ across materials arise from their distinct electronic band structures. Notably, $\alpha$ decreases sharply at longer wavelengths, where the photon energy falls below the bandgap, due to a lack of states for the transitions to occur. Silicon, having an indirect bandgap, requires additional phonon interactions to assist electron excitations. This requirement generally reduces silicon's absorption efficiency, which is shown by the red curve in Figure 1-4. Consequently, thick silicon absorbers are needed in photovoltaic applications compared to direct bandgap materials.

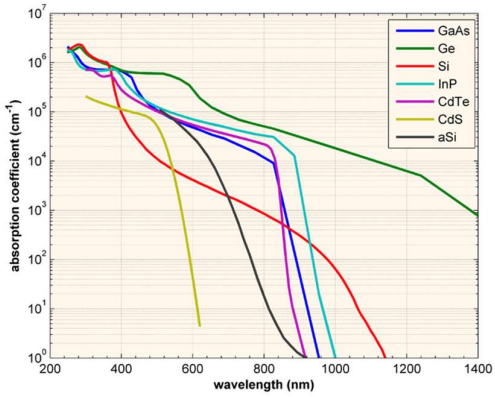


*Figure 1-4 The absorption coefficient α for different semiconductor materials at 300K as a function of wavelength λ. Figure from [19]*

In the context of solar cells, not all absorbed photon energy after generation is converted into electrical output due to inherent physical limits in the energy conversion process. Figure 1-5 describes the photon energy usable by a silicon device after accounting for losses in two steps. The outmost spectrum in Figure 1-5 shows the standardised terrestrial solar spectrum under the representative AM1.5G condition, with the acronym denoting the atmospheric (AM=air mass) and scattering (G=global) conditions. Immediately after generation, carriers with energy above the bandgap will relax to the band edges due to thermalisation. This results in a reduction in

usable photon energy as depicted in the intermediate spectrum in Figure 1-5. Additional loss can arise from entropy increase in thermodynamic cycles, which can be found analogously in heat engines [20]. Shockley and Queisser [21] calculated this second step loss in their detail balanced model to give a theoretical maximum energy conversion efficiency for silicon at ~31%. The innermost spectrum indicates the final converted photon energy as described in the S-Q limit. These three spectra in Figure 1-5 illustrate the additional limits involved in photo-electrical energy conversion, which are commonly cited as benchmarks for assessing the practical performances of solar device.

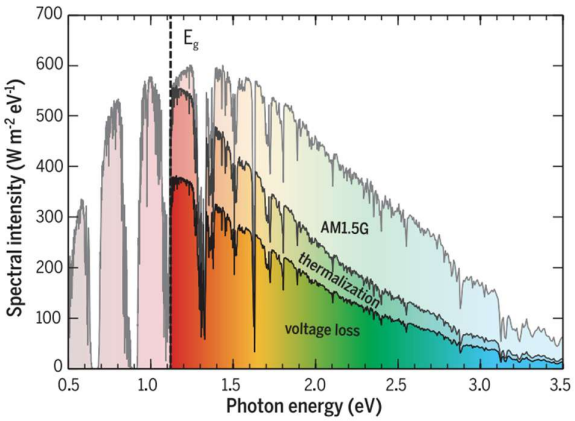


*Figure 1-5 AM1.5G photon energy spectrum, with in-between spectrum representing usable energy after thermalisation, and the inner spectrum for the voltage loss as accounted in S-Q limit. Figure from [22]*

### 1.3.2. Recombination

Recombination is the process where an excited conduction band electron falls to the valence band, eliminating an electron-hole pair. Recombination of carriers in solar cell materials reduces the excess carrier densities under illumination until a quasi-thermal equilibrium is reached. Electrons and holes have split quasi-Fermi energy levels in a solar cell device under illumination, the difference of which translates to the implied device voltage that can be extracted at contacts. Increased recombination in the device results in a reduced separation of carrier energy levels and hence major losses in device voltage outputs. Figure 1-6 describes the three major types of recombination losses in silicon: radiative recombination, Auger recombination and defect-assisted recombination [23]

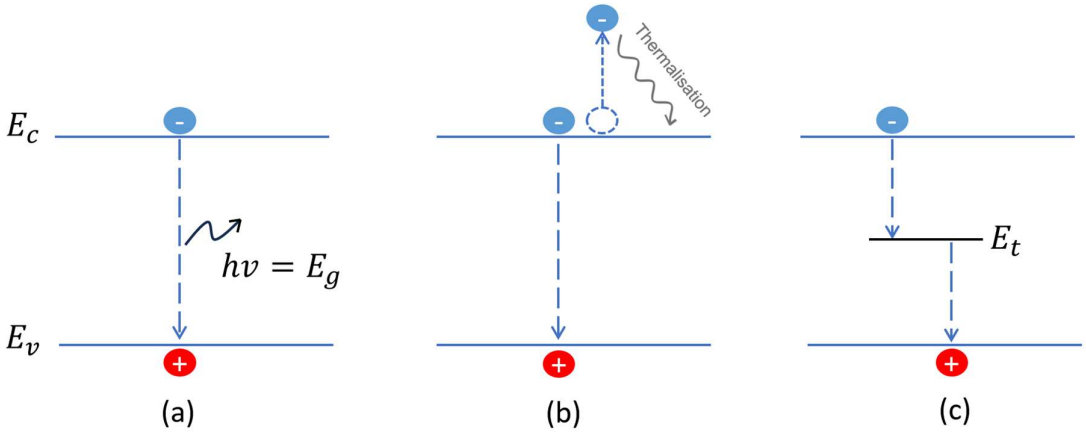


*Figure 1-6 Schematic of three types of recombination: (a) band-to-band radiative (b) non-radiative Auger (c) defect-assisted Shockley-Read-Hall recombination*

### Radiative recombination

Radiative recombination, shown in Figure 1-6 (a), is the reverse process of optical electron-hole generation, resulting in the emission of a photon at the bandgap energy $E_g$, corresponding to a wavelength centred around 1150 nm for Si. Due to silicon's indirect bandgap, radiative recombination is less likely compared to non-radiative processes. The spontaneous photon emission from radiative recombination is also referred to as luminescence, which gives rise to electroluminescence (EL) [24] and photoluminescence (PL) [25] characterisation techniques. The radiative recombination rate $U_{rad}$ is described by eq. 1-3:

$$U_{rad} = B_{rad}(np - n_i^2) = \frac{\Delta n}{\tau_{rad}} \qquad 1\text{-}3$$

Where $B_{rad}$ is the radiative recombination coefficient and $\tau_{rad}$ is defined as the radiative lifetime. While $n, p$ are spatial electron and hole densities, $n_i$ is the spatial intrinsic carrier density and $\Delta n$ denotes spatial excess carrier density.

### Auger recombination

Auger recombination, shown in Figure 1-6 (b), is a non-radiative process by which the energy from the recombination of an electron-hole pair is passed to the kinetic energy of a third free carrier. The excess kinetic energy is quickly dissipated by thermalisation. Since Auger recombination involves the participation of an additional third carrier, it becomes significant in conditions of high carrier densities, such as in heavily doped regions or under high-injection conditions. The Auger recombination rate $U_{Aug}$ is given by eq. 1-4:

$$U_{Aug} = \left(C_n n + C_p p\right)(np - n_i^2) = \frac{\Delta n}{\tau_{Aug}} \qquad 1\text{-}4$$

Where $C_n$, $C_p$ are the electron and hole Auger capture probabilities and $\tau_{Aug}$ is the Auger lifetime.

**Shockley-Read-Hall (SRH) recombination**

Shockley-Read-Hall (SRH) or defect-assisted recombination, as shown in Figure 1-6 (c), takes place via silicon crystal defects that induce electrical levels inside the bandgap. These defect states can capture electrons and holes to mediate recombination at accelerated rates. Shockley-Read-Hall theory [26], [27] formulates the defect-assisted recombination rate $U_{SRH}$ for a single defect state as eq. 1-5:

$$U_{SRH} = \frac{np - n_i^2}{\tau_{p,SRH}(n + n_1) + \tau_{n,SRH}(p + p_1)} \qquad 1\text{-}5$$

Where $\tau_{p,SRH}$, $\tau_{n,SRH}$ are SRH lifetimes for hole and electron capture processes, respectively. SRH parameters $n_1$, $p_1$ are given in the following eq. 1-6, representing carrier densities at the trap state energy $E_t$.

$$n_1 = n_i exp\left(\frac{E_t - \phi_i}{kT}\right) \quad p_1 = n_i exp\left(\frac{\phi_i - E_t}{kT}\right) \qquad 1\text{-}6$$

It can be concluded from the above equations that SRH recombination rate increases when the trap state $E_t$ is closer to the mid-gap intrinsic level $\phi_i$. This means that deep trap levels around the mid-gap are more efficient at facilitating recombination compared to shallow trap states near the band edges. Following the SRH statistics, defect energy states and their carrier capture lifetimes can be measured for silicon defects, including distributed impurity clusters, dislocations and grain boundaries [28], [29], [30].

**Surface recombination**

At the surface of the crystalline silicon material, the lattice terminates, naturally creating unsaturated atomic bonds, i.e. dangling bonds. Such structural disruptions result in the formation of a continuum of defect energy states within the band gap that mediates recombination. In contemporary monocrystalline devices, advances in wafer quality have greatly reduced bulk defects, thereby making surface recombination an increasingly dominant recombination pathway.

Surface recombination can be similarly described by the SRH statistics. The agglomerated surface recombination rate $U_s$ can be calculated by integrating SRH recombination across all defect energies within band gap as follows:

$$U_s = \int_{E_v}^{E_c} \frac{n_s p_s - n_i^2}{\frac{n + n_1}{S_{n0}} + \frac{p + p_1}{S_{p0}}} \, dE \qquad 1\text{-}7$$

Where $n_s, p_s$ are surface carrier concentrations. It is stressed here that surface parameters such as surface densities and surface recombination rate have a per area unit different from bulk rates. Additionally, $S_{n0}$ and $S_{p0}$ are electron and hole surface recombination velocities respectively, also expressed as:

$$S_{n0} = \nu_{th} D_{it}(E) \sigma_n(E) \,, \quad S_{p0} = \nu_{th} D_{it}(E) \sigma_p(E) \qquad 1\text{-}8$$

Where the surface recombination velocities are linked to the respective mean thermal velocity $\nu_{th}$, density of states $D_{it}$, and carrier capture cross-sections $\sigma_n$, $\sigma_p$.

Following such definitions, an associated surface recombination velocity (SRV), can be given as the surface recombination rate $U_s$ divided by the excess surface carrier $\Delta n_s$:

$$SRV = \frac{U_s}{\Delta n_s} \qquad 1\text{-}9$$

SRV is measured in velocity units, conceptually capturing the rate at which charge carriers travel toward the surface to recombine [31]. In reality, near-surface band bending arising from space-charge layers complicates direct interpretation of the excess carrier concentration ($\Delta n_s$) at the surface. Consequently, a lumped effective surface velocity $S_{eff}$ is typically defined at a distance $d$ from the surface, encompassing all recombination mechanisms within the near-surface region [32].

$$S_{eff} = \frac{U_d}{\Delta n_d} \qquad 1\text{-}10$$

Where $U_d$is the recombination rate at a virtual charge-neutral layer at $d$ from the surface. And $\Delta n_d$ is the excess carrier density at $d$.

The effective surface lifetime $\tau_s$ can be correlated to the surface velocity $S_{eff}$. Under symmetrical sample geometry, the relation reads as [33]:

$$\tau_s = \frac{W}{2\,S_{eff}} + \frac{1}{D}\left(\frac{W}{\pi}\right)^2 \qquad 1\text{-}11$$

Where $\tau_s$ is surface lifetime, $W$ is the sample thickness and $D$ is the minority carrier diffusivity.

Alternatively, surface recombination can also be described by a current $J_{rec,s}$ flowing towards the near-surface region at a shallow distance $d$ to the surface:

$$J_{rec,s} = qU_d = J_{0,s}\left(\frac{n_d\,p_d}{n_{i,d}^2} - 1\right) \qquad 1\text{-}12$$

This surface recombination current ($J_{rec,s}$) scales with normalised carrier densities with a coefficient $J_{0,s}$ known as a surface recombination parameter. More generally, the current parameter $J_0$ can be similarly used as a parameter for all recombination mechanisms including Auger and radiative recombination in the Shockley diode equation [34].

Both effective surface velocity $S_{eff}$ and surface recombination current $J_{0,s}$ are used in surface characterisations. However, due to dependence of $S_{eff}$ on surface doping and injection level $\Delta n$ under typical testing conditions, McIntosh [31] recommended $J_{0,s}$ as a more universal parameter. Historically, recombination in emitter layers has been described by $J_{0,E}$, a term with compatible definition with $J_{0,s}$ for a thin surface skin [35], which further supports $J_{0,s}$ as the preferred surface recombination parameter.

**Overall effective lifetime**

All the abovementioned recombination mechanisms occur simultaneously in silicon wafers. The total sample effective lifetime is reciprocally related to the sum of bulk and surface lifetimes, given by

$$\frac{1}{\tau_{eff}} = \frac{1}{\tau_{surf}} + \frac{1}{\tau_{bulk}} = \frac{1}{\tau_{surf}} + \frac{1}{\tau_{intrinsic}} + \frac{1}{\tau_{SRH}} \qquad 1\text{-}13$$

Where the sample's overall effective lifetime $\tau_{eff}$ is divided into surface $\tau_{surf}$ and bulk $\tau_{bulk}$. The bulk lifetime $\tau_{bulk}$ can be further divided into the contribution of bulk defect lifetime $\tau_{SRH}$ and bulk intrinsic lifetime $\tau_{intrinsic}$ (Auger and radiative).

Figure 1-7 shows an example from literature [36] that decomposes the effective lifetime over a range of excess minority carrier densities. The total effective lifetime curve, shown in red, is a modelled result fitted with measurement data. The three dashed curves represent the contribution from the three abovementioned components. In this sample, a shift in the limiting

recombination mechanism can be observed as the minority carrier density increases. The trend underlines the general trend that (a) bulk SRH can be important at lower minority injection levels, (b) surface recombination tends to be the limiting factor at 1-sun illumination at ~$10^{15}$ $cm^{-3}$ injection, and (c) intrinsic (mostly Auger) processes can dominate at higher injection levels. This decomposition shows how different recombination mechanisms can dominate the effective lifetime under various injection conditions.

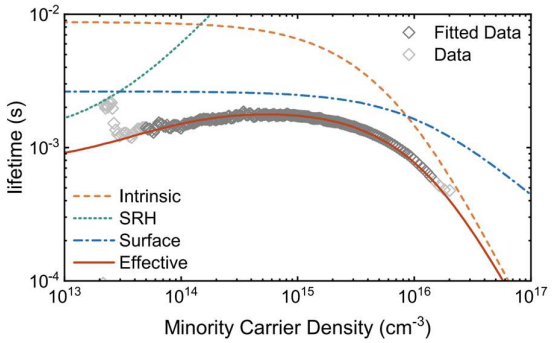


*Figure 1-7 Lifetime profiles as functions of excess minority carrier density. Three components of the fitted overall effective lifetime (red curve) are shown: intrinsic (orange curve), SRH (green curve) and surface lifetime (blue curve). The modelled effective lifetime curve is fitted to a selected range of measured lifetime data marked as fitted data, with a small proportion of data points at both the low and high injection end being ignored. This figure with its associated sample and modelling conditions is found in [36]*

### 1.3.3. Transport

#### The Drift Diffusion Transport

To understand the operation of solar cell devices, we also need to consider the dynamics of carrier transport, which is how carriers move under the influence of various forces. The carrier drift-diffusion model provides the foundational framework of carrier transport in semiconductors. This model describes the behaviour of charge carriers in response to both electric fields and chemical concentration gradients, combining drift and diffusion mechanisms [37].

The combined drift-diffusion current can be expressed as following the gradients of the electrochemical potential, also often referred to as the quasi-Fermi level.

$$\boldsymbol{J_n} = q\mu_n n \cdot \nabla \phi_n \qquad 1\text{-}14$$

Where $\phi_n$ is the electron quasi-Fermi level. The concept of the Fermi level originates from the result of the equilibrium filling of energy states following Fermi-Dirac distribution. The "quasi-" label indicates its applicability is extended to non-equilibrium conditions, such as external

carrier injection by illumination. Importantly, carrier densities are linked to their quasi-Fermi levels by definition, following an exponential expression:

$$n = n_i \exp\left(\frac{\phi_n - E_i}{k_B T}\right) \qquad 1\text{-}15$$

The intrinsic levels (intrinsic energy $E_i$ and intrinsic carrier density $n_i$) serve as the chosen reference point, though other references could be used equivalently.

The last part of the drift-diffusion model is the continuity equation, which dictates the conservation of carriers while considering the simultaneous generation and recombination in space [38].

$$\nabla \cdot \boldsymbol{J_n} - q(G - R) = \frac{\partial n}{\partial t} \qquad 1\text{-}16$$

Where the $\nabla \cdot \boldsymbol{J_n}$ is the divergence of electron current in space, $G$ and $R$ are spatial electron generation and recombination rates. The continuity equation dictates that the net balance among transfer, generation and recombination equates the change of carriers over time $\partial n/\partial t$. Under steady-state condition, there can be further $\partial n/\partial t = 0$, which is applicable in most solar cell operation situations.

As such, the drift-diffusion model describes the correlated drift-diffusion physical mechanism of carrier transport, incorporating generation and recombination processes. Its simplicity and applicability make it not only a key analytical framework but also the foundation of numerical simulation methods.

### Transport in solar devices

Within a solar cell, carriers must travel to electrodes/contacts to generate an electrical output. A selective transport mechanism ensures the separate collection of electrons and holes at opposite contacts. Traditionally, the p–n junction in a homojunction device is credited with providing this selectivity. The built-in electric field in the junction's depletion region drives electrons toward the n-side and holes toward the p-side, sweeping minority carriers across to the opposite polarity region and enabling carrier separation.

However, the idea that the built-in field is strictly required for separation has recently been questioned. Recent studies [39], [40] highlight how differences in electron and hole conductivities in various device regions can foster selective transport under illumination. Such

interpretations are particularly valuable when analysing emerging device architectures such as the silicon heterojunction, which lack a conventional diffused p–n junction.

### 1.3.4. Device Characteristics

To characterise solar cell performance experimentally, we need to start with the device-level outputs, or the current–voltage ($J$-$V$) characteristics of the cell. For a single junction silicon device, these characteristics can be modelled by the ideal diode equation with an additional photogeneration current source:

$$J = J_{ph} - J_0[\exp\left(\frac{qV}{mkT}\right) - 1] \qquad 1\text{-}17$$

Where $J_{ph}$ is the photocurrent, which depends on the generation rate under illumination. The second term $J_0[\exp\left(\frac{qV}{mkT}\right) - 1]$ is the ideal diode current following Shockley's equation, where $J_0$ is the diode dark saturation current and $m$ is the ideality factor depending on the effective recombination mechanism. Figure 1-8 (a) shows the equivalent electrical circuit of the ideal diode model.

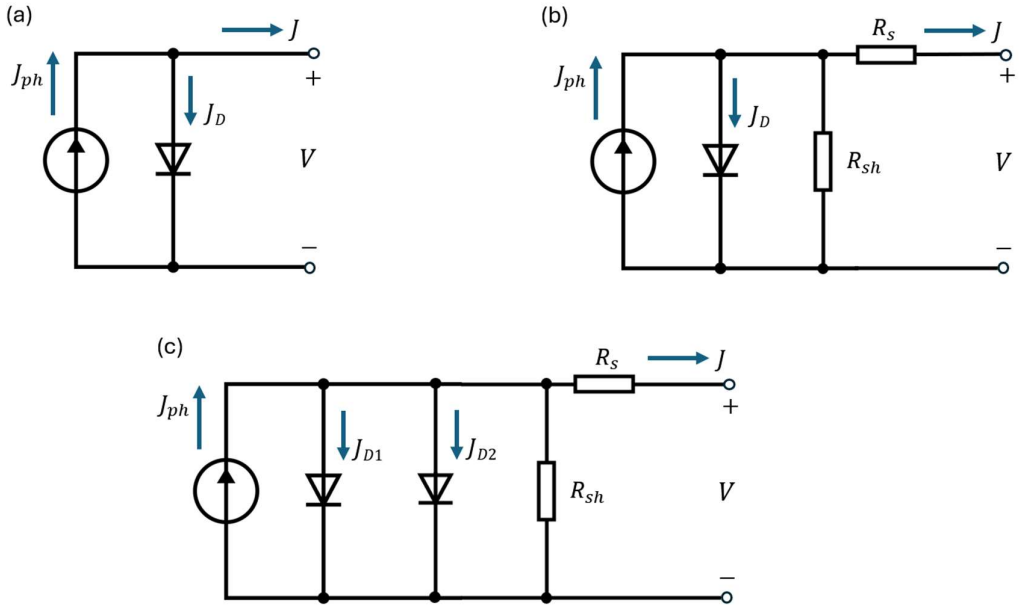


*Figure 1-8 Circuit diagram of (a) ideal diode model, (b) one-diode model with shunt and series resistances, and (c)two-diode model with shunt and series resistances.*

Importantly, the diode saturation current parameter $J_0$ represents the overall recombination in the device. The total device recombination $J_0$ can be decomposed into bulk ($J_{0,bulk}$), surface ($J_{0,s}$) and metal contact recombination ($J_{0,contact}$). Because $J_0$ is closely tied to measurable

diode characteristics, it serves as a key metric for comparing different recombination mechanisms [31].

Under practical conditions, internal and parasitic resistance cannot be ignored in the presence of currents. Figure 1-8 (b) shows the incorporation of resistive effects by adding a series component $R_s$ and shunt component $R_{sh}$. This results in the complete one-diode equation:

$$J = J_{ph} - J_0 \left[\exp\left(\frac{q(V + JR_s)}{mkT}\right) - 1\right] - \frac{V + JR_s}{R_{sh}} \qquad 1\text{-}18$$

Following eq.1-18, the $J$-$V$ and corresponding power-voltage $P$-$V$ characteristics of the solar cell can be obtained. The fill factor ($FF$) measures how close is the $J$-$V$ curve to an ideal rectangle with the short-circuit current $J_{sc}$ and the open circuit voltage $V_{oc}$ as sides. FF is defined in eq. 1-19 as the ratio between the power output $P_{max}$ at the max power point to the product of $V_{oc}$ and $J_{sc}$. The solar cell conversion efficiency $\eta$ given in eq. 1-20 can be obtained as the ratio between $P_{max}$ and the total incident power of light $P_{in}$.

$$FF = \frac{P_{\max}}{J_{sc}V_{oc}} = \frac{J_m V_m}{J_{sc}V_{oc}} \qquad 1\text{-}19$$

$$\eta = \frac{P_{max}}{P_{in}} = \frac{J_{sc}V_{oc}FF}{P_{in}} \qquad 1\text{-}20$$

Figure 1-9 (a) shows a typical $J$-$V$ and $P$-$V$ with the maximum power point marked. Excess recombination and excess resistive effects can both induce power losses as illustrated by Figure 1-9 (b)-(d). Additional recombination $J_0$ is added in Figure 1-9 (b). The increase in $J_0$ is closely linked to a decrease (leftward shift) in voltage and hence the power output. Figure 1-9 (c) and (d) demonstrate respectively the effect of additional series resistance ($R_s$) and shunt resistance ($R_{sh}$). Both resistance-related losses lead to a reduction in $FF$, which can be visualised as a loss of squareness under the $J$-$V$ curve.

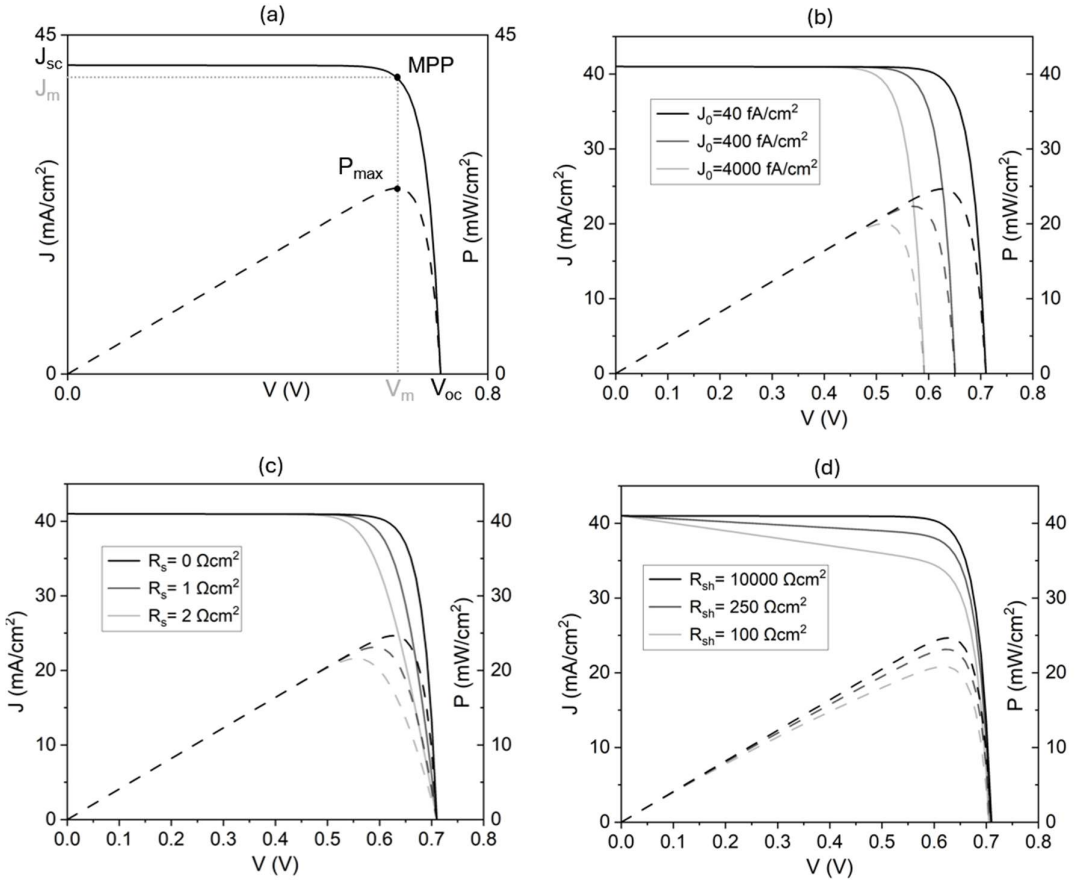


*Figure 1-9 (a) Solar cell device current-voltage (J-V) and power-voltage (P-V) characteristics following the one-diode model in eq.1-18, marked with parameters. The rest figures show effect of (b) recombination $J_0$, (c) series resistance $R_s$, and (d) shunt resistance $R_{sh}$ on device performance.*

As an expansion on the one-diode model, a revised two-diode model can be employed to account for additional recombination mechanisms. The two-diode model offers better accuracy at representing recombination at low injection conditions. The formulation of this model appends a secondary diode with ideality factor $m_2$ and recombination current $J_{02}$ [41] as follows:

$$J = J_{ph} - J_{01}\left[\exp\left(\frac{q(V+JR_s)}{m_1 kT}\right) - 1\right] - J_{02}\left[\exp\left(\frac{q(V+JR_s)}{m_2 kT}\right) - 1\right] - \frac{V+JR_s}{R_{sh}} \quad \textit{1-21}$$

## 1.4. The TOPCon solar cell architecture

### 1.4.1. Technology evolution and development of the TOPCon cell

The rapid growth of the silicon solar industry has driven major changes in device architecture over the years. Figure 1-10 illustrates three designs that have successfully transitioned from laboratory development to industrial mass production: (1) Al-BSF (aluminium back surface

field), (2) PERC (passivated emitter rear contact), and (3) TOPCon (tunnelling oxide passivated contact), also known as POLO (polysilicon on oxide). By 2024, TOPCon has overtaken its predecessors, Al-BSF and PERC, as the mainstream silicon cell technology, largely thanks to its higher energy conversion efficiency enabled by its improved contact structure.

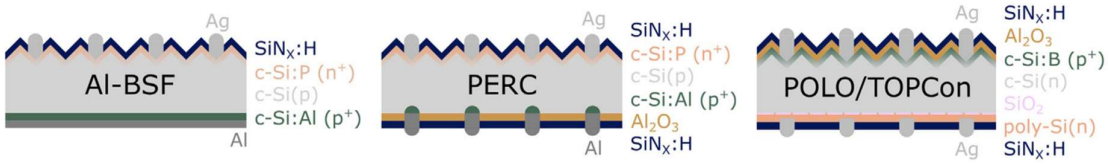


*Figure 1-10 Schematics of the Al-BSF, PERC and TOPCon/POLO architecture. Figure courtesy to [42]*

The Al-BSF design, as illustrated in Figure 1-10, represents the first industrially adopted silicon solar cell architecture and has laid the foundation for subsequent developments in crystalline silicon photovoltaics [42], [43]. Its front surface features the thermally diffused emitter [44] and a thin dielectric $SiN_x$ capping layer. The front silver contacts, in the shape of connected gridlines or metal fingers, are made via the screen-printing and firing approach. The rear side of the wafer is fully covered with aluminium, which upon firing forms local $p^+$ doping to create a back surface field (as the name Al-BSF suggests). This surface field repulses electrons and boosts hole extraction. However, the full-area intimate Al-Si contact introduces a high defect density at the interface, which incurs energy losses due to significant rear contact recombination. As a second-generation design, the PERC structure shown in Figure 1-10, is built upon the Al-BSF with modifications to both the front and rear surfaces [45], [46]. The key distinguishing feature is the addition of the rear passivation layer $Al_2O_3$ with laser ablation openings for localised Al-Si contacts. This design reduces rear contact recombination by minimising the Al-Si interface area, enabling efficiency enhancement over Al-BSF.

The direct metal-silicon (M-S) contact in both Al-BSF and PERC inherently produces a high density of defect states at the interface, leading to a high level of defect-assisted recombination. To address such contact recombination losses, passivating contact designs such as TOPCon emerge, which commonly insert a passivation layer and a conducting layer between silicon and metal to ensure a high carrier selectivity at the near contact zone. This carrier selectivity, crucial for minimising recombination while allowing efficient charge extraction, is characterised: (a) low contact resistance for the majority carrier current flow (b) low contact recombination enabled by low interface defect density and effective rejection of incoming minority carriers. Figure 1-10 shows the idealised band diagram for a silicon device with carrier-selective

contacts [47]. The improved contact passivation is demonstrated by the fact that carrier quasi-Fermi levels ($E_{Fn}$ and $E_{Fp}$ in the figure) stay well separated throughout the wafer bulk and even extended to the surface layers. The band bending ($E_c$ and $E_v$) at the surface layers, which is a result of doping, illustrates the rejection of minority carriers integral to the contact selectivity.

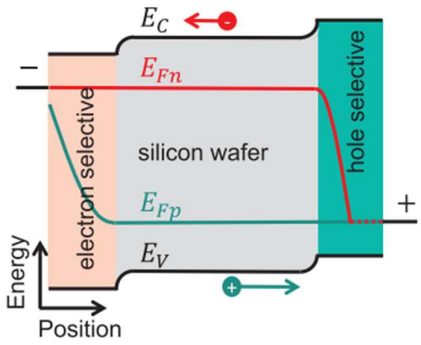


*Figure 1-11 Ideal band diagram across silicon wafer thickness showing electron and hole contacts, under illumination, figure from [47]*

The TOPCon or POLO design refers to a doped poly-Si on $SiO_x$ structure typically applied on the rear surface. The ultra-thin oxide ranges between 1-3 nm [48] and passivates the wafer bulk surface while allowing sufficient current conduction through it. Majority carrier transport through the oxide occurs via a combination of direct pinhole flow and tunnelling [49], [50]. The oxide layer can be precisely grown using a variety of methods including solution oxidation, thermal oxidation or plasma deposition [51]. The subsequent doped polysilicon layer, either in-situ doped or with an extra ex-situ doping step, is formed through designated deposition techniques, and requires a further thermal process for crystallisation. The formed doped polysilicon layer allows low electrical resistivity for current transfer both laterally and across the silicon-metal contact interface. But the heavy doping also incurs losses such as Auger recombination and parasitic absorption [52]. The TOPCon layers are capped with a hydrogen-rich $SiN_x$:H layer for further passivation. The release of hydrogen from $SiN_x$:H further reduces defect-assisted recombination in the polysilicon layer and the $SiO_x$ interface [53]. During the final metallisation firing, the applied metal paste etches through the dielectric $SiN_x$ to form an electrical contact with the underlying silicon layers. The complete rear TOPCon structure offers excellent reduction of rear contact recombination, resulting in significant $V_{oc}$ and efficiency improvements over PERC or Al-BSF. The advantage of TOPCon is demonstrated by the large-area TOPCon device efficiency record at 26.4% [54], compared to PERC at 24.5% [55] and Al-BSF at 20.3% [56].

### 1.4.2. Tackling loss mechanisms towards higher cell efficiencies

Despite the efficiency gains of the TOPCon design, there is still room for further improvements. Ongoing work is focused on identifying and tackling the remaining energy loss factors in TOPCon devices to exploit an ultimate efficiency limit up to 28% [22], [57], [58]. This section provides an overview of the energy loss mechanism and outlines potential strategies for addressing them.

**Optical losses**

Optical losses can be primarily manifested as a reduction of device current or $J_{sc}$. Processes that reduce photocurrent generation include (a) residual reflection (from the front side) and transmission (from the rear side), (b) metal shading and (c) parasitic absorption.

To reduce reflection and transmission optical losses, modern wafers use a combination of surface texturing and the anti-reflection $SiN_x$ coating (ARC) designs on both sides [59]. In addition, TOPCon devices are bifacial and can retain over 80% efficiency when illuminated from the rear [60], which boosts energy output in practical conditions by using the albedo from the ground. The metal shading optical loss arises from the physical blockage of light by the front metallisation gridlines. It is reduced by minimising metallisation coverage and gridline finger width [61].

In TOPCon devices, parasitic absorption has become the remaining optical limitation [62]. The parasitic absorption process, which results in photon absorption by parts of the cell that do not result in collectable carriers, readily takes place in both the heavily doped emitter and the poly-Si layer in the TOPCon structure [52]. Because surface doping is critical for carrier selectivity and lateral conductivity, the thickness and doping concentration of these layers are carefully optimised in a trade-off between necessary doping functionalities and doping-related losses. Recent research efforts have turned to strategies such as selective doping, using dopant-free heterojunction contact layers [63] or relocation junctions to the rear [57] to mitigate parasitic absorption losses.

**Recombination in bulk**

Because of silicon's relatively low absorption coefficient, silicon cells require a thick absorber (usually around 150 μm) bulk compared to thin-film cells (< 500 nm). This allows a large room for bulk recombination losses to happen. As the industry shifts towards the TOPCon architecture, monocrystalline wafer substrates produced via the Czochralski (Cz) crystal

growing process have replaced formerly dominant multi-crystalline wafers. The lower defect density in monocrystalline bulk translates into higher effective lifetimes suitable for high-efficiency designs.

However, long-term performance studies of monocrystalline wafers have identified degradation of bulk quality under operation conditions. Boron-doped p-type monocrystalline wafers are affected by a reduction in minority carrier lifetime upon illumination known as light-induced degradation (LID), the mechanism of which is linked to the metastable boron-oxygen defects [64], [65] [66], [67]. The formation of BO defects is related to the thermally activated process of mobile interstitial oxygen capturing by boron [68]. The BO defects can be cycled between electrical states through a combination of illumination and temperature conditions, which enables partial lifetime recovery via annealing or light soaking [69], [70]. Additionally, because of the extensive introduction of hydrogen for bulk defect passivation in TOPCon routes, wafer lifetime degradation can also occur because of hydrogen movement in a process referred to as light and elevated temperature-induced degradation (LeTID) [71].

Because of the detrimental effects of LID and LeTID, solar cell manufacturers have swiftly shifted to gallium for p-type doping [72], which is less susceptible to the formation of metastable defect states; or to n-type bulk entirely. Such successful avoidance of bulk defects has, in turn, made fundamental Auger recombination the dominant bulk process in high-quality n-type monocrystalline devices with 26%, according to Richter et al [73].

### Surface and contact recombination

As previously outlined in section 1.3.2, the surface of silicon exhibits high recombination activity due to the presence of a high density of sub-bandgap defect states. Modelling work on assessing surface recombination has shown that even a very low front emitter surface recombination $J_{0,e}$ value at ~7.5 fA/cm$^2$ can induce a high-efficiency loss of 0.5 %abs. Surface losses in silicon devices have been effectively mitigated by the deposition of a dielectric surface passivation layer, such as the silicon nitride capping layer in TOPCon [74]. The dielectric layer supresses surface recombination via a combination of two mechanisms [74], [75], [76]: (a) reduction of the density of surface defect states by satisfying the surface dangling bonds, known as chemical passivation and (b) introduction of built-in surface charges to reject incoming minority carriers, known as field-effect passivation [77]. Additionally, the surface dielectric film contains hydrogen, which is released during processing to further improve

passivation at key interfaces. Due to its relevance to this thesis, an in-depth discussion of hydrogen passivation can be found in section 1.5.

The surface passivation layer must be partially disrupted at the metal-silicon contacts to allow sufficient current transfer, which leaves room for excess recombination at the M-S interface. For fire-through metallisation schemes using silver, the glass frit component in the metal paste reacts with dielectric passivation layer upon firing. Silver in the paste partially dissolves in this process and precipitates when cooled as finely dispersed nanocrystals in a glass interface layer between metal and silicon [78], [79]. However, extra silver deposition on the silicon surface known as 'spiking' can cause a high local density of metal-induced defect states, associated with significantly elevated recombination currents. Studies on front surface metallisation on thermally diffused emitter layers have reported front fire-through contacts with extremely high contact recombination current $J_{0,c}$ >1000 fA/cm$^2$ [80], [81], a value found to be largely influenced by the emitter doping profiles [82].

For passivated contact structures, recombination at the metal interface is reduced but still significant compared to passivated surfaces. Reported $J_{0,c}$ values for TOPCon rear contacts have seen a reduction from 100-400 fA/cm2 [83], [84] to recent cases below 50 fA/cm2 [85], [86]. The reduction of TOPCon $J_{0,c}$ is achieved with careful tuning of poly-silicon layer crystallinity and doping profiles.

**Current transport losses**

Current transport losses refer to resistive losses throughout the current paths, which can be significant at locations with high current densities. The total device resistance can be separated into bulk resistance, lateral transport resistance in surface layers, resistance at the metal-silicon interface, and external metal resistance [61]. These resistive losses can amount to ~0.6%abs efficiency loss in a front junction solar cell, according to Richter et al [57]. Minimising such resistive losses is integral in the TOPCon contact designs. For example, the n$^+$ poly-silicon layer serves the key functionality in enhancing conduction, which enables sufficient lateral current collection and lowers the metal-silicon contact resistivity.

In summary, a detailed investigation into the remaining energy loss factors is central in the effort towards pushing the efficiency of TOPCon architecture to the ultimate silicon limit. As structural adaptations and new fabrication methods are developed, reliable and accurate evaluation of their impact is crucial to pinpoint even the smallest improvement in mitigating energy losses. This thesis focuses on assessing TOPCon performance by characterising its

contact recombination and contact resistance, which are key energy loss pathways. Further microstructural analyses explore how the electrical properties of TOPCon correlate with interface morphology and chemistry. These detailed evaluations offer insights into the fundamentals of contact selectivity and provide a foundation for future TOPCon optimisation.

## 1.5. Hydrogen Passivation

### 1.5.1. Overview

Hydrogen passivation refers to the suppression of recombination in either the wafer bulk or surface layers by deliberately introducing hydrogen. Hydrogen passivation has become a crucial step in improving the minority carrier lifetime of silicon wafers. When introduced into silicon, hydrogen atoms can effectively bind to unsaturated bonds at defect sites and become immobile, known as hydrogen trapping. Hydrogen incorporation results in reduced electrical activity of various crystal defects [87], [88] and interfaces [89].

The most common method for hydrogen incorporation is through controlled hydrogen release from the H-rich surface dielectric film, which includes two steps. The first step is the deposition of a hydrogenated film, most typically a silicon nitride ($SiN_x$:H) layer by PECVD (plasma-enhanced chemical vapour deposition) [90]. During the PECVD process, plasma reaction at the surface introduces local damages such as dislocation tangles and stacking faults. According to Bhushan et al. such damages work as processing-induced traps to temporarily store H near the surface [91]. A subsequent high-temperature annealing step is needed for adequate H release into the bulk. Figure 1-12 illustrates a comparison of calibrated photoluminescence images (a description of PL is found in the methodology) of a boron-doped Cz wafer before and after hydrogen anneal [92]. The disappearance of dark rings from B-O defects and the improvement of image brightness show the excellent passivation efficacy achieved with the H release. Hydrogen can also be introduced via other routes, including microwave-induced remote hydrogen plasma (MIRHP) techniques [93], low-energy hydrogen implantation [94] or forming gas ($N_2$+$H_2$) anneal [95], [96].

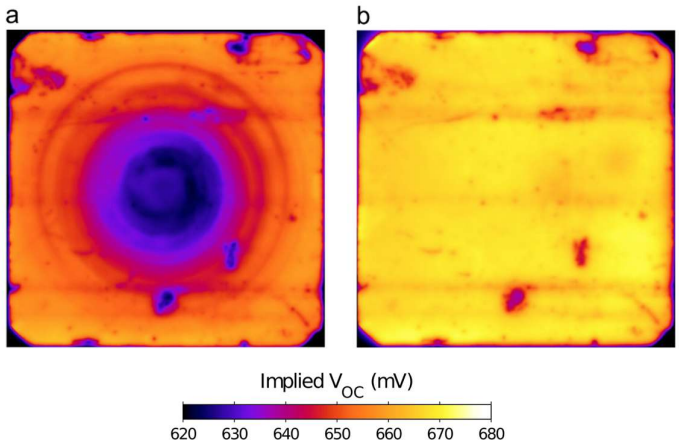


*Figure 1-12 1-sun implied $V_{oc}$ map as calibrated PL images of a boron-doped Cz wafer (a) with SiNx:H surface layer deposited but before H anneal (b) after H anneal. The oxygen precipitate defects are revealed by the dark segregation rings at the centre in (a) but completely passivated in (b). Wafers used in the work are 125×125 mm in size [92].*

Recent studies reported that the effectiveness of hydrogen passivation can depend strongly on the processing conditions [97], [98]. The reduction of passivation effectiveness is attributed to atomic hydrogen occupying low mobility or low reactivity charge states [98]. This can be mitigated by light soaking which is shown to increase the concentration of mobile neutral-charge state hydrogen [99], [100]. Thermal dissociation of hydrogen-defect complexes can happen through the processing steps, making fast-firing steps difficult to tune. Prolonged thermal exposure can also drive hydrogen out of the wafer or lead to hydrogen clustering rather than bonding at active defects [101].

### 1.5.2. Hydrogen at silicon defects

Studies on hydrogen migration behaviour in silicon bulk have reported its strong dependence on the presence of hydrogen traps [102]. High-temperature hydrogen diffusion in monocrystalline silicon is relatively fast with a low activation energy [103]. On the other hand, the mechanism of hydrogen diffusion in the presence of silicon defects is under debate. Jackson et al. argued that GBs in poly-Si thin films are efficient hydrogen traps rather than diffusion enhancer [104], which is in contradiction to common reports of improved diffusion length through GBs [105], [106] or dislocations [107], [108]. It is safer to say that impurity-decorated GBs and dislocations can act as either faster diffusion channels or hydrogen traps depending on defect types, impurity levels and thermal conditions. When trapped at electrical active sites in the bulk, monatomic hydrogen can bond to defects with deep-level states. It is suggested that metal hydride complex formation and coordination of Si dangling bonds both contribute to a reduction of the density of deep-level centres [109], [110].

Hydrogen passivation is not uniformly efficient across all defects. The efficacy of passivation can be related to both the defect type and the density of impurity atoms at the defect sites [111], [112]. Bertoni et al. suggested a correlation between a high degree of GB faceting and a clearer response to passivation [113]. Chen et al. reported a weaker passivation effect for random and small-angle GBs, which is not consistent with results from Bertoni. It is however agreed that in highly contaminated wafer regions, passivation of all types of GBs becomes less efficient [112]. Passivation of dislocations and dislocation clusters by hydrogenation is less frequently discussed [108], [114], possibly due to difficulty in characterisation.

### 1.5.3. Hydrogen in TOPCon structure

In the TOPCon structure, the hydrogen is released from the H-rich dielectric layer capped on top of the passivation stack. This $SiN_x$:H coating has become ubiquitous since its stoichiometry is tunable, allowing variation in hydrogen content. Atomic hydrogen from this layer is released during contact firing, which can reduce the concentration of electrically active defect states at the interfacial oxide [115] and likely also within the poly-Si layer [89]. The high-temperature firing step is essential in redistributing the hydrogen through the TOPCon. The efficacy of hydrogen uptake plays an essential part in TOPCon passivation.

Several studies have recently reported a firing-induced degradation in TOPCon passivation related to hydrogen [116], [117], [118], [119]. This degradation mode can lead to a four-fold increase in surface $J_0$ and is solely attributed to a deterioration of surface passivation [120]. Some studies have identified a relation between excess H content at the $SiO_x$ interface and deterioration of passivation in n-type TOPCon [121], [122]. Figure 1-13 illustrates the hydrogen profiles after firing at a range of temperatures measured by secondary ion mass spectrometry (SIMS). The increasing wafer $J_0$ associated with a higher firing temperature, is linked to a higher H dose at the presumed oxide location. This indicates that the fast-firing step for contact formation could increase atomic hydrogen concentration at/near the interfacial $SiO_x$, which can either (i) substantially improve surface passivation or (ii) cause severe surface-related degradation, depending on the amount of hydrogen dose. In contrast to such findings, Polzin et al. investigated the thermal stability of a hydrogenated TOPCon structure without a dielectric capping layer and attributed the loss of passivation to hydrogen out-diffusion upon thermal treatments [117]. The authors revealed that inserting a thin $AlO_x$ layer between polysilicon and $SiN_x$ can enhance thermal stability by obstructing the hydrogen out-diffusion movement. Hamman et al. [123] suggested in their review the existence of an upper limit of

hydrogen incorporation to prevent surface-related degradation in $AlO_x/SiN_x$ passivated structures.

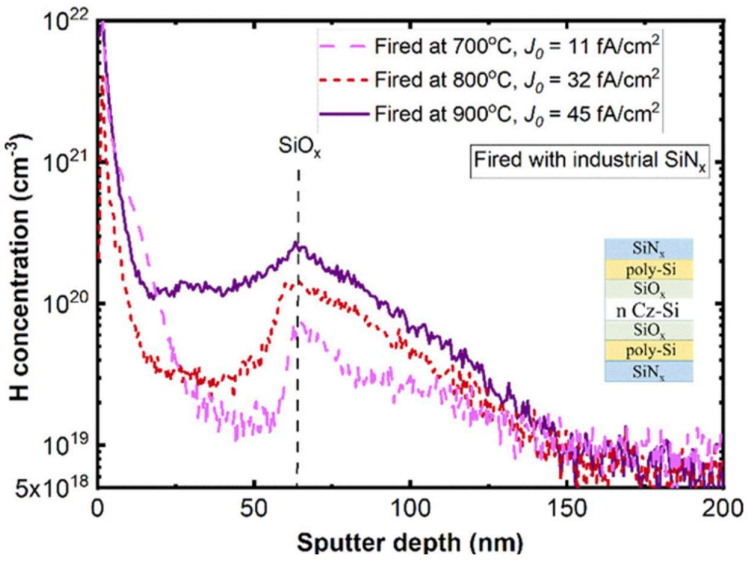


*Figure 1-13 SIMS hydrogen profiles of a symmetrical TOPCon structure with an industrial $SiN_x$ capping layer, fired at temperatures from 700 °C to 900 °C. Associated sample $J_0$ after firing is marked along with the profiles [121]*

As such, despite widespread recognition of the usefulness of hydrogen introduction in TOPCon structure, its behaviour and passivation efficacy under various processing conditions remain unclear. An evaluation of the hydrogen distribution within the structure would help the understanding of the hydrogen interaction with interfaces and defects within the TOPCon structure, further facilitating the understanding of interface passivation mechanisms. This thesis employs state-of-the-art chemical characterisation techniques with nanoscale resolution and improved analytical accuracy—both essential for assessing hydrogen distribution in the complex TOPCon architecture.

## 1.6. Aims and Objectives

This thesis aims to evaluate key contact properties of the TOPCon solar structure. It also aims to link microstructural and chemical interface characteristics to changes in electrical behaviour. The overall aim can be split into the following:

1. Developing and implementing an in-situ method to accurately quantify recombination losses at the contact interface.
2. Evaluation of contact electrical properties, identifying variations associated with modified TOPCon processing.

3. Detailed microstructural investigations of the TOPCon interfaces to identify morphological variations associated with modified processing.
4. Assessing the hydrogen distribution in hydrogenated TOPCon by two complementary chemical analysis methods to clarify the role of hydrogen in TOPCon passivation.
5. Development of an optoelectronic method in investigating spatial current collection variations across a broader range of solar devices.

## 1.7. Structure of the thesis

Chapter 1 presented the fundamental context, focusing on photovoltaic principles and device physics. It also highlighted the developments of silicon device architectures, including the TOPCon structure, which is the main subject of investigation in this work. It ended with the remaining energy loss factors in silicon devices, which underlined the importance of detailed characterisation in understanding and addressing these losses.

Chapter 2 to 6 detail the experimental results. Because each chapter uses different characterisation techniques, separate methodology descriptions and literature backgrounds can be found in individual chapters and associated appendices.

Chapter 2 presents an in-situ approach in evaluating TOPCon contact recombination, eliminating the need for ex-situ sample preparations. Chapter 3 presents electrical characterisations of TOPCon contacts with modified processing. The microstructural analysis is performed to establish links between morphology and performance. Chapters 4 and 5 employ two complementary chemical profiling routes to evaluate the distribution of hydrogen and other elements in hydrogen-passivated TOPCon structure. Chapter 6 presents an independently developed optoelectronic characterisation technique to reveal current collection variations in various solar devices.

The final section, Chapter 7, summarises the key findings from each chapters and highlights the directions for future work.

# 2. PL assessment of metal recombination $J_{0,c}$: the Fourier analysis approach

The methodology and results presented in this chapter have been accepted for publication in the journal EES Solar as *'Extracting Contact Recombination from FFT-Filtered Photoluminescence Imaging of Half-Metallized Silicon Solar Cells"*.
The author would like to thank Dr. Andreas Fell for running parallel Quokka3 simulation for confirmatory tests included in this chapter.

## 2.1. Introduction

The recombination parameter $J_0$, representing the dark recombination current density, is a widely adopted standard for evaluating recombination processes [34],[124]. To distinguish recombination contributions from contacted versus non-contacted surfaces, the contact-related $J_{0,c}$ is used explicitly for the recombination at the metal-silicon interface in contrast to the free surface $J_{0,s}$, with $J_{0,c} > J_{0,s}$ as a general assumption. $J_{0,c}$ is hence further established as an important contact metric, adopted in both experiments and simulations for silicon architectures such as TOPCon [125], [126]. As discussed in section 1.4.2, contact recombination at TOPCon interfaces, although comparably lower than emitter contact recombination, remains a contributor to the energy conversion losses. Therefore, the ongoing developments of the TOPCon architecture depend critically on reliable and accurate assessments of contact $J_{0,c}$ as a key performance indicator.

A promising way to extract $J_{0,c}$ values for the TOPCon contacts is through photoluminescence imaging (PLI) measurements aided by device simulation. Photoluminescence imaging provides a fast, versatile, non-destructive method for wafer and device characterisation [25]. During standard PL experiments, the silicon sample is under constant illumination for carrier generation under steady-state conditions. The radiative recombination of the excess carriers gives rise to the luminescence signal detected by an imaging camera. The luminescence emission intensity depends on the fraction of excess carriers undergoing radiative recombination [127]. This allows quantitative analyses of PL to assess carrier loss mechanisms, including the effect of contact recombination $J_{0,c}$. A detailed description of PL basic principles is given in Appendix A.

Early studies used samples with varying metallisation coverage fractions to delineate the metal contribution. The common assumption used is that the overall areal surface $J_0$ is the sum of

contributions from metallised and unmetallised surfaces. Hence, by a linear fitting of the overall $J_0$ to the metal fraction, the area-weighted metal recombination $J_{0,c}$ is separated [128]. Further PL investigations on this topic are aided by modelling tools such as Quokka and Griddler [126], [129], [130]. Griddler modelling allows electrical connections among components with different $J_0$ values to better interpret the effect of metal recombination on overall PL. Work by Hermann [131] et al. used Quokka 3 to account for non-uniform carrier density distribution in spatial PL modelling, which facilitates more accurate $J_{0,c}$ parameter determination. Hermann's work extracted $J_{0,c}$ within regions with varied metallisation geometries and observed variation of $J_{0,c}$ both at different wafer locations and with different finger widths [132], [133]. A major limitation of these approaches is that they require specially designed metallisation patterns with regions of varying metallised fractions. This added difficulty in tailored sample making prevents wider applications in regular solar cell production line metrology.

In an effort to utilise the spatial periodicity of the metal grid pattern, Saint-Cast et al. [134], [135] employed the Fourier transformation in the analysis of PL data. In their method, the PL signal is converted into $V_{oc}$ maps after calibration with a contact voltage measurement. Their work used an analytical model to derive an estimated average PL intensity and its oscillation amplitude based $iV_{oc}$ and emitter contact $J_{0,c}$. Experimental data from PL can hence be compared to the model outputs to estimate the sample $iV_{oc}$ and $J_{0,c}$ values. However, their method utilised samples with contacts on the imaging side, which introduces an inherited inaccuracy: part of the periodicity in PL images originated directly from the metal finger shading, complicating the determination of contact recombination.

Here, the author proposes an innovative PL methodology to extract $J_{0,c}$ based on Fourier data analysis. The method can be applied directly on wafers contacted with finished grid metallisation as used in industrial applications. My method is comparable to Saint-Cast's approach due to the coincidental adoption of Fourier analysis of image periodicity. However, the independently developed route in this study circumvents finger shading limitations and adopts device modelling for improved PL data interpretation accuracy. The following sections 2.2 to 2.6 are dedicated to the explanation of the methodology, covering experimental conditions, PL imaging results, data analysis and simulation approach for data interpretation. Section 2.7 provides a case study application of the method. Section 2.7 provides a discussion on experimental factors underlying the efficacy of this method.

## 2.2. Experimental Details

Figure 2-1 (a) depicts the half-metallised TOPCon sample structure. They are 210×210 mm monocrystalline Si cell precursors with $AlO_x$ passivated diffused boron emitter at the front, and a poly-Si on oxide TOPCon structure at the rear, both capped with a silicon nitride surface passivation layer. Industrial silver metallisation via screen printing and fast-firing was applied only to the rear TOPCon surface. The silver metallisation fingers formed a grating/grid pattern. A finger width of 30 µm and a finger pitch of 1.5 mm were measured with optical microscopy. Figure 2-1(b) depicts the room temperature photoluminescence imaging setup. The PL system by BT imaging has a 650 nm LED array as the illumination source. An Apogee AltaF silicon CCD camera with a Kodak KAF-3200ME sensor was used with the default optical filter by BT Imaging. Due to the low quantum efficiency of the silicon sensor at the sample's luminescence wavelengths, a high sensitivity setting was required, which resulted in amplified pixel noise. Future studies should consider using specialised sensors to reduce sensor noise and improve image quality. The camera offers a resolution of 2184 × 1472 pixels. The samples were placed on a low-reflectivity black stage to reduce back reflections, with the metallised TOPCon side facing down and the non-metallised emitter side facing up. An image integration time of 12 seconds was consistently used for all images. To mitigate camera sensor noise, five images per sample were acquired and averaged. Unless otherwise noted in designated illumination tests, PL experiments were conducted under an illumination intensity equivalent to 1-sun.

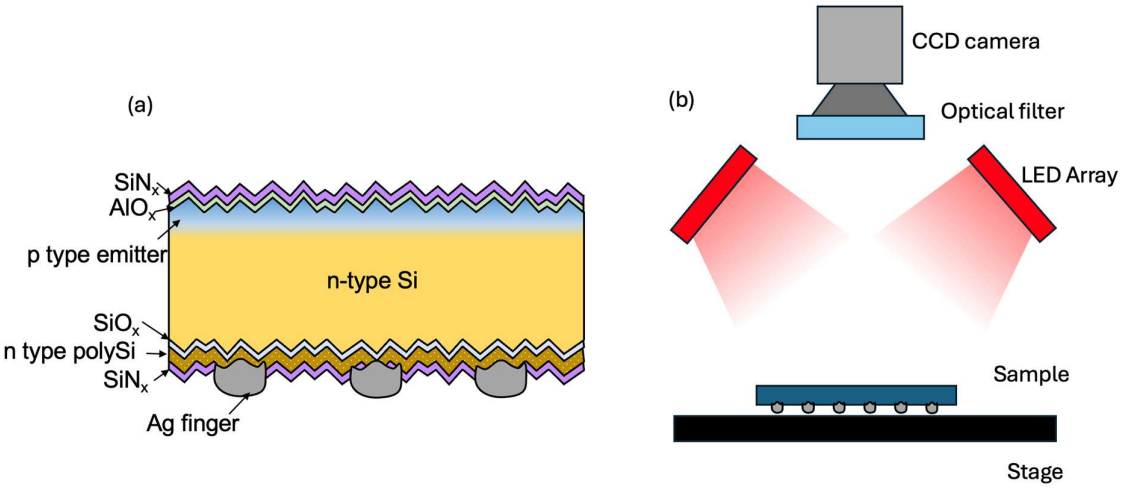


*Figure 2-1(a) The half-metallised TOPCon sample structure. (b) Schematic of the PL setup, the sample has the metal side facing down*

## 2.3. PL imaging data

The following Figure 2-2 (a) shows the imaging field of PL as viewed from the rear metallised surface, which is marked by the dashed rectangle covering the central 170×115 mm. Note that PL images are taken from the unmetallised front side instead. Figure 2-2 (b) is an example of an acquired full PL image, covering a region containing a total of 112 vertical metal fingers from left to right. The pixel size of the image is calibrated according to the field of view dimension to be 78 µm per pixel. Spatial sampling at 78 µm/pixel leads to information loss when evaluating detailed carrier distribution profiles between individual fingers, given that the estimated sample diffusion length ranges from approximately 800 to 2500 µm. Direct assessment of PL profiles in the spatial domain is inadequate for reliably correlating with metal-related losses, and an alternative method is required. Important features in the PL image are revealed in the two following close-ups in Figure 2-2 (b). Region A shows stripes with shallow contrast following the rear metal grid, which is a 1D periodic grid. Region B contains dark defective patches that typically originate from manual handling. Such features cause significant PL intensity drops, which can mask the contrast from the stipes.

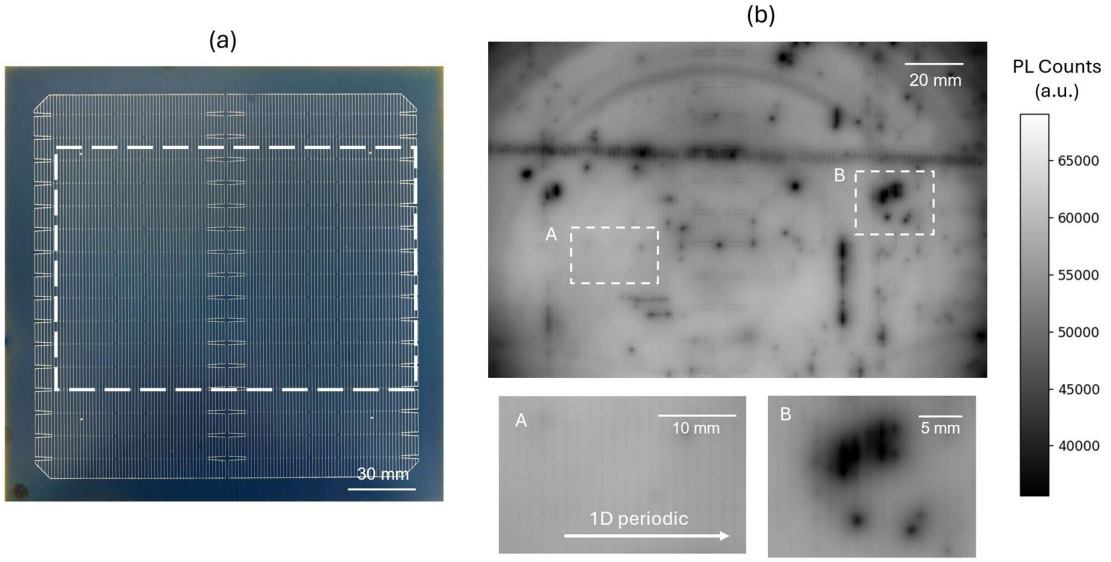


*Figure 2-2 (a) Metallisation grid pattern on a 210×210 mm wafer, the square indicates the field of view for PL imaging. (b) An PL image example taken with metallisation on the rear, with close-ups of region A and B*

Notably, the periodic PL intensity variation shown in region A, is a result of excess metal recombination at the metal-silicon interface. In other words, since $J_{0,c} > J_{0,TOPCon}$, recombination of excess carriers happens excessively at metal surfaces, causing lower local PL

intensity. This PL spatial variation, hereafter referred to as the metal contrast, is exploited to quantitatively assess $J_{0,c}$.

The direct description of such spatial variation is obstructed by the superimposed long-range spatial features in Figure 2-2 (b), as well as the camera pixel noise. To deconvolve the periodic signal from noise, Fourier analysis is employed in PL data analysis to enhance signal detection. Fourier transformation enables the isolation of the periodic signal associated with metal contrast, which allows for noise filtering and enhances the detection of the metal contrast. This process of Fourier data analysis is described next.

## 2.4. Fourier analysis of PL data

The Fourier data analysis method is based on the Fourier transform, a mathematical integral transformation. For a discrete PL signal array of finite length, one-dimensional (1D) Discrete Fourier Transform (DFT) is applied, as formulated in eq. 2-1.

DFT: $$X_k = \sum_{n=0}^{N-1} x_n e^{-i2\pi \frac{k}{N} n} \quad 2\text{-}1$$

This process converts the spatial domain series $x_n$ into a complex-valued (spatial) frequency domain series $X_k$. Where $x_n$ is the $n$-th element of the space domain series, $X_k$ is the $k$-th element of the frequency domain series (complex valued), and $N$ is the total sample number. The inverse Discrete Fourier Transform (IDFT), shown in eq. 2-2, converts the frequency domain representation back to the space domain.

IDFT: $$x_n = \frac{1}{N} \sum_{k=0}^{N-1} X_k e^{i2\pi \frac{n}{N} k} \quad 2\text{-}2$$

In practice, the computationally efficient Fast Fourier Transform (FFT) algorithm is used in scientific data processing, which is a rapid implementation of DFT.

Figure 2-3 (a)-(d) illustrates the four-step Fourier analysis process based on an experimentally measured PL image. Data processing and analysis were performed using Python 3.11.7 with package SciPy.

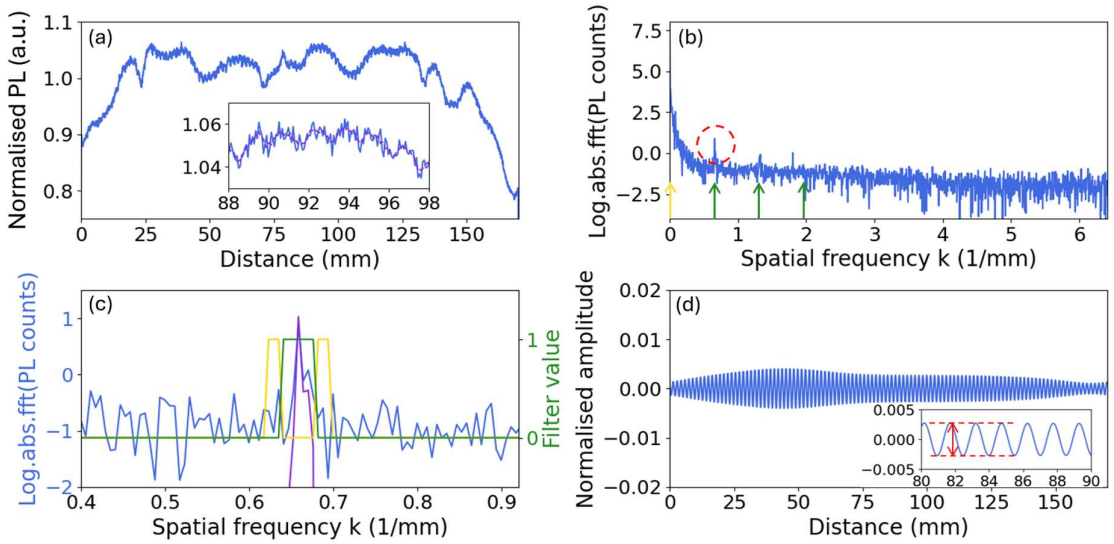


*Figure 2-3 (a) Original PL counts in x-domain along a line profile in the horizontal image direction, with inset showing noise-covered periodicity. (b) FFT- transformed line profile in k-domain. (c) A zoom-in in k-domain towards the peak at the fundamental metal line frequency, with filter windows displayed as overlays. (d) Reconstructed signal and with an inset showing wave amplitude.*

Figure 2-3 (a) is a line profile $x_n$ along a random line from the above PL image, showing the normalised photoluminescence intensity as a function of distance. The PL counts detected at each pixel are normalised to the line average intensity to demonstrate only relative variations. A notable feature of this profile is long-range dips from sample imperfections. The inset plot is a zoom in within a 10 mm region, with the additional dashed curve representing the moving average of 5 adjacent pixels. The moving average trendline reveals the periodic pattern covered in camera pixel noise. Such a heavy noise superimposes on the periodic metal variation signal, which needs to be subtracted.

Figure 2-3 (b) presents the frequency-domain spectrum of the line profile after applying the Fast Fourier Transform (FFT). Here, the y-axis represents the complex modulus of the Fourier-transformed series $X_k$, while the x-axis displays the positive half of the frequency range from 0 to half the sampling rate. The prominent initial peak at zero frequency $X_0$, as indicated by the yellow arrow, is related to the numerical sum of the series.

When a periodic signal undergoes Fourier analysis, fingerprint peaks, i.e. sinusoid components, appear at the fundamental frequency as well as its higher harmonics. In Figure 2-3 (b), the first three harmonics of the metallisation frequency (~0.66 $mm^{-1}$) are marked by green arrows. Given that weaker peaks at higher harmonics (order number $n \geq 2$) blend into the noise floor, only the first harmonic, as circled in Figure 2-3 (b), is under analysis.

Figure 2-3 (c) takes a closer look around the marked peak at the first harmonic. It can be observed that the noise floor level is significant, lying only about 1.5 units below the peak on a natural base logarithmic scale. The broadband k-space noise floor is a result of decomposed space domain noise sources. A band-pass filter (green) centred around the 0.66 $mm^{-1}$ frequency is used to isolate the metallisation signal, with a filter bandwidth set at 0.04 $mm^{-1}$. Average noise levels are estimated from adjacent normalisation windows (yellow) with a bandwidth of 0.02 $mm^{-1}$. The noise level is first subtracted from the signal in the normalisation process. Subsequently, the rectangular band-pass filter (green) is applied to cut out frequencies outside the window. The resulting noise-subtracted and frequency-filtered signal is shown in purple.

Figure 2-3 (d) displays the waveform reconstructed from the filtered signal using the inverse Fourier transform. Due to the rectangular band-pass filtering, this wave has an enveloped appearance. The key information is the amplitude of the oscillation, which is used to calculate the metal-induced PL periodic contrast $C_{metal}$, given by:

Metal Contrast:
$$C_{metal} = \frac{A_{ave}}{S_{ave}} \times 100\% \qquad 2\text{-}3$$

Where $A_{ave}$ is the average amplitude of oscillations in the reconstructed signal. It is the average of the differences between each adjacent maxima and minima, as highlighted in by the red arrow in Figure 3 (d) inset. $S_{ave}$ denotes the average signal level of the line profile, with $S_{ave} = 1$ in this case, since the PL signal has been normalised. The percentage metal contrast $C_{metal}$ is defined as the figure of merit in contact characterisation, representing the metal-induced variation over the average in PL profiles.

The FFT metal contrast of the full image is obtained by summing the results from all horizontal lines, since only periodicity in the horizontal direction is relatable to the metal. This process is hence applied to all the measured PL images, which can be further extended to all industrial samples with known metal periodicity.

## 2.5. Device simulation for PL experiments

### 2.5.1. Simulation approach

Detailed device simulation is required to provide a physical interpretation of the PL data and the metal contrast. In this section, sample electrical (spatial carrier distribution) and optical (PL emission) responses under experimental conditions are modelled with numerical simulation tools. Two comparable approaches using specialised silicon cell simulation programmes: (A)

PC3D [136] and (B) Quokka 3 [137] are employed in this section. Both tools offer 2D numerical device simulation capabilities, which have increased result accuracy over the 1D analytical framework previously reported in [138] by considering the depth-dependence of carrier distribution.

Both PC3D and Quokka calculate first the spatial optical generation rates under the PL illumination conditions using a simplified Basore model accounting for front transmission and wafer light-trapping properties [139]. Quokka 3 further utilises the reciprocity of absorption and emission in the calculation of escaped luminescence using the same device optics [140]. PC3D does not incorporate algorithms for modelling PL emission response, hence, interpretation of PL signal from PC3D carrier distribution results is required for completing the PC3D approach.

The electrical carrier transport modelling in both approaches is based on the drift-diffusion framework [136], [141]. The drift-diffusion model couples the carrier diffusion processes with electrical drift movement, parameterised by the interconnected carrier electrochemical energy ($\phi_{Fn}$, $\phi_{Fp}$) and electrostatic potential energy ($\psi$) in space, respectively. The differential equations consisting of these scalar energies are solved in space with either (A) the finite element method in Quokka 3, or (B) a fast Fourier series solution in PC3D [142]. Both implement additional conductive boundary simplification where surface layers, i.e. front emitter and rear passivation, are treated optically and electronically as boundary conditions for the bulk modelling domain [142], [143]. The following sections 2.5.2 and 2.5.3 describe the simulation details in the PC3D process. Key results from the parallel Quokka 3 process are provided as a comparison to PC3D[1].

### 2.5.2. Simulation parameters

Figure 2-4 (a) illustrates the modelling domain extending halfway between two adjacent fingers. The full geometrical unit cell with full translational symmetry encompasses two such adjacent domains. In practice, the modelling domain was further reduced as half of the translational unit cell to simplify the computation process, leveraging the additional mirror symmetry present between the neighbouring domains. Figure 2-4 (b) schematic shows the dimensions of the domain and the recombination conditions for the boundaries. Different types of domain

[1] The Quokka 3 simulations were conducted by Dr. Andreas Fell in Fraunhofer ISE. I provided the parameters but had no licenced access to the Quokka 3 tool.

boundaries are marked with colours in the figure legend, including the metal recombination boundary, non-contacted surface recombination boundary and symmetrical boundary. Following such definitions of the unit cell, PC3D divides the spatial domain into a mesh with evenly spaced nodes as dictated by the Fourier series approach of solving the drift-diffusion equations. The PC3D mesh in this study features 50×50 nodes, while higher resolution is possible at the cost of computation time.

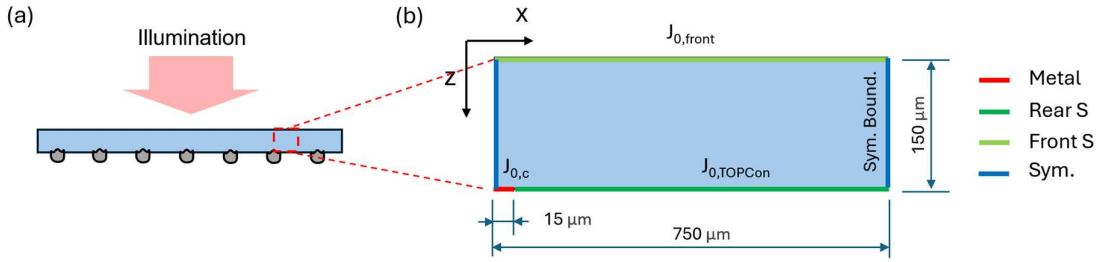


*Figure 2-4 (a) schematic of the wafer under PL experimental, with the defined simulation domain*

The input device parameters, including wafer electrical and optical properties, surface and bulk recombination parameters, are listed in Table 2-1. The doping at $4.00\times10^{-15}$ $cm^{-3}$ is set to provide a typical condition matching the prevailing industry wafer resistivity at close to 1 Ωcm [144]. PC3D is equipped with a tabulated database for the calculation of input-dependent parameters such as carrier diffusivities.

*Table 2-1 Device input parameters in PC3D simulation*

| | | | |
|---|---|---|---|
| **Device Information** | n-type Base doping | | Resistivity |
| | $4.00\times10^{15}$ $cm^{-3}$ | | 1.21 Ωcm |
| **Bulk Recombination** | Bulk SRH $\tau_{n0}$ | Bulk SRH $\tau_{p0}$ | Auger Recombination Coefficient |
| | 0.5 ms | 5 ms | $8.3\times10^{-31}$ $cm^6/s$ |
| **Surface Recombination** | Front $J_{01}$ $(J_{0,front})$ | Rear $J_{01}$ $(J_{0,TOPcon})$ | Rear metal $(J_{0,c})$ |
| | 25 $fA/cm^2$ | 5-100 $fA/cm^2$ | 5-140 $fA/cm^2$ |
| **Illumination Condition** | Type | Wavelength | Generation Current Density |
| | Monochromatic | 650 nm | 48.8 $mA/cm^2$ |

To represent the experimental PL condition at 1-sun, the optical generation is set to be monochromatic 650 nm with a result generation current density of 48.8 $mA/cm^2$. The

illumination condition is used in PC3D to calculate a spatial carrier generation profile with its optical model. The generation profile features a highest generation rate at $1.1\times 10^{21}$ $cm^{-3}s^{-1}$ at the surface, which quickly diminishes over the micrometre scale due to the short absorption length of 3.6 μm at 650 nm.

The remaining device recombination parameters listed in the table are matched to experimental measurements of the test samples. This is enabled because PC3D can also simulate IV as outputs from fully defined device properties, which, when fit to the experimentally measured average $V_{oc}$, $J_{sc}$ and $FF$ values, provides a realistic estimation of device inputs to improve modelling accuracy. It is additionally noted that the parallel device $V_{oc}$ , $J_{sc}$ and $FF$ measurements were conducted on both-side contacted sister wafers, which have undergone the same process routes as the single side contacted wafers for PL tests, which are reported in chapter 3.

### 2.5.3. Simulation results

The key outcome of the PC3D modelling is a 2D spatial distribution map of excess carriers. Figure 2-5 (a) presents a colourmap of the excess carrier density within the unit cell domain under a realistic condition of $J_{0,c}$=50 fA/cm$^2$,$J_{0,TOPCon}$=10 fA/cm$^2$ ($J_{0,c}$ is significantly larger than $J_{0,TOPCon}$). A gradual decrease in excess carrier density over depth is evident from the map, which can be attributed to the decrease of generation rate over depth. The spatial distribution of the excess carrier density shows further unevenness horizontally. The trend of spatial carrier variation can be better demonstrated by a carrier density gradient plot in Figure 2-5 (b). The gradient vectors depicted here also have the physical meaning of the steady-state excess carrier currents. Within the close-up region in Figure 2-5 (b), it can be observed that gradient vectors point both downwards and leftwards with a general trend aiming towards the metal boundary. This is a result of excess recombination at the metal boundary, which effectively acts as a sink of excess carriers to draw in more bulk carriers to recombine.

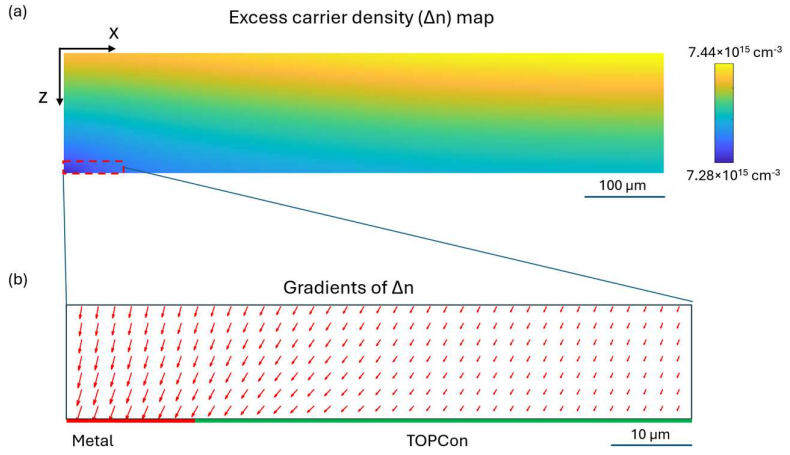


*Figure 2-5 (a) Excess carrier map by PC3D, (b) An arrow map of excess carrier density gradients in a close-up region towards the metal boundary. The arrows indicate both the gradient vector magnitude and direction.*

The combined act of spatial dependence of generation and excess metal recombination results in the lowest carrier density at the metal boundary centre and the highest density at the opposite corner at the top surface. The variation in spatial carrier densities, however, is contained within a small 2.1% relative range ($7.28\times10^{15}$ -$7.44\times10^{15}$ $cm^{-3}$). This is because the generated excess carriers in the wafer are well-dispersed at a scale close to the wafer dimensions, because of the high bulk diffusion lengths, as shown in the wafer bulk carrier lifetimes parameters.

The excess carrier density results calculated by PC3D are further interpreted into PL emission profile along the x direction, in an effort to provide the spatial PL signal linked to imaging data. This PL emission profile along the horizontal $x$-direction is computed from the 2D carrier profile by integrating the radiative recombination multiplied by an escape probability term over the depth $z$. A simplified equation is implemented as in eq. 2-4:

$$PL_x = \int_{z=0}^{D} \Delta n_{x,z} \left(\Delta n_{x,z} + n_0\right) \times B_{rad} \times exp\left(-\alpha z\right)\ dz \qquad 2\text{-}4$$

Where $\Delta n_{x,z}$ is the excess carrier density at location $(x, z)$, $n_0$ is the equilibrium concentration, $B_{rad}$ is the radiative recombination coefficient, and $\alpha$ is the photon absorption coefficient for the characteristic wavelength of Si photoluminescence. The first two terms describe the band-to-band recombination emission rate. The final exponential term accounts for attenuation from the reabsorption of emission at depths $z$ within the wafer. The reabsorption of PL photons is approximated by one absorption coefficient $\alpha = 6.8\times10^{-5}$ $\mu m^{-1}$ at 1150 nm to go around adding any spectral complexity. This low $\alpha$ value yields a close to 1 exponential term, indicating minimum reabsorption from depths of concern. It is acknowledged that this formulation is a

simplified interpretation of PL intensity. A hyperspectral and comprehensive expression of luminescence signal detected at the camera includes three parts: (A) a spectral emission function, (B) an escape probability function related to wafer internal optics, and (C) an additional camera detection sensitivity term or a spectral filtering term [140], [145]. Such formulations are equipped in dedicated PL modelling packages such as Quokka 3 [143].

Figure 2-6 presents the horizontal PL line profile result from PC3D, as well as from the parallel Quokka 3 under the same sample definition. The PC3D profile is calculated from excess carrier densities using eq. 2-4. Quokka 3 profile is generated by its built-in luminescence model, which additionally includes a 1200 nm short pass filter on the hyperspectral PL emission to represent further realistic camera detection conditions. Both profiles show a lowest PL emission at the metal finger edge at $x = 0$ µm, which originates from the local dip of excess carriers caused by excess metal recombination. By comparison of the two profiles, it is notable that Quokka 3 PL dip at 0.81% on a relative scale is smaller than the PC3D dip at 0.92%. The difference between PC3D and Quokka3 profiles can be attributed to: (i) simplified silicon physical models used in PC3D, including negligence of the band-gap narrowing effect in bulk for such high lifetime samples, which limits accuracy in electrical modelling in PC3D; (ii) simplified PL optical interpretation in PC3D without spectral information and filtering.

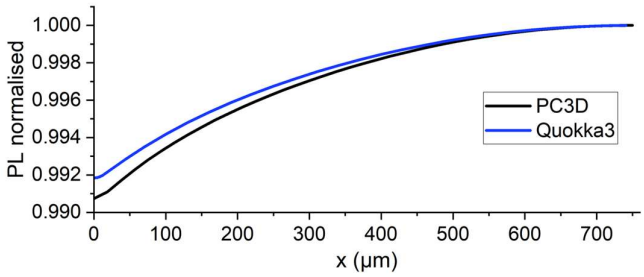


*Figure 2-6 Normalised PL line profile by both PC3D and Quokka3, Quokka3 results additionally assume a 1150nm short-pass filtering*

To illustrate the effect of metal and bulk recombination on PL profiles, recombination parameter sweeps are conducted with PC3D. Figure 2-7 (a) illustrates the normalised PL intensity profiles for a series of $J_{0,c}$ values with the same $J_{0,TOPCon}$. The metal recombination condition is presented here as the excess over TOPCon surface level $J_{0,c} - J_{0,TOPCon}$, which separates $J_{0,TOPCon}$ as an additional parameter as a baseline value for $J_{0,c}$. The step increase in excess metal recombination $J_{0,c} - J_{0,TOPCon}$ is translated to larger dip amplitudes in the profiles. This is because a higher $J_{0,c}$ translates to more carriers lost at the metal boundary, which brings a higher difference in PL intensity between metallised and unmetallised regions.

Additionally, Figure 2-7 (b) presents a profile series for a range of bulk lifetimes. PC3D assumes a simplified case in which bulk SRH lifetime for holes $\tau_p$ is one order of magnitude greater than for electrons $\tau_n$. This approximation applies since higher electron capture cross-sections parameters are reported for bulk SRH recombination processes [146], [147] (a description of SRH statistics is provided in section 1.3.2). The results in Figure 2-7 (b) reveal that higher bulk lifetimes correlate with more extensive relative PL intensity dips, but with diminishing effects at lifetimes above $\tau_n$= 200 µs. This correlation can be attributed to the carrier diffusion length $L \sim \sqrt{D\tau}$ increasing with higher bulk lifetimes. The larger diffusion lengths allow further carriers to be drawn towards the metal interface, thus amplifying the dip caused by metal recombination. This effect diminishes at higher lifetime scenarios because once the diffusion lengths reach near the simulation unit cell dimensions, further diffusion length increases would have a limited influence on observed spatial distributions. It is notable, by a comparison of dip ranges in Figure 2-7 (a) and (b), that the effect of bulk lifetimes within the sample-realistic range of concern is secondary compared to the effect of metal recombination.

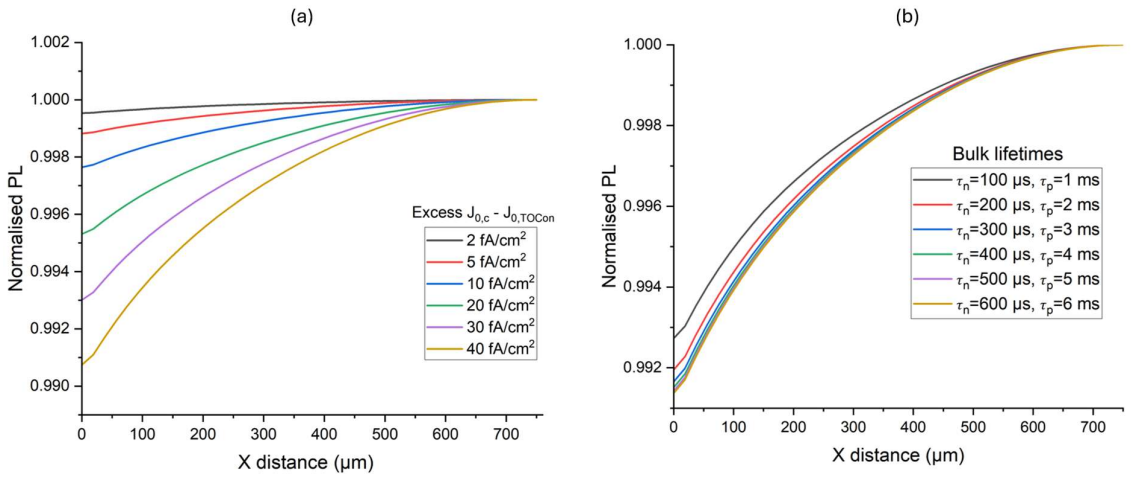


*Figure 2-7 PC3D normalised PL intensity line profile series under 1-sun illumination for (a) varying excess $J_{0,c}$-$J_{0,TOPCon}$ on top of constant $J_{0,TOPCon}$=10 fA/cm$^2$, and (b) varying bulk SRH carrier lifetimes based on a combination of $J_{0,TOPCon}$=10 fA/cm$^2$ and $J_{0,c}$=50 fA/cm$^2$*

## 2.6. Linking simulation results to PL data

The unit cell simulation from both PC3D and Quokka provides useful information on how conditions such as $J_{0,c}$ affect PL spatial variation. To establish a link between the unit cell to the experimental acquired PL data, the author adopts the previously established FFT metal contrast as the comparison standard, which requires building full lines from the unit cell to

enable the Fourier analysis. Figure 2-8 illustrates the process of converting a representative unit cell profile to signals in the frequency domain. The unit cell profile is combined with its mirror image to make up one repetition period. The repetition number of 112 is used as identical to the number of metal fingers in a PL image. The line profile built from concatenated unit cells is shown in the second step. The Fourier spectrum in the third step shows the harmonic peaks from the periodicity in the line profile, which are analysed following the same route as applied to experimental PL images described in section 2.4. The absence of broadband noise is notable in this spectrum as a major difference from the spectrum of PL images. The result of this process is the extracted FFT metal contrast from the simulation as a function of the sample parameters.

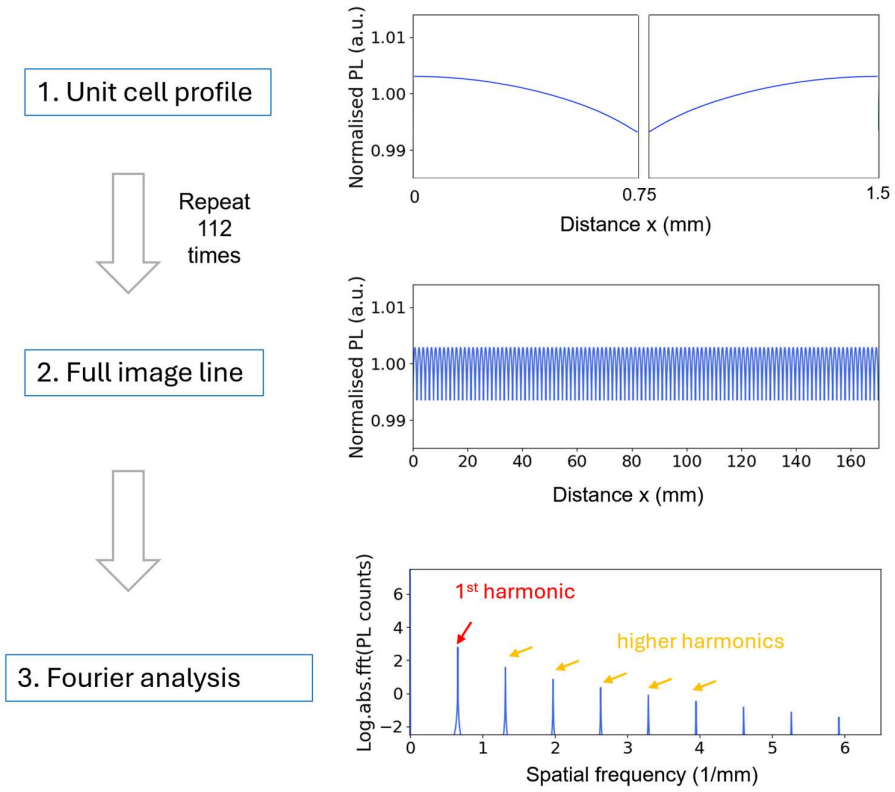


*Figure 2-8 Process flow of integrating simulation profiles with Fourier analysis, showing (1) two unit cell profiles combined as a repetition unit, (2) a line profile built from simulation results, (3) frequency*

Figure 2-9 (a) illustrates the FFT metal contrasts from the PC3D simulation as a function of metal recombination as excess $J_{0,c} - J_{0,TOPCon}$. The red data points in this figure are from the case of a baseline surface $J_{0,TOPCon}$ =10 fA/cm$^2$, which corresponds directly to unit cell profiles in Figure 2-7 (a). The near-linear relationship shared among all curves (with Pearson correlation coefficients ρ > 0.9999) points to a strong correlation between contrast and excess

$J_{0,c}$ within the shown range (0 – 40 fA/cm$^2$). This correlation underlines the high linear dependence of contrast on metal contact recombination, making it feasible to determine metal recombination through PL metal contrast measurements.

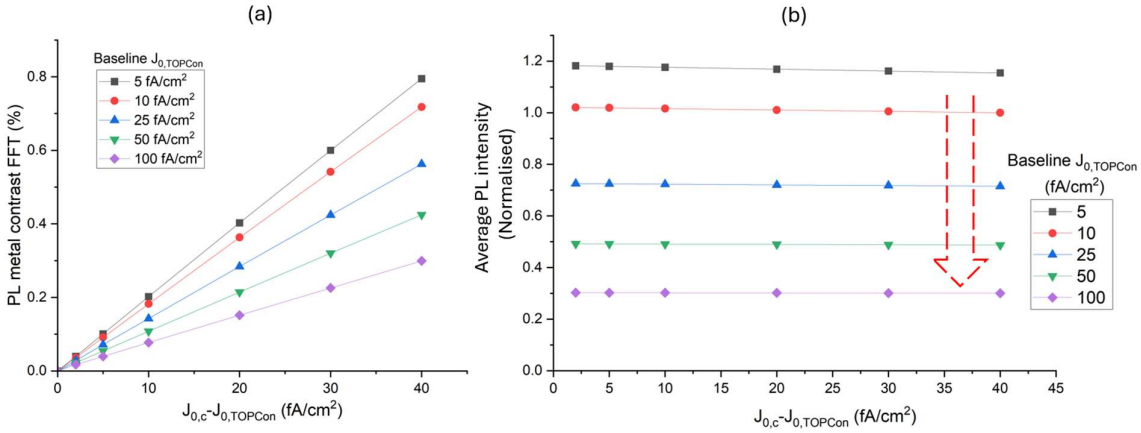


*Figure 2-9 (a) PL metal contrasts extracted by FFT analysis vs excess $J_{0,c}$-$J_{0,TOPCon}$, the series shows different baseline $J_{0,TOPCon}$ scenarios, (b) Average PL intensity series vs excess $J_{0,c}$-$J_{0,TOPCon}$, under different baseline $J_{0,TOPCon}$ scenarios, intensity normalised to $J_{0,TOPCon}$= 10 fA/cm$^2$case .*

A comparison between the curves in Figure 2-9 (a) highlights a shift in the correlations between metal recombination and FFT contrast when the baseline $J_{0,TOPCon}$ condition changes. It is found that higher baseline surface recombination $J_{0,TOPCon}$ reduces the contrast at the same excess $J_{0,c} - J_{0,TOPCon}$. This is evident since worse recombination at the free surface makes less difference between the carrier densities, both under the contact and non-contacted regions. Such a finding illustrates the importance of establishing the baseline $J_{0,TOPCon}$ before contrast calibration, as it strongly impacts the correlation between metal contrast and $J_{0,c}$ in this methodology.

The baseline surface recombination $J_{0,TOPCon}$ can be linked to the overall PL intensity. In Figure 2-9 (b), the simulated average PL intensity over a line is plotted as a function of excess $J_{0,c} - J_{0,TOPCon}$ for different baseline $J_{0,TOPCon}$ values. This average PL intensity is minimally influenced by the excess $J_{0,c}$ on x-axis within the range of concern since the local metal recombination at metal fingers (which covers only 2 % surface area) has a restricted impact on overall bulk carrier density. On the other hand, the average PL intensity is sensitive to the changes in surface $J_{0,TOPCon}$. This correlation of PL intensity to surface recombination enables a calibration of the $J_{0,TOPCon}$ of individual measured samples to their average image luminance first before subsequent assessment of $J_{0,c}$. After the surface level $J_{0,TOPCon}$ of each sample is

estimated, the relationships between the FFT metal contrast and the excess $J_{0,c} - J_{0,TOPCon}$ are then interpolated following the curves in Figure 2-9 (a). Such a $J_{0,TOPCon}$ calibration takes into account different sample conditions and facilitates accuracy in the Fourier analysis of $J_{0,c}$.

As a summary, an illustrative diagram is shown in Figure 2-10 for summarising this two-step process for determining $J_{0,c}$ from a sample image spectrum. Information at both the 0th order peak and the 1st order peak on the frequency spectrum is used in this process as marked by circles. The first step is the calibration of average PL intensity, which corresponds to the 0-frequency integral at position A. The second step is the extraction of metal contrast by selecting the signal under the 1st order peak at position B. Information at higher harmonics is not used due to the high noise floor in data. Since higher harmonics represent waveform details, it is acknowledged that the current method cannot assess waveform characteristics because of data quality limitations. Further investigation of higher harmonics could provide a promising direction for expanding the method.

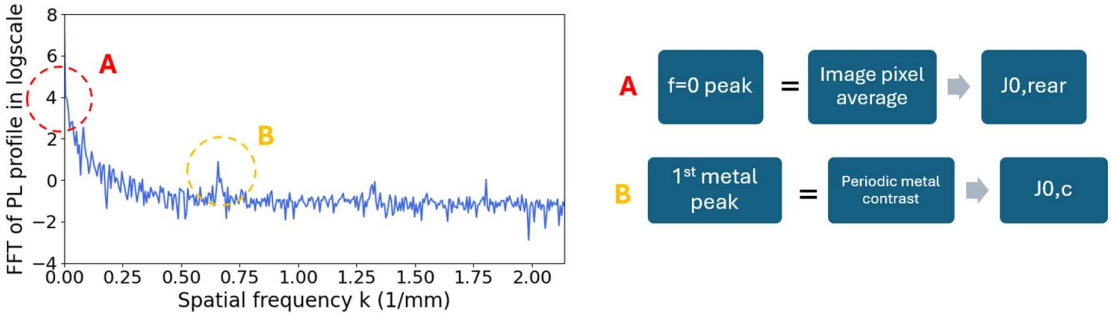


*Figure 2-10 Two-step A&B process of determining $J_{0,c}$ from the Fourier spectrum of a sample image line, with Fourier peaks marked on the spectrum*

## 2.7. Case study: contact recombination from different screen-printed Ag pastes

As a direct result of applying the two-step process in the sample images analysis, Figure 2-11 (a) illustrates a bar plot set that shows $J_{0,TOPCon}$ and $J_{0,c}$ values from two measured sample groups. These two groups have the same TOPCon surface finish but different metallisation pastes. They are chosen to demonstrate the capability of the analysis presented in this chapter. The similar surface passivation shared by the groups is indicated by a common estimated $J_{0,TOPCon}$ average at ~10 fA/cm$^2$, as shown by the orange bars. The error bars of the estimations in Figure 2-11 (a) originate from the standard deviation among the 9 sample values within each group.

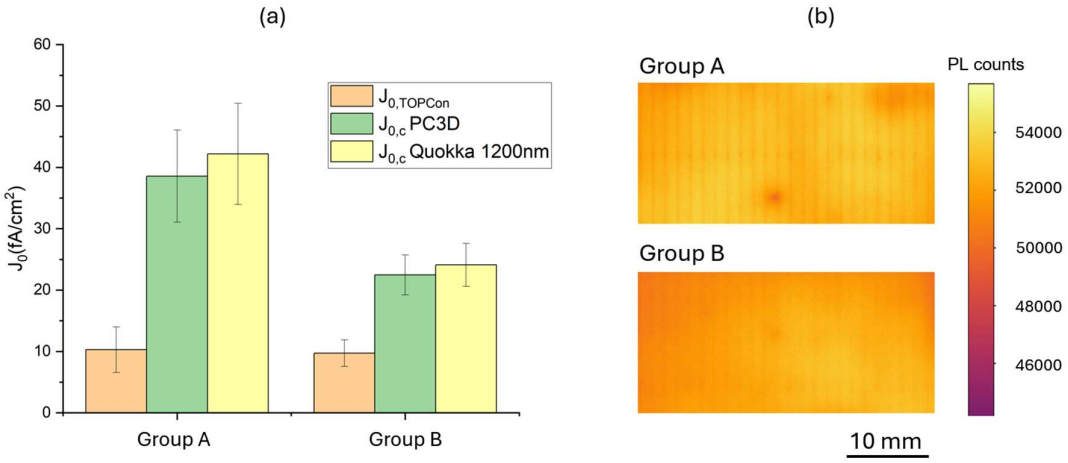


*Figure 2-11 (a) Estimated baseline $J_{0,TOPCon}$ values, and $J_{0,c}$ values extracted using both PC3D and Quokka for sample group A & B. (b) PL image close-ups from a group A sample and a group B sample, on the same colour scale, to demonstrate the difference in metal line contrast.*

The PC3D interpreted $J_{0,c}$ results given in green bars illustrate a difference between groups, which entails that samples in group B have significantly lower $J_{0,c}$ values at 22.5 ± 2.2 fA/cm$^2$ (n = 10) compared to group A at 38.5 ± 7.5 fA/cm$^2$ (n = 10). Estimations via Quokka 3 route given in yellow bars tell the same difference but standing at slightly higher values: group B at 24.1 ± 3.5 fA/cm$^2$ and group A at 42.2 ± 8.2 fA/cm$^2$. Evidence of the difference in $J_{0,c}$ can be found in Figure 2-11 (b), which shows enlarged PL images of a group A and a group B sample on the same colour scale. It can be observed from the comparison of images that the periodic metal contrast from paste B is weaker than paste A, which is reflected by the lower estimated $J_{0,c}$ results of paste B. The reduced $J_{0,c}$ underscores the efficacy of group B's metallisation design in minimising surface damage. The Quokka 3 estimations in Figure 2-11 are slightly higher as compared to the PC3D values. The minor difference is due to the more detailed electrical model and the additional consideration of camera filtering at 1200 nm in Quokka 3.

## 2.8. Discussion

The $J_{0,c}$ extraction method described in this chapter relies on the key finding that the metal contact recombination parameter $J_{0,c}$ is strongly correlated with the metal periodic contrast from Fourier analysis. The utilisation of this insight allows metal recombination to be evaluated from the PL images data. Upon comparison between my approach to the previously reported Saint-Cast's method [138], my methodology has the following differences: (A) PL images are taken on single-sided metallised samples with the non-metallised surface facing the PL camera, which eliminates metal finger shading effects obfuscating metal contrast. (B) Comprehensive

2D numerical device simulations are utilised to determine spatial carrier distributions, significantly improving $J_{0,c}$ parameter extraction accuracy over the previous 1D analytical model. (C) Additional PL data processing, including noise normalisation and filtering, is implemented to enhance the detection sensitivity of periodic metal contrast signals. The method in this work thus enables the extraction of low $J_{0,c}$values suitable for passivated silicon contacts.

However, the $J_{0,c}$ extraction approach in this work is susceptible to systematic errors potentially introduced in both simulation interpretation and PL data processing. It is safer to say that the $J_{0,c}$ estimates from the PL data are to be taken for comparative purposes, the values of which can benefit from further confirmation and calibration with other viable characterisation approaches. A potential error source is that neither PC3D nor Quokka 3 simulation accounts for the effect of optical blurring. The image blurring that occurs at the PL camera sensor is known to cause lateral spread-out of PL profiles and reduce any image contrast amplitude. The $J_{0,c}$ values extracted for a simplified blurring-free scenario will be underestimates of realistic values. PL experimental setups are equipped with standards to limit blurring to some extent, by using a short-pass filtering before the camera placed at 1200 nm to cut off the long-wavelength signal most prone to later blurring. This short-pass filtering is reflected in Quokka by integrating wavelengths until 1200 nm. The effect of image blurring at photon wavelengths below 1200 nm has not been evaluated in my method. It is proposed for future studies on this topic that (A) a short-pass filter be placed at lower wavelengths, e.g. at 950 nm, to further limit blurring and increase image sharpness, and (B) incorporate blurring correction algorithms in further PL data processing to mitigate optical blur.

On the other hand, the Fourier PL data analysis in this work relies on the accurate extraction of the periodic signal from the peaks in k-space. It is observed from section 2.4 that the k-space spectrum of measured images features a high broadband noise floor that limits the sensitivity of peak extraction. This implies that low metal contrasts with peak signal close to the noise floor cannot be detected with accuracy, which puts a lower limit on the detectable $J_{0,c}$. This intrinsic limitation can be avoided by either suppressing noise or enhancing the k-space peak above the noise floor as reflected by a high FFT metal contrast. The noise reduction in PL image would be beyond the scope of this work. The author advances further here to identify experimental conditions that can enhance the peak signal, which is reflected by an increasing noise-subtracted metal contrast.

Firstly, it has been noted in experiments that PL illumination intensity has an influence on the extracted metal contrast. Figure 2-12 (a) shows the experimental data points measured from a selected wafer sample by the red dots. These scattered measurement points indicate a trend that metal contrast increases with illumination intensity. Complementing such an experimental observation, PC3D simulations were conducted for an illumination intensity sweep, showing metal contrasts from FFT analysis at varying illumination intensities. The simulations, illustrated as the line traces in Figure 2-12 (a), show the contrast vs illumination relation under different $J_{0,c}$ scenarios (with the same baseline $J_{0,TOPCon}$=10 fA/cm2). The simulation results corroborate the experimental trend that higher illuminations lead to enhanced metal contrasts under all metal recombination scenarios. Therefore, higher illumination is helpful in improving signal clarity for such a Fourier analysis method.

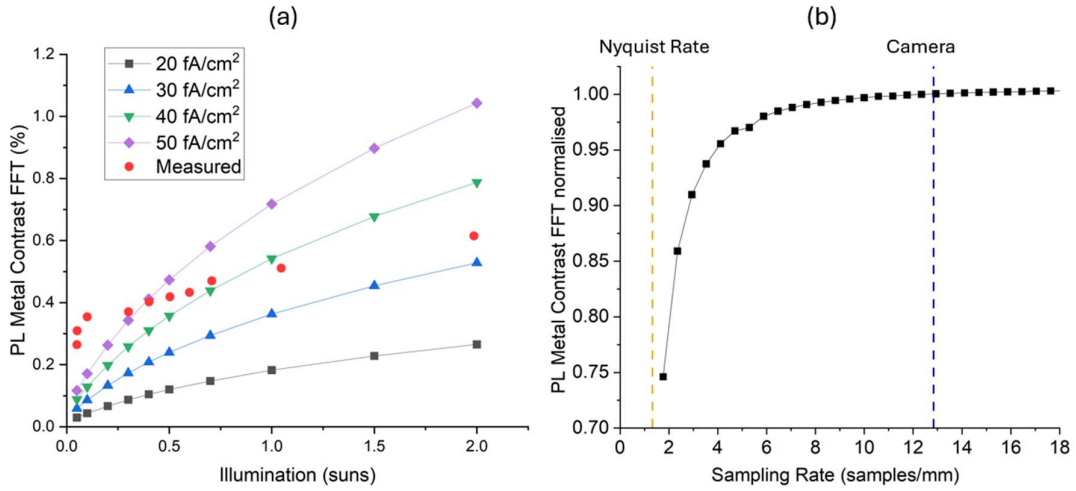


*Figure 2-12 (a) Metal contrast extracted via FFT under a range of illumination conditions, the curve series show different metal recombination scenarios. (b) Normalised metal contrast extracted via FFT vs sampling rate*

A possible reason for the trend is the injection dependence of bulk and surface recombination processes. Surface recombination can become an increasingly important component under higher injection conditions, contributing more to the overall lifetime. Hence, using higher illumination levels enhances the prominence of rear surface metal features ($J_{0,c} > J_{0,TOPCon}$) in the spatial distribution of carrier density, thus improving the detectability of such features.

Secondly, camera resolution can also influence metal contrast. The camera's horizontal resolution (along its long detector axis) dictates the sampling rate of the line profile, which in turn determines the sampling interval size in both x-space and k-space. Figure 2-12 (b) presents the PC3D-simulated metal contrast as a function of sampling rate, measured in $mm^{-1}$. The y-

axis shows the contrast normalised to the standard contrast at a sampling rate of 12.8 $mm^{-1}$, representing the camera's operational rate (indicated by the blue line) with a horizontal resolution of 2184 pixels. The theoretical minimum Nyquist rate for sampling with a repetition number of 112 (metal fingers) is marked by an orange line. Inadequate sampling can lead to information loss, as indicated on the left side of the curve. The plot also demonstrates that while the contrast significantly increases above the Nyquist threshold, it plateaus at higher sampling rates, suggesting minimal improvement beyond the current camera rate. This relationship highlights the sampling requirement necessary for accurately assessing metal contrast.

## 2.9. Conclusions

In this chapter, an effective and versatile method has been demonstrated for extracting contact recombination $J_{0,c}$ from photoluminescence images of single-side metallised TOPCon wafer samples, without the need for specially designed metallisation geometries. The key to this method is exploiting the periodicity of the metal grid for isolation of the metal contrast signal in the k-space after performing Fast Fourier Transformation (FFT). Noise normalisation and filtering can be implemented as part of the Fourier analysis process, vastly enhancing the ability to extract information out of in-line PV manufacturing metrology.

Numerical device simulations, including PC3D and Quokka 3 are used for modelling 2D carrier distributions and corresponding PL intensity profiles within a local unit cell. The PC3D simulation results show the spatial carrier non-uniformity because of excess metal recombination. A higher amplitude of the non-uniformity is found to be strongly linked to a larger $J_{0,c}$, and to a minor extent a higher bulk lifetime.

Interpretation of simulation results via the same Fourier analysis procedure demonstrates a linear-like relation of $J_{0,c}$ and PL metal contrast. This $J_{0,c}$-contrast relationship is affected by $J_{0,TOPCon}$ which needs to be determined first. A two-step process is employed to estimate $J_{0,c}$ from PL images for two sample sets with different metallisation approaches. The results demonstrate that using such method, $J_{0,c}$ values of 38.5 $fA/cm^2$ and 22.5 $fA/cm^2$ were found for the two sample sets A and B respectively, based on the assumption of a $J_{0,TOPCon}$ of 10 $fA/cm^2$. This difference highlights the recombination reduction of sample group B in agreement with its design. Parallel results from Quokka3 simulation are comparable to PC3D, with the difference in $J_{0,c}$ estimation attributed to the additional consideration of short-pass filtering conditions. The author acknowledges optical blurring as the major limitation factor to the quantitative analysis and highlights the need for result calibration. Furthermore, factors to

potentially enhance the sensitivity of the Fourier method are investigated, including the illumination intensity and camera resolution. It is shown that increasing illumination and camera sampling rate are beneficial to a higher metal contrast and hence a better efficacy of the Fourier analysis process.

The effectiveness of this Fourier analysis method in estimating low $J_{0,c}$ levels make it broadly applicable to various solar cell metallisation schemes, provided they exhibit spatial periodicity. The insights gained in this work have direct implications for enhancing both PL imaging analysis and contact characterisation, both of which are key tools for the continued optimisation of future solar cell designs.

# 3. Linking microstructure to the electrical performance of metallisation technologies in TOPCon solar cells

## 3.1. Introduction

The TOPCon design incorporates two aspects of a carrier-selective contact: efficient conduction of the majority current and effective suppression of the minority recombination current. Performance characterisation of TOPCon structures focuses accordingly on two aspects: contact-related resistance and contact recombination current, both of which constitute carrier selectivity. These parameters can be experimentally measured and are suitable for benchmarking and comparison across various processing routes [148], [149], [150].

Metallisation on n-TOPCon structure in industry is predominantly reliant on the fire-through contact formation approach, which was inherited from earlier established processing lines. This metallisation scheme consists of: (a) application of an Ag paste-based contact precursor to form the surface metallisation pattern via screen printing, and (b) solidification of contacts via rapid firing [151]. During the screen-printing process, the viscous paste is pushed through a mesh screen to form grid lines and bus bars with designed dimensions. Readers are directed to ref. [152] for descriptions of screen printing. The metal paste, made of silver powder, glass frit and additional organic binders, is fired within a belt furnace in a processing line for 2-5 seconds [153]. The integrated fast-firing step provides not only the thermal condition for contact formation but also enables hydrogen release and surface film annealing [153], [154]. To enhance compatibility with the TOPCon structure, adaptations to the fire-through process have been explored, including modifications to the paste precursor composition [155], [156] and firing conditions [153].

Figure 3-1 illustrates the sequential formation process of fire-through contacts. During the rapid firing step with a peak temperature above 850°C, lead oxide (PbO) within the glass frit etches the surface silicon nitride film and forms a glass interlayer between silver grains and silicon substrate. Simultaneously, the powdered silver grains partially dissolve in the glass phase and agglomerate in a sintering process. Upon cooling, the dissolved silver precipitates as either finely dispersed nano-crystallites embedded in the glass phase, or as epitaxial grown deposits on the silicon substrate, as shown in Figure 3-1 (d). Additionally, voids form during firing due to evaporation of the organic binders in the metal paste.

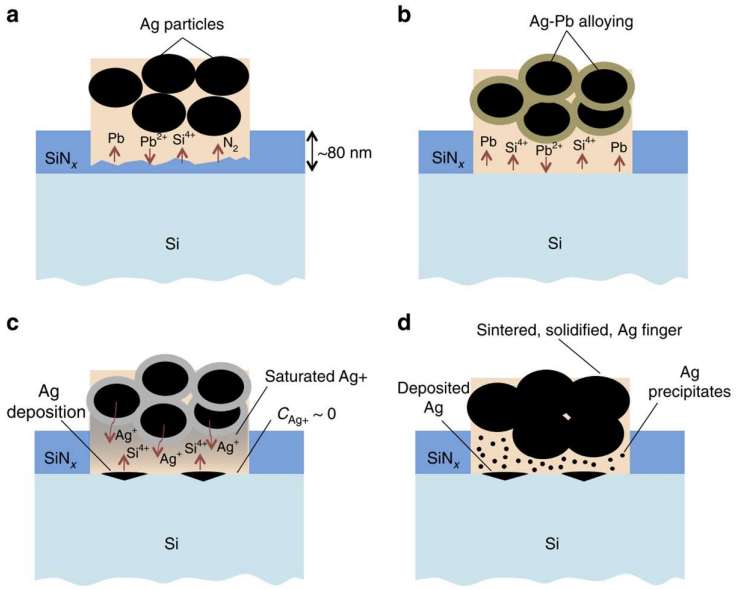


*Figure 3-1 The four-step process of firing contact formation for the screen-printed fire-through silver contact. (a) the PbO glass frit content in the contact paste melts and etches the $SiN_x$, (b) Ag alloys with Pb from the glass frit, (c) Ag is dispersed in the glass and deposited on the silicon substrate, (d) formed fired-through contact morphology. Figure from [79]*

The firing-through process, however, can incur degradation in TOPCon contact selectivity. Fırat et al. [150] investigated the peak firing temperature and reported an increase of contact recombination current ($J_{0,c}$>100 fA/cm$^2$) at higher temperatures. Similarly, Liu et al. [153] confirmed that an increase of heat budget during firing leads to excessive $J_{0,c}$, while insufficient heat is associated with high contact resistivity $\rho_c$ and a lack of Ohmic contact behaviour. Such results underscore the necessity for precise tuning of thermal conditions to achieve the designed TOPCon contact performance. Parallel studies [131], [157] propose that the electron selectivity of n-TOPCon structure relies on a contact microstructure featuring a thin interface glass layer containing embedded nano-crystallites between metal and the $n^+$ layer, while largely preserving the integrity of the underlying tunnelling oxide passivation. Higher contact resistances are linked to incomplete etching of surface nitride during contact firing. Conversely, excessive etching leads to local disruptions of the TOPCon passivation stack and excessive Ag ingress on the silicon surface (also referred to as Ag spiking), which mediates increased contact recombination [131], [154], [157], [158], [159]. Notably, microstructural investigations of the contact interface often distinguish metal, glass, and silicon based on electron imaging contrast (as found in [157]), but provide limited chemical identification of the complex phases.

The ongoing improvements to the TOPCon metallisation have targeted further adaptation in processing to maximise contact performance [150], [151], [160]. Studies by [52], [161]

systematically investigated the impact of the thickness of the polysilicon layer, demonstrating that a thinner polysilicon layer < 100 nm can reduce parasitic absorption and Auger recombination losses but exhibit increased susceptibility to metal ingress during firing. The metal ingress is manifested as increased damage to the silicon surface morphology and excessive Ag spiking into the substrate [162], [163], both of which are linked to high $J_{0,c}$ values. Ciftpinar et al [162], [164] also reported high sensitivity of TOPCon contact $J_{0,c}$ on n-type polysilicon film thickness, changing from <100 fA/cm$^2$ for 200 nm polysilicon to 400 fA/cm$^2$ for 75 nm polysilicon. Recent polysilicon studies [85] [86] demonstrated the possibility of achieving low $J_{0,c}$ values ~50 fA/cm$^2$ on thin <100 nm $n^+$ polysilicon structures through precise control of amorphous layer deposition and doping process. To maintain a thin polysilicon layer while limiting contact-induced damage, several studies introduced a barrier layer such as titanium nitride [165] or silicon oxide [166], [167] to limit etching depth during firing. Madani et al. [168] showed that the use of a thin ~7 nm aluminium oxide as the capping film on polysilicon significantly improves the firing stability of TOPCon passivation, suggesting $AlO_x$ as another promising candidate barrier layer to limit contact firing damages. Additionally, the control of paste precursor composition has been shown to effectively limit etch damage. Results by Padhamnath et al. [156] demonstrated that a commercial metal paste with an optimised glass frit composition can achieve $J_{0,c}$ as low as 30 fA/cm$^2$ while maintaining low contact resistivity.

In this chapter, three promising modifications in TOPCon processing are investigated: (a) reduction of polysilicon thickness (b) addition of $AlO_x$ between polysilicon and silicon nitride surface layer (c) reduction of glass frit content in the metal paste precursor. Both recombination and resistivity properties of the formed TOPCon contacts after the adaptations are investigated following either established or innovatively developed methodology. Microstructure examinations are performed to understand the morphological and chemical characteristics at the contact interface that underpin the observed contact properties.

## 3.2. Sample information and characterisation methods

Figure 3-2 (a) describes the structure of the finished TOPCon cells with a boron emitter front surface and TOPCon passivated rear surface. Figure 3-2 (b) shows TOPCon passivation layers on the rear side. The complete sample set also includes subsets with single-sided metallised groups among which a selection was used previously in chapter 2. The wafer substrates with surface passivation and metallisation were produced by Fusion Materials, with a detailed description found in [144]. The wafer was double-sided textured in prior processing steps,

while the TOPCon surface was subsequently single side etched using $HF/HNO_3$, which largely removes the pyramid texturing. The relevant steps for forming TOPCon contact structure include: (a) thermally grown $SiO_x$, (b) industrial LPCVD deposition of an intrinsic amorphous silicon layer, (c) phosphorus thermal diffusion using $POCl_3$ and simultaneous polysilicon crystallisation, (d) PECVD silicon nitride coating, and (e) Metal paste screen-printing and firing. The final integrated firing step was done in a belt furnace at an estimated peak temperature between 840 °C and 860 °C.

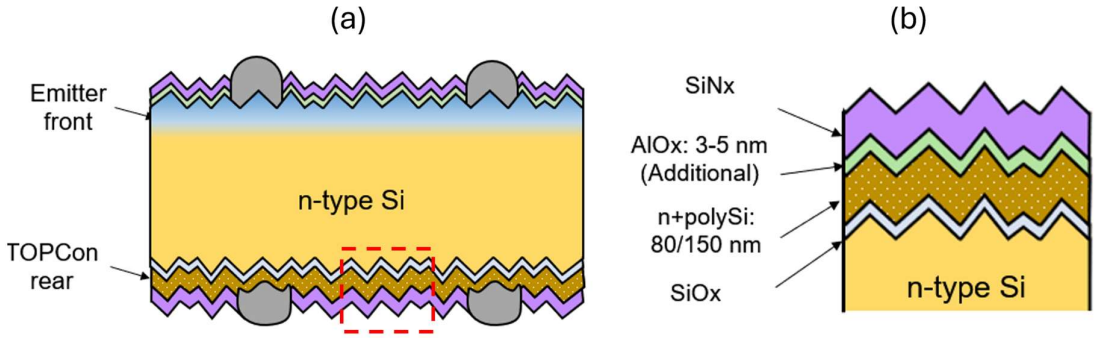


*Figure 3-2 (a) The complete TOPCon cell structure with front emitter and rear passivation. (b) Enlarged view of the TOPCon layers.*

Table 3-1 lists samples variations in polysilicon thickness, presence of additional $AlO_x$ and metal paste. The reference TOPCon structure has 150 nm polysilicon with a variation group with a thickness of 80 nm. The insertion of an $AlO_x$ layer between polysilicon and nitride is done by 30 atomic layer deposition (ALD) cycles with an estimated thickness of 3-5 nm. Two pastes A and B are used to contact the TOPCon surface, with paste B having reduced glass frit content than paste A. Specific sample groups are abbreviated by the variation type, e.g. A150AlOx means group with paste A, 150 nm polysilicon and $AlO_x$ addition.

*Table 3-1 List of samples with structure variations and characterisation methods*

| **Contact Paste** | **Contact side** | **150 nm poly-Si** | | **80 nm poly Si** | | **Measurements** |
|---|---|---|---|---|---|---|
| | | AlOx | No AlOx | AlOx | No AlOx | |
| Paste A | TOPCon side | 12 pcs | 12 pcs | | | PL, TLM |
| | Both sides | 4 pcs | 4 pcs | | | IV test |
| Paste B | TOPCon side | 12 pcs | 12 pcs | 6 pcs | 6 pcs | PL, TLM |
| | Both sides | 4 pcs | 4 pcs | 2 pcs | 2 pcs | IV test |
| No contact | -- | 4 pcs | 4 pcs | 2 pcs | 2 pcs | lifetime |

The sample groups are made with several metallisation variations: either no contacts, TOPCon side-only contacts, or both sides contacts. The device properties were provided by the manufacturers via standard IV testing on double-side contacted cells. The wafer's effective lifetimes were measured on non-contact cell precursors by a Sinton WCT120 photoconductance tester [169]. Surface $J_{0,s}$ values were estimated via the excess carrier lifetime data as described in Appendix G. The contact-related resistances were measured via TLM and line resistance tests, described in Appendix E. The contact recombination $J_{0,c}$ values were extracted by the PL analysis method detailed in Chapter 2

For microstructural characterisation, cross-sectional samples were prepared via cleaving the wafers. Focused ion beam milling and polishing of the cross-section surfaces were conducted using a Zeiss NVision 40 FIB/SEM system. Volumetric evolution of the cross-sections was exposed by slicing along depth with a 1 μm gap size. An illustration of the FIB slicing is given in Appendix H. Milling was done at a 64-degree angle to the surface restricted by stage rotation. Low-energy X-ray analysis was conducted using a Zeiss Merlin system with an Oxford instrument XMax energy-dispersive x-ray (EDX) detector. An electron beam energy of 5 kV and a 500 pA current aperture were used to limit the electron interaction volume for high EDX spatial resolution.

## 3.3. Device performance results

Figure 3-3 presents the device metrics, including cell efficiency, $V_{oc}$, $J_{sc}$, and FF of sample groups, illustrating the overall performance differences among sample groups. Notably, the test devices exhibit reduced efficiencies compared to state-of-the-art TOPCon efficiencies at over 25 % [170]. The samples have comparable $V_{oc}$ but show low $J_{sc}$ and FF relative to optimised industrial TOPCon values reported [144]. These parameters indicate overall high optical losses (potentially due to parasitic absorption in TOPCon layers) and high resistance losses in the test TOPCon batches.

Differences are observed after comparisons across the groups. The addition of $AlO_x$ improves efficiency, $V_{oc}$ and $J_{sc}$. The cell efficiency improves by 0.2 % in 150 nm polysilicon samples and by an even larger gain at 0.4 % for 80 nm polysilicon samples when $AlO_x$ is present. The efficiency improvements can be related to the improvements in both $V_{oc}$ and $I_{sc}$, which is indicative that the additional $AlO_x$ significantly benefit rear side passivation after firing. Conversely, the addition of $AlO_x$ negatively affects the fill factor for samples with 150 nm

polysilicon. Because FF is strongly dependent on total cell resistance (see section 1.3.4), this observation indicates that $AlO_x$ in the TOPCon structure can be potentially related to increasing resistances specifically at TOPCon contacts. Notably, large dispersion is present in $J_{sc}$ and FF for group A150$AlO_x$, which is indicative of a potential large variation in resistance under a combination of paste A and $AlO_x$.

Change from metal paste A to B also contributes to a modest cell efficiency gain. Sample group B150$AlO_x$ achieves the highest average efficiency overall. A distinct $V_{oc}$ gain of 2.4 mV is observed after a comparison between A150 and B150 groups, which is indicative that paste B can potentially reduce contact recombination losses. However, the changes associated with paste modification are not significant in other comparison scenarios as the ranges overlap. Reduction of polysilicon thickness from 150 nm to 80 nm primarily lowers $V_{oc}$, which implies loss of surface or contact passivation in these structures. In the absence of the $AlO_x$ layer, the thinner polysilicon group B80 shows the lowest cell efficiency, characterised by a low $V_{oc}$ and fill factor.

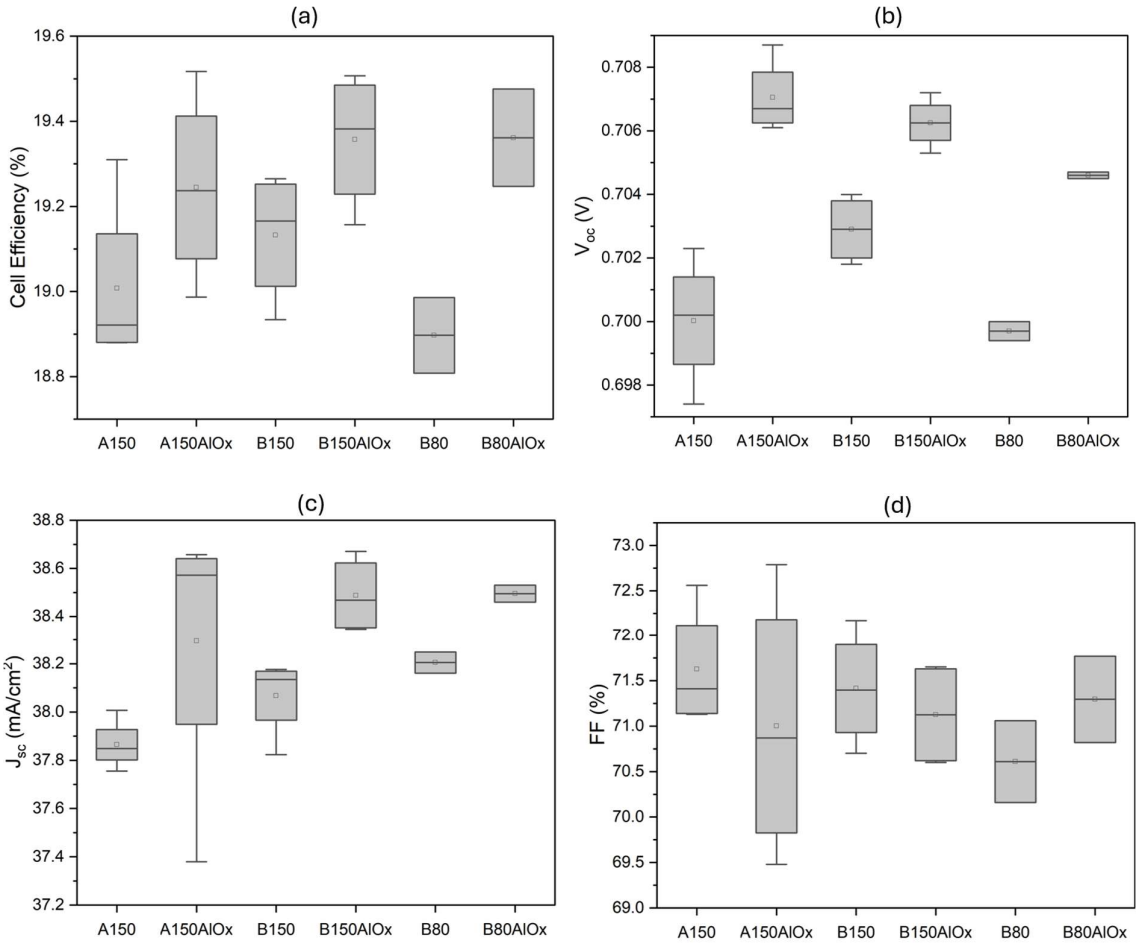


*Figure 3-3 Device-level I-V characteristics of the sample groups, showing: Efficiency, $V_{oc}$, $J_{sc}$, and FF. The sample group label A150AlOx means group with metal paste A, 150 nm polysilicon and with presence of an $AlO_x$ layer.*

## 3.4. Contact recombination results

Following the methodology established in chapter 2, it is essential to assess the surface recombination prior to the determination of contact recombination $J_{0,c}$. A lumped $J_{0,s}$ of both surfaces is provided by analysis of photoconductance decay (PCD) data, in a process detailed in Appendix G following the approach described in [171] [172]. Figure 3-4 illustrates (a) the PCD wafer effective lifetimes at $1\times10^{15}$ cm$^{-3}$ excess carrier density, and (b) the extracted $J_{0,s}$ for both surfaces. It is evident from Figure 3-4 (a) that the addition of $AlO_x$ increases the effective lifetime by a factor of 3, both for the 150 nm polysilicon and 80 nm polysilicon structure. Reduction of polysilicon thickness introduces a slight lifetime drop, the effect of which is secondary to the $AlO_x$ addition. Figure 3-4 (b) further reveals that the addition of AlOx significantly suppresses surface recombination, with 150 nm and 80 nm polysilicon wafers

reaching a comparable lumped $J_{0,s}$ at 17.7 ± 2.2 fA/cm$^2$ and 16.7 ± 0.6 fA/cm$^{2,}$ respectively. The highest surface recombination at 128 ± 7 fA/cm$^2$ is found in 80 nm polysilicon group without $AlO_x$. These results emphasise the efficacy of $AlO_x$ insertion on TOPCon surface passivation improvement after firing, which is in agreement with findings in [168]. The deterioration of passivation groups without $AlO_x$ or with reduced polysilicon thickness can be attributed to a firing-induced surface degradation and their lack of firing stability.

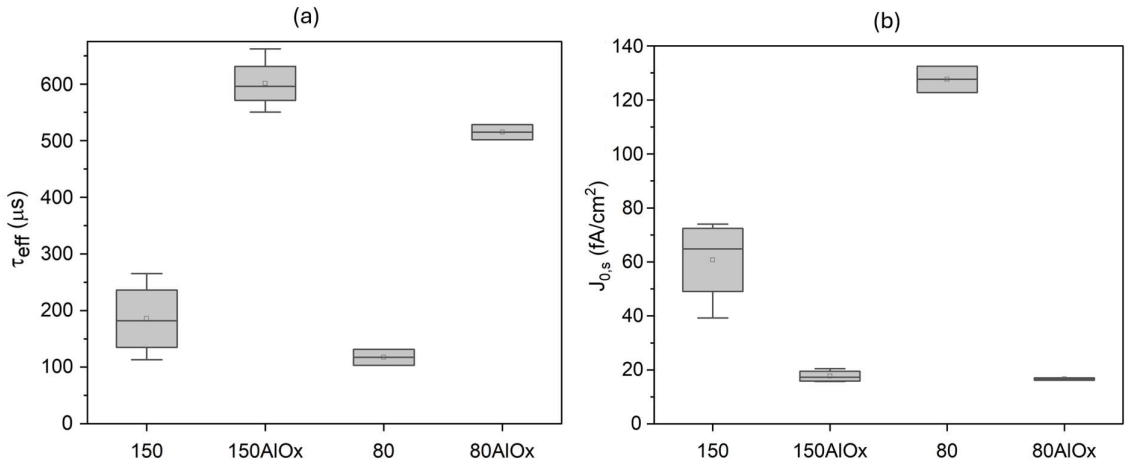


*Figure 3-4 Wafer effective lifetimes $\tau_{eff}$ and lumped surface recombination currents J0,s from different sample groups. Lifetimes measured via PCD using a Sinton WCT-120 tester. J0,s extracted from lifetime data reflects the 'lumped' recombination of two different surfaces.*

It is noted that Figure 3-4 (b) presents the extracted lumped surface recombination currents $J_{0,s}$ as an output under symmetrical sample assumption not met by the tested wafers, which are cell precursors with different front and rear finish. Hence the $J_{0,s}$ values reported here are taken as the lumped effect approximating an average of top and rear surfaces. The TOPCon side surface recombination $J_{0,TOPCon}$ provides the prior condition and the baseline for $J_{0,c}$ extraction by PL image periodicity analysis. This is because the $J_{0,TOPCon}$ values are correlated to the average image illuminance in the assessment of the impact of $J_{0,c}$ on spatial PL variations. A calibration point is chosen at $J_{0,TOPCon} = 10$ fA/cm$^2$ as the average of group 150$AlO_x$. This TOPCon surface value is lower than the PCD extracted 17.7 fA/cm$^2$ due to the non-symmetrical sample condition and the general observation that $J_{0,TOPCon} < J_{0,emitter}$. The experimentally inferred TOPCon recombination at 10 fA/cm$^2$ is notably higher than the reported number for optimised passivation as low as ~3 fA/cm$^2$ [85], [144], but likely to be close to the realistic sample passivation situation for such industrial samples.

Figure 3-5 presents the outcomes of extracted $J_{0,TOPCon}$ and $J_{0,c}$ values of all groups from the simulation-assisted PL analysis presented in chapter 2. It should be noted that the $J_{0,c}$ values of in $AlO_x$ free groups are unavailable, as spotted from the figure, because of limitations in extracting periodic signal from them via the PL method. The high surface $J_{0,TOPCon}$ values in these two $AlO_x$-free groups produce low PL intensity under current experimental condition, which obstructs the extraction of periodic PL metal contrast due to low signal-to-noise ratios. Further assessment of $J_{0,c}$ from these groups would require a change of imaging condition, which is beyond the scope of this result chapter.

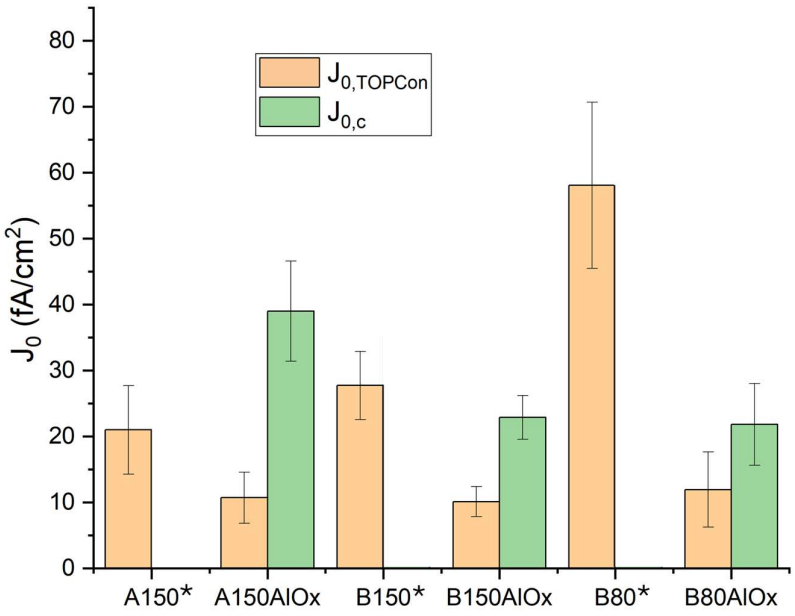


*Figure 3-5 TOPCon surface recombination $J_{0,TOPCon}$ and TOPCon contact recombination $J_{0,c}$ results of six sample groups. Note that $J_{0,c}$ results of A150, B150 and B80 groups, marked by *, are absent because of method limitations*

As shown by the orange bars in Figure 3-5, the addition of $AlO_x$ effectively reduces surface recombination $J_{0,TOPCon}$. This suppression is most pronounced in the case of 80 nm polysilicon, where in the absence of $AlO_x$, the highest $J_{0,TOPCon}$ value is observed. The finding aligns with the trend shown in the PCD measurements of $J_{0,s}$ results in Figure 3-4. However, the $J_{0,TOPCon}$ values derived from PL intensities should not be directly compared to the PCD-derived $J_{0,s}$ values. This is because PCD measurement assumes identical $J_{0,s}$ values for both surfaces, whereas the PL interpretation assumes a fixed value for emitter front and a variable rear TOPCon $J_{0,s}$. Establishing a correlation between these two approaches would require symmetrical TOPCon samples, which were not available in this study. This limitation provides

a direction for a future validation study to assess the accuracy and effectiveness of the PL simulations.

In terms of contact recombination $J_{0,c}$, as shown by the green bars in Figure 3-5, comparisons can be made across the three groups available. By comparing group A150AlOx and B150AlOx, it can be observed that metal paste B reduces $J_{0,c}$ by 42% from 38.5 ± 7.5 fA/cm$^2$ to 22.5 ± 2.2 fA/cm$^2$. Lastly, the negligible difference between group B150AlO$_x$ and B80AlO$_x$ indicate that the reduction of polysilicon thickness has a minimum influence on contact passivation when combined with insertion of AlOx. Such a result indicates the efficacy of AlO$_x$ insertion in retaining both surface and contact passivation structures in thin polysilicon structures.

## 3.5. Contact-related resistance results

Contact-related resistances include three components in the contact current collection path as illustrated in Appendix E. The three components are characterised by contact resistivity $\rho_c$, surface layer sheet resistance $R_{sheet}$ and finger line resistivity $r_{line}$. Figure 3-6 (a) illustrates the metal-silicon contact resistivity $\rho_c$ results from TLM measurements with the detailed experimental process described in in Appendix E. It can be observed that AlO$_x$ insertion is linked to an increase in the contact resistance, which is most significant in the sharp gain from 4.2 ± 1.3 mΩ.cm$^2$ in group A150 to 8.7 ± 2.3 mΩ.cm$^2$ in group A150AlO$_x$. The contact resistivity of group A150AlO$_x$ stands out with the highest average and widest variation, indicating increased contact degradation. Such results agree with the reduction of FF in finished cells in AlOx structures shown in Figure 3-6. The change of metal paste from A to B, is effectively linked to a reduction of contact resistivity. This is supportive of the benefits of paste B in both recombination and resistance terms. Further reduction of $\rho_c$ can be associated with the thinner 80 nm polysilicon layer, which confirms with findings in [173].

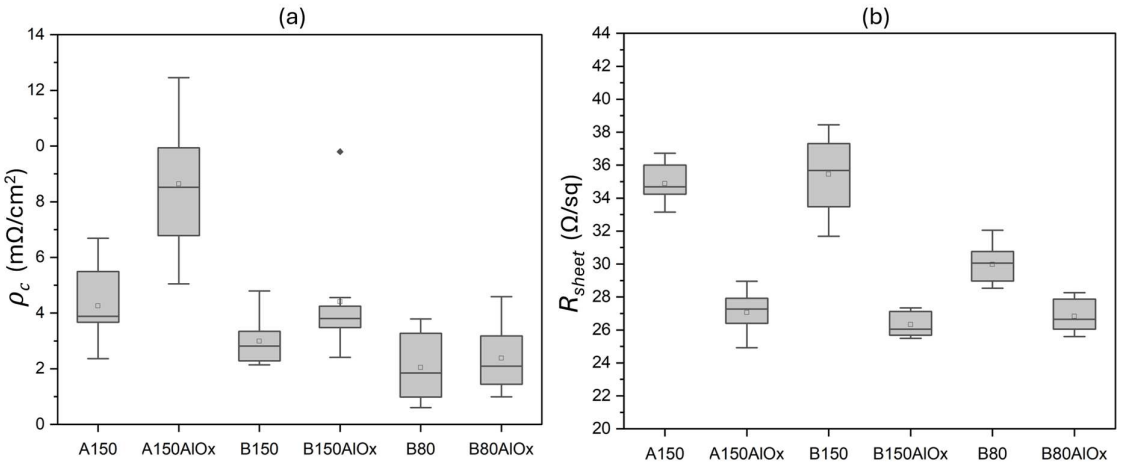


*Figure 3-6 Metal-silicon contact resistivity $\rho_c$ and the polysilicon layer sheet resistance $R_{sheet}$ results from six sample groups. Both originate from TLM measurements.*

Figure 3-6 (b) illustrates the surface layer sheet resistance results from TLM measurements, the values of which indicate current conduction in the heavily doped polysilicon layer and the Si bulk. A general trend of a $R_{sheet}$ reduction is observed with the insertion of $AlO_x$, which ranges up to a 26% relative reduction from 35.4 ± 2.3 Ω/sq in B150 to 26.3 ± 0.8 Ω/sq in B150AlOx. The change in metal paste and polysilicon thickness appears to have little influence on the sheet resistance with minor relative differences. Factors influencing $R_{sheet}$ in the ex-situ doped polysilicon layer can include dopant diffusion profiles [155], polysilicon crystallinity and potential dopant deactivation via grain boundary segregation [173]. It may be speculated that the $AlO_x$ benefits can be attributed to an improved polysilicon microstructure, but further $R_{sheet}$ interpretation cannot be confidently drawn without advanced polysilicon characterisation beyond the scope of the chapter.

Figure 3-7 illustrates finger line resistivity results from separate finger resistance measurements. Data range from 6 groups overlap, indicating no significant change observed with fingers made with two pastes. The results show that the change in glass frit composition in metal paste has a minimal effect on current conduction in metal fingers.

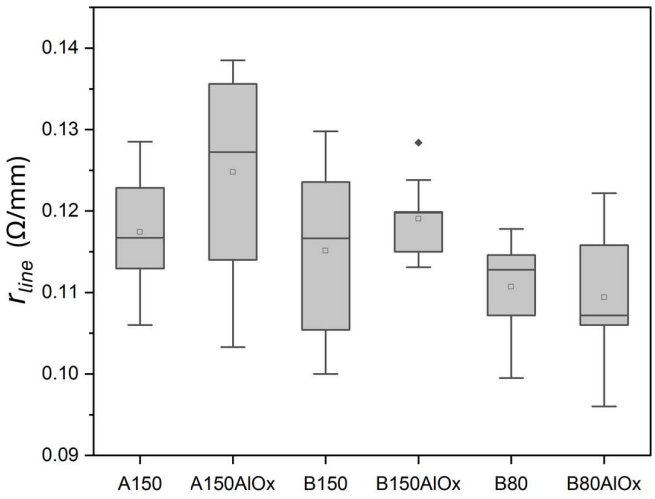


*Figure 3-7 Metal finger line resistivity results from six sample groups, obtained from the line resistivity measurement.*

Additional information is revealed by an intra-sample distribution map of $\rho_c$ and $R_{shee}$ . Figure 3-8 (a) and (b) depict the distribution of $\rho_c$ and $R_{sheet}$, respectively, from a group B80AlOx wafer. Each rectangular segment in the colour map indicates the region of individual TLM test samples. A key trend in both maps is a reduction towards the centre of the wafer. The variation magnitude is more significant for $\rho_c$ which drops by 95% from a highest 5.4 mΩ.cm$^2$ in an edge piece to a 0.4 mΩ.cm$^2$ in a centre piece. The variation scale is smaller for $R_{sheet}$ contained within a 12% range of 25.0-28.4 Ω/sq. Such spatial distribution is likely due to non-uniform heating during the belt-furnace firing process, which typically exhibits a temperature maximum near the centre of the wafer. The distribution indicates that, specific to this wafer structure, a higher firing temperature leads to a sharp decrease in $\rho_c$ and a smaller decrease in $R_{sheet}$. The effect of higher temperatures is supported by findings in [173], where the link is established via increased driving-in of phosphorus dopants at elevated temperatures. The magnitude of the 95% $\rho_c$ change may be indicative of additional changes in current conduction paths at the interface which merits microstructural examinations of the metal-silicon interface.

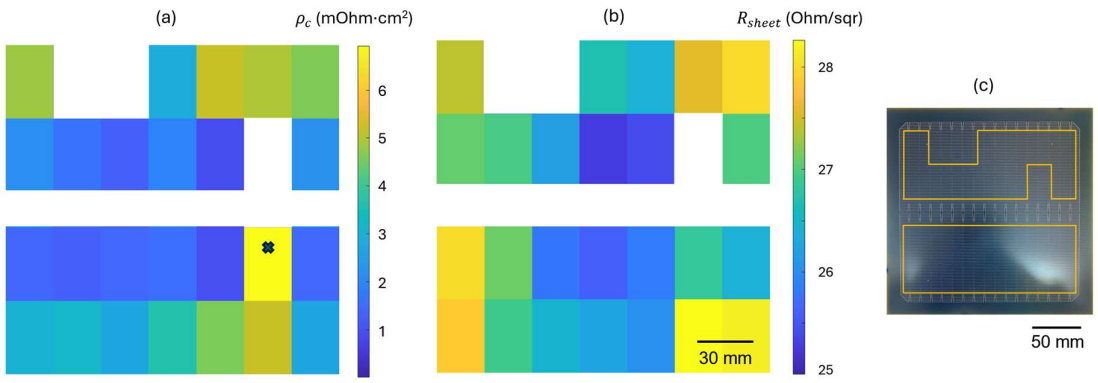


*Figure 3-8 (a) spatial distribution of $\rho_c$ in a group B80AlOx wafer, a data outlier is indicated by a cross. (b) spatial distribution of $R_{sheet}$, missing pieces because of handling damage (c) Location of the displayed regions on a wafer*

## 3.6. Microstructural examination of the contact interface

Figure 3-9 illustrates the cross-section of the contact-free TOPCon surface. The surface appears mostly flat with scattered surface pyramids remaining from the single-sided etching process. The nitrogen map shows uniform and full surface coverage of the nitride layer. In contrast, the phosphorus signal, originating from the heavy doping in the polysilicon layer, appears non-uniform and clustered. This behaviour is likely due to phosphorus grain boundary segregation within the polysilicon layer. The results of element distributions within TOPCon surface layers, enabled through the high-resolution EDX capability, have not been reported elsewhere.

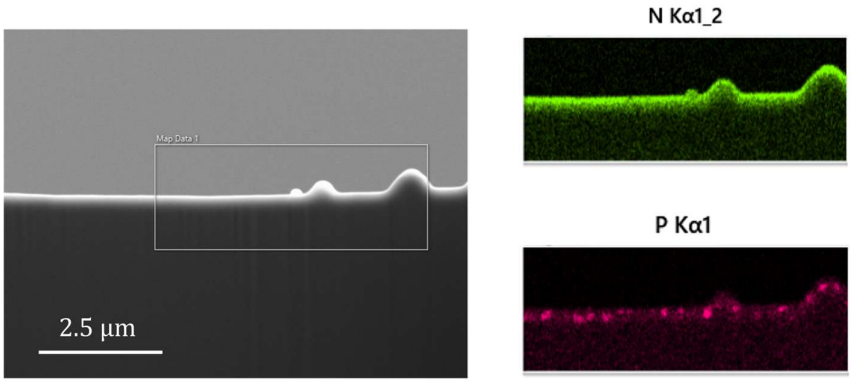


*Figure 3-9 SEM cross-sectional image of non-contacted TOPCon surface from group A150AlOx, and associated EDX element maps for nitrogen and phosphorous distribution.*

Figure 3-10 (a) illustrates the cross-section under metal fingers from a selected group B80AlOx wafer, which provides the general microstructure template of the contact interface common to the industrial fire-through contacts. The FIB-cleaved cross-section SEM image displays the silver finger at the top and the silicon substrate at the bottom. A continuous silver phase in the

finger is visible as a result of the sintering of grains. The presence of large pores is spotted, which is likely due to both the escape of organic binders and the liquefaction of glass frit during firing. Figure 3-10 (b) provides a magnified view towards the metal-silicon interface and with associated EDX elemental maps in Figure 3-10 (c). A continuous glass interlayer, rich in oxygen and lead, is observed between silicon and silver. The Pb glass wets the substrate surface and acts as an etchant on the nitride during firing, a function which is evident from the partial opening of the nitride layer. Closer examination of the two major opening sites, marked by locations A and B, reveals distinctive microstructural features. At site A, silver colloidal precipitates are embedded within the glass layer. The alignment of high local precipitate density with the nitride removal opening suggests that this region can facilitate current conduction between metal and silicon via nano-Ag colloid assisted tunnelling [174][175]. In contrast, site B shows no silver but oxygen incorporation into the underlying polysilicon, which is shown by the coincidence of oxygen and phosphorus enrichment location under the glass interlayer. This finding suggests that glass-etched openings can also expose the underlying polysilicon to excess oxidation. The absence of silver precipitates at site B is likely due to the void separating silver grains. These observations indicate that an opening on $SiN_x$ does not necessarily contribute to current pathways in the absence of silver dissolution and precipitation.

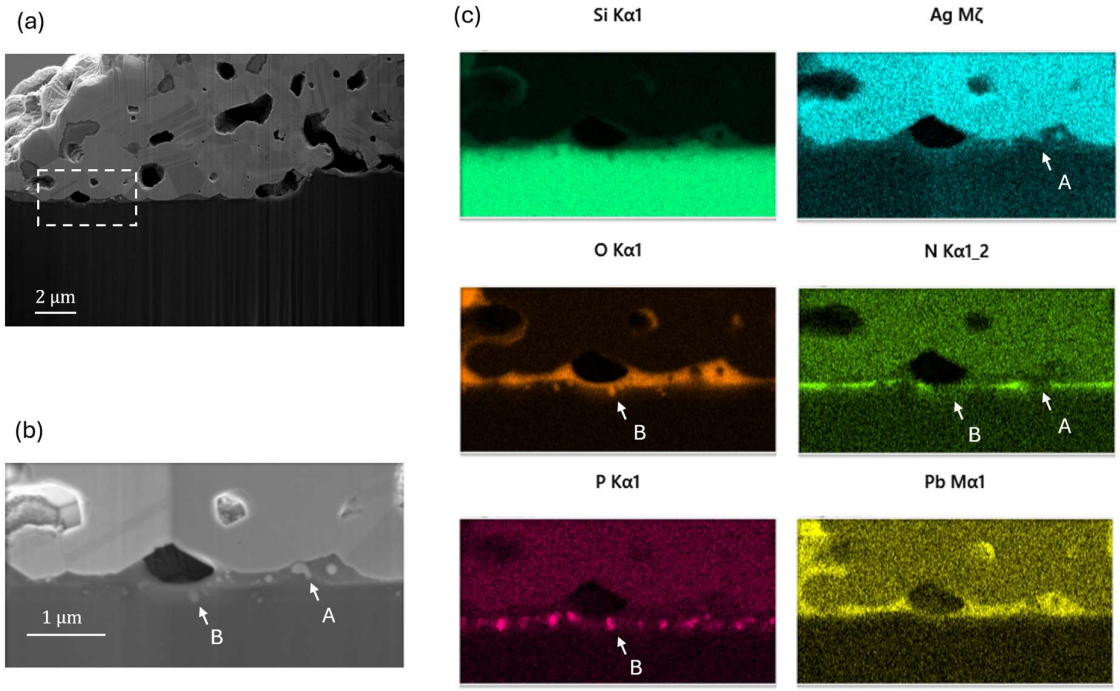


*Figure 3-10 (a) SEM micrograph showing the cross-sectional view of silver contacts on silicon. (b) a high-magnification SEM micrograph towards the interface. (c) EDX maps of elemental distribution within the same region in (b).*

Direct comparisons between sample groups are possible following such detailed morphological and chemical examinations. Figure 3-11 (a) and (b) presents results from sample group A150AlO$_x$ and B150AlO$_x$ which differ only by metal paste composition. A distinctive crack, as marked by the arrow, is found between glass interlayer and silver grains above in the A150AlO$_x$ image. Sequential cross-sectional images along the depth direction, included in Appendix H, show the extension of the 2D crack in both horizontal and depth directions. Such a separation reduces the effective metal-silicon contact areas, which is likely responsible for the highest contact resistivity in sample A150AlO$_x$ shown in Figure 3-11. This formation of the crack is hypothesised to originate from shrinkage mismatch during cooling, which is a result of excessive glass interlayer thickness linked to the high glass frit ratio in paste A. No crack is found in other groups than A150AlO$_x$.

A second key difference between the two groups is the integrity of nitride layer under the interfacial glass. Compared to paste A150AlOx, the nitride layer in sample B150AlO$_x$ sample appears to be denser with fewer breakages. The increased number of openings in nitride layer in sample A150AlO$_x$ compared to B150AlO$_x$ can be associated with the elevated contact recombination shown in Figure 3-5. This supports a link between areas of nitride discontinuities to excessive recombination, in agreement with Hermann's findings in [78].

Such microstructure evidence indicates that reducing glass frit content in the paste is beneficial in limiting nitride opening. Nevertheless, the author notes that the current microstructural evidence is based on a limited number of sites, and these trends are to be generalised with only moderate confidence.

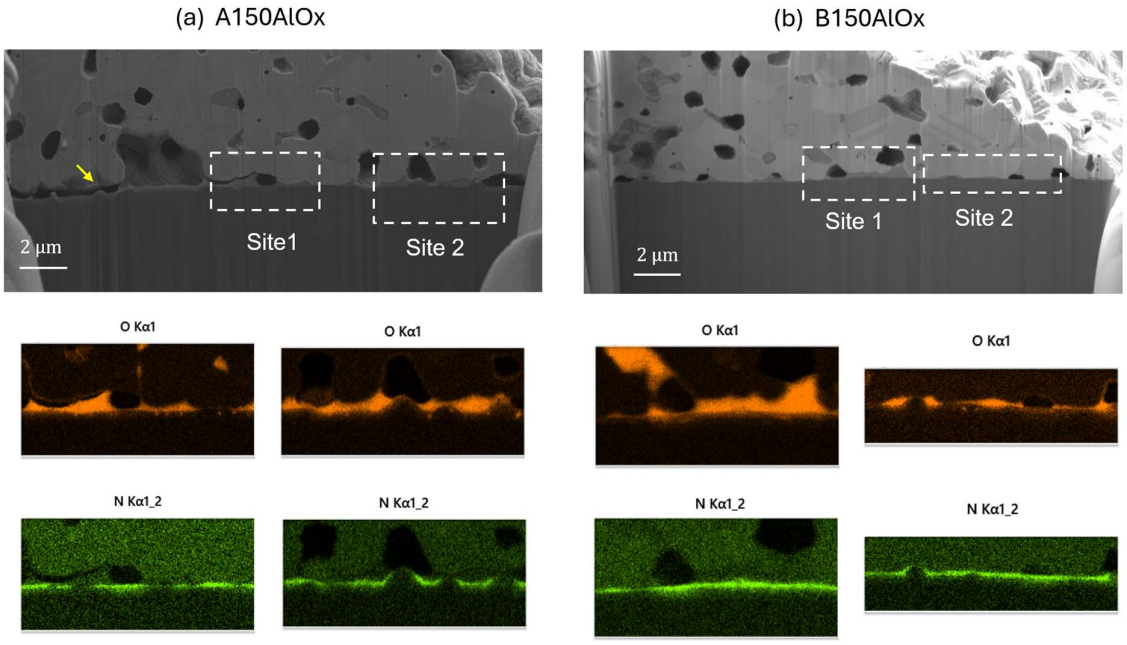


*Figure 3-11 SEM images showing contact cross-sections and EDX oxygen and nitrogen element maps for (a) a sample in group A150AlOx and (b) a sample in group B150AlOx*

Figure 3-12 illustrates a comparison of FIB sequential slicing results from B150 and B150AlOx. Five slices are shown for each sample to demonstrate the depth evolution of the contact structure. Ag precipitates, marked by arrows, can be spotted mostly as dispensed colloids in the glass interlayer with <100 nm diameter, with very few as deposition on the silicon substrate surface. A similar microstructure can be found across other sample groups (shown in Appendix I). The most notable difference between the B150 and B150AlOx lies in the density of the Ag precipitates, with significantly more found in the $AlO_x$-free sample. Since B150$AlO_x$ has been correlated with higher $\rho_c$ shown in Figure 3-6 (a), it can be further deduced that the reduction in Ag colloid density is responsible for the increase in contact resistivity. Such findings are supportive of dispersed Ag colloids as current pathways [174][175].

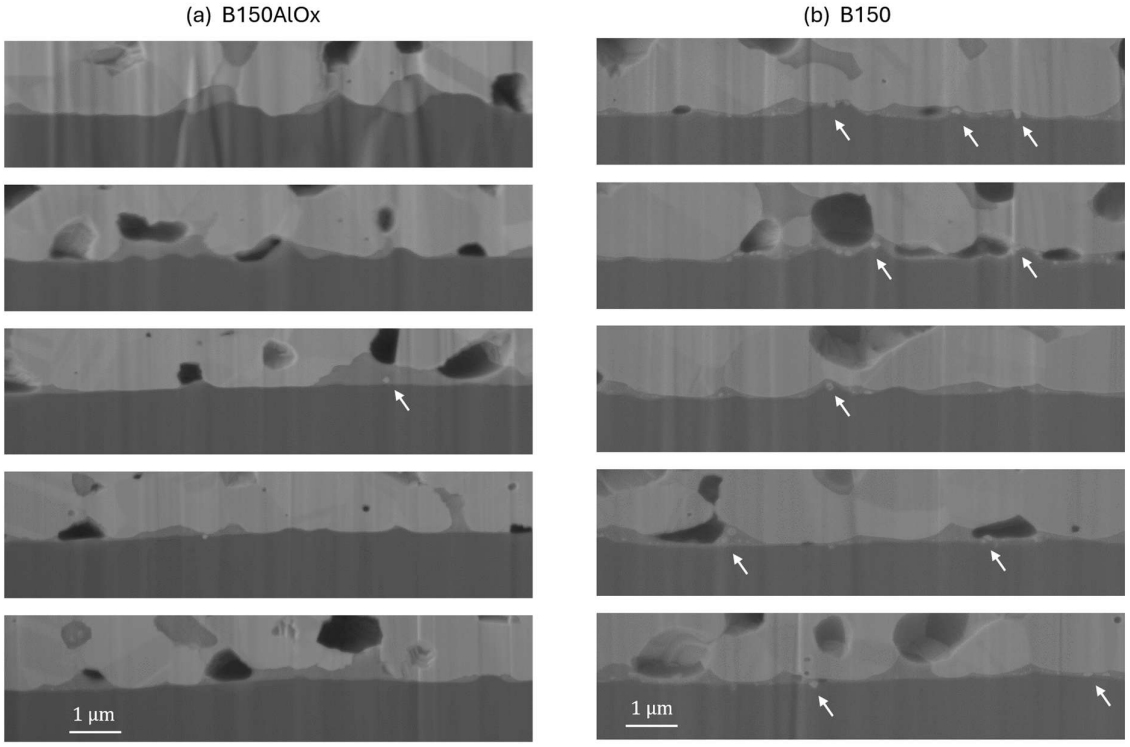


*Figure 3-12 SEM images for sequential FIB slicing cross-sections of (a) a sample in group B150AlOx and (b) a sample in group B150, locations with Ag colloid is marked by arrows*

Figure 3-13 further presents the microstructure of group B80. Most damage in the nitride is found in this group as compared to the nitrogen signal in both Figure 3-10 and Figure 3-11. This finding is indicative that a thinner polysilicon structure, in the absence of extra $AlO_x$ protection, is highly susceptible to glass etching damages during contact firing. The increased discontinuity of the nitride can be related to the highest recombination levels in group B80.

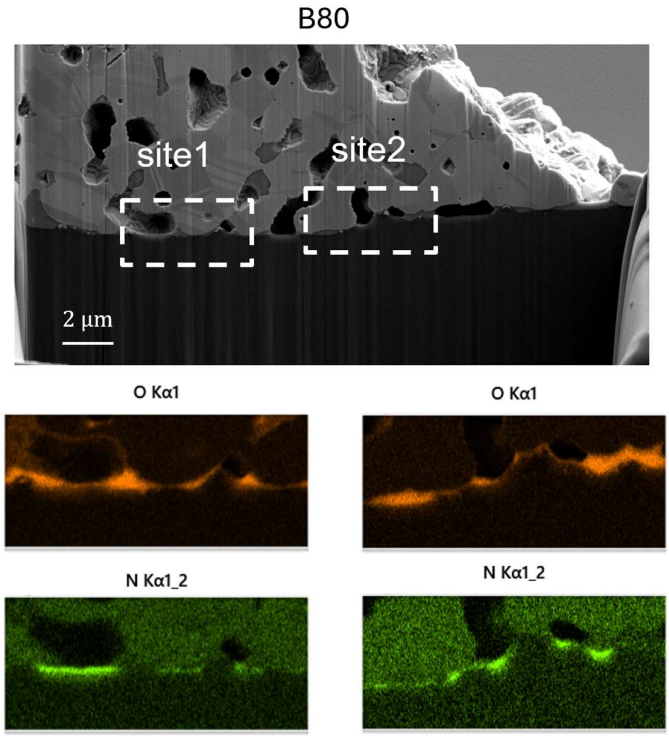


*Figure 3-13 SEM images showing contact cross-sections and EDX oxygen and nitrogen element maps fora sample in group B80*

## 3.7. Discussion

The author would like to note that the electrical performance measurements from section 2.3-2.6 were on complete groups of samples. From these, only a random piece from each group was used for microstructural analysis due to the extensive effort required for electron microscopy. As such, only the most prominent correlations between microstructure and performance are discussed here, including the following:

Firstly, it is demonstrated in this chapter that the insertion of $AlO_x$ appears to help preserve the structural integrity of silicon nitride passivation after firing. This protective effect is evidenced by the contrast of improved nitride integrity in the B150$AlO_x$ and the extensively damaged nitride in the B80 sample. Since $AlO_x$ addition is linked to significant reduction in surface recombination $J_{0,TOPCon}$ irrespective of polysilicon thickness, it is speculated that contact recombination $J_{0,c}$ is likewise suppressed (despite non-available data) following the improved nitride integrity. This observation that nitride layer integrity is critical to contact passivation aligns with Herrmann et al. in [78], who showed that $J_{0,c}$ is primarily governed by the area fraction of nitride removal, rather than by the area fraction of deep metal ingression. Such microstructural insights thus offer a passivation performance improvement direction by

enhancing the firing stability of the surface dielectric. The ultra-thin $AlO_x$ has been shown here as one of the possible addition options to promote thermal stability, which provides a useful reference for future designs of compatible dielectric passivation for fire-through TOPCon contacts.

Secondly, in the absence of large surface Ag depositions, dispersed colloids embedded in glass provide current pathways. Prior literatures suggest that Ag can grow epitaxially on the substrate in a sheet shape, or into silicon in a pyramid shape, depending on the silicon crystal orientation [83], [176]. The direct Si-Ag contact provided by surface depositions was regarded as an efficient conduction location [175]. By contrast, no such large-scale Ag growth on Si surface has been observed in this study, which is possibly due to the consistent separation between Ag grains and Si surface by the glass interlayer. Instead, migrated Ag during fast firing shows up predominantly as dispersed colloids within the glass layer, the density of which has been related to contact resistivity. This supports the alternative conduction model that dispersed colloids can form efficient current pathways across the glass while avoiding deep metal penetrations. This finding is particularly relevant for understanding the balance between low resistivity and passivation preservation, which is a central challenge in fire-through contact design. Such results can also direct future investigations into the role of silver colloids in contact resistivity and potentially recombination, which can be further detailed via quantifying its density and distribution under various processing conditions.

Thirdly, it is found that a thin and uniform interfacial glass layer is beneficial to improving contact performance. Cross-sectional images demonstrate uniform wetting of the silicon surface, forming a continuous interlayer. However, excessive viscous flow of glass from intergranular spaces towards the surface could leave coalesced pores and even crack detachment at the interface, as seen in the A150$AlO_x$ structure. The reduction of glass in paste B has been further shown to potentially correlate to reduced nitride damage. Such microstructure evidence reinforces prior work in [156], who reported that the glass frit ratio controls both the etch pit area and depth in planar-view SEM examinations. It is hence speculated from the microstructural examinations that adequate wetting of the metal-silicon interface and avoidance of local glass accumulation are both essential in low contact $J_{0,c}$ and $\rho_c$. This provides practical guidance for adapting TOPCon-compatible glass frit formulations, with objectives including (a) thinning of the glass interlayer, (b) limiting nitride dissolution, and (c) facilitating Ag dissolution and precipitation during fast-firing. Furthermore, the complex cross-sectional morphologies observed for the glass layer suggest potential local

variations in current collection efficiencies, which offers the direction for correlative chemical-electrical microscopy characterisation as a future step.

## 3.8. Summary

This chapter provides a combination of electrical and microstructural characterisation of TOPCon structural variations. Contact properties are evaluated through both the recombination term $J_{0,c}$ and the resistivity term $\rho_c$. The incorporation of a 3-5 nm $AlO_x$ beneath the nitride is shown to enhance overall cell efficiency via improving both surface and contact passivation. The side effect of $AlO_x$ is also found by the resistivity $\rho_c$ and FF increase. The reduction of glass frit content in metal paste is effective in further minimising contact recombination while maintaining low resistivity. A decrease in polysilicon thickness is found to significantly degrade surface passivation, although this can be remedied by the $AlO_x$ insertion. A spatial distribution of $\rho_c$ indicates its high sensitivity to firing temperature non-uniformities.

Microstructural investigations in this work provide a correlation between improved contact passivation with reduced nitride damages in $AlO_x$ protected samples. The thickening of the glass interlayer is associated to potential crack formation and an increase in resistance. Moreover, the dispersed Ag colloids are linked to contact resistivity, supporting their role as current conduction pathways across the interface. The insights delivered in this study improve microstructural understandings of contact passivation and recombination in relevant TOPCon structures, offering valuable guidance for the further development of the metallisation pastes and thermal processing conditions. Such results are hence directly relevant to industrial optimisation and scaling of TOPCon solar technology.

# 4. Characterisation of TOPCon passivating contact structure via time-of-flight elastic recoil detection analysis

The methodology and results presented in this chapter have been accepted for publication in the journal Applied Physics Letters under the title, "*Characterization of solar cell passivating contacts using time-of-flight elastic recoil detection analysis*". The author extends gratitude to Jana-Isabelle Polzin from Fraunhofer Institute for Solar Energy Systems ISE for sample preparation, and Matthew Sharpe and Callum McAleese from the Surrey Ion Beam Centre for conducting the ERD experiments included in this chapter.

## 4.1. Introduction

As introduced in section 1.5, the TOPCon passivation efficacy is dependent on the optimised hydrogenation of the thin-film surface structure, achieved via a high-temperature hydrogen release from a H-rich dielectric layer [177], [178], [179]. Excessive hydrogen accumulation near the tunnelling oxide layer is reported to cause degradation of passivation properties [121], [122], [180]. Therefore, analysing the hydrogen distribution throughout the structure after firing is critical to further improving TOPCon contacts.

Detection of elemental hydrogen in semiconductor thin-film structures is typically achieved via secondary ion mass spectrometry (SIMS) [181], [182], [183], [184]. SIMS provides chemical analysis by sputtering the sample's surface with a primary ion beam with high energy and fluence. The sputtering causes the ejection of secondary ions from the surface layer, which are detected by a mass analyser to reflect on surface composition. The dynamic sputtering process continuously removes surface layers to allow compositional profiling into depth. A detailed description of SIMS measurement is given in Appendix B.

However, SIMS depth profiling results are susceptible to a spreading-out measurement artefact, as shown in relevant SIMS studies on TOPCon-like structures [89], [121], [185]. The reasons include (a) displacement of H by the knock-on effect from the SIMS primary beam [183], and (b) changes of secondary ion yield as the solid matrices change during sputtering of the multi-layers (also known as the matrix effect) [186], [187]. In addition to the artefacts, SIMS sensitivity of sample hydrogen is poor [188] because of the environmental hydrogen noise. The residual hydrogen-containing species, which are present ubiquitously in vacuum systems, will

arrive and attach to the exposed sample surface throughout the SIMS sputtering process. This environmental H content is not differentiable from sample H content by the SIMS mass detector [189], [190], and introduces large uncertainty in H quantifications at low concentration levels. One way to circumvent the environmental H complication is to use a hydrogen isotope, i.e. deuterium ($^2$H/D) with low natural occurrence [185], [191]. The SIMS detection limit for D is $10^{16}$ atoms/cm$^3$, much lower than the typical H limit at $10^{18}$ atoms/cm$^3$ [186], [188]. However, an additional challenge in using deuterium in SIMS studies arises from the overlap between the complex ion $^1H^{2+}$ and the $^2D^+$ signal on SIMS mass spectra, leading to ambiguity over sample D assignment.

In contrast to SIMS, the elastic recoil detection (ERD) analysis method utilises the elastic recoiling process, in which the elastic collision between an incident high-energy primary ion and a sample atom results in recoiling of the sample atom [192], [193], [194]. Sample atoms recoil from a shallow depth below the surface with certain energy attenuation caused by the stopping force of the material matrix, which allows for depth compositional profiling. Modern ERD setups additionally implement a time-of-flight (ToF) detector along with the conventional ion energy detector for improved mass separation [195], [196]. A detailed description of ToF-ERD can be found in Appendix D. The difference in ion signal generation makes ToF-ERD less prone to environmental H noise, since environmental contaminants are limited to the sample surface. ToF-ERD also offers enhanced hydrogen detectability, because sample $^2$D and $^1$H signals can be further fully separated by the paired energy-ToF measurement in ToF-ERD experiments. Due to these advantages, a few studies on silicon passivation structures have implemented ERD in detecting H contents [197], [198], [199].

In this chapter, ToF-ERD is employed in the analysis of H distribution in a partially deuterated TOPCon structure. The ToF-ERD capability of fully differentiating D and H is utilised to provide complementary information to conventional SIMS results in the detailed characterisation of the elemental profiles in TOPCon contacts.

## 4.2. Experimental Details

Figure 4-1 (a) demonstrates the sample structure investigated in the chapter. The sample substrate is a 200 μm n-type float zone silicon wafer with a shiny etched surface. It features a 50 nm $n^+$ polysilicon layer on top of a 1.3 nm tunnelling oxide by design. The SiOx interlayer was thermally grown, and the polysilicon layer was formed via plasma-enhanced chemical vapour deposition (PECVD) of amorphous silicon and a subsequent crystallisation annealing

at 900 °C for 10 min in a nitrogen atmosphere. H/D is released from the 70 nm surface silicon nitride layer. This nitride layer was PECVD deposited with silane $SiH_4$ and deuterated ammonia ($ND_3$) as gas precursors, leading to a partial D substitution. A final hotplate annealing at 500 °C for 2 min was used for adequate H/D release. The TOPCon sample described above was prepared by collaborators at Fraunhofer ISE. SIMS measurements were conducted by specialists in Fraunhofer ISE first on an identical sample of same batch. The surface roughness of the wafer was measured in Oxford using a CoreAFM atomic force microscope from Nanosurf™.

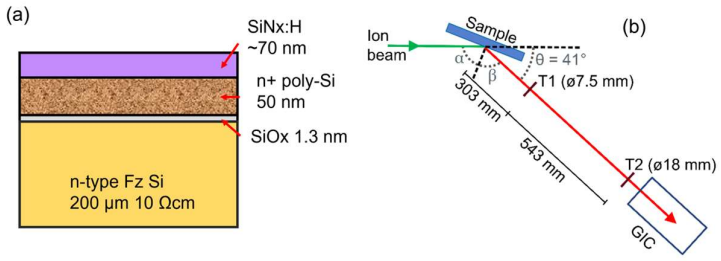


*Figure 4-1 (a) TOPCon surface structure. (b) ToF-ERD experimental setup. The ion beam angles, time-of-flight timing foils (T1 and T2) and GIC energy detector are marked.*

The ERD experimentation and software data processing discussed below were conducted by collaborators in Surrey Ion Beam Centre. Figure 4-1 (b) illustrates the ToF-ERD setup at the Surrey Ion Beam Center, featuring two timing foils (T1/T2) for time-of-flight (ToF) measurements and a gas ionisation chamber (GIC) for ion energy detection. The recoiled-atom detectors are placed at a scattering angle of $\theta = 41°$ to the incident beam direction. This means the incident ($\alpha$) and ($\beta$) exit angles were set to 69.5° to balance between mass sensitivity and depth resolution across the thickness concerned [200], [201]. A negative sputter ion source (HVE 860) generates negatively charged ions, which are directed by an injector magnet toward a 2 MV tandem accelerator. The ions are accelerated in the process to the desired energy and switched to a positive charge. Incident beams of $^{127}I^{8+}$ at 12 MeV or $^{35}Cl^{6+}$ at 8 MeV were employed for the TOPCon sample measurement with an energy dispersion below 10 keV. These energies were selected based on recoiling cross-sections, detection count rate, and mass separation [201]. Lower Cl beam energy is used to avoid the near-surface recoiled D having enough energy to hit the GIC detector back wall and register incorrect energy readings. The incident beam projectile covers a 3 × 4 mm² spot on the sample surface defined by slits placed before the sample chamber. Each measurement was run for 30 minutes. The ion counts at both the second timing foil and GIC detector reached around 715 counts/s for Cl and 555 counts/s for I, with a background below 20 counts/s.

The ToF-ERD measurement results were first recorded as energy-ToF coincidence histograms by the analysis software Potku [202]. Potku was first used to filter out false coincidence events following the statistics of the ToF-energy data. The signals for individual elements were identified and separated from the coincidence histogram. The conversion from recoiling energy to the depth of origin was further done in Potku, which involves determining the material stopping force. Potku took an initial guess of the material composition for a stopping force from tabulated values in the library and used it to derive depth profiles (in this case, a dense stoichiometric silicon nitride). It then used the result-inferred new composition to adjust the stopping force parameter in an iterative process until a consistent solution of depth profiles is found. The coincidence histogram and elemental depth profile results are discussed in sections 4.3 and 4.4.

## 4.3. The coincidence histogram

Figure 4-2 presents the histograms of detected true coincidences from ToF-ERD measurement. It illustrates the measured energy on y-axis and time-of-flight (ToF) between timing foils on the x-axis. Such coincidence histograms are displayed for $^{35}Cl^{6+}$ in Figure 4-2 (a) and $^{127}I^{8+}$ in Figure 4-2 (b). Because of the difference in atomic masses, elements produce distinctive energy vs. ToF parabolic relations as shown in the 'banana' shaped traces histograms. This allows separation between elements as labelled next to each trace. Each elemental trace spans over a range of energy and time-of-flight channels, resulting from the ion energy loss along the incident and recoiling path by the attenuation effect of the sample matrix known as the electronic stopping force. This means atoms from deeper within the sample appear further along each parabola at the low-energy end. The logarithmic colour scale of the histogram indicates detector count density, which relates to the concentration of detected species. Clear elemental traces in both histograms include the main composition of interest: Si, O, N as well as both H and D at lower energies. Crucially, in this work H and D signals can be fully separated, which presents the first report of an unambiguous distinction between H and D in a TOPCon

structure. This highlights the strength of ToF-ERD method in detecting deuterium-substituted samples.

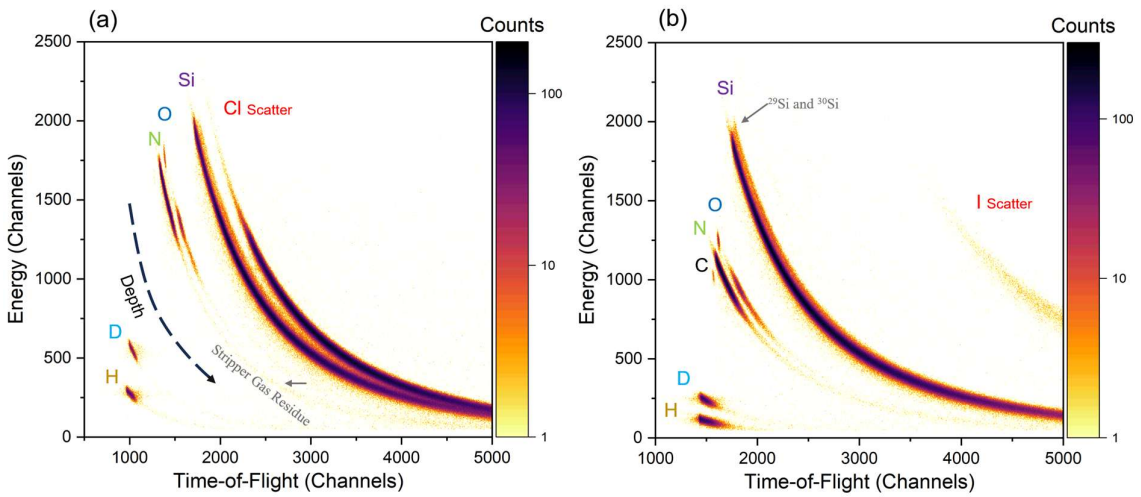


*Figure 4-2 Coincidence histograms showing energy and time-of-flight of atomic species, produced from an incident beam of (a) $^{35}Cl^{6+}$ at 8 MeV energy and (b) $^{127}I^{8+}$ at 12 MeV energy.*

Compared to the I source, the Cl source can allow deeper hydrogen measurement with better depth resolution, thanks to the smaller mass difference between Cl and H atoms. This is because an incident ion with a mass closer to that of the target atom imparts more energy in a collision (see Appendix D), which allows deeper signal generation. This difference can be shown by the downshifts of parabolic traces on the y-scale in the iodine histogram compared to the chlorine histogram. On the other hand, using the $^{127}I$ source helps to avoid overlap between the scattered Cl source and Si signal at lower energies and can reveal elements heavier than $^{35}Cl$. It is also noted that a low-energy nitrogen signal, indicated by the dark pointer in Figure 4-2 (a), appears in the Cl histogram. This minor experimental artefact stems from nitrogen leakage in the stripper gas, which was used to produce positively charged $Cl^{6+}$ ions by the accelerator. Since these low-energy N signals would correspond to depths beyond the region of interest, they do not affect the measurements. In contrast, minimal stripper gas is required for $I^{8+}$ ions production, so the iodine histogram remains free of such leakage artefacts.

Phosphorus, present as a dopant within the polysilicon layer, is not clearly distinguishable from silicon in such histograms. The chlorine ion source does not provide sufficient mass separation between phosphorus ($^{31}P$) and the neighbouring silicon isotopes ($^{30}Si$, $^{29}Si$, $^{28}Si$), making the phosphorus trace merge with silicon traces. Moreover, silicon's natural isotopic distribution (from masses 28 to 30, with isotope $^{30}Si$ having 3.1% natural abundance [203]) significantly broadens its elemental trace, which complicates clear differentiation from phosphorus. While

using iodine as a heavier source can theoretically enhance mass separation, the high energy dispersion of silicon traces still poses a substantial challenge, limiting reliable quantification of P signals in such energy-ToF coincidence histograms.

## 4.4. Depth Profiling

Potku analysis outputs the elemental depth profiles on thin film units (TFU, a TFU unit is $10^{15}$ atoms/cm$^2$) based on the calculated areal density of elements. A thin film thickness measured in TFU can be converted into nanometres with known atomic density of the material [196]:

$$\frac{t[TFU]}{t[nm]} = \frac{\rho n N_A}{10^{22} m_r} \qquad 4\text{-}1$$

Where $\rho$ is material's mass density (g/cm$^3$), $n$ is atoms per molecule, $N_A$ is Avogadro's constant ($6.022\times10^{23}$ mol$^{-1}$), and $m_r$ is the relative molecular mass (g/mol). The right-hand side of the equation represents the atomic density (atoms/cm$^3$) plus an additional unit conversion factor of $10^{22}$. In the thickness conversion process used in this chapter, a uniform density of $\rho$=2.33 g/cm$^3$ following Si substrate density at 20 °C is assumed for all layers.

Figure 4-3 illustrates the ToF-ERD elemental depth profiles constructed from results using Cl source. Depths on x-axis are given as TFU on the bottom scale as well as corresponding nanometres on the top scale of this figure. Concentration profiles are divided into suggested layers of the TOPCon structure. Within the first 20 nm, a surface contamination layer containing oxygen and carbon (trace) is visible, likely as a result of sample handling. The following 20–100 nm range indicates a clear silicon nitride layer with an approximate 1:1 ratio of silicon to nitrogen. $SiN_x$ film density can range between 2.37-3.17g/cm$^{2,}$ depending on both stoichiometry and synthesis method. The simplification of using c-Si density 2.33 g/cm$^3$ can result in an overestimation of nm thickness in conversion from TFU to nm, which can be circumvented by complementary density measurement of the surface film in future studies. Within the same 20–100 nm region, average concentrations of 13.0 at.% and 5.4 at.% are measured for deuterium and hydrogen, respectively. This reveals the D-rich hydrogen incorporation in the nitride layer.

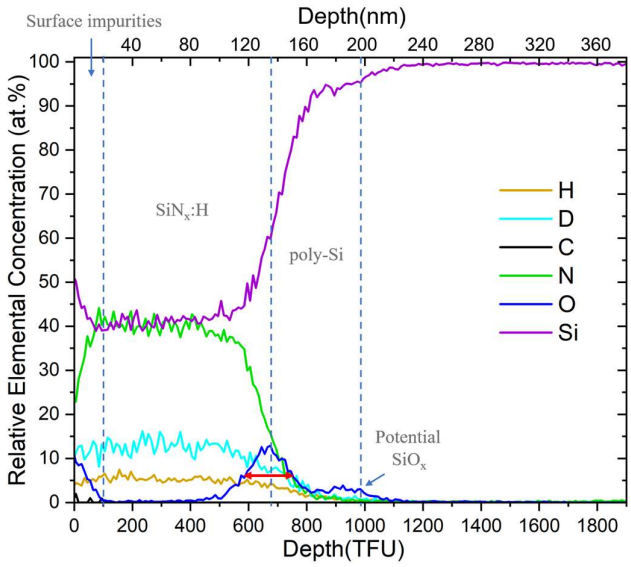


*Figure 4-3 ToF-ERD depth profiles of elements including H,D,C,N,O and Si, with a 8 MeV $^{35}Cl^{6+}$ incident ion source. Depth scale give in both TFU (bottom) and nanometre (top)*

The nitrogen signal gradually drops from 38% to 1% over a 60 nm range starting at around 100 nm. This corresponds to the change from nitride to polysilicon layer. Two broad oxygen peaks appear at the upper (around 140 nm), and the lower (around 200 nm) interfaces of the poly-Si. The first 140 nm strong oxygen peak is likely linked to furnace oxide formation on top of the heavily doped polysilicon during its high-temperature crystallisation annealing. The heavy doping in polysilicon aids the formation of such an unintentional oxide. This first oxygen peak is notably wide, with a half-peak width of 30 nm marked by red line with arrows. This is likely due to broadening caused by sample roughness, the effect of which is also reflected by the 20 nm thick surface contamination layer. The second 200 nm minor 'lump' marked by an arrow is thought to be related to the interfacial oxide content. The oxygen level drops slowly to 0% beyond 200 nm when moving into bulk pure silicon. The D and H levels both decrease beyond the source nitride layer; however, the ratio of H to D increases. No accumulation of H or D on the at% scale is observed at the potential thin interfacial $SiO_x$ location, which is in partial contradiction to the commonly reported interfacial H accumulation in previously reported SIMS results [117], [121], [122].

Furthermore, Figure 4-4 illustrates the elemental profiles from the 12 MeV Iodine source. The profiles are similarly divided into suggested layers. The first 20 nm surface contamination layer is in good agreement with Cl profiles. The concentration levels of D and H in the nitride layer are on par with Cl results, which confirms the high D/H contents. However, the concentration transitions at the deeper interfaces span over a longer range. This is evident in the increased

half-peak width of the first oxide peak, 52 nm (marked in red), compared with the previous 35 nm width observed in the Cl profiles. Due to the broadened oxygen profile, the second minor oxygen peak that should be located at the end of polysilicon is no longer distinguishable. The increased blurring in the deeper regions in Figure 4-4 results arises from the rapid decline in depth resolution when using the iodine source, as previously noted.

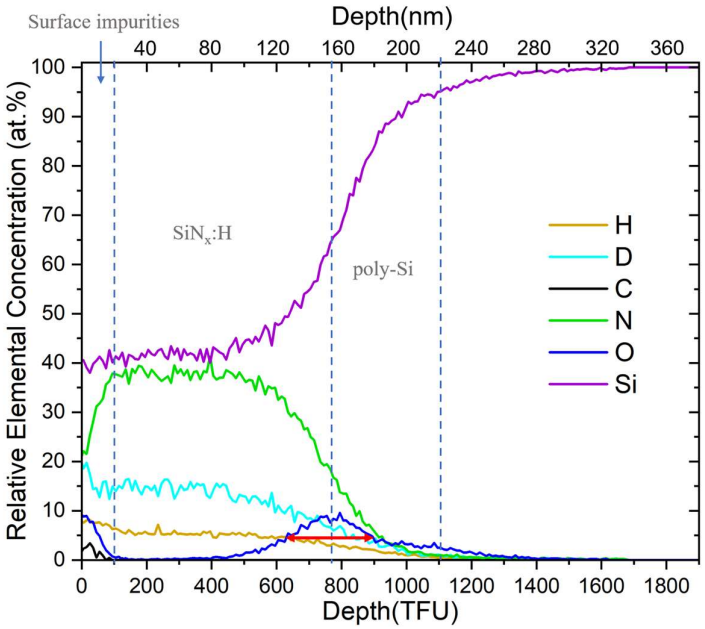


*Figure 4-4 ToF-ERD depth profiles of elements including H,D,C,N,O and Si, with a 12 MeV $^{127}I^{8+}$ incident ion source. Depth scale given in both TFU (bottom) and nanometre (top)*

Both Cl and I results show limited depth resolution beyond the $SiN_x$ layer for several reasons. Firstly, the sample's surface roughness is significant at such a nanometre scale because the specimens were chemically 'shiny' etched and not been through the mechanical polishing process. This is revealed by the AFM surface scan given in Appendix F. AFM scan over a 40 μm ×40 μm area reveals a root mean square roughness of 15.0 nm, which is much larger than the ~1.3 nm designed thickness of the interfacial tunnelling oxide. This roughness broadens the depth concentration profiles, obscuring the clear identification of peaks and transitions at the interface. Secondly, the limited depth resolution is related to the geometry of the experimental setup, in which both incident and exit angles $(\alpha, \beta)$ for the recoiled atoms are 69.5°. Any roughness effect will be amplified at such high angles due to the beam spreading across the surface. Lastly, an intrinsic limitation of ERD arises from the scattering process that the ion beam undergoes during both the incident and exit paths. While ToF-ERD can provide 1–3 nm depth resolution for perfectly flat interfaces, its depth resolution deteriorates with increasing depth due to additional scattering energy loss and larger uncertainty in the measured

energy of recoiled atoms. This is readily shown by the increased broadening of elemental profiles in both Figure 4-3 and Figure 4-4. To address these challenges, the author suggests future experimental modifications including: (a) using chemically mechanically polished samples to minimise surface roughness, and (b) removing or thinning the front dielectric layer to position the interface closer to the surface, thereby improving depth resolution.

## 4.5. Comparison to SIMS parallel results

As a reference to the ERD profiles, Figure 4-5 presents the parallel SIMS results on an identical sample. Note that the SIMS profiles are shown in volumetric concentrations (at/cm$^3$) on a logarithmic scale, converted from count rates, with values not directly relatable to the percentage concentrations in ERD. The two oxygen peaks in SIMS profiles, both before and after the polysilicon layer, align with ERD findings. Additionally, the high deuterium (D) enrichment in the nitride layer, which reaches a level comparable to the first oxygen peak on top of the polysilicon, is also consistent with the ERD results. The minor D pickup at the interfacial oxide (marked as location B), with a concentration of $3\times10^{19}$ at/cm$^3$ (corresponding to <0.01 at%), would be undetectable in ERD if present.

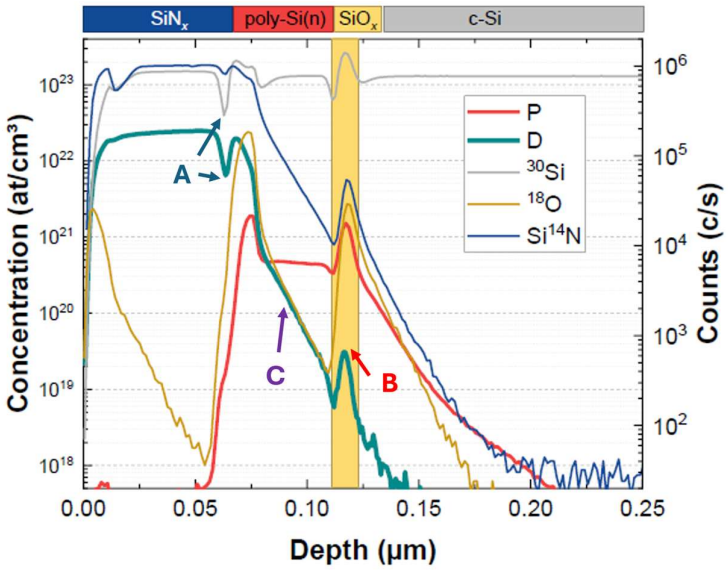


*Figure 4-5. SIMS depth profiles of species in at/cm$^3$ of an equivalent TOPCon sample, recorded by CAMECA IMS 4fE6 instrument using primary-ion: Cs+ at 14.5 keV. Si- calibration on implantation standard 2H in Si; P, D are calibrated at at/cm$^3$; Uncalibrated (conts/s): $^{30}$Si, $^{18}$O, Si$^{14}$N. Data produced by collaborators in Fraunhofer ISE*

Two artefacts in the SIMS measurements can be identified. The change in the substrate /matrix during sputtering results in fluctuations in secondary ion yields, leading to an artefactual increase or dip in SIMS counts. This is evident in the D and $^{30}$Si dips at the $SiN_x$/polysilicon

interface (location A), which do not appear in the ERD profiles. Such a matrix effect can also explain the increase of all signals at the interfacial $SiO_x$ location (location B), which diminishes the significance of the minor D peak. This effectively hinders quantification of the true interfacial D dose by SIMS. Such a finding from comparing SIMS and ERD serves as the first reported evidence of SIMS inaccuracy in deuterium profiling. The other SIMS artefact is revealed by the prolonged decrease of concentrations shown as the long tails at location C. Such features come from the inward displacement of atoms during SIMS sputtering and should not be interpreted as real element distributions in the sample.

## 4.6. Conclusions

In conclusion, this work presents a detailed report of ToF-ERD analysis of the industrial-relevant TOPCon solar structure. It serves as the first report of utilising ToF-ERD in unambiguous separation of deuterium ($^{2}D$) and hydrogen ($^{1}H$) within the deuterated TOPCon structure, establishing it as a strong complementary technique for studying hydrogen distribution in passivating contact structures without the detection challenges encountered in SIMS. Coincidence histograms from ToF-ERD clearly distinguish species, including Si, O, N, C, as well as H and D. A comparison of results shows that the 8 MeV $^{35}Cl^{6+}$ beam delivers better depth resolution but reduced mass separation compared to the 12 MeV $^{127}I^{8+}$ beam. Further comparison to parallel SIMS tests reveals the SIMS profiling inaccuracy caused by the matrix change. By combining energy–ToF information with material stopping force, the depth origins of detected signals can be obtained to generate composition depth profiles. Two oxide peaks are identified on the depth profiles, corresponding to oxides both atop and beneath the poly-Si. High H/D contents (combined into over 15 at %) can be quantified clearly in the silicon nitride layer. Surface roughness, however, causes layer intermixing and peak broadening. Intrinsic ERD limitation causes deterioration of depth resolution further at greater depths. To mitigate such issues in future studies, samples with improved surface flatness and shallower structures are recommended.

# 5. Characterisation of TOPCon passivating contact structure via atom probe tomography

The characterisation work presented in this chapter has been accepted for publication in the journal Solar Energy Materials and Solar Cells under the title, "*Towards accurate atom-scale characterisation of hydrogen passivation of interfaces in TOPCon architectures*". The author would like to thank Jana-Isabelle Polzin from Fraunhofer ISE for sample provision.

## 5.1. Introduction

Hydrogen plays an important part in the surface passivation efficacy of the widely adopted TOPCon structure. As introduced in section 1.5, the hydrogen migration during thermal processing and its correlation with interface passivation remains an area of ongoing investigation. This is largely due to the inherent challenges associated with direct and accurate hydrogen detection in such complex silicon-based structures. Advancing the understanding of hydrogen distribution within TOPCon passivation layers hence requires a reliable and accurate characterisation route.

Atom probe tomography (APT) is a powerful near-atomic scale chemical analysis technique suited for thin-film structures such as TOPCon [204], [205]. Figure 5-1 presents a schematic of APT instrumentation. In an APT experiment, atoms from the apex surface of a needle-shaped specimen are ionised and evaporated under the influence of a strong electrostatic field. For semiconductors (less-conductive) materials, the evaporation process is thermally assisted using a high-frequency pulsed laser. The evaporated ions, which can be either monoatomic or polyatomic, pass through a time-of-flight mass spectrometer, enabling chemical identification based on their mass-to-charge ratios. These ions are then projected onto the position-sensitive detector following designed trajectories defined by the electrostatic fields. The recorded spatial positions of individual ion hit on the detector, in combination with the historical detection sequence, allows reverse-projection to achieve a 3D reconstruction atom-by-atom map of the specimen [206], [207]. A more comprehensive explanation of the APT working principles, operation procedures, and limitations is provided in Appendix C. In comparison to the standard SIMS approach for semiconductor analysis, APT also relies on a mass analyser, but provides 3D mapping capabilities and superior spatial resolution. Additionally, because signal ion generation in APT occurs via field evaporation rather than sputtering, APT avoids several common SIMS artefacts associated with ion bombardment.

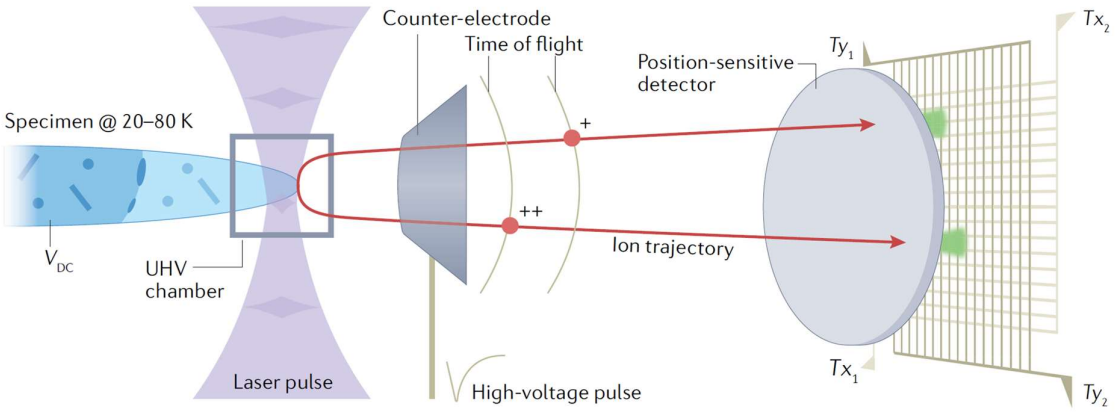


*Figure 5-1 Schematic of APT instrumentation, showing from left to right: the sample under field evaporation, the time-of-flight spectrometer, and the position-sensitive detector. Figure from [206].*

Both APT and SIMS systems operate under vacuum, hence they are both susceptible to environmental noises from gas remnants in the vacuum chamber, among which the hydrogen-containing species are most notable because of their low mass. The presence of ambient H in a high-vacuum system interferes with the detection of sample-originating hydrogen and leads to large uncertainty, especially in the measurement of low sample hydrogen concentrations. The H detection uncertainty and the associated detection limit of APT [208], [209], [210] is often worse than that of SIMS [188], [189] due to continuous condensation of ambient H onto the specimen tip held at cryogenic temperatures. To further complicate matters, hydrogen evaporated from the specimen tip can take several ionic forms, including $H^+$, $H_2^+$, or $H_3^+$(rare) as well as polyatomic ions involving sample constituents such as Si or O. Moreover, post-evaporation processes such as further ionisation into higher charge states and molecular dissociation can occur depending on the local electric field conditions, which can further multiply the types of hydrogen-related signals, increasing the possibility of mass spectrum overlaps and complicating data interpretation [208]. To mitigate these challenges, H substitution with isotope deuterium (D), which has a low natural abundance of 0.015%, is implemented in many studies [211], [212] to improve sample hydrogen detectability with a possible distinguished D signal. Lastly, the underlying assumption in APT characterisations of hydrogen is that the sample H/D content exhibits minimal redistribution during the ex-situ sample preparation and experimentation. This assumption is based on previous APT investigations [204], [213] which show hydrogen atoms bonded at silicon defects can be preserved in place after a carefully tuned room temperature APT specimen preparation process (detailed description found in Appendix C).

In this work, atom probe tomography is employed to characterise hydrogen passivated TOPCon samples with partial deuterium ($^2$H) substitution. The influence of various APT experimental conditions on the detectability of deuterium within the complex silicon-based structure is investigated. Mass spectrum overlaps are addressed via peak deconvolution, as a key step in identifying deuterium amidst the background hydrogen. The analysis results are utilised to compare the D contents in two samples from different hydrogen processing conditions. This study also identifies the remaining challenges associated with characterising TOPCon structures.

## 5.2. Experimental method

The sample description of the annealed, partially deuterated, n-type TOPCon under investigation can be found in chapter 4. In addition to this, the present chapter investigates a reference sample which did not undergo the post-deposition hydrogen annealing step. The two wafer samples are hereafter referred to as the annealed and the unannealed sample.

The needle-shaped APT specimens, extracted from the wafer surface, were prepared following the ex-situ lift-out process using focus ion beam milling (FIB) as comprehensively detailed in Appendix C. Figure 5-2 (a) illustrates the target position of the APT needle specimen, which should vertically cover the TOPCon stack, including the $SiN_x$:H, polysilicon, interfacial oxide and bulk silicon. A section of the wafer material encompassing the target position is extracted via FIB micromachining in the lift-out process. Given the high susceptibility of the sample surface to unintended FIB milling damage, special care was taken to preserve the integrity of the nanoscale surface layers by covering the surface with a sacrificial tungsten layer over 500 nm in thickness. Tungsten is chosen as the capping material for (a) good silicon surface adhesion and (b) good structure stability under ion beam milling conditions associated with its high melting point and strength.

Figure 5-2 (b) presents a scanning electron microscope (SEM) image of a pre-sharpened APT specimen-to-be. The top layer with bright contrast denotes the thick tungsten protection layer. This tungsten cap was continuously milled away during the needle sharpening process. The completed APT needle specimen is shown in Figure 5-2 (c) with a sharp tip with a radius typically below 100 nm. At this stage, the tungsten cap had been completely removed, exposing the underlying structure. The electron transparency of the tip in Figure 5-2 (c) indicates its extreme thinness, while the ring-like feature with shallow contrast just below the tip is indicative of the TOPCon layers being preserved.

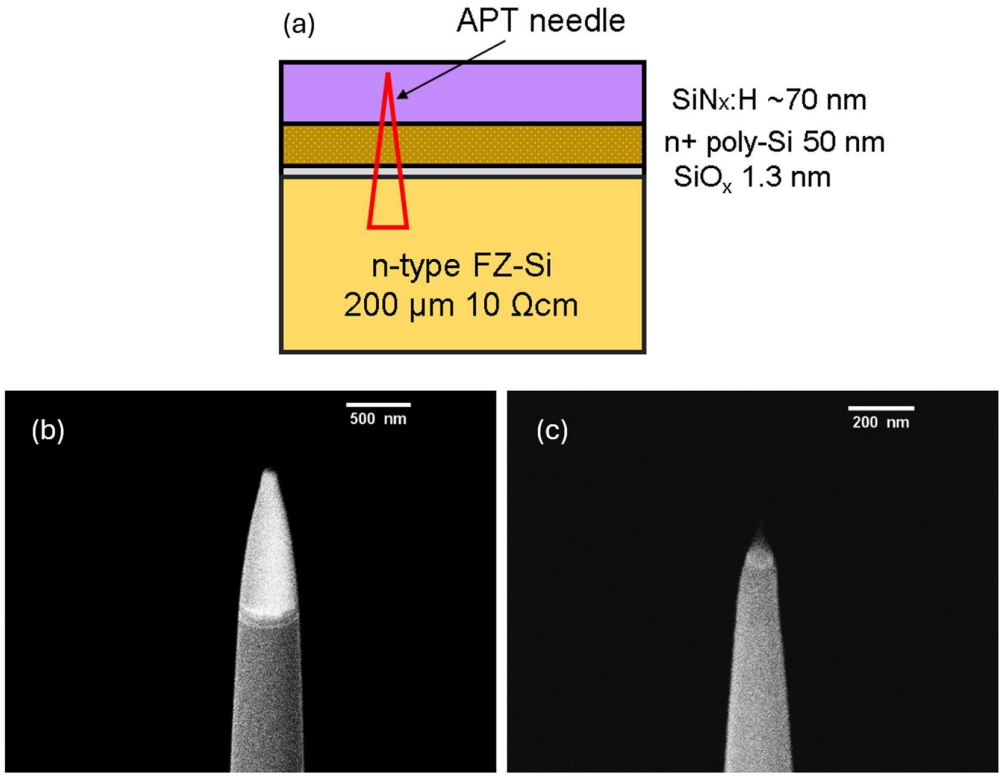


*Figure 5-2 (a) Schematic of the TOPCon structure with the location of APT needle specimen marked (b) SEM image of a pre-sharpened needle-to-be with thick tungsten cap, and (c) SEM image of a finished APT needle specimen. Note the difference in scales of the images.*

APT analysis was performed using a CAMECA local electrode atom probe (LEAP) 5000 XR model with a detection efficiency of 52%. Laser pulsing mode was used instead of voltage pulsing mode due to specimen viability concerns. The laser-assisted evaporation process poses less field-induced stress to the complex semiconductor structure, which is essential in the prevention of premature needle fracture during APT experiments. However, the conditions of laser mode enhance polyatomic/molecular ion formation, leading to multiple overlaps of detected species on the mass spectrum. The mass-spectrum overlaps are statistically addressed by peak deconvolution via the open-source script AtomProbeLab (v.0.2.4) developed by London et al. [214], [215].

All APT specimens were run at a fixed cryogenic 50 K base temperature with a fixed laser pulse frequency at 200 kHz. Variable parameters, including the laser energy, target detection rate and estimated surface field, are systematically tested to optimise the detection of the deuterium signal. The visualisations of APT data were performed using AP Suite 6.1 software

by CAMECA. The 3D reconstruction followed the voltage evolution geometry protocol, whereby the specimen radius is inferred from the voltage history throughout the experiment.

## 5.3. APT mass spectrum

The initial outcome of the APT experiment is the mass spectrum, which represents a histogram of all detection events or hits. Figure 5-3 provides an example of a mass spectrum from the dataset of the annealed TOPCon specimen. Each detection event, corresponding to an ionic species, is sorted by its measured mass-to-charge ratio (m/z) measured in Daltons (Da) on the x-axis across a defined mass range and resolution. The y-axis displays the total counts of the detection events on a logarithmic scale.

Prominent peaks rising above the background level in Figure 5-3 are ranged and labelled with likely candidate species. The tallest of the peaks correlate to the main constituent silicon signals from the silicon-based structure. Due to the formation of complex/polyatomic ions, many peaks can be attributed to multiple chemical identities, comprising combinations of Si, P, N, O, and H/D atoms. In other words, the ion candidates overlap at certain masses (usually groups of neighbouring masses), leading to complexity in ion interpretation. Such groups of overlaps, although not distinguishable by the masses alone, are subject to further statistical data deconvolution to facilitate further quantitative analysis of chemical compositions in a process addressed in section 5.6.

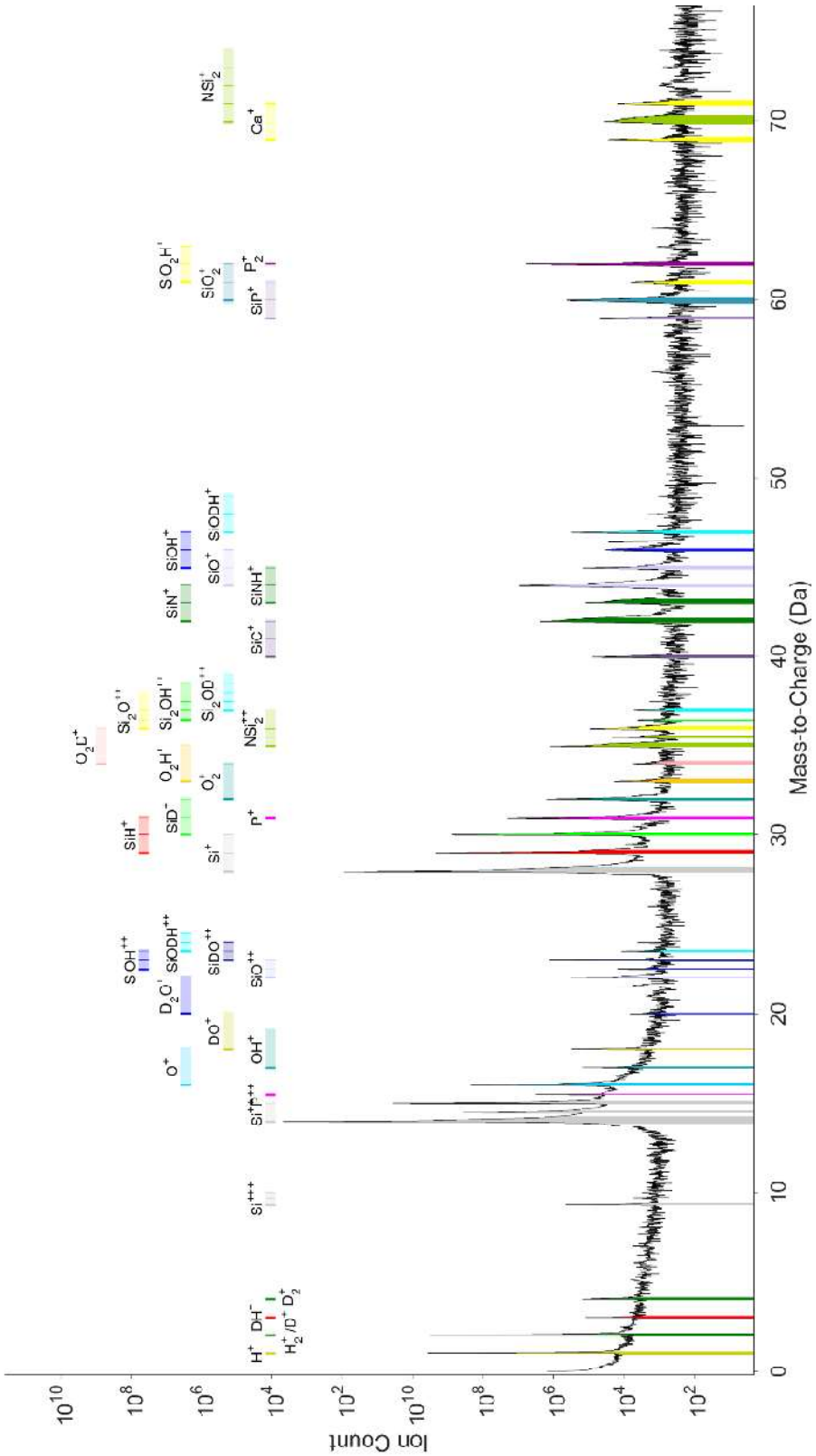


*Figure 5-3 The APT mass spectrum from a TOPCon specimen dataset. Peaks of strong signal above $10^5$ are ranged and labelled. The overlaps of the labels in the figure indicate multiple possible identities within certain peaks.*

## 5.4. Effect of laser energy on H background

As previously discussed, the ambient H background, primarily detected as atomic $H^+$ at 1 Da or molecular $H_2^+$ at 2 Da the mass spectrum poses a significant barrier in distinguishing the true deuterium D signal from the sample. To address this, this section presents a systematic investigation of hydrogen background levels under varying laser pulse energies, a key APT measurement parameter. The energy of laser pulses is known as a critical factor influencing the detected hydrogen background [208], [209]. For this test, a blank crystalline silicon needle was prepared from the wafer bulk where no intrinsic hydrogen or deuterium is expected. Therefore, any detected hydrogen during the tests is attributed solely to the environmental H background from the vacuum chamber.

To isolate the effect of laser energy, APT was conducted under fixed conditions: a base temperature of 50 K, a laser pulse frequency of 200 kHz, and a target detection rate of 1.4%. Figure 5-4 (a) illustrates the results, showing the impact of laser energy variation on the measured hydron and silicon-related species. The blue data points plotted against the left scale of Figure 5-4 (a) is the ratio between the sum of $H^+$ at 1 Da and $H_2^+$ at 2 Da and the combined $^{28}Si$ counts. This relative ratio indicates the background to signal level. It can be shown that the detected H background is higher at intermediate laser energies around 30 pJ and drops at both higher and lower energy ends. Notably, laser energies above 50 pJ are particularly effective in suppressing the hydrogen background. This trend aligns with previous findings [208], [209].

This effect is explained by the inverse correlation between the surface field strength and laser pulse energy applied under the constant detection rate running mode. The correlation is that with application of higher laser energies, the surface electric field strength required to maintain the same evaporation rate decreases. To further support this interpretation, the $Si^{2+}/Si^{+}$ charge state ratio, which is used as a proxy for surface field strength, is plotted as orange data points on the right y-axis Figure 5-4 (a). As the laser energy increases, the $Si^{2+}/Si^{+}$ ratio decreases, indicating a reduction in surface electric field strength. The weaker field reduces the surface adsorption of ambient H at the tip and results in a reduced H background level. Results of such tests confirm that high laser energies (> 50 pJ) can be advantageous for minimising H background in APT measurements.

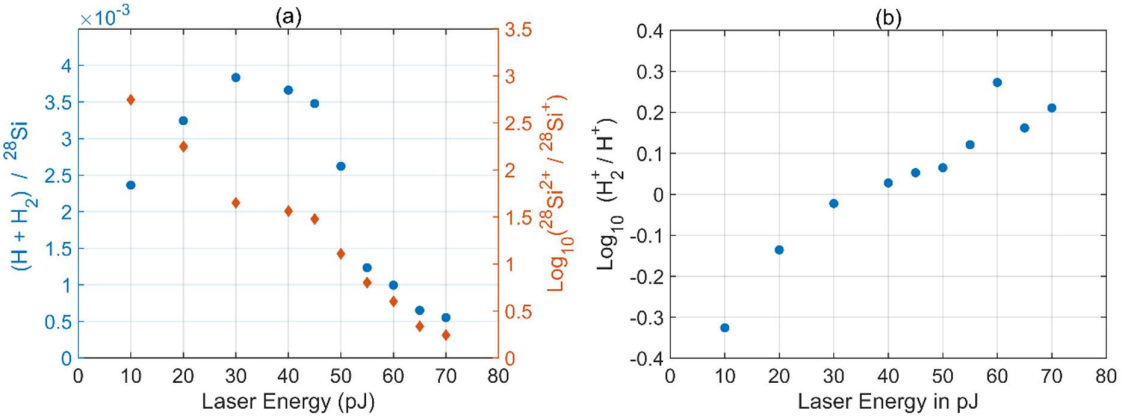


*Figure 5-4. Ratios of APT detected species from a blank Si specimen as functions of laser pulse energy. (a) the ratio of H counts at 1 Da and 2 Da to total Si counts on left scale, and the log ratio of $^{28}Si^{2+}$ at 14 Da to $^{28}Si^{+}$ at 28 Da on the right scale. (b) logarithmic ratio of $^{2+}$ to $H^{+}$ plotted against laser pulse energy.*

Figure 5-4 (b) displays the logarithmic ratio of molecular $H_2^+$ to atomic $H^+$as a function of laser energy. The observed trend indicates a progressive transition of the hydrogen background from $H^+$ rich to $H_2^+$ rich with increasing laser energy. This shift can be explained by the field dependence of molecular dissociation immediately after surface evaporation. Molecular $H_2^+$ dissociation into $H^+$ is suppressed at low surface field strength conditions, hence the H content detected shifts from $H^+$ to $H_2^+$ at conditions towards the higher laser energies. The data point at 60 pJ, which deviates from the general trend, is considered an outlier, potentially due to fluctuations in chamber conditions.

This shift towards more $H_2^+$ at higher laser energies, however, is disadvantageous for the detection of deuterium from the sample, since the background $H_2^+$ overlaps with the $^2D^+$ signal at 2 Da on the mass spectrum. The ambiguity at 2 Da adds uncertainty in quantifying deuterium due to the unsolvable nature of the superposition. As such, a trade-off is identified: increasing applied laser energies reduces the total ambient H background, but complicates the separation of potential sample D from the H background. In light of such a result, the laser energy of 60 pJ is selected as the standard APT operation condition for further analysing TOPCon samples containing deuterium.

## 5.5. 3D reconstruction of the TOPCon structure

Figure 5-5 shows the atom-by-atom 3D reconstruction resulting from a representative needle specimen of an annealed TOPCon sample. The different layers in the structure are labelled in the figure, including the crystalline silicon wafer, the thin tunnel $SiO_x$ layer, the $n^+$ doped

polysilicon layer, and the H-rich capping nitride layer. Each of the five maps shown in Figure 5-5 illustrates a different ionic species, as identified by the corresponding mass-to-charge ratios on the mass spectrum presented in section 5.3. Figure 5-5 (a) represents the oxygen signal using only the 16 Da $O^+$ signal, from which two oxygen-rich layers are clear. The first oxygen layer on the top aligns with the surface nitride. This oxygen signal originates from the oxidation of the nitride-polysilicon interface, potentially during the polysilicon crystallisation and nitride deposition processes. The second oxygen-rich layer is the interfacial $SiO_x$ in TOPCon, the presence of which indicates the complete structure is preserved in this specimen.

Figure 5-5 (b) represents the signal for nitrogen obtained using the complex ion $SiN^+$ 42 Da signal. A direct $N^+$ signal would appear at mass-to-charge of 14 Da, but $N^+$ at 14 Da from this silicon-based specimen overlaps with doubly charged $^{28}Si^{2+}$. To avoid ambiguity, the $SiN^+$ complex ion at 42 Da is displayed instead, providing a clearer representation of N distribution to indicate the location of the top nitride layer. It is observed here that only part of the nitride cap is preserved in this APT specimen, a result attributed to surface removal during FIB needle milling.

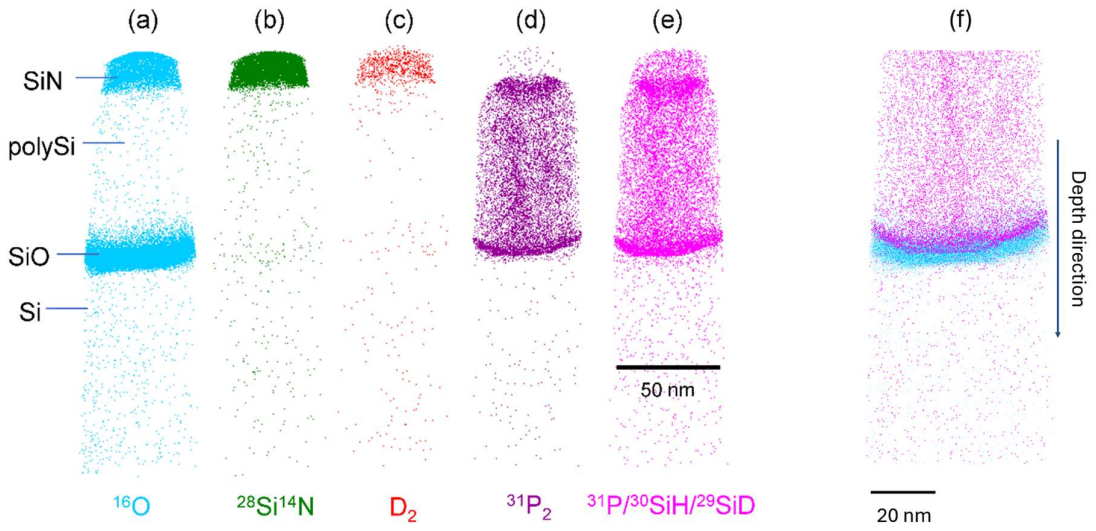


*Figure 5-5 3D reconstruction of a TOPCon specimen showing chemical species including: (a) $^{16}O^+$ (b) $^{28}Si^{14}N^+$ (c) $D_2^+$ (d) $^{31}P^{2+}$ (e) $^{31}P^+$ or $^{30}SiH^+$ or $^{29}SiD^+$ at 31 Da. (f) close-up showing the interface curvature as a result of the reconstruction bowl artefact*

Figure 5-5 (c) represents the distribution of ions with a mass-to-charge ratio of 4 Da ($D_2^+$), which is selected to represent the sample D distribution. Since the background hydrogen noise appears at either 1Da or 2 Da, whereas the 4 Da peak is uniquely attributable to deuterium $^2D_2^+$, allowing for unambiguous detection of deuterium from the sample. The signal counts of $^2D_2^+$ are low due to: (a) low D overall sample incorporation, and (b) a significant portion of

deuterium is likely present in other complex ions. A higher concentration of $^{2}D_{2}^{+}$in the $SiN_x$ layer is observed, which is consistent with its role as the deuterium source. No significant $^{2}D_{2}^{+}$is seen in this map at the interfacial oxide location.

The species shown in Figure 5-5 (d) has a mass-to-charge-state ratio of 62 Da. It represents molecular phosphorus $^{31}P_{2}^{+}$. Given that no other species are expected at 62 Da, this signal unambiguously represents the distribution of phosphorus. The results confirm that phosphorus is only concentrated within the $n^{+}$ doped polysilicon layer. Accumulations of P at both ends of the doped polysilicon layer are clearly observed, which is consistent with the finding by Feldmann et al. [216]. This segregation behaviour is attributed to the redistribution of phosphorus towards the interfaces during the crystallisation annealing of the polysilicon.

Figure 5-5 (e) presents the distribution of species at 31 Da. This signal is dominated by $^{31}P^{+,}$ which explains the similarity between Figure 5-5 (e) and Figure 5-5 (d). However, this 31 Da signal also includes contributions from silicon-hydrogen complex ions, since both $^{30}SiH^{+}$ and $^{29}SiD^{+}$ share the same 31 Da mass. Thus, the difference in map (d) and (e) is related to the presence of D or H in the structure. This further explains the additional counts in Figure 5-5 (e) within the top $SiN_x$ layer. The overlap between P, SiH and SiD signals at 31 Da prevents a clear illustration of the distributions of each individual species, which serves as a direct example underlying the necessity of tackling mass spectrum overlaps.

Additionally, Figure 5-5 (f) displays both the 16 Da and 31 Da signals in a close-up view towards the oxide interface. This view reveals that the dopant phosphorus accumulation is restricted to top oxide surface with minimal diffusion into the underlying silicon substrate. The curved, bowl-like appearance of the oxide and phosphorus layer is an artefact from the 3D reconstruction, which is a result of both (a) geometrical simplification in assuming the needle radius evolves with voltage, and (b) ion trajectory aberration caused by change in surface field conditions occurring to compositional discontinuities. Such ‘bowl’ artefacts impact the spatial resolution of APT analysis (further discussed in Appendix C) and needs to be addressed in further spatial composition analysis.

## 5.6. Overlap solving and depth profiles

The presence of overlaps on the mass spectrum and their effects have been identified in the previous section. To address these overlaps, a deconvolution procedure by London et al. [214], [215] is applied to mass datasets for the TOPCon layers. It is based on maximum likelihood estimation (MLE), which calculates the likelihood of observed peak counts as a function of

simulated compositions and identifies the composition at the maximum likelihood point as detailed in [214]. The likelihood function also provides an uncertainty range associated with the composition estimation. This MLE process relies on known isotopic abundances of the involved elements and has limited applicability depending on the number of overlapping candidates. Figure 5-6 presents a histogram example of the solved overlap peak group at 28-32 Da from an oxide interface ROI. Each peak in this group, except for the 28 Da, which is assigned solely to $^{28}Si$, can be divided into multiple ion components as illustrated by the stacked bars. The result here confirms the significant $SiH^+$ contribution in the 31 Da peak. It is also determined that the majority of D in this overlap group is detected as $^{28}SiD^+$ at 30 Da.

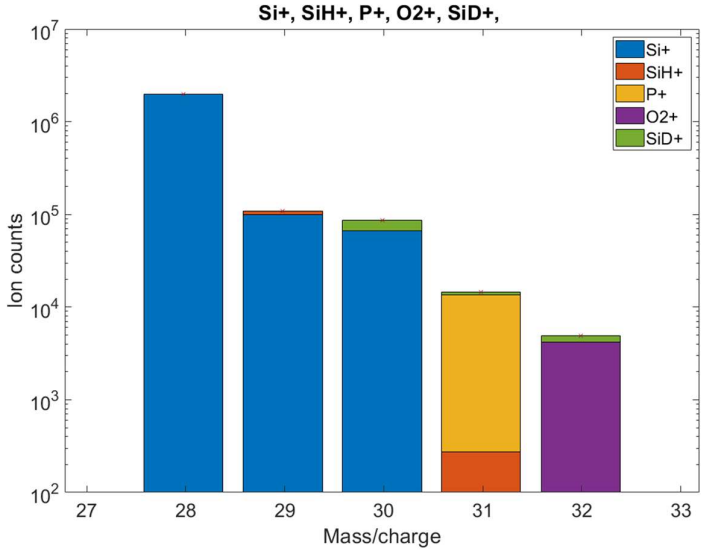


*Figure 5-6 Example histogram of solved peaks within the overlap group 28-32 Da, produced using open open-source programme AtomProbeLab (v.0.2.4). The coloured bars within each stack give the fitted contribution of each ionic species to each peak.*

This overlap solving process is essential in the quantitative analysis of elements and utilised to obtain 1D profiles of elements with nanometre depth increments. The depth profiling is achieved by splitting the needle specimen into a number of data bins along the needle axis (assumed to run in the depth direction) and finding the overlap solved, mean local compositions within the bins. The result for the specimen from annealed TOPCon is presented in Figure 5-7 with a 1 nm depth bin width.

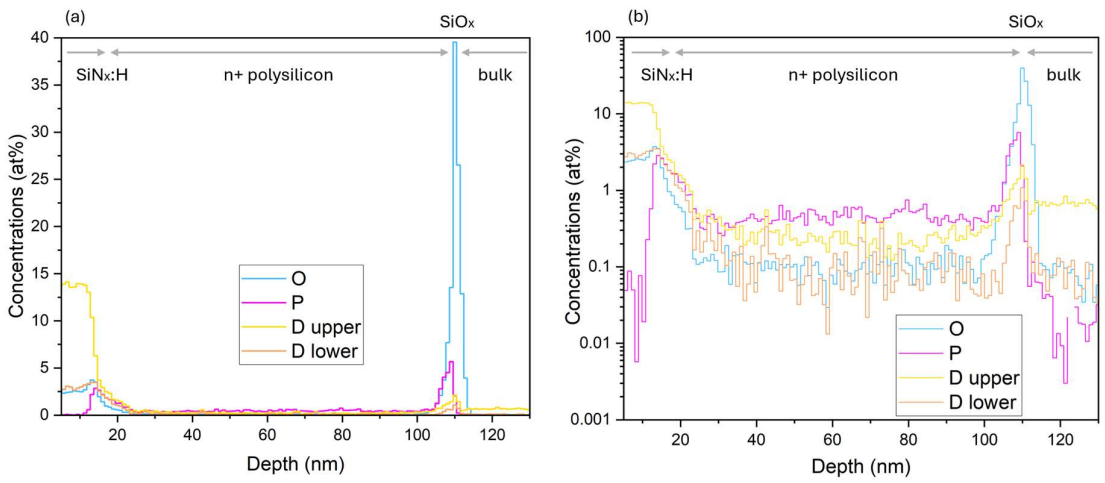


*Figure 5-7 Depth profiles of deuterium, phosphorus and oxygen from APT data analysis in both (a) linear scale (b) logarithmic scale.*

The blue curves in Figure 5-7 (a) and (b) represent the oxygen profile. A flat oxygen concentration of around 3 at % is found in the nitride layer, and a sharp peak up to 38 at % is found at the interfacial oxide location. The oxide peak for the 1.5 nm thermally grown interfacial oxide spans across a 13 nm peak base width (measured when oxygen is above the baseline level). Such apparent widening of peaks, which is also evident for other element profiles, is a result of the reconstruction 'bowl' artefact, which causes spreading of the measured depth coordinate for detected ions near the interface. To address this, a useful direction for future work is correlated microscopy with transmission electron microscopy (TEM). By calibration the APT chemical information against high-resolution structural imaging, a more precise detection of layer boundaries and interfacial features can be achieved.

The phosphorus profiles in purple show accumulation at both ends of the polysilicon. At the oxide end of the polysilicon, the P concentration falls sharply over 2 orders of magnitude within a 3 nm length scale, which confirms with earlier statement of minimum P penetration into the bulk. This provides direct evidence against extended P diffusion beyond intact oxide layers, contrasting the SIMS long tails observed in results reported in Figure 4-5 (location C) from an identically processed wafer. This discrepancy in P profiles above the oxide interface can be attributed to: (a) P extended tails are caused by knock-in displacement of P atoms in SIMS as a measurement artefact. (b) P in-diffusion can still happen at localised pinholes on the oxide, whereas the APT nanometre-volume specimen may represent a region with an intact oxide barrier. To the author's knowledge, such a major discrepancy between APT and SIMS is reported here for the first time. It highlights the limitations of SIMS in accurately resolving

dopant profiles and underlines the importance of refining SIMS data interpretation, particularly in the case of mapping phosphorus dopant diffusion through ultra-thin oxides.

Because both $H_2^+$ and $^2D^+$ can equally contribute to the peak at 2 Da with an unknown abundance ratio, this 2 Da peak is unsolvable by MLE due to insufficient parameters input. To overcome this, two D profiles are generated, indicating (a) an upper bound of D when the 2 Da peak counts are all assigned to $D^+$ in the specimen, and (b) a lower bound of D when 2 Da is assigned to $H_2^+$ with all the D content in this case coming from complex ions such as $SiD^+$. The true concentration of D lies between these bounds. Both D profiles have the highest concentration in the $SiN_x$:H layer at 3.5 at% for the lower bound and 14 at % for the upper bound. Additionally, the lower bound profile reveals a small build-up of D to a level of 1.0 at% (corresponding to a volumetric density of ~$10^{20}$ $cm^{-3}$) at the location of the interfacial oxide layer.

## 5.7. Effect of field strength on H background

The depth profile results of D show a gap between the higher bound and lower bound, which leaves large uncertainty in D quantification and underpins the need to reduce this ambiguity. As revealed in section 5.4, the formation of molecular $H_2^+$ is facilitated under lower surface field conditions. An effective measure to suppress the ambiguity of $H_2^+$ within the 2 Da peak is to run the needle at a higher and constant field strength. To evaluate this strategy, a comparison of two APT needles made from same annealed TOPCon wafer but run at different APT conditions is reported, with (i) run at constant detection rate mode of 1% DR, and (ii) run at constant surface field mode at relatively high estimated field of 20.6 V/nm ($Si^{2+}$ to $Si^+$ ratio at around $10^{0.6}$). Under the constant field strength mode, the APT instrument continuously monitors surface fields signalled by the detected $Si^{2+}$ to $Si^+$ charge state ratio (CSR) and adjusts the applied voltage to maintain the same CSR.

Figure 5-8 presents the overlap solved D profiles from the two runs zoomed in towards the interface location. Both are plotted within the same concentration and depth range and both show a D accumulation peak at the interfacial oxide location. Under the constant DR mode in Figure 5-8 (a), the gap between the two bounds goes up to 1.0% at the interface location and exhibits an overall widening trend with increasing depths. On the other hand, no widening is observed in the case of the constant field strength run in Figure 5-8 (b). The widening of the gap in (a) in comparison to (b) is due to decreasing surface field strength under constant detection rate mode. This is explained by the fact that the needle apex radius and surface area

increase as the needle evaporates. The surface field strength, related to the evaporation rate per area, is reduced to maintain the overall detection rate under constant DR mode. This decrease in surface field strength provides the condition for increased molecular $H_2^+$ detection from the ambience, as shown by the widening gap between higher and lower D bounds. The narrow gap between D bounds in figure (b), on the other hand, can be related to the maintained high constant surface field. The author further deduces that the content within the gap under constant DR mode is likely dominated by ambient $H_2^+$ rather than unaccounted D. Therefore, the sample D content is likely closer to the lower D bound. It is also evident that operating in constant surface field mode is advantageous for minimising ambient hydrogen convolution and ensuring a more consistent D detection environment. Lastly, it is important to note a trade-off: maintaining high field strengths increases the risk of premature needle fracture during the experiment. As such, experimental parameters must be balanced carefully depending on specimen robustness and measurement objectives.

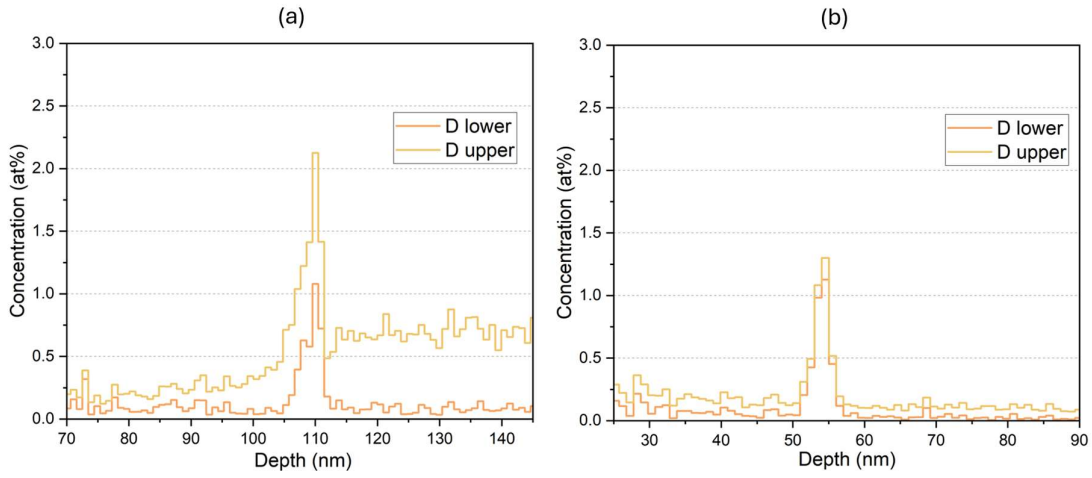


*Figure 5-8 Comparison of APT result of (a) a constant detection rate run and (b) a constant field strength run*

## 5.8. Comparison of $^2$H accumulation at the oxide interface

To address the relationship between deuterium dose and interface passivation, D contents within specimens made from hydrogen annealed and unannealed samples are compared. The reconstruction 'bowl' artefact in APT results in the spatial broadening of D profiles, rendering direct comparison of interface peaks unreliable. Instead of directly comparing the D peaks, the Gibbsian interfacial excess (GIE) is used as the comparison metric, which is the standard for quantifying impurity segregation towards a 2D interface such as grain boundaries. The definition of GIE and the region of interest for GIE calculations are included in Appendix C.

The use of GIE in comparing interfacial segregation is a straightforward method, insensitive to the placement of the interface along the depth direction. The ROI for GFE calculation is selected to minimise the influence of interface curvature.

Table 5-1 depicts results of GIE of D, P and O at the oxide interface. It lists results from two successful runs of specimens from an annealed TOPCon specimen and one from an unannealed specimen. All GIE values are calculated after the mass overlap solving. The D dose is derived from the lower D bound as a better estimation and comparison figure instead of the upper D bound, because of the heavy noise content in the upper D bound results. The error ranges read on the table originate from the confidence intervals in peak overlap solving. A comparison of the D doses between annealed and unannealed specimens shows that interface D excess increases by approximately 25% after annealing, with values rising from 1.19 (95% CI 0.97-1.50) cts/nm² (unannealed) to 1.46 (1.37-1.59) cts/nm² and 1.50 (1.35-1.78) cts/nm² (annealed). This trend supports the hypothesis of hydrogen enrichment during annealing. Additionally, comparison of wafer lifetimes from the table shows evidence of the positive lifetime contribution and hence better surface passivation from a slightly higher interface D dose. The author notes the relatively high D uncertainty range to emphasise the error susceptibility in such a comparison.

*Table 5-1 Gibbsian interface excesses of elements at the 2D interfacial oxide surface. The range in parentheses represents the confidence interval originating from the errors in overlap solving calculations. The ratio of excess P and excess O is additionally displayed*

| | **Excess D [cts/nm²]** | **Excess P [cts/nm²]** | **Excess O [cts/nm²]** | **P/O** | **Lifetime** |
|---|---|---|---|---|---|
| **Annealed 1** | 1.50 (1.35-1.78) | 10.0 (9.6-10.5) | 50.0 (49.2-50.8) | 0.201 (0.191-0.210) | 23 ms |
| **Annealed 2** | 1.46 (1.37-1.59) | 6.8 (6.7-7.0) | 31.4 (31.0-31.8) | 0.218 (0.212-0.225) | |
| **Unannealed** | 1.19 (0.97-1.50) | 5.6 (5.2-6.1) | 27.1 (26.2-28.1) | 0.207 (0.190-0.227) | 17 ms |

In addition to the D results, comparison of P and O interfacial excess between the three samples shows substantial variations, with as high as 79 % difference in P and 80 % difference in O comparing the annealed specimen 1 and the unannealed specimen. The difference in oxygen dose may result from variations in local interfacial oxide thickness as a result of inhomogeneous oxide growth. The inhomogeneity is revealed because of the highly restricted

analysis volume of the APT. Despite the large absolute differences, the ratios of P to O among the three specimens, as listed in the table, fall closely within a narrow window roughly between 0.20 - 0.22. This is indicative of the correlation between the extent of P segregation to the oxide thickness during the thermal crystallisation processes. marking the first sub-nanometre scale report of this correlation. Notably, the P/O ratio appears unaffected by whether the sample went through hydrogen annealing, since P segregation movement occurred earlier at a much higher temperature, typically over 900 °C during polysilicon formation, compared to the H annealing step at 500 °C.

## 5.9. Discussion

As demonstrated in the results, this APT study faces two major challenges in the quantitative analysis of sample deuterium content: mass spectrum signal overlaps and ambient hydrogen noise. Both factors lead to uncertainty in the quantitative analysis of element distribution, especially hydrogen distribution. Despite the optimisation of experimental conditions to suppress noise, a notable gap exists between the lower and upper bounds for deuterium estimation after overlap solving. The relatively low absolute D accumulation at the interface further amplifies the statistical uncertainty, making its impact more significant in a relative context. For instance, the unannealed sample in Table 5-1 shows a wide uncertainty range of 0.97 to 1.50 cts/nm², which weakens the confidence in data comparisons. This study highlights the inherent challenges of deuterium quantification in APT and underscores the importance of explicitly reporting error margins and critically assessing the data quality, which remains largely absent in many published APT reports on passivating structures [204], [205].

Comparison can be drawn between APT profiles in Figure 5-7 (b) and SIMS resulting in Figure 4-5 on the same TOPCon structure. SIMS depth profiles in Figure 4-5 report traces of certain masses without noting potential overlaps of ion candidates at the masses, which leaves errors in labelling the masses with a single candidate. Despite the fact that APT is also an ion spectrometry-based technique, the APT analysis in this work utilises decomposition of mass overlaps for additional data interpretation, which enables true quantification of element compositions. The other main difference is the sharp decrease of O, P and D after the interfacial oxide in APT results as contrast to the long tails in SIMS. This provides strong evidence that the SIMS results are susceptible to the knock-in artefact (inward displacement of ions during SIMS sputtering).

Similar comparisons can also be drawn between the APT results and the ERD results in chapter 4 (Figure 4-3). As previously discussed, the depth resolution in ERD deteriorates due to surface roughness effects and the relatively large field of view inherent to the technique. In contrast, APT provides superior depth resolution in elemental profiling owing to its atom-by-atom spatial reconstruction and nanoscale analysis volume. However, the highly localised nature of APT comes with trade-offs, most notably, limited data statistics and potential specimen variability as exemplified by the large variation in interface composition among needles extracted from the same sample. As a result, generalisations about the overall interface characteristics from APT data must be made with caution, at risk of underrepresentation by a few local sites. It is also important to note that because ERD implements double detection of ionic mass and ionic energy, as seen in the ERD coincidence histograms, it is capable of unambiguous differentiation of deuterium and other light elements. Therefore, while APT excels in spatial resolution, ERD data is complementary by its accuracy in compositional analysis.

## 5.10. Conclusions

Accurate analysis of the distribution of hydrogen in TOPCon passivated contact is critical in understanding surface passivation and degradation mechanisms. In this chapter, atom probe tomography was employed to investigate hydrogen distribution in hydrogenated TOPCon structures before and after annealing, using deuterium as a marker for sample hydrogen. However, residual hydrogen in the vacuum chamber and mass spectrum overlaps induce significant uncertainty in composition analysis, which poses challenges in quantifying $^{2}H/D$ reliably.

This study firstly demonstrates that the choice of laser energy and the surface field strength in the APT experiment can be made to effectively suppress the ambient hydrogen background detected. The APT 3D volumetric reconstruction of a needle specimen revealed clearly resolved complete TOPCon layers and interfaces. The spatial distribution of 31 Da mass species labelled as $^{31}P^{+}$ shows inconsistencies with true phosphorus distribution due to mass overlaps with other complex ions. Overlap solving of mass peaks based on the maximum likelihood method enables the production of vertical depth profiles of D, O and P with reduced uncertainty caused by grouped overlaps. It has been revealed by overlap solving that a large proportion of D contents is found in the $SiD^{+}$ complex ion.

The lower-bound estimates of D show a minor peak at approximately 1.0 at % at the interfacial oxide, indicating positive hydrogen enrichment at the ultrathin oxide. Gibbsian interface excess analysis for interfacial segregation shows a moderate 25% increase in the hydrogenation annealed specimen compared to unannealed specimen. This provides potential evidence towards a weak link between higher D interface enrichment and improved passivation quality of the TOPCon structure. It must be noted that confidence in such a link is only low, because of (a) possible sample-to-sample variation, (b) large statistical uncertainty range from the overlap solving analysis, and (c) difficulties in further distinguishing H content given the ambient H contamination. The quantitative analysis of deuterium within the complex TOPCon structure presented in this chapter contributes to a viable approach as well as critical assessments of the difficulties.

In comparing multiple APT specimens, substantial variation in interfacial oxygen and phosphorus excess was observed, which is possibly due to the uneven oxide thickness and nanoscale ROI of the APT analysis. Notably, APT did not show extended phosphorus diffusion beyond the oxide interface, in contrast to parallel SIMS data, providing evidence that the commonly observed SIMS dopant penetration findings are influenced by the knock-in measurement artefact.

In summary, the near-atomic-scale APT analysis provided in this study provides critical compositional understanding of the hydrogenated TOPCon structures. The findings from APT characterisation here are crucial for the future development and optimisation of the passivation contacts for high-efficiency silicon solar devices.

# 6. High-resolution LBIC characterisation of solar cell devices

A selection of the work presented in this chapter has been accepted for publication in AIP Conference Proceedings, "*NanoLBIC characterisation of silicon solar cells using a laser pick-up unit*". The author would like to thank collaborators from the Snaith group in the Department of Physics for providing high-efficiency mixed-halide perovskite samples for characterisation.

## 6.1. Introduction

Laser beam induced current measures the photocurrent generated by a PV device from a localised microscopic injection [217]. LBIC systems can raster-scan the injection spot in two dimensions, so that a spatially resolved photocurrent map can be generated. These maps provide valuable insight into local variations in device performance, such as regions of high recombination activity [218]. LBIC has an analogous counterpart electron beam induced current (EBIC), which relies on an electron beam for injection [219]. LBIC offers key advantages in its wider applicability as it operates in ambient conditions and avoids electron beam damage in EBIC injection.

An LBIC system integrates several key components: an illumination source, focusing optics, a scanning mechanism and current detection circuitry. Multiple monochromatic laser sources are typically included to allow wavelength-dependent sample analysis. The focusing optics is responsible for manipulating the beam so it achieves a minimum lateral spot size on the sample surface, thereby achieving high spatial mapping resolution. Importantly, the minimum achievable beam waist size is limited by diffraction as well as the system focusing power, as further explained in Appendix J. High spatial resolution LBIC systems, often termed micro-LBIC, can achieve spatial resolution ranging from 1-10 micrometres [217], [220], [221]. The scanning movement for map formation can be achieved in a configuration of either (a) laser scanning, where the laser beam is deflected over a fixed sample stage [222] [219][223], or (b) stage scanning, where the beam is stable while the sample is mechanically moved using a precision translation stage [224]. The latter design allows for close working distances and small laser spot size, as it is freed of beam deflection requirements. The trade-off of the stage scanning design is the slow mapping speed limited by the mechanical motion. Advanced LBIC systems can include additional functions such as simultaneous mapping of surface reflection [225], photoluminescence [219] or Raman spectrometry [223] for correlative analysis.

LBIC has a history of applications in evaluating current loss mechanisms in crystalline silicon structures. LBIC scans of multi-crystalline silicon reveal current profiles around recombination defects, which are used in the interpretation of defect recombination properties [226] [227] [228] [229]. Spatial distribution of minority diffusion lengths can also be calculated when using IR laser with an absorption length comparable to the minority diffusion lengths [230]. Laser modulated LBIC systems with AC currents can further enable mapping of series and shunt resistances [231] [232].

More recently, LBIC has also been applied in investigating halide perovskite solar cells (PSC), which have been demonstrated cell efficiencies comparable to crystalline silicon devices [233] and are progressing towards scalable industrial production [234]. Unlike silicon, the halide perovskite absorber layer in PSC, fabricated via either solution-based or vapour-based processing, is polycrystalline with a submicron grain size [235]. Perovskite material exhibits substantial structural and chemical heterogeneities across length scales ranging from nanometres to centimetres [236]. Such heterogeneities have a strong influence on local optical and electronic properties revealed by LBIC characterisations. Mastroianni et al. combined LBIC with spatially resolved PL to reveal that non-radiative recombination dominates the loss in efficiency in a hybrid organic–inorganic halide perovskite cell [237]. Giles et al. found an anticorrelation between spatial PL and spatial current, which supported high recombination losses at contact interfaces [238]. Additionally, Song et al. studied perovskite degradation under humidity with LBIC and identified a final irreversible decomposition step involving water [239].

In this chapter, the author presents an independently developed LBIC system capable of achieving one of the highest spatial resolutions reported to date. This is accomplished through adopting a simplified optical configuration departing from the complex laser-focusing schemes in traditional micro-LBIC systems. The developed system is demonstrated on both silicon and perovskite solar cell architectures, establishing its broad applicability and potential for advanced spatial characterisation in photovoltaic research.

## 6.2. An LBIC setup with sub-micron resolution

The key component in the LBIC system responsible for the laser focusing is a laser pick-up unit (LPU). LPU is a compact optoelectronic part used for reading/writing data from/to an optical disk. It is designed to detect data pits as small as 130 nm on a Blu-ray disc [240]. The LPU is repurposed to focus laser beams of two wavelengths, 650 nm (red, DVD standard) and

405 nm (violet, Blu-ray standard), on the sample surface localised optical injection. Table 6-1 summarises the resulting focused spot size and working distances for both wavelengths. The tight focus, benefited from the close working distances, provides nanoscale excitation volumes that underlie the outstanding spatial mapping resolution, exceeding the highest reported in literature [224].

*Table 6-1 Optical parameters for a dual-wavelength optical pick-up unit, from [240][241]*

| Wavelengths | First ring diameter | FWHM | Working distance | Depth of focus |
|---|---|---|---|---|
| 650 nm | 1.32 μm | 530 nm | ~2.0 mm | 8.4 μm |
| 405 nm | 0.58 μm | 250 nm | ~0.5 mm | 2.6 μm |

The LPU includes a mechanism to find the precise focus within the DoF shown in Table 6-1. This is achieved by fine adjustment using a focus error signal (FES) that indicates the vertical laser position relative to the sample surface. Figure 6-1 describes the laser optical path and associated components. The system utilises an astigmatic beam to generate the FES from the reflected beam shape [242]. When the objective lens is actuated near the focal position, the astigmatic reflected beam exhibits a moving elliptical profile, which is captured by the quadrant photodetector.

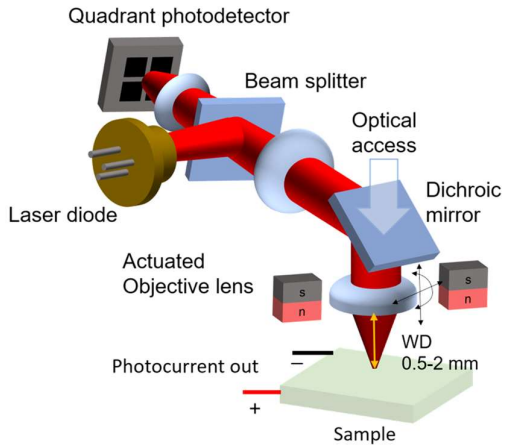


*Figure 6-1 The optical path of red 650 nm laser with key components labelled. The blue 405 laser path shares same route except for a separate laser source and collimator lens.*

Figure 6-2 illustrates the detected FES from (a) a high-reflectance metal sheet surface and (b) a low-reflectance textured silicon cell. The S-shaped FES curve in Figure 6-2 (a) corelates to the signal generated by the difference between the sum of diagonal quadrants ((A+C)-(B+D)) illustrated by the inset sketch, which indicates the changing beam ellipticity near focus with the optimum focal point found at the mid-point of the curve. It is observed from Figure 6-2 (b)

that the FES signal is significantly weaker from a silicon surface, because of the lack of mirror reflection. Therefore, focusing is preferably performed on reflective sample regions to ensure accurate alignment.

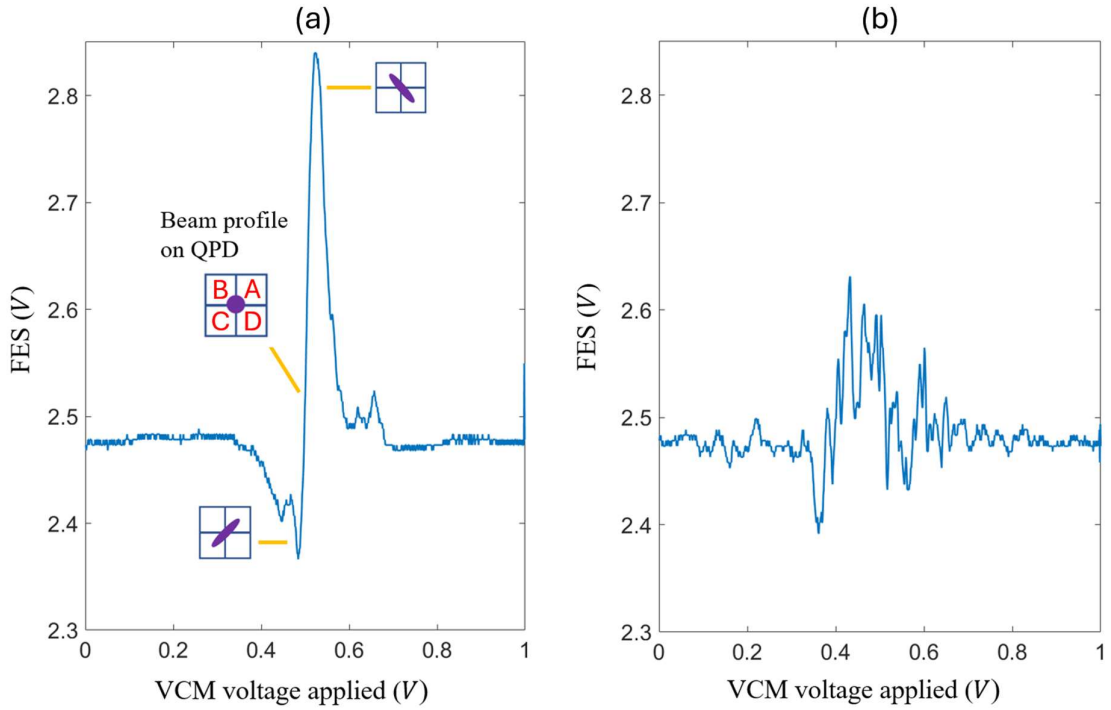


*Figure 6-2 Example of focus error signal curves detected by the QPD vs voice coil motor voltage at the same gain. (a): from a reflective metal surface, (b): from a finished Si solar cell front surface.*

Figure 6-3 demonstrates the complete assembly of the LBIC system. The LPU is mounted on a top plate supported by three coarse positioning screws. A customised driver board connects the LPU with a National Instrument signal I/O DAQ device. The DAQ device sets laser power, reads the FES signal from the LPU, and controls the actuators of the objective lens. The lens actuation range is approximately 1 mm. The photocurrent from laser injection from the solar cell device is measured by a Keithley 236 Source Measure Unit (SMU). The SMU typically operates with photocurrents in the microampere (μA) range for reduced measurement noise. The 2D current map is constructed by the raster scanning of the sample, enabled with a set of two motorised translation stages. The movement range of the stages is 2.5 cm with a positioning accuracy of 50 nm, allowing for spatial mapping across different scales. A typical scanning speed at 0.3 s/pixel is achieved, which is constrained by both pixel dwell time for current measurement integration and the mechanical translation speed. All hardware components are integrated and controlled via a LabVIEW interface.

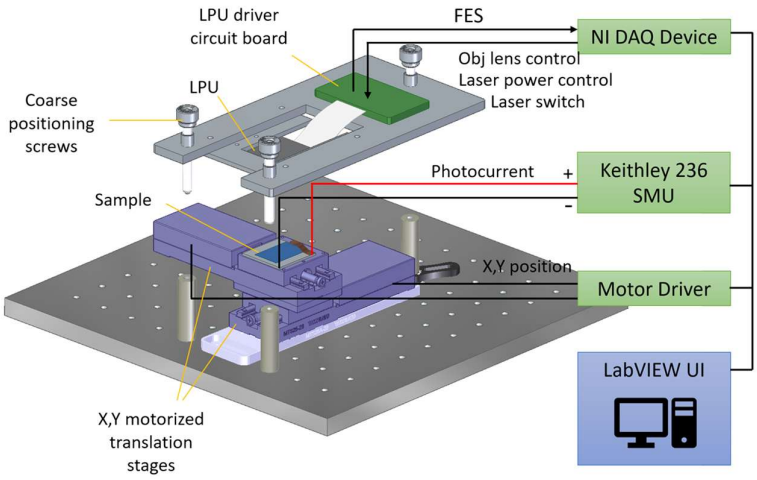


*Figure 6-3 Schematic of the system mechanical setup with signal flows*

## 6.3. Characterisation of silicon solar devices

The silicon samples under testing are industrial p-type monocrystalline PERC cells. Detailed descriptions of the passivated structure are included in section 1.4.1 of this thesis. Figure 6-4 presents a schematic of the finished PERC front, encompassing an n-type diffused emitter, the nitride anti-reflection coating and silver finger contacts. A key feature of the PERC front side is the application of laser-assisted selective doping beneath the metal fingers. These selectively doped regions, approximated 130 μm wide, larger than the ~30 μm finger width, are introduced to form local $n^{++}$ emitters. The local $n^{++}$ emitter design reduces the heavy doping losses in the rest surface compared to a uniform emitter layer [243], [244].

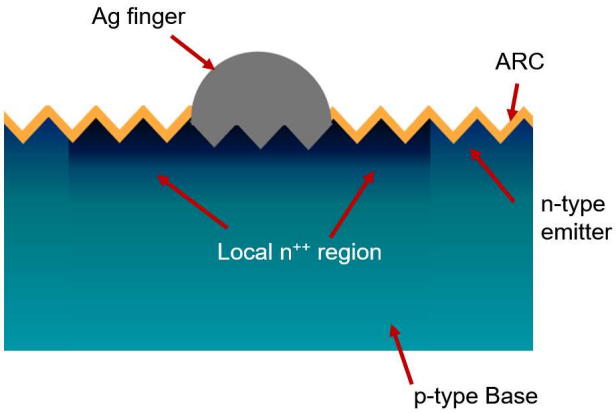


*Figure 6-4 Front structure of the industrial PERC cell*

To validate the reliability and spatial accuracy of the system, LBIC maps are compared first to optical microscope images. Figure 6-5 (a) demonstrates the optical microscope image of a

region showing a metal finger going diagonally and artificial surface markings. The LBIC scan of the same region is shown in Figure 6-5 (b) with a 2 µm scanning step size. The surface markings made with a diamond scriber pen, indicated by grey arrows in both images, provide additional alignment features which show excellent alignment between the two images. The results demonstrate that both positioning accuracy and effective focusing are maintained in an LBIC scan. The photocurrent reduction at metal finger locations is a result of the shadowing effect by the metal blocking light injection. However, the signal does not drop to zero because of reflection from metal surfaces and subsequent absorption of scattered light. The scribed markings exhibit sharp photocurrent suppression, due to destruction of the front structure, including surface passivation and the emitter layer. Furthermore, it is also evident that the selective doped region adjacent to the fingers show lower currents. This observation aligns with previous reports that the laser-doped $n^{++}$ region can introduce additional recombination losses [245][246].

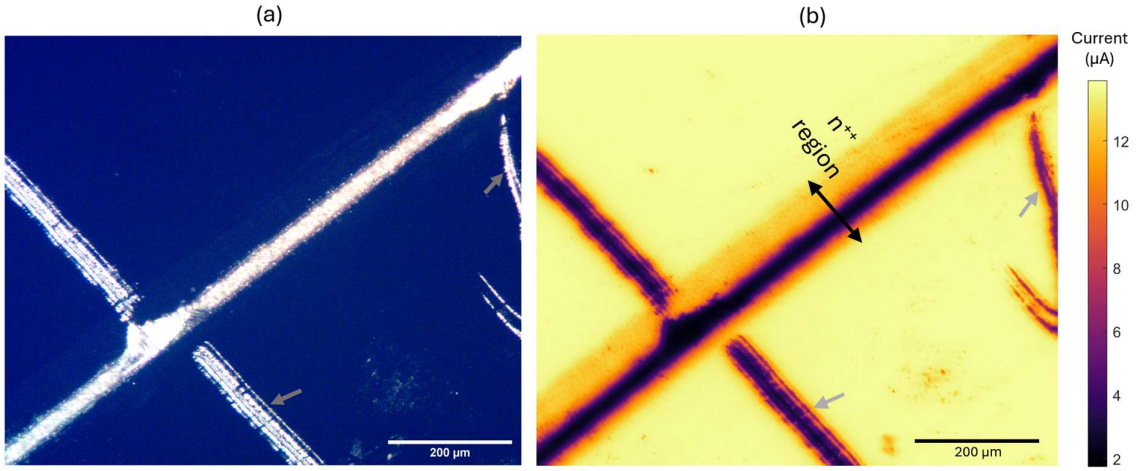


*Figure 6-5 (a) Optical microscope image of PERC cell front with marks. (b) 405 nm LBIC map of same region, mapping step size: 2 µm, current level indicated by the colour bar.*

As further validation of the LBIC results, Figure 6-6 demonstrates (a) an electron image and (b) an EBIC map of front metal fingers. It can be confirmed in EBIC results that the $n^{++}$ region, as marked by the span of the red line, is linked to current reduction. It is noted that EBIC offers higher spatial resolution inherent to the short electron beam wavelengths.

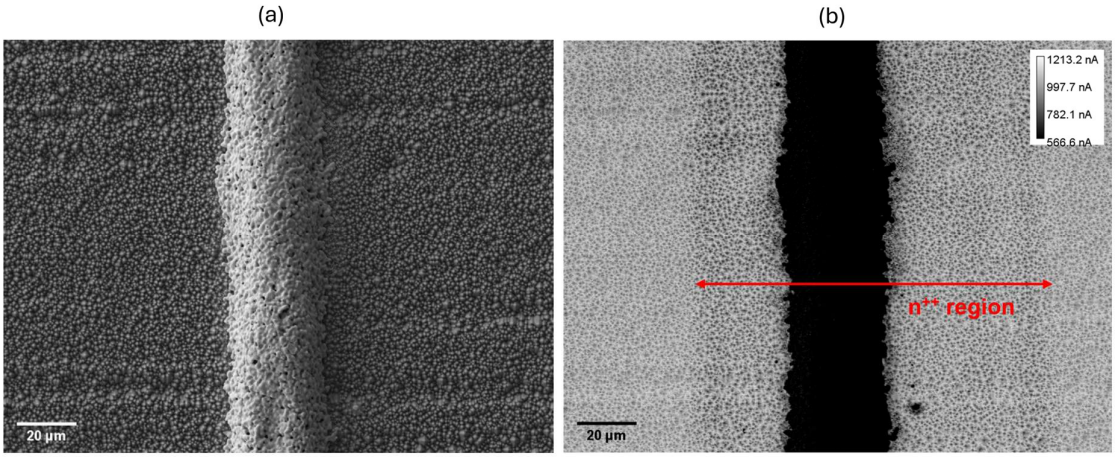


*Figure 6-6 (a) SEM image of a front metal finger on a PERC cell. (b) EBIC image of the same region, electron beam energy at 10 kV*

The dual-wavelength laser source makes LBIC capable of probing at different depths. Figure 6-7 (a) and (b) demonstrate images of PERC front metallisation with 405 nm injection and 650 nm injection, with 1 µm scanning step size. A comparison between the two maps reveals the different contrast of the $n^{++}$ region, with the current reduction being more pronounced in 405 nm map than the 650 nm map, as expected because of the near-surface absorption for blue light. Figure 6-7 (c) and (d) show the line profiles spanning across the $n^{++}$ region from the LBIC maps. From the profiles, the current reduction within $n^{++}$ region (denoted as $I_D$ in Figure 6-7 (c)) stands at approximately 9% relative to the free-surface maximum under 405 injection, and 3% for 650 nm injection. Such a difference originates from the larger injection depth of 650 nm compared to 405 nm. It can be further interpreted that, under the assumption that losses are constrained within a surface $n^{++}$ emitter layer, the doping damage approximately lies between the absorption lengths of two lasers from 0.13 µm to 3.56 µm (silicon absorption lengths from [247]). The finding is consistent with the shallow nature of the structural damage from laser doping as reported in the literature [246].

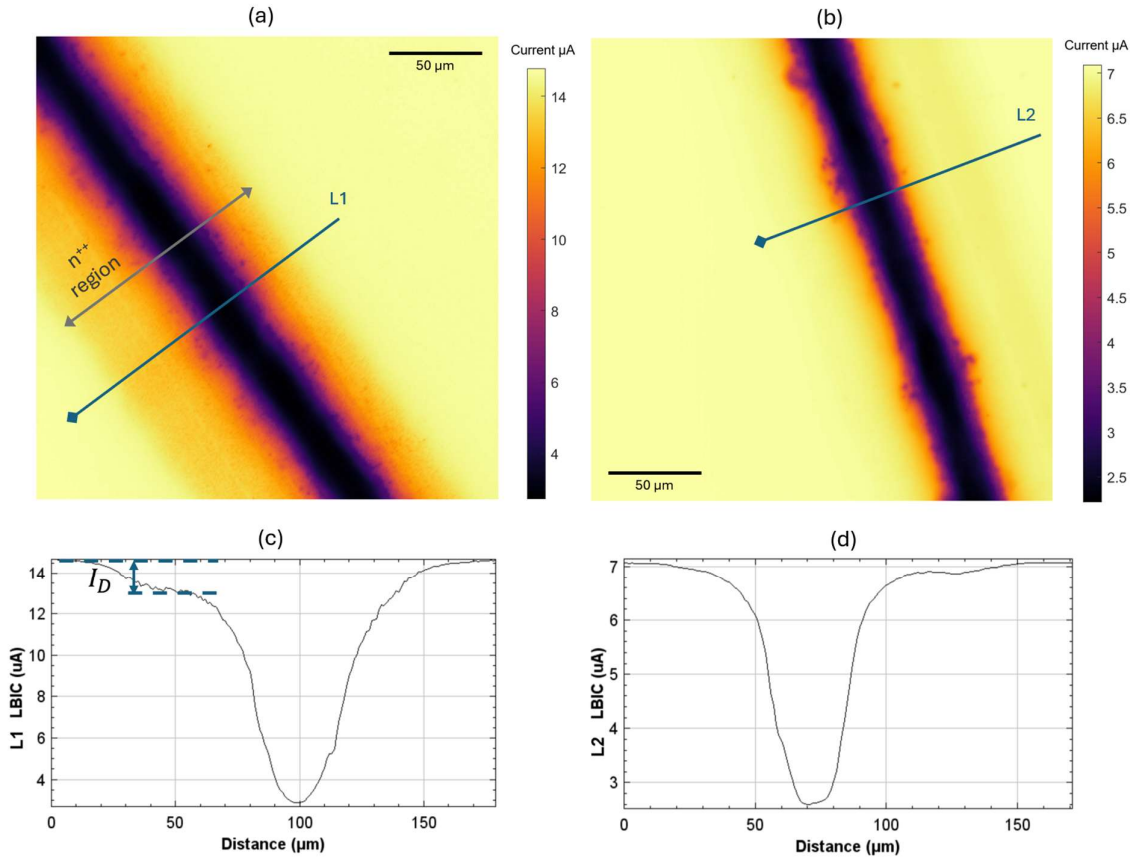


*Figure 6-7 (a) 405 nm LBIC map of PERC front metallisation. (b) 650 nm map from the same sample. (c)&(d) Current line profiles from LBIC maps (a) and (b) respectively.*

Since the optical unit has a focus spot diameter as low as 250 nm, the LBIC setup is capable of mapping at submicron spatial resolutions. Figure 6-8 (a) demonstrates the highest-resolution 405 nm laser map of the $n^{++}$ region with a 200 nm scanning step size. The spotted texture reveals effects of the surface pyramid texture. To illustrate this, EBIC results are attached in Figure 6-8 (b), where reduced currents are extracted from the pyramid tips. This variation of current collection between pyramid bases and tips can be analogously found in the LBIC map in Figure 6-8 (a). Figure 6-8 (c) explains possible reasons for the current variation, including: (i) the laser processing during selective $n^{++}$ doping can cause extensive heat damage to the tip and partial melting, which induces enhanced surface recombination losses [245]. (ii) The valley-shaped pyramid bases can reduce light escape by the multiple angled surfaces, which only becomes discernible with nanometre optical injection at comparable scales to the tomography structure. Since pyramidal tips in the LBIC map are as close as 500 nm apart, the feature provides direct evidence of the state-of-the-art LBIC spatial resolution.

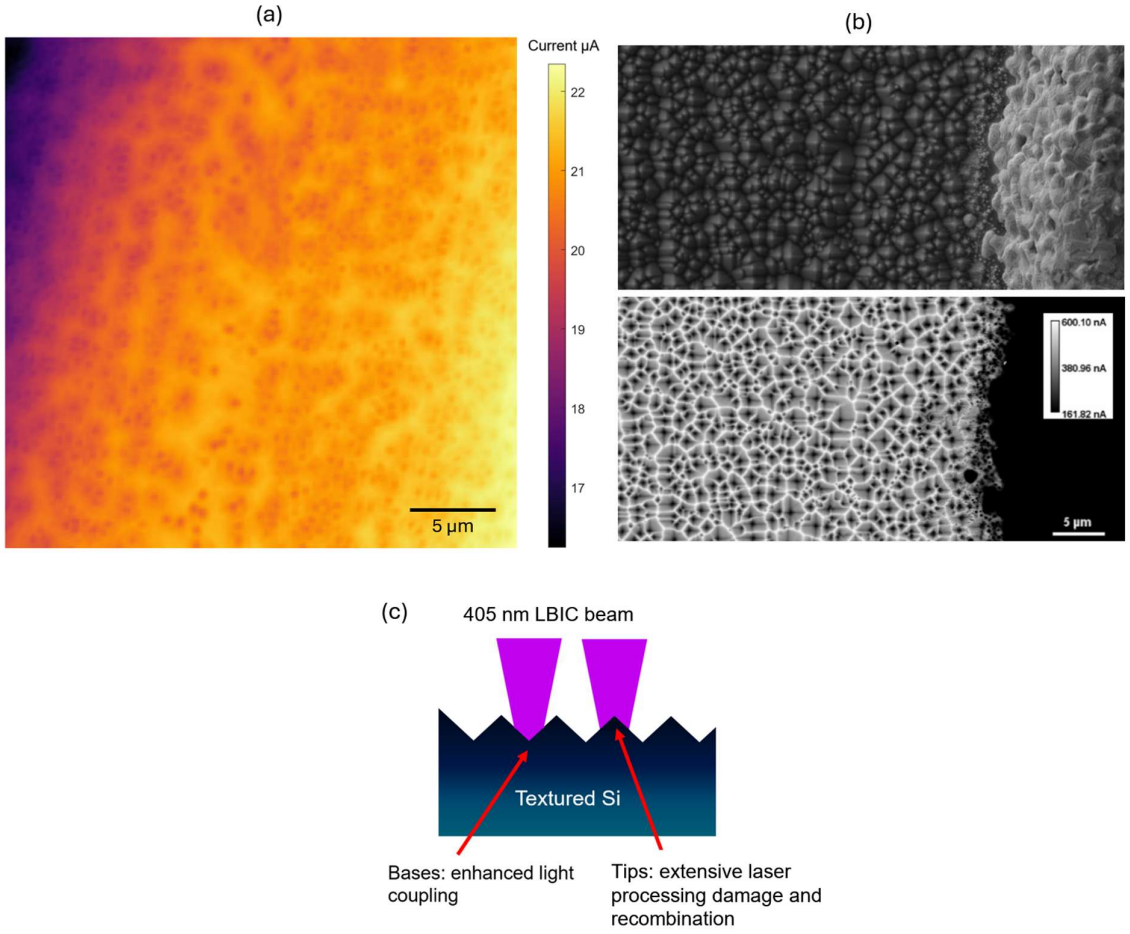


*Figure 6-8 (a) 405 nm LBIC map of $n^{++}$ selective emitter region of PERC front, scanning step size 200 nm (b) SEM and EBIC map of the $n^{++}$ selective emitter region adjacent to a metal finger, electron beam energy at 7.5 kV. (c) possible reasons for reduced tip current collection*

## 6.4. Characterisation of perovskite solar devices

LBIC is also implemented in the characterisation of high-efficiency perovskite solar cell samples. The encapsulated perovskites have a p-i-n structure shown in Figure 6-9. The structure includes (a) [4-(3,6-dimethyl-9H-carbazol-9-yl)butyl]phosphonic acid (Me-4PACz) serving as hole transport layer, (b) a perovskite absorber layer $FA_{0.83}Cs_{0.17}Pb(Br_xI_{1-x})_3$ with varied Br content, and (c) a bilayer of [6,6]-phenyl-C61-butyric acid methyl ester (PCBM) and Bathocuproine (BCP) serving as the electron transport layer (ETL). The layers are fabricated via solution processing in sequence on an ITO-coated glass substrate, shown as the bottom of Figure 6-9, which is now the side for laser illumination. Because the optical length in the 1.2 mm thick glass layer is larger than the working distance of 405 nm laser, only 650 nm red layer

can reach focus through the glass. EBIC measurements are not viable on the sample because of the encapsulated absorber layer and the sensitivity of perovskite materials to electron beam damage [248], [249].

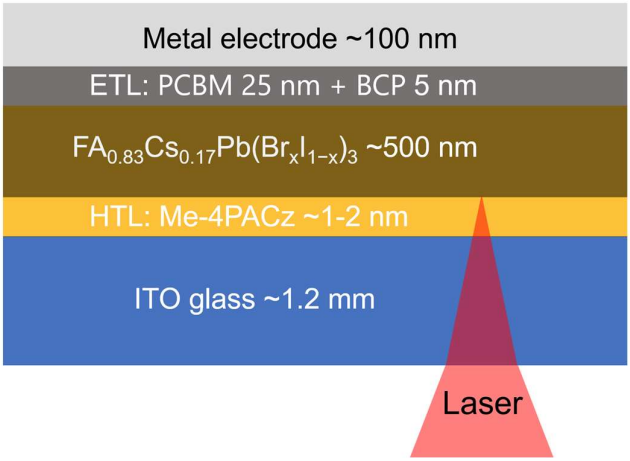


*Figure 6-9 p-i-n perovskite structure with LBIC injection direction. Injection comes from the glass side.*

Here, LBIC is used to spatially resolve a phase segregation phenomenon in perovskite samples. It is well-documented that an increase of Br/I ratio widens the material bandgap [250] making it ideal for bandgap tuning. However, the mixed I-Br perovskites undergo injection-induced halide segregation, leading to the formation of I-rich and Br-rich domains and cell performance degradation. The loss in current has been attributed to increased recombination in the relatively emissive segregated I-rich domains [251], [252].

Figure 6-10 illustrates 650 nm (1.70 eV photon energy) LBIC maps from two device compositions $FA_{0.83}Cs_{0.17}Pb(Br_xI_{1-x})_3$ with Br content at x=10% and x=30%. During LBIC measurements, injection-induced phase segregation is expected to have reached saturation due to the high local carrier injection intensity and the relatively long injection time (> 0.3 second) at each scanning step, which corresponds to the scanning speed limit. The saturation of any injection-related changes is supported by the observation that repeated LBIC scans yield consistent results same as the initial scan. A comparison between Figure 6-10 (a) and (b) reveals that the Br-rich device exhibits larger spatial current collection variation amplitude and an interconnected low-current phase. The <50% photocurrent yield from the secondary phase can be attributed to a combination of (a) low red response from a wide-bandgap Br-rich phase (650 nm wavelength corresponds to 1.70 eV photon energy) and (b) additional carrier recombination

losses in segregated domains. The gradual boundary between domains indicates that phase separation likely results in a continuum of composition transition over the micrometre scale. Table 6-2 shows the bandgaps and device properties measured prior to LBIC tests. The changes in $V_{oc}$ and $J_{sc}$ associated with different bandgaps follow the thermodynamic limit predictions [253]. The further reduced fill factor in the 30% Br is likely reflective of the additional carrier losses associated with enhanced phase segregation as revealed by LBIC. It is noteworthy that such direction LBIC observations of phase-segregated domains in mixed halide devices present the first report of its kind.

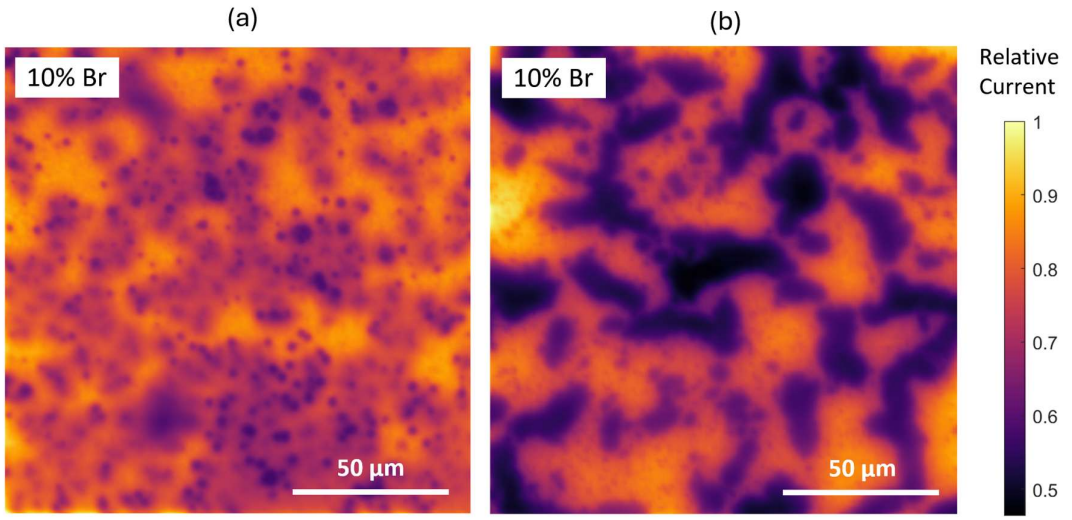


*Figure 6-10 LBIC maps of $FA_{0.83}Cs_{0.17}Pb(Br_xI_{1-x})_3$ perovskite solar cells with Br content: (a) x=10% (b) x=30%.*

*Table 6-2 Perovskite cell properties of 10% Br and 30% Br halide compositions, measured by collaborators right after fabrication prior to LBIC scanning. The $V_{oc}$ and $J_{sc}$ changes associated with different bandgaps follows the thermodynamic SQ limit.*

| Br Content | Bandgap (eV) | Voc (V) | Jsc (mA/cm$^2$) | FF | PCE (%) |
|---|---|---|---|---|---|
| 10% | 1.61 | 1.14 | 21.0 | 0.818 | 19.7 |
| 30% | 1.72 | 1.21 | 18.4 | 0.797 | 17.8 |

A high-resolution LBIC scan on a separate $FA_{0.83}Cs_{0.17}Pb(Br_{0.4}I_{0.6})_3$ device further reveals distinctive current variation induced by surface topography. Figure 6-11 illustrates the 0.5 µm step size scan with 650 nm injection. The current colour scale is constrained within a 0.6-1.0 relative range to enlarge contrasts for better visualisation. Micrometre scale waviness can be found in the high-current region, presenting a feature comparable to the high-resolution silicon results in Figure 6-8, which can be attributed to the surface topography. It supports a wrinkling

perovskite surface induced by the thermal strain during film processing, as also reported in [236], [254]. The surface topography was previously only visible on exposed surfaces via electron microscopy, which highlights the unique potential that the new sub-micron LBIC measurements of this work provide.

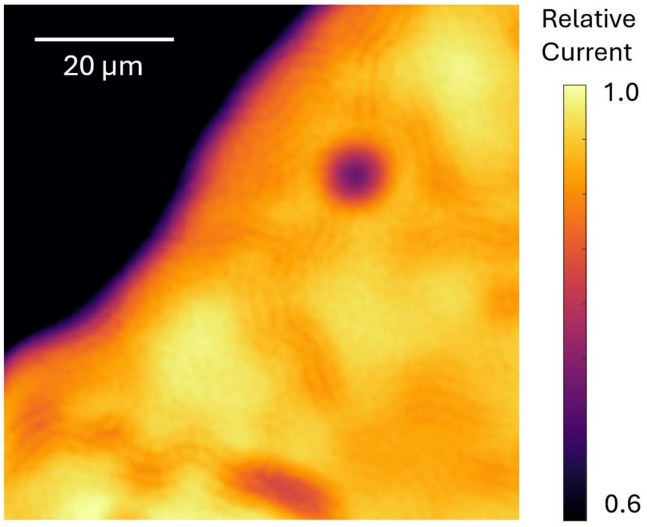


*Figure 6-11 high-resolution LBIC map of a $FA_{0.83}Cs_{0.17}Pb(Br_{0.4}I_{0.6})_3$ sampling. Wrinkling feature induced by surface topography.*

## 6.5. Discussion and summary

The high-resolution capability of the LBIC system developed in this chapter has been utilised to reveal the impact of surface morphology on carrier collection in both silicon and perovskite solar cells. Such an observation has rarely been reported in the literature except for [224], since it can only be resolved with a nanoscale laser beam waist size and high beam divergence. It is acknowledged that the effect of surface morphology on the LBIC signal can originate from both optical and electrical mechanisms. This implies that the local surface features not only affect light coupling efficiency but can also induce changes in the collection of generated carriers via variation in surface doping for silicon cells or the perovskite-HTL interface for perovskite cells. For the improved interpretation of the LBIC results, optical modelling detailing the interaction between the laser beam and the surface geometry can be pursued to evaluate the optical effect at nanoscale, which will allow separation of the optical mechanism. This future work direction will require substantial modelling efforts following different optical methods, such as raytracing for silicon and the transfer matrix method for thin-film perovskites.

In addition to high spatial resolution, dual-wavelength LBIC mapping enables probing of depth-dependent current collection in the silicon structure. An estimate of the surface current

loss layer thickness is made in section 6.3 by exploiting the difference in penetration depths of the two wavelengths. However, such an estimation simply assumes constant collection efficiency within both the defective surface layer and bulk, which is inaccurate for a detailed assessment of carrier loss mechanisms. As established in prior EBIC studies [255], [256] a comprehensive interpretation of spatially resolved current signal requires a two-step modelling framework, which involves building a spatial generation profile (the optical step) and a current collection function near the defect (electrical step). The LBIC datasets obtained using this system offer a promising foundation for future modelling-assisted analysis, enabling deeper investigation into carrier recombination and transport mechanisms in advanced solar structures.

Furthermore, the demonstrated sensitivity of LBIC to detect phase segregation in perovskites highlights its applicability to emerging solar cell architectures. The system can be further expanded to meet unique characterisation requirements of perovskite and perovskite-silicon tandem devices, in ways including: (a) imaging through encapsulation layers via adaptation to the laser optics, and (b) implementing time-resolved LBIC using laser frequency modulation and high-speed current detection, which would be particularly valuable for monitoring transient processes such as ion migration in perovskites.

In summary, a robust LBIC system has been developed by adapting the precision focusing optics of a laser pick-up unit. Its performance has been carefully benchmarked against both optical imaging and EBIC, demonstrating consistent and reliable current mapping. The cooperation between the optical focusing and mechanical scanning enables precise mapping at varying length scales. The sub-micron spatial resolution, which correlates to laser wavelength, approaches the physical diffraction limit. The system is used to resolve the current collection effect of nanoscale surface morphology in both silicon and perovskite solar cells. The dual-wavelength mapping further offers insights into current losses in surface layers by leveraging wavelength-dependent absorption. The resolution capability, versatility and reliability of the developed system establish it as a powerful, low-cost, low-preparation optoelectrical characterisation route. The system offers a versatile, low-cost, and low sample preparation optoelectronic characterisation platform that complements existing techniques, particularly for sensitive devices where electron-beam methods like EBIC are unsuitable. The LBIC results shed insights into carrier losses in the laser-doping layer in the silicon device and halide segregated phases in the spatially non-uniform perovskite device. Looking forward, the LBIC system opens promising avenues for experimental design and data analysis, with the potential

to advance the understanding of carrier recombination and transport phenomena at the sub-micron scale.

# 7. Conclusions and future work

This thesis contributes to the understanding of performance-limiting mechanisms in TOPCon structures through a variety of approaches covering photoluminescence imaging, laser mapping, electrical testing, microstructural analysis, and chemical profiling. The development of novel characterisation methodologies, involving PL periodicity analysis and high-resolution LBIC, offers valuable tools for both research and industrial application. The findings also point to future directions in contact optimisation and hydrogen passivation strategies. The key findings and contributions of this work are summarised as follows:

**a) PL spatial periodicity analysis for contact recombination assessment**

Photoluminescence (PL) imaging of grid-metallised industrial TOPCon cells reveals a periodic spatial signal arising from contact recombination. The spatial periodicity is analysed via a Fourier transform-based method to extract the contrast amplitude. Device-specific numerical simulations confirms that this amplitude of periodic contract correlates strongly with the contact recombination current, $J_{0,c}$. This approach enables the extraction of $J_{0,c}$ values for comparison across different metallisation schemes.

The independently developed data analysis framework, aided by physical device simulation, provides offers a new approach to interpreting PL imaging data by linking spatial features collectively with the underlying recombination mechanism. Its application has revealed limitations in scenarios involving poorly passivated surfaces, where elevated image noise hinders signal extraction. Nevertheless, given the widespread adoption of PL imaging in both research and industrial settings, this method shows strong potential as a fast test route tool for grid-metallised structures, broadening the utility of PL imaging in recombination assessments.

**b) Electrical and microstructural characterisation of TOPCon contacts**

The contact recombination and resistance of TOPCon structures have been evaluated using a combination of both the new PL methodology and standard contact testing techniques. FIB slicing and EDX mapping of contact cross-sections provide microstructure evidence of performance changes. It has been found that incorporation of an ultra-thin $AlO_x$ beneath the surface nitride significantly reduces surface and contact recombination via preserving integrity of the passivation layers from firing damage. The glass content in the metallisation paste influences formed glass interfacial layer thickness and uniformity, with a thin and continuous glass layer being ideal for reducing both contact recombination and resistance. Thinner polysilicon layers are shown to be more vulnerable to firing-induced degradation, resulting in

increased recombination. The microstructural studies reveal a favourable contact structure feature well-dispersed Ag colloids for conduction and minimal nitride opening to preserve passivation. The results also suggest the high variability of the contact microstructure in industrial samples sensitive to firing, highlighting the need for processing tuning during TOPCon contact formation. Such findings offer valuable guidance for TOPCon structural adaptation in further optimising the contact performances.

**c) ToF-ERD analysis of a TOPCon structure**

Detecting hydrogen within the TOPCon structure is critical for understanding hydrogen passivation. Significant challenges exist following traditional chemical analysis routes because of environmental contamination and signal ambiguity. My project tackles the issues by implementing ToF-ERD characterisation on a partially deuterated sample. Due to its atomic recoil-based mechanism, ToF-ERD provides clear separation of $^{1}H$ and $^{2}H$ signals, allowing for unambiguous identification of deuterium incorporation. The ERD profiles reveal inaccuracies in conventional SIMS profiling caused by the changing matrix effect in SIMS. Although ToF-ERD can resolve near-surface layers, its depth resolution deteriorates, preventing clear depiction of buried oxide interface composition. The depth uncertainty is shown to relate to both ion energy dispersion and errors in energy-depth conversion. ERD alone is hence likely not sufficient in profiling $^{2}H$ at the buried interfacial oxide without sample structure change. highlighting the need for complementary nanoscale chemical analysis.

**d) APT analysis of the TOPCon structure**

As the continuation on hydrogen analysis of TOPCon structure, I employed APT in quantification of hydrogen distribution before and after hydrogen annealing. The near-atomic resolution in APT 3D reconstruction enables clear depiction of the layered structure. Chemical depth profiling using APT results show sharp composition transition at interfaces, in contrast to long artefact tails in SIMS. It is also revealed that phosphorous dopants segregate towards the interfacial oxide but does not diffuse through. Variation in oxide thickness among APT specimen sites points to a spatial non-uniform oxide.

The interpretation of detected hydrogen contents is taken with extra caution due to the ambient H background and mass overlaps. Mass overlap solving following method in [215] reduces the signal ambiguity and produces an estimated range for $^{2}H$ profiling. APT conditions of higher evaporation fields and lower laser energies are shown to benefit $^{2}H$ quantification. APT results show a 25% increase in H accumulation at the oxide interface after annealing, while significant

uncertainty remains associated with the low accumulation level. This suggests a correlation between interfacial oxide hydrogenation and TOPCon passivation enhancement. The work paves the way of H analysis in nanolayer surface passivation structure. The APT results also illustrate the source of uncertainty in quantitively H analysis and the necessity of reporting it.

**e) High-resolution LBIC characterisation of solar devices**

An independently built LBIC system, based on a laser pick-up unit, demonstrates sub-micron spatial resolution. Its application reveals current losses in (a) a shallow laser-damaged layer in a PERC silicon cell, and (b) halide-segregated phases in a mixed-halide perovskite device. High magnification LBIC maps reveal surface texture in both silicon and perovskite cells, suggesting both optical and electrical influences of surface morphology. The LBIC results demonstrate both versatility and details with promising applications across solar devices.

In summary, this thesis expands experimental methodologies and data analysis techniques for evaluating residual energy losses in solar devices, offering practical pathways for broader implementations. The work, with a particular focus on the important TOPCon structure, deepens the understanding of contact behaviour and interface passivation, both critical in further advancing device performances. The knowledge from the work provides actionable guidance for targeted optimisation of contact architectures and passivation strategies, and establishes a strong foundation for future studies in advanced optoelectronic characterisation and solar cell interface engineering.

## Future work

A variety of new studies can be proposed following the findings in the work, on the following topics:

**a) Expansion of the Fourier analysis-based PL method**

This study demonstrated that metal contact signal extraction from PL images using Fourier analysis is hindered by high image noise, particularly from high recombination surfaces. To enhance the applicability and accuracy of this method, further noise suppression is needed via both PL experimental condition optimisation and post-processing techniques. A key limitation factor reducing the signal contrast is the optical blurring, which can be further modelled in the simulation framework to account for its effects. Owing to the periodicity-based approach, the method can be applied in a wide range of grid metallisation structures A promising avenue is

the extension to finished cells with double-sided contacts with different finger pitches at front and rear.

**c) Further contact microstructure examination with EBIC**

Microstructural examination of the contract interface reveals key features underlying contact performance changes. Such relationships are usually very generic. The SEM based EBIC characterisation can potentially reveal the electrical impact of the important contact feature including nitride damages and Ag colloids in glass, which could elucidate the understanding of carrier recombination and transport in fire-through contact structures.

**d) Combined ERD and APT Investigations of Hydrogen Distribution**

It is shown that ERD experimental results suffer from degradation in depth resolution. Future studies may benefit from using shallower, flatter sample architectures to enhance ERD profiling resolution. The unambiguous $^{2}H$ signal provided by ERD, if improved in spatial resolution, can be used in calibration of APT data to help reducing its detection uncertainty and increasing H analysis accuracy. The demonstrated ERD and APT routes can be extended to study hydrogen dynamics in other passivation schemes, although the experimentation and data analysis takes a significant amount of time.

**e) Improvement of LBIC data interpretation and extending LBIC applications**

The development of modelling frameworks that detail LBIC optical generation and carrier collection processes is a key direction for enhancing the interpretation of current LBIC data, which is particularly useful for assessing local carrier recombination mechanisms. Additionally, the application of LBIC can be further extended to perovskite and tandem solar cells, where spatial non-uniformities across multiple length scales and their effects on carrier collection are still to be understood.

# 8. References


[1] International Energy Agency, “Energy Statistics Data Browser,” Paris, 2023.

[2] Intergovernmental Panel on Climate Change, “Climate Change 2023: Synthesis Report,” 2023. doi: 10.59327/IPCC/AR6-9789291691647.001.

[3] International Renewable Energy Agency, “Reaching zero with renewables : eliminating $CO_2$ emissions from industry and transport in line with the 1.5°C climate goal,” p. 214, 2020.

[4] R. Ehrlich, H. A. Geller, and J. R. Cressman, “Renewable Energy : A First Course,” Jul. 2022, doi: 10.1201/9781003172673.

[5] “COP28: New deals and evasive tactics,” *Economist*, Dec. 19, 2023. Accessed: Oct. 07, 2024. [Online]. Available: https://impact.economist.com/sustainability/cop28-new-deals-and-evasive-tactics

[6] John. Perlin, *From space to Earth: the story of solar electricity*. AATEC ; James & James, 2002. Accessed: Oct. 08, 2024. [Online]. Available: https://books.google.com/books/about/From_Space_to_Earth.html?id=xHFK9cM77a8C

[7] Małgorzata Wiatros-Motyka, Nicolas Fulghum, and Dave Jones, “Global Electricity Review 2024,” May 2024. Accessed: Oct. 08, 2024. [Online]. Available: https://ember-climate.org/insights/research/global-electricity-review-2024/

[8] Euan Graham and Nic Fulghum, “Solar power continues to surge in 2024,” 2024.

[9] J. Prime *et al.*, “Renewable Energy Statistics 2024, International Renewable Energy Agency,” 2024. Accessed: Oct. 08, 2024. [Online]. Available: https://www.irena.org/Publications/2024/Jul/Renewable-energy-statistics-2024

[10] Fraunhofer Institute for Solar Energy Systems, “Photovoltaics Report - Fraunhofer ISE,” 2024. Accessed: Oct. 10, 2024. [Online]. Available: https://www.ise.fraunhofer.de/en/publications/studies/photovoltaics-report.html

[11] “International Technology Roadmap for Photovoltaic (ITRPV) 15th Edition.”

[12] M. A. Green, A. Ho-Baillie, and H. J. Snaith, “The emergence of perovskite solar cells,” *Nature Photonics 2014 8:7*, vol. 8, no. 7, pp. 506–514, Jun. 2014, doi: 10.1038/nphoton.2014.134.

[13] R. Sharma, A. Sharma, S. Agarwal, and M. S. Dhaka, “Stability and efficiency issues, solutions and advancements in perovskite solar cells: A review,” *Solar Energy*, vol. 244, pp. 516–535, Sep. 2022, doi: 10.1016/J.SOLENER.2022.08.001.

[14] P. Zhu *et al.*, “Toward the Commercialization of Perovskite Solar Modules,” *Advanced Materials*, vol. 36, no. 15, p. 2307357, Apr. 2024, doi: 10.1002/ADMA.202307357.

[15] D. Wang, M. Wright, N. K. Elumalai, and A. Uddin, “Stability of perovskite solar cells,” *Solar Energy Materials and Solar Cells*, vol. 147, pp. 255–275, Apr. 2016, doi: 10.1016/J.SOLMAT.2015.12.025.

[16] “https://www.longi.com/en/news/.”

[17] “https://www.acap.org.au/post/world-leading-27-perovskite-efficiency-record-achieved-by-unsw-and-soochow-university-with-acap-su.”

[18] J. Liu *et al.*, “Perovskite-silicon tandem solar cells with bilayer interface passivation,” *Nature 2024*, pp. 1–3, Sep. 2024, doi: 10.1038/s41586-024-07997-7.

[19] “Absorption Coefficient | PVEducation.” Accessed: Nov. 27, 2024. [Online]. Available: https://www.pveducation.org/pvcdrom/pn-junctions/absorption-coefficient

[20] R. Alicki, D. Gelbwaser-Klimovsky, and A. Jenkins, “A thermodynamic cycle for the solar cell,” *Ann Phys (N Y)*, vol. 378, pp. 71–87, Mar. 2017, doi: 10.1016/J.AOP.2017.01.003.

[21] W. Shockley and H. J. Queisser, “Detailed Balance Limit of Efficiency of p-n Junction Solar Cells,” *American Institute of Physics*. doi: 10.1063/1.1736034.

[22] A. Polman, M. Knight, E. C. Garnett, B. Ehrler, and W. C. Sinke, “Photovoltaic materials: Present efficiencies and future challenges,” *Science (1979)*, vol. 352, no. 6283, 2016, doi: 10.1126/science.aad4424.

[23] M. A. Green, “Silicon solar cells : advanced principles and practice,” 1995, *Sydney*.

[24] T. Fuyuki and A. Kitiyanan, “Photographic diagnosis of crystalline silicon solar cells utilizing electroluminescence,” *Appl Phys A Mater Sci Process*, vol. 96, no. 1, pp. 189–196, Jul. 2009, doi: 10.1007/S00339-008-4986-0/METRICS.

[25] T. Trupke, B. Mitchell, J. W. Weber, W. McMillan, R. A. Bardos, and R. Kroeze, “Photoluminescence Imaging for Photovoltaic Applications,” *Energy Procedia*, vol. 15, pp. 135–146, Jan. 2012, doi: 10.1016/J.EGYPRO.2012.02.016.

[26] W. Shockley and W. T. Read, “Statistics of the recombinations of holes and electrons,” *Physical Review*, vol. 87, no. 5, pp. 835–842, Sep. 1952, doi: 10.1103/PhysRev.87.835.

[27] R. N. Hall, “Electron-hole recombination in germanium,” Jul. 15, 1952, *American Physical Society*. doi: 10.1103/PhysRev.87.387.

[28] K. V. Ravi, “Imperfections and impurities in semiconductor silicon,” 1981, *Wiley, New York*.

[29] J. D. Murphy, K. Bothe, R. Krain, V. V. Voronkov, and R. J. Falster, “Parameterisation of injection-dependent lifetime measurements in semiconductors in terms of Shockley-Read-Hall statistics: An application to oxide precipitates in silicon,” *J Appl Phys*, vol. 111, no. 11, p. 113709, Jun. 2012, doi: 10.1063/1.4725475.

[30] R. Gogolin and N. P. Harder, “Trapping behavior of Shockley-Read-Hall recombination centers in silicon solar cells,” *J Appl Phys*, vol. 114, no. 6, p. 34, Aug. 2013, doi: 10.1063/1.4817910/372722.

[31] K. R. McIntosh and L. E. Black, “On effective surface recombination parameters,” *J Appl Phys*, vol. 116, no. 1, Jul. 2014, doi: 10.1063/1.4886595/139167.

[32] R. S. Bonilla and P. R. Wilshaw, “On the c-Si/SiO2 interface recombination parameters from photo-conductance decay measurements,” *J Appl Phys*, vol. 121, no. 13, p. 135301, Apr. 2017, doi: 10.1063/1.4979722/976592.

[33] A. B. Sproul, “Dimensionless solution of the equation describing the effect of surface recombination on carrier decay in semiconductors,” *J Appl Phys*, vol. 76, no. 5, pp. 2851–2854, Sep. 1994, doi: 10.1063/1.357521.

[34] A. Cuevas, “The Recombination Parameter J0,” *Energy Procedia*, vol. 55, pp. 53–62, Jan. 2014, doi: 10.1016/J.EGYPRO.2014.08.073.

[35] D. E. KANE and R. M. SWANSON, “Measurement of the emitter saturation current by a contactless photoconductivity decay method,” pp. 578–583, 1985.

[36] B. Hammann *et al.*, “Quantifying Surface Recombination - Improvements in Determination and Simulation of the Surface Recombination Parameter J0s,” *IEEE J Photovolt*, vol. 13, no. 4, pp. 535–546, Jul. 2023, doi: 10.1109/JPHOTOV.2023.3265859.

[37] D. A. Neamen, “Semiconductor physics and devices,” 2011, *McGraw-Hill Higher Education ; McGraw-Hill [distributor], New York : London*.

[38] Peter. Würfel, “Physics of solar cells : from principles to new concepts,” p. 186, 2005.

[39] U. Wurfel, A. Cuevas, and P. Wurfel, “Charge carrier separation in solar cells,” *IEEE J Photovolt*, vol. 5, no. 1, pp. 461–469, Jan. 2015, doi: 10.1109/JPHOTOV.2014.2363550.

[40] B. Lipovšek, F. Smole, M. Topič, I. Humar, and A. R. Sinigoj, “Driving forces and charge-carrier separation in p-n junction solar cells,” *AIP Adv*, vol. 9, no. 5, p. 55026, May 2019, doi: 10.1063/1.5092948/1070438.

[41] A. M. Humada, M. Hojabri, S. Mekhilef, and H. M. Hamada, “Solar cell parameters extraction based on single and double-diode models: A review,” *Renewable and Sustainable Energy Reviews*, vol. 56, pp. 494–509, Apr. 2016, doi: 10.1016/J.RSER.2015.11.051.

[42] B. Vicari Stefani *et al.*, “Historical market projections and the future of silicon solar cells,” *Joule*, vol. 7, no. 12, pp. 2684–2699, Dec. 2023, doi: 10.1016/J.JOULE.2023.11.006/ATTACHMENT/61ED5B1A-138E-4233-B230-80643F34722B/MMC2.PDF.

[43] T. G. Allen, J. Bullock, X. Yang, A. Javey, and S. De Wolf, “Passivating contacts for crystalline silicon solar cells,” *Nat Energy*, vol. 4, no. 11, pp. 914–928, Nov. 2019, doi: 10.1038/s41560-019-0463-6.

[44] H. Li, K. Kim, B. Hallam, B. Hoex, S. Wenham, and M. Abbott, “POCl3 diffusion for industrial Si solar cell emitter formation,” *Frontiers in Energy 2017 11:1*, vol. 11, no. 1, pp. 42–51, Nov. 2016, doi: 10.1007/S11708-016-0433-7.

[45] B. Min *et al.*, “A Roadmap Toward 24% Efficient PERC Solar Cells in Industrial Mass Production,” *IEEE J Photovolt*, vol. 7, no. 6, pp. 1541–1550, Nov. 2017, doi: 10.1109/JPHOTOV.2017.2749007.

[46] Zhao Jianhua, Wang Aihua, and Green Martin A., “24·5% Efficiency silicon PERT cells on MCZ substrates and 24·7% efficiency PERL cells on FZ substrates,” 1999.

[47] J. Schmidt, R. Peibst, and R. Brendel, “Surface passivation of crystalline silicon solar cells: Present and future,” *Solar Energy Materials and Solar Cells*, vol. 187, pp. 39–54, Dec. 2018, doi: 10.1016/J.SOLMAT.2018.06.047.

[48] Q. Wang, W. Wu, N. Yuan, Y. Li, Y. Zhang, and J. Ding, “Influence of SiOx film thickness on electrical performance and efficiency of TOPCon solar cells,” *Solar Energy*

*Materials and Solar Cells*, vol. 208, p. 110423, May 2020, doi: 10.1016/J.SOLMAT.2020.110423.

[49] R. Peibst *et al.*, "Working principle of carrier selective poly-Si/c-Si junctions: Is tunnelling the whole story?," *Solar Energy Materials and Solar Cells*, vol. 158, pp. 60–67, Dec. 2016, doi: 10.1016/J.SOLMAT.2016.05.045.

[50] R. Peibst *et al.*, "Towards 28 %-efficient Si single-junction solar cells with better passivating POLO junctions and photonic crystals," *Solar Energy Materials and Solar Cells*, vol. 238, p. 111560, May 2022, doi: 10.1016/J.SOLMAT.2021.111560.

[51] S. W. Glunz *et al.*, "Silicon-based passivating contacts: The TOPCon route," *Progress in Photovoltaics: Research and Applications*, 2021, doi: 10.1002/PIP.3522.

[52] S. Deng *et al.*, "Mitigating parasitic absorption in Poly-Si contacts for TOPCon solar cells: A comprehensive review," *Solar Energy Materials and Solar Cells*, vol. 267, p. 112704, Apr. 2024, doi: 10.1016/J.SOLMAT.2024.112704.

[53] P. Hamer, B. Hallam, M. Abbott, and S. Wenham, "Accelerated formation of the boron–oxygen complex in p-type Czochralski silicon," *physica status solidi (RRL) – Rapid Research Letters*, vol. 9, no. 5, pp. 297–300, May 2015, doi: 10.1002/PSSR.201510064.

[54] "JinkoSolar's High-efficiency N-Type Monocrystalline Silicon Solar Cell Sets Our New Record with Maximum Conversion Efficiency of 26.4%," JinkoSolar. Accessed: Mar. 02, 2025. [Online]. Available: https://www.jinkosolar.com/en/site/newsdetail/1827

[55] "Trina Solar Sets 24th World Record with 24.5% Efficient 210 PERC Cell | Trinasolar." Accessed: Mar. 02, 2025. [Online]. Available: https://www.trinasolar.com/us/resources/newsroom/210-perc-cell-sets-world-record-24.5%25-efficiency

[56] K. H. Kim *et al.*, "Record high efficiency of screen-printed silicon aluminum back surface field solar cell: 20.29%," *Jpn J Appl Phys*, vol. 56, no. 8, p. 08MB25, Aug. 2017, doi: 10.7567/JJAP.56.08MB25/XML.

[57] A. Richter *et al.*, "Design rules for high-efficiency both-sides-contacted silicon solar cells with balanced charge carrier transport and recombination losses," *Nature Energy 2021 6:4*, vol. 6, no. 4, pp. 429–438, Apr. 2021, doi: 10.1038/s41560-021-00805-w.

[58] P. Procel-Moya, Y. Zhao, and O. Isabella, "Unlocking the potential of carrier-selective contacts: Key insights for designing c-Si solar cells with efficiency beyond 28 %," *Solar*

*Energy Materials and Solar Cells*, vol. 285, p. 113504, Jun. 2025, doi: 10.1016/J.SOLMAT.2025.113504.

[59] M. F. Abdullah *et al.*, "Research and development efforts on texturization to reduce the optical losses at front surface of silicon solar cell," *Renewable and Sustainable Energy Reviews*, vol. 66, pp. 380–398, Dec. 2016, doi: 10.1016/J.RSER.2016.07.065.

[60] L. Wang, Y. Tang, S. Zhang, F. Wang, and J. Wang, "Energy yield analysis of different bifacial PV (photovoltaic) technologies: TOPCon, HJT, PERC in Hainan," *Solar Energy*, vol. 238, pp. 258–263, May 2022, doi: 10.1016/J.SOLENER.2022.03.038.

[61] A. Ebong and N. Chen, "Metallization of crystalline silicon solar cells: A review," *2012 9th International Conference on High Capacity Optical Networks and Enabling Technologies, HONET 2012*, pp. 102–109, 2012, doi: 10.1109/HONET.2012.6421444.

[62] A. Fell *et al.*, "Modeling parasitic absorption in silicon solar cells with a near-surface absorption parameter," *Solar Energy Materials and Solar Cells*, vol. 236, p. 111534, Mar. 2022, doi: 10.1016/J.SOLMAT.2021.111534.

[63] J. Bullock *et al.*, "Efficient silicon solar cells with dopant-free asymmetric heterocontacts," *Nature Energy 2016 1:3*, vol. 1, no. 3, pp. 1–7, Jan. 2016, doi: 10.1038/nenergy.2015.31.

[64] T. Niewelt, J. Schön, W. Warta, … S. G.-I. J. of, and undefined 2016, "Degradation of crystalline silicon due to boron–oxygen defects," *ieeexplore.ieee.orgT Niewelt, J Schön, W Warta, SW Glunz, MC SchubertIEEE Journal of Photovoltaics, 2016•ieeexplore.ieee.org*, Accessed: Jan. 09, 2025. [Online]. Available: https://ieeexplore.ieee.org/abstract/document/7637039/

[65] J. Lindroos and H. Savin, "Review of light-induced degradation in crystalline silicon solar cells," *Solar Energy Materials and Solar Cells*, vol. 147, pp. 115–126, Apr. 2016, doi: 10.1016/J.SOLMAT.2015.11.047.

[66] Z. Y. Yeo, Z. P. Ling, J. W. Ho, Q. X. Lim, Y. H. So, and S. Wang, "Status review and future perspectives on mitigating light-induced degradation on silicon-based solar cells," *Renewable and Sustainable Energy Reviews*, vol. 159, p. 112223, May 2022, doi: 10.1016/J.RSER.2022.112223.

[67] J. Lindroos and H. Savin, “Review of light-induced degradation in crystalline silicon solar cells,” *Solar Energy Materials and Solar Cells*, vol. 147, pp. 115–126, Apr. 2016, doi: 10.1016/J.SOLMAT.2015.11.047.

[68] J. Schmidt and K. Bothe, “Structure and transformation of the metastable boron- and oxygen-related defect center in crystalline silicon,” *Phys Rev B*, vol. 69, no. 2, p. 024107, Jan. 2004, doi: 10.1103/PhysRevB.69.024107.

[69] A. Herguth, G. Schubert, M. Kaes, and G. Hahn, “A new approach to prevent the negative impact of the metastable defect in boron doped CZ silicon solar cells,” *Conference Record of the 2006 IEEE 4th World Conference on Photovoltaic Energy Conversion, WCPEC-4*, vol. 1, pp. 940–943, 2006, doi: 10.1109/WCPEC.2006.279611.

[70] T. Niewelt, J. Schon, W. Warta, S. W. Glunz, and M. C. Schubert, “Degradation of Crystalline Silicon Due to Boron-Oxygen Defects,” *IEEE J Photovolt*, vol. 7, no. 1, pp. 383–398, Jan. 2017, doi: 10.1109/JPHOTOV.2016.2614119.

[71] D. Chen *et al.*, “Progress in the understanding of light- and elevated temperature-induced degradation in silicon solar cells: A review,” *Progress in Photovoltaics: Research and Applications*, vol. 29, no. 11, pp. 1180–1201, Nov. 2021, doi: 10.1002/PIP.3362.

[72] S. W. Glunz, S. Rein, J. Knobloch, W. Wettling, and T. Abe, “Comparison of Boron-and Gallium-doped p-Type Czochralski Silicon for Photovoltaic Application”, doi: 10.1002/(SICI)1099-159X(199911/12)7:6.

[73] A. Richter, J. Benick, F. Feldmann, … A. F.-36th E. P., and undefined 2019, “Both sides contacted silicon solar cells: options for approaching 26% efficiency,” *ise.fraunhofer.de*, Accessed: Jan. 15, 2025. [Online]. Available: https://www.ise.fraunhofer.de/content/dam/ise/de/documents/publications/conference-paper/36-eupvsec-2019/Richter_2BP13.pdf

[74] R. S. Bonilla, B. Hoex, P. Hamer, and P. R. Wilshaw, “Dielectric surface passivation for silicon solar cells: A review,” *Physica Status Solidi (A) Applications and Materials Science*, vol. 214, no. 7, Jul. 2017, doi: 10.1002/PSSA.201700293.

[75] J. Schmidt, R. Peibst, and R. Brendel, “Surface passivation of crystalline silicon solar cells: Present and future,” *Solar Energy Materials and Solar Cells*, vol. 187, pp. 39–54, Dec. 2018, doi: 10.1016/J.SOLMAT.2018.06.047.

[76] R. S. Bonilla and P. R. Wilshaw, “A technique for field effect surface passivation for silicon solar cells,” *Appl Phys Lett*, vol. 104, no. 23, p. 58, Jun. 2014, doi: 10.1063/1.4882161/131009.

[77] A. G. Aberle, S. Glunz, and W. Warta, “Field effect passivation of high efficiency silicon solar cells,” *Solar Energy Materials and Solar Cells*, vol. 29, no. 2, pp. 175–182, Mar. 1993, doi: 10.1016/0927-0248(93)90075-E.

[78] D. Herrmann *et al.*, “Microstructure beneath screen-printed silver contacts and its correlation to metallization-induced recombination parameters,” *Solar Energy Materials and Solar Cells*, vol. 230, Sep. 2021, doi: 10.1016/J.SOLMAT.2021.111182.

[79] J. D. Fields *et al.*, “The formation mechanism for printed silver-contacts for silicon solar cells,” *Nature Communications 2016 7:1*, vol. 7, no. 1, pp. 1–7, Apr. 2016, doi: 10.1038/ncomms11143.

[80] T. Fellmeth, A. Born, A. Kimmerle, F. Clement, D. Biro, and R. Preu, “Recombination at Metal-Emitter Interfaces of Front Contact Technologies for Highly Efficient Silicon Solar Cells,” *Energy Procedia*, vol. 8, pp. 115–121, Jan. 2011, doi: 10.1016/J.EGYPRO.2011.06.111.

[81] V. Shanmugam, T. Mueller, A. G. Aberle, and J. Wong, “Determination of metal contact recombination parameters for silicon wafer solar cells by photoluminescence imaging,” *Solar Energy*, vol. 118, pp. 20–27, Aug. 2015, doi: 10.1016/J.SOLENER.2015.05.010.

[82] M. Li, J. Wong, N. Chen, A. G. Aberle, and R. Stangl, “Determination of metallization-induced recombination losses of screen-printed silicon solar cell contacts and their dependence on the doping profile,” *IEEE J Photovolt*, vol. 8, no. 6, pp. 1470–1477, Nov. 2018, doi: 10.1109/JPHOTOV.2018.2866177.

[83] H. E. Çiftpinar *et al.*, “Study of screen printed metallization for polysilicon based passivating contacts,” *Energy Procedia*, vol. 124, pp. 851–861, Sep. 2017, doi: 10.1016/J.EGYPRO.2017.09.242.

[84] M. K. Stodolny *et al.*, “Material properties of LPCVD processed n-type polysilicon passivating contacts and its application in PERPoly industrial bifacial solar cells,” *Energy Procedia*, vol. 124, pp. 635–642, Sep. 2017, doi: 10.1016/J.EGYPRO.2017.09.250.

[85] N. Nandakumar *et al.*, “Approaching 23% with large-area monoPoly cells using screen-printed and fired rear passivating contacts fabricated by inline PECVD,” *Progress in Photovoltaics: Research and Applications*, vol. 27, no. 2, pp. 107–112, Feb. 2019, doi: 10.1002/PIP.3097.

[86] P. Padhamnath *et al.*, “Development of thin polysilicon layers for application in monoPoly$^{TM}$ cells with screen-printed and fired metallization,” *Solar Energy Materials and Solar Cells*, vol. 207, p. 110358, Apr. 2020, doi: 10.1016/J.SOLMAT.2019.110358.

[87] G. Hahn, D. Sontag, S. Seren, and A. Schönecker, “Hydrogenation of multicrystalline silicon : the story continues,” in *19th European Photovoltaic Solar Energy Conference*, 2004. Accessed: May 26, 2020. [Online]. Available: http://kops.uni-konstanz.de/handle/123456789/32203

[88] M. I. Bertoni *et al.*, “Influence of defect type on hydrogen passivation efficacy in multicrystalline silicon solar cells,” *Progress in Photovoltaics: Research and Applications*, vol. 19, no. 2, pp. 187–191, Mar. 2011, doi: 10.1002/pip.1008.

[89] T. N. Truong *et al.*, “Hydrogenation Mechanisms of Poly-Si/SiOx Passivating Contacts by Different Capping Layers,” *Solar RRL*, vol. 4, no. 3, Mar. 2020, doi: 10.1002/SOLR.201900476.

[90] B. Sopori *et al.*, “A Comprehensive Model of Hydrogen Transport into a Solar Cell During Silicon Nitride Processing for Fire-Through Metallization,” 2005.

[91] B. Sopori *et al.*, “A Comprehensive Model of Hydrogen Transport into a Solar Cell During Silicon Nitride Processing for Fire-Through Metallization,” 2005. Accessed: May 26, 2020. [Online]. Available: http://www.osti.gov/bridge

[92] B. Hallam, C. Chan, M. Abbott, and S. Wenham, “Hydrogen passivation of defect-rich n-type Czochralski silicon and oxygen precipitates,” *Solar Energy Materials and Solar Cells*, vol. 141, pp. 125–131, Oct. 2015, doi: 10.1016/J.SOLMAT.2015.05.009.

[93] M. Spiegel Konstanz, “MICROWAVE INDUCED REMOTE HYDROGEN PLASMA (MIRHP) PASSIVATION OF MULTICRYSTALLINE SILICON SOLAR CELLS,” 1998.

[94] L. Ammor and S. Martinuzzi, “Influence of hydrogen implantation on properties of n+p polycrystalline silicon solar cells,” *Solid State Electronics*, vol. 29, no. 1, pp. 1–6, Jan. 1986, doi: 10.1016/0038-1101(86)90190-5.

[95] R. Sharma, A. P. Chong, J. B. Li, A. G. Aberle, and Y. Huang, “Role of post-metallization anneal sequence and forming gas anneal to mitigate light and elevated temperature induced degradation of multicrystalline silicon solar cells,” *Solar Energy Materials and Solar Cells*, vol. 195, pp. 160–167, Jun. 2019, doi: 10.1016/j.solmat.2019.02.036.

[96] P. Sana, A. Rohatgi, J. P. Kalejs, and R. O. Bell, “Gettering and hydrogen passivation of edge-defined film-fed grown multicrystalline silicon solar cells by Al diffusion and forming gas anneal,” *Appl Phys Lett*, vol. 64, no. 1, pp. 97–99, Jan. 1994, doi: 10.1063/1.110880.

[97] B. J. Hallam *et al.*, “Overcoming the Challenges of Hydrogenation in Silicon Solar Cells*,” *Aust J Chem*, vol. 71, no. 10, pp. 743–752, Sep. 2018, doi: 10.1071/CH18271.

[98] L. Song, Z. Hu, D. Lin, D. Yang, and X. Yu, “Progress of hydrogenation engineering in crystalline silicon solar cells: a review,” *J Phys D Appl Phys*, vol. 55, no. 45, p. 453002, Sep. 2022, doi: 10.1088/1361-6463/AC9066.

[99] M. Kim, D. Chen, M. Abbott, S. Wenham, and B. Hallam, “Role of hydrogen: Formation and passivation of meta-stable defects due to hydrogen in silicon,” *AIP Conf Proc*, vol. 1999, no. 1, Aug. 2018, doi: 10.1063/1.5049329/727724.

[100] B. J. Hallam, P. G. Hamer, A. M. Ciesla née Wenham, C. E. Chan, B. Vicari Stefani, and S. Wenham, “Development of advanced hydrogenation processes for silicon solar cells via an improved understanding of the behaviour of hydrogen in silicon,” *Progress in Photovoltaics: Research and Applications*, vol. 28, no. 12, pp. 1217–1238, Dec. 2020, doi: 10.1002/PIP.3240.

[101] J. I. Polzin, B. Hammann, T. Niewelt, W. Kwapil, M. Hermle, and F. Feldmann, “Thermal activation of hydrogen for defect passivation in poly-Si based passivating contacts,” *Solar Energy Materials and Solar Cells*, vol. 230, p. 111267, Sep. 2021, doi: 10.1016/J.SOLMAT.2021.111267.

[102] J. P. Kalejs and S. Rajendran, “Model for diffusion and trapping of hydrogen in crystalline silicon,” *Appl Phys Lett*, vol. 55, no. 26, pp. 2763–2765, Dec. 1989, doi: 10.1063/1.101947.

[103] A. Van Wieringen and N. Warmoltz, “On the permeation of hydrogen and helium in single crystal silicon and germanium at elevated temperatures,” *Physica*, vol. 22, no. 6–12, pp. 849–865, Jan. 1956, doi: 10.1016/S0031-8914(56)90039-8.

[104] W. B. Jackson, N. M. Johnson, C. C. Tsai, I. -W. W. Wu, A. Chiang, and D. Smith, "Hydrogen diffusion in polycrystalline silicon thin films," *Appl Phys Lett*, vol. 61, no. 14, doi: 10.1063/1.108446.

[105] N. M. Johnson, D. K. Biegelsen, and M. D. Moyer, "Deuterium passivation of grain-boundary dangling bonds in silicon thin films," *Appl Phys Lett*, vol. 40, no. 10, pp. 882–884, May 1982, doi: 10.1063/1.92934.

[106] C. Dubé, J. I. Hanoka, and D. B. Sandstrom, "Hydrogen diffusion along passivated grain boundaries in silicon ribbon," *Appl Phys Lett*, vol. 44, no. 4, pp. 425–427, Feb. 1984, doi: 10.1063/1.94797.

[107] B. L. Sopori, K. Jones, and X. J. Deng, "Observation of enhanced hydrogen diffusion in solar cell silicon," *Appl Phys Lett*, vol. 61, no. 21, pp. 2560–2562, Nov. 1992, doi: 10.1063/1.108126.

[108] C. Dubé and J. I. Hanoka, "Hydrogen passivation of dislocations in silicon," *Appl Phys Lett*, vol. 45, no. 10, pp. 1135–1137, Nov. 1984, doi: 10.1063/1.95045.

[109] S. J. Pearton, J. W. Corbett, and T. S. Shi, "Hydrogen in crystalline semiconductors," *Applied Physics A Solids and Surfaces*, vol. 43, no. 3, pp. 153–195, Jul. 1987, doi: 10.1007/BF00615975.

[110] C. E. Dubé and J. I. Hanoka, "Hydrogen passivation of multicrystalline silicon," 2005.

[111] A. Fedotov, A. Mazanik, and A. Ulyashin, "Electrical activity of grain boundaries in silicon bicrystals and its modification by hydrogen plasma treatment," in *Solar Energy Materials and Solar Cells*, North-Holland, Apr. 2002, pp. 589–595. doi: 10.1016/S0927-0248(01)00208-2.

[112] J. Chen, D. Yang, Z. Xi, and T. Sekiguchi, "Electron-beam-induced current study of hydrogen passivation on grain boundaries in multicrystalline silicon: Influence of GB character and impurity contamination," *Physica B Condens Matter*, vol. 364, no. 1–4, pp. 162–169, Jul. 2005, doi: 10.1016/j.physb.2005.04.008.

[113] M. I. Bertoni *et al.*, "Influence of defect type on hydrogen passivation efficacy in multicrystalline silicon solar cells," *Progress in Photovoltaics: Research and Applications*, vol. 19, no. 2, pp. 187–191, Mar. 2011, doi: 10.1002/pip.1008.

[114] K. Adamczyk *et al.*, “Recombination Strength of Dislocations in High-Performance Multicrystalline/Quasi-Mono Hybrid Wafers During Solar Cell Processing,” *physica status solidi (a)*, vol. 215, no. 2, p. 1700493, Jan. 2018, doi: 10.1002/pssa.201700493.

[115] M. Schnabel *et al.*, “Hydrogen passivation of poly-Si/SiOx contacts for Si solar cells using Al2O3 studied with deuterium,” *Appl Phys Lett*, vol. 112, no. 20, p. 203901, May 2018, doi: 10.1063/1.5031118.

[116] M. Winter, S. Bordihn, R. Peibst, R. Brendel, and J. Schmidt, “Degradation and Regeneration of n+-Doped Poly-Si Surface Passivation on p-Type and n-Type Cz-Si under Illumination and Dark Annealing,” *IEEE J Photovolt*, vol. 10, no. 2, pp. 423–430, Mar. 2020, doi: 10.1109/JPHOTOV.2020.2964987.

[117] J. I. Polzin, B. Hammann, T. Niewelt, W. Kwapil, M. Hermle, and F. Feldmann, “Thermal activation of hydrogen for defect passivation in poly-Si based passivating contacts,” *Solar Energy Materials and Solar Cells*, vol. 230, p. 111267, Sep. 2021, doi: 10.1016/J.SOLMAT.2021.111267.

[118] D. Kang, H. C. Sio, D. Yan, J. Stuckelberger, X. Zhang, and D. Macdonald, “Firing stability of phosphorus-doped polysilicon passivating contacts: Factors affecting the degradation behavior,” *Solar Energy Materials and Solar Cells*, vol. 234, p. 111407, Jan. 2022, doi: 10.1016/J.SOLMAT.2021.111407.

[119] D. Chen *et al.*, “Investigating the degradation behaviours of n+-doped Poly-Si passivation layers: An outlook on long-term stability and accelerated recovery,” *Solar Energy Materials and Solar Cells*, vol. 236, p. 111491, Mar. 2022, doi: 10.1016/J.SOLMAT.2021.111491.

[120] D. Kang *et al.*, “Long-term stability study of the passivation quality of polysilicon-based passivation layers for silicon solar cells,” *Solar Energy Materials and Solar Cells*, vol. 215, p. 110691, Sep. 2020, doi: 10.1016/J.SOLMAT.2020.110691.

[121] D. Kang *et al.*, “Optimum Hydrogen Injection in Phosphorus-Doped Polysilicon Passivating Contacts,” vol. 13, no. 46, pp. 55164–55171, Nov. 2021, Accessed: Feb. 04, 2022. [Online]. Available: https://pubs.acs.org/doi/abs/10.1021/acsami.1c17342

[122] C. Hollemann *et al.*, “Changes in hydrogen concentration and defect state density at the poly-Si/SiOx/c-Si interface due to firing,” *Solar Energy Materials and Solar Cells*, vol. 231, p. 111297, Oct. 2021, doi: 10.1016/J.SOLMAT.2021.111297.

[123] B. Hammann, F. Schindler, J. Schön, W. Kwapil, M. C. Schubert, and S. W. Glunz, "Review on hydrogen in silicon solar cells: From its origin to its detrimental effects," *Solar Energy Materials and Solar Cells*, vol. 282, p. 113432, Apr. 2025, doi: 10.1016/J.SOLMAT.2025.113432.

[124] K. R. McIntosh and L. E. Black, "On effective surface recombination parameters," *J Appl Phys*, vol. 116, no. 1, Jul. 2014, doi: 10.1063/1.4886595/139167.

[125] A. Edler, V. D. Mihailetchi, L. J. Koduvelikulathu, C. Comparotto, R. Kopecek, and R. Harney, "Metallization–induced recombination losses of bifacial silicon solar cells," *Progress in Photovoltaics: Research and Applications*, vol. 23, no. 5, pp. 620–627, May 2015, doi: 10.1002/PIP.2479.

[126] M. Li, J. Wong, N. Chen, A. G. Aberle, and R. Stangl, "Determination of metallization-induced recombination losses of screen-printed silicon solar cell contacts and their dependence on the doping profile," *IEEE J Photovolt*, vol. 8, no. 6, pp. 1470–1477, Nov. 2018, doi: 10.1109/JPHOTOV.2018.2866177.

[127] T. Trupke, B. Mitchell, J. W. Weber, W. McMillan, R. A. Bardos, and R. Kroeze, "Photoluminescence Imaging for Photovoltaic Applications," *Energy Procedia*, vol. 15, pp. 135–146, Jan. 2012, doi: 10.1016/J.EGYPRO.2012.02.016.

[128] M. Fırat *et al.*, "Industrial metallization of fired passivating contacts for n-type tunnel oxide passivated contact (n-TOPCon) solar cells," *Solar Energy Materials and Solar Cells*, vol. 240, p. 111692, Jun. 2022, doi: 10.1016/J.SOLMAT.2022.111692.

[129] D. Herrmann, S. Lohmuller, H. Hoffler, A. Fell, A. A. Brand, and A. Wolf, "Numerical Simulations of Photoluminescence for the Precise Determination of Emitter Contact Recombination Parameters," *IEEE J Photovolt*, vol. 9, no. 6, pp. 1759–1767, Nov. 2019, doi: 10.1109/JPHOTOV.2019.2938400.

[130] A. Fell, D. Walter, S. Kluska, E. Franklin, and K. Weber, "Determination of Injection Dependent Recombination Properties of Locally Processed Surface Regions," *Energy Procedia*, vol. 38, pp. 22–31, Jan. 2013, doi: 10.1016/J.EGYPRO.2013.07.245.

[131] D. Hermann, "Characterization of Metallization-Induced Recombination Losses of Screen-Printed Silicon Solar Cells," 2021.

[132] D. Herrmann *et al.*, “Spatially Resolved Determination of Metallization-Induced Recombination Losses Using Photoluminescence Imaging,” *IEEE J Photovolt*, vol. 11, no. 1, pp. 174–184, Jan. 2021, doi: 10.1109/JPHOTOV.2020.3038336.

[133] M. Li *et al.*, “A Comprehensive Evaluation of Contact Recombination and Contact Resistivity Losses in Industrial Silicon Solar Cells,” *IEEE J Photovolt*, vol. 10, no. 5, pp. 1277–1282, Sep. 2020, doi: 10.1109/JPHOTOV.2020.3003792.

[134] C. Leon, P. Saint-Cast, A. Fell, J. M. Greulich, and S. Rein, “On the Robustness of the Determination of Metal-Induced Recombination from Photoluminescence Images on Solar Cells,” *Solar RRL*, vol. 7, no. 22, p. 2300539, Nov. 2023, doi: 10.1002/SOLR.202300539.

[135] P. Saint-Cast, D. Herrmann, and H. Hoffler, “Information on Recombination under Front Fingers Based on Fourier Analysis of Photoluminescence Images,” *IEEE J Photovolt*, vol. 10, no. 2, pp. 554–559, Mar. 2020, doi: 10.1109/JPHOTOV.2019.2955072.

[136] P. A. Basore, “PC3D [Online] http:// www.pc3d.info.”

[137] A. Fell, J. Schön, M. C. Schubert, and S. W. Glunz, “The concept of skins for silicon solar cell modeling,” *Solar Energy Materials and Solar Cells*, vol. 173, pp. 128–133, Dec. 2017, doi: 10.1016/J.SOLMAT.2017.05.012.

[138] P. Saint-Cast, D. Herrmann, and H. Hoffler, “Information on Recombination under Front Fingers Based on Fourier Analysis of Photoluminescence Images,” *IEEE J Photovolt*, vol. 10, no. 2, pp. 554–559, Mar. 2020, doi: 10.1109/JPHOTOV.2019.2955072.

[139] J. Rand, P. B.-T. C. R. of the Twenty, and undefined 1991, “Light-trapping silicon solar cells-experimental results and analysis,” *ieeexplore.ieee.orgJA Rand, PA BasoreThe Conference Record of the Twenty-Second IEEE Photovoltaic, 1991•ieeexplore.ieee.org*, Accessed: May 01, 2025. [Online]. Available: https://ieeexplore.ieee.org/abstract/document/169207/

[140] A. Fell, T. Niewelt, B. Steinhauser, F. D. Heinz, M. C. Schubert, and S. W. Glunz, “Radiative recombination in silicon photovoltaics: Modeling the influence of charge carrier densities and photon recycling,” *Solar Energy Materials and Solar Cells*, vol. 230, p. 111198, Sep. 2021, doi: 10.1016/J.SOLMAT.2021.111198.

[141] A. Fell *et al.*, “Modeling parasitic absorption in silicon solar cells with a near-surface absorption parameter,” *Solar Energy Materials and Solar Cells*, vol. 236, p. 111534, Mar. 2022, doi: 10.1016/J.SOLMAT.2021.111534.

[142] P. A. Basore, “Multidimensional Fourier-Series Solution of the Quasi-Neutral Drift-Diffusion Equations,” *IEEE J Photovolt*, vol. 10, no. 3, pp. 905–911, May 2020, doi: 10.1109/JPHOTOV.2020.2966831.

[143] A. Fell, “A free and fast three-dimensional/two-dimensional solar cell simulator featuring conductive boundary and quasi-neutrality approximations,” *IEEE Trans Electron Devices*, vol. 60, no. 2, pp. 733–738, 2013, doi: 10.1109/TED.2012.2231415.

[144] D. Chen *et al.*, “24.58% total area efficiency of screen-printed, large area industrial silicon solar cells with the tunnel oxide passivated contacts (i-TOPCon) design,” *Solar Energy Materials and Solar Cells*, vol. 206, p. 110258, Mar. 2020, doi: 10.1016/j.solmat.2019.110258.

[145] C. Schinke, D. Hinken, J. Schmidt, K. Bothe, and R. Brendel, “Modeling the spectral luminescence emission of silicon solar cells and wafers,” *IEEE J Photovolt*, vol. 3, no. 3, pp. 1038–1052, 2013, doi: 10.1109/JPHOTOV.2013.2263985.

[146] N. P. Harder, R. Gogolin, and R. Brendel, “Trapping-related recombination of charge carriers in silicon,” *Appl Phys Lett*, vol. 97, no. 11, Sep. 2010, doi: 10.1063/1.3490240.

[147] S. Steingrube, “Recombination models for defects in silicon solar cells,” 2011, Accessed: Oct. 13, 2025. [Online]. Available: https://repo.uni-hannover.de/bitstream/handle/123456789/7816/663963133.pdf?sequence=1

[148] Z. ; Liu *et al.*, “Performance of Large Area n-TOPCon Solar Cells with Selective Poly-Si Based Passivating Contacts Prepared by PECVD Method,” *Materials 2024, Vol. 17, Page 849*, vol. 17, no. 4, p. 849, Feb. 2024, doi: 10.3390/MA17040849.

[149] M. Chu *et al.*, “Review of the silicon oxide and polysilicon layer as the passivated contacts for TOPCon solar cells,” *koreascience.krM Chu, MQ Khokhar, H Yousuf, X Fan, S Han, Y Kim, SK Dhungel, J YiJournal of the Korean Institute of Electrical and Electronic Material, 2023•koreascience.kr*, doi: 10.4313/JKEM.2023.36.3.4.

[150] M. Fırat *et al.*, “Industrial metallization of fired passivating contacts for n-type tunnel oxide passivated contact (n-TOPCon) solar cells,” *Solar Energy Materials and Solar Cells*, vol. 240, p. 111692, Jun. 2022, doi: 10.1016/J.SOLMAT.2022.111692.

[151] S. W. Glunz *et al.*, “Silicon-based passivating contacts: The TOPCon route,” *Progress in Photovoltaics: Research and Applications*, vol. 31, no. 4, pp. 341–359, Apr. 2021, doi: 10.1002/PIP.3522.

[152] S. W. Glunz, A. Mette, M. Alemán Martínez, P. L. Richter, A. Filipovic, and G. Willeke, “New concepts for the front side metallization of silicon solar cells,” 2006, doi: 10.24406/PUBLICA-FHG-353306.

[153] Z. bin Liu *et al.*, “Effect of firing process on electrical properties and efficiency of n-TOPCon solar cells,” *Solar Energy*, vol. 267, p. 112205, Jan. 2024, doi: 10.1016/J.SOLENER.2023.112205.

[154] B. Uygun *et al.*, “Hydrogen thermal activation of defects enabling firing stable Poly-Si based passivating contacts for TOPCon solar cells,” 2024, doi: 10.1016/j.solener.2024.112838.

[155] P. Padhamnath *et al.*, “Metal contact recombination in monoPoly$^{TM}$ solar cells with screen-printed & fire-through contacts,” *Solar Energy Materials and Solar Cells*, vol. 192, pp. 109–116, Apr. 2019, doi: 10.1016/J.SOLMAT.2018.12.026.

[156] P. Padhamnath *et al.*, “Progress in screen-printed metallization of industrial solar cells with SiOx/poly-Si passivating contacts,” *Solar Energy Materials and Solar Cells*, vol. 218, p. 110751, Dec. 2020, doi: 10.1016/J.SOLMAT.2020.110751.

[157] M. Lu *et al.*, “Screen-Printable Contacts for Industrial N-TOPCon Crystalline Silicon Solar Cells,” *IEEE J Photovolt*, vol. 12, no. 2, pp. 469–473, Mar. 2022, doi: 10.1109/JPHOTOV.2021.3138248.

[158] J. M. Greulich, C. Leon, S. Mack, D. Ourinson, J. D. Huyeng, and S. Rein, “Microstructure Analysis of Current-Fired Contacts on TOPCon Layers,” *Solar RRL*, p. 202500197, 2025, doi: 10.1002/SOLR.202500197;PAGE:STRING:ARTICLE/CHAPTER.

[159] M. Stöhr, J. Aprojanz, R. Brendel, and T. Dullweber, “Firing-Stable PECVD SiO xN y/n-Poly-Si Surface Passivation for Silicon Solar Cells,” *ACS Appl Energy Mater*, vol. 4, no. 5, pp. 4646–4653, May 2021, doi: 10.1021/ACSAEM.1C00265/ASSET/IMAGES/LARGE/AE1C00265_0006.JPEG.

[160] B. Kafle, B. S. Goraya, S. Mack, F. Feldmann, S. Nold, and J. Rentsch, “TOPCon – Technology options for cost efficient industrial manufacturing,” *Solar Energy Materials and Solar Cells*, vol. 227, p. 111100, Aug. 2021, doi: 10.1016/J.SOLMAT.2021.111100.

[161] F. Feldmann, M. Nicolai, R. Müller, C. Reichel, and M. Hermle, “Optical and electrical characterization of poly-Si/SiOx contacts and their implications on solar cell design,” *Energy Procedia*, vol. 124, pp. 31–37, Sep. 2017, doi: 10.1016/J.EGYPRO.2017.09.336.

[162] H. E. Çiftpinar *et al.*, “Study of screen printed metallization for polysilicon based passivating contacts,” *Energy Procedia*, vol. 124, pp. 851–861, Sep. 2017, doi: 10.1016/J.EGYPRO.2017.09.242.

[163] P. Padhamnath *et al.*, “Metal contact recombination in monoPoly$^{TM}$ solar cells with screen-printed & fire-through contacts,” *Solar Energy Materials and Solar Cells*, vol. 192, pp. 109–116, Apr. 2019, doi: 10.1016/J.SOLMAT.2018.12.026.

[164] M. K. Stodolny *et al.*, “Material properties of LPCVD processed n-type polysilicon passivating contacts and its application in PERPoly industrial bifacial solar cells,” *Energy Procedia*, vol. 124, pp. 635–642, Sep. 2017, doi: 10.1016/J.EGYPRO.2017.09.250.

[165] J. Yu *et al.*, “Enhancing poly-Si contact through a highly conductive and ultra-thin TiN layer for high-efficiency passivating contact silicon solar cells,” *Solar Energy Materials and Solar Cells*, vol. 260, p. 112491, Sep. 2023, doi: 10.1016/J.SOLMAT.2023.112491.

[166] A. B. Morales-Vilches *et al.*, “ZnO:Al/a-SiOx front contact for polycrystalline-silicon-on-oxide (POLO) solar cells,” *AIP Conf Proc*, vol. 1999, no. 1, p. 40016, Aug. 2018, doi: 10.1063/1.5049279/727850.

[167] D. Adachi, T. Terashita, T. Uto, J. L. Hernández, and K. Yamamoto, “Effects of SiOx barrier layer prepared by plasma-enhanced chemical vapor deposition on improvement of long-term reliability and production cost for Cu-plated amorphous Si/crystalline Si heterojunction solar cells,” *Solar Energy Materials and Solar Cells*, vol. 163, pp. 204–209, Apr. 2017, doi: 10.1016/J.SOLMAT.2016.12.029.

[168] K. Madani, A. Rohatgi, B. Rounsaville, M. G. Kang, H. E. Song, and Y. W. Ok, “Enhanced Stability of Exposed PECVD Grown Thin n+Poly-Si/SiOxPassivating Contacts with Al2O3Capping Layer during High Temperature Firing,” *IEEE J Photovolt*, vol. 11, no. 2, pp. 268–272, Mar. 2021, doi: 10.1109/JPHOTOV.2020.3043259.

[169] R. A. Sinton, A. Cuevas, J. B. Vac Sci Technol, and A. Phys Lett, “Contactless determination of current–voltage characteristics and minority-carrier lifetimes in semiconductors from quasi-steady-state photoconductance data,” *Appl Phys Lett*, vol. 69, no. 17, pp. 2510–2512, Oct. 1996, doi: 10.1063/1.117723.

[170] “Trinasolar sets 27th world record with n-type i-TOPCon cell achieving 25.9% efficiency | Trina Solar.” Accessed: Jan. 08, 2025. [Online]. Available: https://static.trinasolar.com/eu-en/resources/newsroom/eu-trinasolar-sets-27th-world-record-n-type-i-topcon-cell-achieving-259

[171] A. Kimmerle, J. Greulich, and A. Wolf, “Carrier-diffusion corrected J0-analysis of charge carrier lifetime measurements for increased consistency,” *Solar Energy Materials and Solar Cells*, vol. 142, pp. 116–122, Nov. 2015, doi: 10.1016/J.SOLMAT.2015.06.043.

[172] H. Steinkemper, M. Rauer, P. Altermatt, F. D. Heinz, C. Schmiga, and M. Hermle, “Adapted parameterization of incomplete ionization in aluminum-doped silicon and impact on numerical device simulation,” *J Appl Phys*, vol. 117, no. 7, Feb. 2015, doi: 10.1063/1.4913255/282455.

[173] D. Yan, A. Cuevas, J. Bullock, Y. Wan, and C. Samundsett, “Phosphorus-diffused polysilicon contacts for solar cells,” *Solar Energy Materials and Solar Cells*, vol. 142, pp. 75–82, Nov. 2015, doi: 10.1016/J.SOLMAT.2015.06.001.

[174] H. MacKel and P. P. Altermatt, “Current transport through lead-borosilicate interfacial glass layers at the screen-printed silver-silicon front contact,” *IEEE J Photovolt*, vol. 5, no. 4, pp. 1034–1046, Jul. 2015, doi: 10.1109/JPHOTOV.2015.2409561.

[175] P. Kumar, M. Pfeffer, B. Willsch, and O. Eibl, “Contact formation of front side metallization in p-type, single crystalline Si solar cells: Microstructure, temperature dependent series resistance and percolation model,” *Solar Energy Materials and Solar Cells*, vol. 145, pp. 358–367, Feb. 2016, doi: 10.1016/J.SOLMAT.2015.10.042.

[176] P. Kumar *et al.*, “Combined Microstructural and Electrical Characterization of Metallization Layers in Industrial Solar Cells,” *Energy Procedia*, vol. 67, pp. 31–42, Apr. 2015, doi: 10.1016/J.EGYPRO.2015.03.285.

[177] T. N. Truong *et al.*, “Hydrogenation of Phosphorus-Doped Polycrystalline Silicon Films for Passivating Contact Solar Cells,” vol. 11, no. 5, pp. 5554–5560, Feb. 2019, Accessed:

Oct. 31, 2021. [Online]. Available: https://pubs.acs.org/doi/abs/10.1021/acsami.8b19989

[178] B. Steinhauser, F. Feldmann, D. Ourinson, H. Nagel, T. Fellmeth, and M. Hermle, "On the Influence of the SiNx Composition on the Firing Stability of Poly-Si/SiNx Stacks," *Physica Status Solidi (A) Applications and Materials Science*, vol. 217, no. 21, Nov. 2020, doi: 10.1002/PSSA.202000333.

[179] B. W. H. van de Loo *et al.*, "On the hydrogenation of Poly-Si passivating contacts by Al2O3 and SiNx thin films," *Solar Energy Materials and Solar Cells*, vol. 215, p. 110592, Sep. 2020, doi: 10.1016/J.SOLMAT.2020.110592.

[180] Y. Yang *et al.*, "Effect of carrier-induced hydrogenation on the passivation of the poly-Si/SiOx/c-Si interface," *AIP Conf Proc*, vol. 1999, no. 1, p. 40026, Aug. 2018, doi: 10.1063/1.5049289/727610.

[181] N. P. Lockyer *et al.*, "Secondary ion mass spectrometry," *Nature Reviews Methods Primers 2024 4:1*, vol. 4, no. 1, pp. 1–21, May 2024, doi: 10.1038/s43586-024-00311-9.

[182] D. S. McPhail, "Applications of Secondary Ion Mass Spectrometry (SIMS) in materials science," *J Mater Sci*, vol. 41, no. 3, pp. 873–903, Feb. 2006, doi: 10.1007/S10853-006-6568-X/METRICS.

[183] P. Van Der and H. Wiley, "Secondary ion mass spectrometry: an introduction to principles and practices," 2014, Accessed: Feb. 07, 2025. [Online]. Available: https://books.google.com/books?hl=zh-CN&lr=&id=4xdVBAAAQBAJ&oi=fnd&pg=PT9&dq=Secondary+ion+mass+spectrometry&ots=3li8LUQSCm&sig=magZHHQh6fQU3-GL3nUYStnk0GQ

[184] A. Benninghoven, F. G. Rudenauer, and H. W. Werner, "Secondary ion mass spectrometry: basic concepts, instrumental aspects, applications and trends," Jan. 01, 1987, *John Wiley and Sons,New York, NY*.

[185] M. Lehmann *et al.*, "Analysis of hydrogen distribution and migration in fired passivating contacts (FPC)," *Solar Energy Materials and Solar Cells*, vol. 200, p. 110018, Sep. 2019, doi: 10.1016/J.SOLMAT.2019.110018.

[186] Z. Zhu, V. Shutthanandan, and M. Engelhard, “An investigation of hydrogen depth profiling using ToF-SIMS,” *Surface and Interface Analysis*, vol. 44, no. 2, pp. 232–237, Feb. 2012, doi: 10.1002/SIA.3826.

[187] M. Cwil, P. Konarski, and J. Ciosek, “Ion mass interferences and matrix effects on SIMS depth profiling of thin Ti/Si multilayer films induced by hydrogen, carbon and oxygen contaminations,” *Int J Mass Spectrom*, vol. 263, no. 1, pp. 54–58, May 2007, doi: 10.1016/J.IJMS.2006.12.004.

[188] F. A. Stevie, C. Zhou, M. Hopstaken, M. Saccomanno, Z. Zhang, and A. Turansky, “SIMS measurement of hydrogen and deuterium detection limits in silicon: Comparison of different SIMS instrumentation,” *Journal of Vacuum Science & Technology B, Nanotechnology and Microelectronics: Materials, Processing, Measurement, and Phenomena*, vol. 34, no. 3, p. 03H103, Jan. 2016, doi: 10.1116/1.4940151.

[189] K. Wittmaack, “Background formation in SIMS analysis of hydrogen, carbon, nitrogen and oxygen in silicon,” *Nuclear Instruments and Methods in Physics Research*, vol. 218, no. 1–3, pp. 327–332, Dec. 1983, doi: 10.1016/0167-5087(83)91001-3.

[190] C. W. Magee and E. M. Botnick, “Hydrogen depth profiling using SIMS—Problems and their solutions,” *Journal of Vacuum Science and Technology*, vol. 19, no. 1, p. 47, Jun. 1998, doi: 10.1116/1.571015.

[191] G. Dingemans, W. Beyer, M. C. M. Van De Sanden, and W. M. M. Kessels, “Hydrogen induced passivation of Si interfaces by Al2O3 films and SiO2/Al2O3 stacks,” *Appl Phys Lett*, vol. 97, no. 15, p. 152106, Oct. 2010, doi: 10.1063/1.3497014.

[192] P. Trocellier and T. Sajavaara, “Elastic Recoil Detection Analysis,” *Encyclopedia of Analytical Chemistry*, Sep. 2008, doi: 10.1002/9780470027318.A6205.PUB2.

[193] A. Bergmaier, G. Dollinger, and C. M. Frey, “Quantitative elastic recoil detection,” *Nucl Instrum Methods Phys Res B*, vol. 99, no. 1–4, pp. 488–490, May 1995, doi: 10.1016/0168-583X(94)00666-0.

[194] W. Assmann, H. Huber, C. Steinhausen, M. Dobler, H. Glückler, and A. Weidinger, “Elastic recoil detection analysis with heavy ions,” *Nucl Instrum Methods Phys Res B*, vol. 89, no. 1–4, pp. 131–139, May 1994, doi: 10.1016/0168-583X(94)95159-4.

[195] K. Yasuda, “Time-Of-Flight ERDA for Depth Profiling of Light Elements,” *Quantum Beam Science 2020, Vol. 4, Page 40*, vol. 4, no. 4, p. 40, Nov. 2020, doi: 10.3390/QUBS4040040.

[196] L Mikko, “Improvement of time-of-flight spectrometer for elastic recoil detection analysis,” University of Jyvaskyla, 2013. Accessed: Jun. 19, 2023. [Online]. Available: https://jyx.jyu.fi/handle/123456789/42953

[197] R. Sharma, S. Vajandar, T. Osipowicz, J. B. Li, A. G. Aberle, and Y. Huang, “Hydrogen diffusion from PECVD silicon nitride into multicrystalline silicon wafers: Elastic recoil detection analysis (ERDA) measurements and impact on light and elevated temperature induced degradation (LeTID),” *AIP Conf Proc*, vol. 2147, no. 1, p. 140009, Aug. 2019, doi: 10.1063/1.5123896.

[198] N. Phung *et al.*, “Effective Hydrogenation of Poly-Si Passivating Contacts by Atomic-Layer-Deposited Nickel Oxide,” *IEEE J Photovolt*, vol. 12, no. 6, pp. 1377–1385, Nov. 2022, doi: 10.1109/JPHOTOV.2022.3206895.

[199] T. Matsui, M. Bivour, M. Hermle, and H. Sai, “Atomic-Layer-Deposited TiOxNanolayers Function as Efficient Hole-Selective Passivating Contacts in Silicon Solar Cells,” *ACS Appl Mater Interfaces*, vol. 12, no. 44, pp. 49777–49785, Nov. 2020, doi: 10.1021/ACSAMI.0C14239/ASSET/IMAGES/LARGE/AM0C14239_0006.JPEG.

[200] J. Julin and T. Sajavaara, “Conceptual study of a heavy-ion-ERDA spectrometer for energies below 6 MeV,” *Nucl Instrum Methods Phys Res B*, vol. 406, pp. 61–65, Sep. 2017, doi: 10.1016/J.NIMB.2017.02.039.

[201] S. Giangrandi, T. Sajavaara, B. Brijs, K. Arstila, A. Vantomme, and W. Vandervorst, “Low-energy heavy-ion TOF-ERDA setup for quantitative depth profiling of thin films,” *Nucl Instrum Methods Phys Res B*, vol. 266, no. 24, pp. 5144–5150, Dec. 2008, doi: 10.1016/J.NIMB.2008.08.018.

[202] K. Arstila *et al.*, “Potku – New analysis software for heavy ion elastic recoil detection analysis,” *Nucl Instrum Methods Phys Res B*, vol. 331, pp. 34–41, Jul. 2014, doi: 10.1016/J.NIMB.2014.02.016.

[203] “Atomic Weight of Silicon | Commission on Isotopic Abundances and Atomic Weights.” Accessed: Feb. 02, 2025. [Online]. Available: https://www.ciaaw.org/silicon.htm

[204] S. Pal *et al.*, “Quantification of hydrogen in nanostructured hydrogenated passivating contacts for silicon photovoltaics combining SIMS-APT-TEM: A multiscale correlative approach,” *Appl Surf Sci*, vol. 555, p. 149650, Jul. 2021, doi: 10.1016/J.APSUSC.2021.149650.

[205] H. Park *et al.*, “Role of polysilicon in poly-Si/SiOx passivating contacts for high-efficiency silicon solar cells,” *RSC Adv*, vol. 9, no. 40, pp. 23261–23266, Jul. 2019, doi: 10.1039/C9RA03560E.

[206] B. Gault *et al.*, “Atom probe tomography,” *Nature Reviews Methods Primers 2021 1:1*, vol. 1, no. 1, pp. 1–30, Jul. 2021, doi: 10.1038/s43586-021-00047-w.

[207] B. Gault, M. Moody, J. Cairney, and S. Ringer, *Atom probe microscopy*. 2012. Accessed: Feb. 12, 2025. [Online]. Available: https://books.google.com/books?hl=zh-CN&lr=&id=jSXHPIBjL1UC&oi=fnd&pg=PR5&dq=Atom+probe+Moody&ots=9FK-ATDCG1&sig=LsNpp2QjLkcU1I4-91-piPnAdFs

[208] G. Sundell, M. Thuvander, and H. O. Andrén, “Hydrogen analysis in APT: Methods to control adsorption and dissociation of H2,” *Ultramicroscopy*, vol. 132, pp. 285–289, Sep. 2013, doi: 10.1016/J.ULTRAMIC.2013.01.007.

[209] R. P. Kolli, “Controlling residual hydrogen gas in mass spectra during pulsed laser atom probe tomography,” *Adv Struct Chem Imaging*, vol. 3, no. 1, Dec. 2017, doi: 10.1186/S40679-017-0043-4/.

[210] Y. Kunimune *et al.*, “Quantitative analysis of hydrogen in SiO2/SiN/SiO2 stacks using atom probe tomography,” *AIP Adv*, vol. 6, no. 4, p. 045121, Apr. 2016, doi: 10.1063/1.4948558.

[211] J. Takahashi, K. Kawakami, Y. Kobayashi, and T. Tarui, “The first direct observation of hydrogen trapping sites in TiC precipitation-hardening steel through atom probe tomography,” *Scr Mater*, vol. 63, no. 3, pp. 261–264, Aug. 2010, doi: 10.1016/J.SCRIPTAMAT.2010.03.012.

[212] I. Mouton *et al.*, “Quantification challenges for atom probe tomography of hydrogen and deuterium in Zircaloy-4,” *cambridge.org*, 2019, doi: 10.1017/S143192761801615X.

[213] D. Tweddle, P. Hamer, Z. Shen, V. P. Markevich, M. P. Moody, and P. R. Wilshaw, “Direct observation of hydrogen at defects in multicrystalline silicon,” *Progress in*

*Photovoltaics: Research and Applications*, p. pip.3184, Aug. 2019, doi: 10.1002/pip.3184.

[214] A. J. London, "Quantifying Uncertainty from Mass-Peak Overlaps in Atom Probe Microscopy," *Microscopy and Microanalysis*, vol. 25, no. 2, pp. 378–388, Apr. 2019, doi: 10.1017/S1431927618016276.

[215] A. J. London, D. Haley, and M. P. Moody, "Single-Ion Deconvolution of Mass Peak Overlaps for Atom Probe Microscopy," *Microscopy and Microanalysis*, vol. 23, no. 2, pp. 300–306, Apr. 2017, doi: 10.1017/S1431927616012782.

[216] F. Feldmann, J. Schön, J. Niess, W. Lerch, and M. Hermle, "Studying dopant diffusion from Poly-Si passivating contacts," *Solar Energy Materials and Solar Cells*, vol. 200, p. 109978, Sep. 2019, doi: 10.1016/J.SOLMAT.2019.109978.

[217] J. Navas, "Trichromatic High Resolution-Lbic : a System For The Micrometric Characterization of Solar Cells," IntechOpen. doi: 10.5772/19542.

[218] M. Rinio, H. Möller, M. W.-S. S. Phenomena, and undefined 1998, "LBIC investigations of the lifetime degradation by extended defects in multicrystalline solar silicon," *Trans Tech Publ*, Accessed: Jun. 19, 2021. [Online]. Available: https://www.scientific.net/SSP.63-64.115.pdf

[219] M. Breitwieser *et al.*, "Analysis of solar cell cross sections with micro-light beam induced current (μLBIC)," *Solar Energy Materials and Solar Cells*, vol. 131, pp. 124–128, Dec. 2014, doi: 10.1016/j.solmat.2014.05.002.

[220] B. Moralejo *et al.*, "LBIC and reflectance mapping of multicrystalline Si solar cells," *J Electron Mater*, vol. 39, no. 6, pp. 663–670, Jun. 2010, doi: 10.1007/s11664-010-1174-8.

[221] O. Porre, M. Stemmer, and M. Pasquinelli, "LBIC and diffusion length mapping applied to the investigation of gettering by aluminium diffusion in multicrystalline silicon," *Materials Science and Engineering B*, vol. 24, no. 1–3, pp. 188–191, May 1994, doi: 10.1016/0921-5107(94)90325-5.

[222] E. Dixon and D. Savuas, "APPARATUS AND METHOD FOR SCANNING LASER MAGING OF MACROSCOPC SAMPLES," 1998

[223] A. Büchler, H. Nagel, … M. B.-2017 I. 44th, and undefined 2017, "A New Perspective on Potential-Induced Degradation of the Shunting Type by Micro Raman-Spectroscopy and Micro Light-Beam-Induced Current," *ieeexplore.ieee.org*.

[224] J. Martín, C. Fernández-Lorenzo, J. A. Poce-Fatou, and R. Alcántara, "A versatile computer-controlled high-resolution LBIC system," *Progress in Photovoltaics: Research and Applications*, vol. 12, no. 4, pp. 283–295, Jun. 2004, doi: 10.1002/pip.528.

[225] M. Rinio, A. Yodyungyong, S. Keipert-Colberg, D. Borchert, and A. Montesdeoca-Santana, "Recombination in ingot cast silicon solar cells," *physica status solidi (a)*, vol. 208, no. 4, pp. 760–768, Apr. 2011, doi: 10.1002/pssa.201084022.

[226] J. D. Zook, "Effects of grain boundaries in polycrystalline solar cells," *Appl Phys Lett*, vol. 37, no. 2, pp. 223–226, Jul. 1980, doi: 10.1063/1.91832.

[227] J. Marek, "Light-beam-induced current characterization of grain boundaries," *J Appl Phys*, vol. 55, no. 2, pp. 318–326, Aug. 1984, doi: 10.1063/1.333047.

[228] C. Donolato, "Theory of beam induced current characterization of grain boundaries in polycrystalline solar cells," *J Appl Phys*, vol. 54, no. 3, pp. 1314–1322, Jun. 1983, doi: 10.1063/1.332205.

[229] S. Martinuzzi and M. Stemmer, "Mapping of defects and their recombination strenght by a light-beam-induced current in silicon wafers," *Materials Science and Engineering B*, vol. 24, no. 1–3, pp. 152–158, May 1994, doi: 10.1016/0921-5107(94)90318-2.

[230] M. Stemmer, "Mapping of the local minority carrier diffusion length in silicon wafers," *Appl Surf Sci*, vol. 63, no. 1–4, pp. 213–217, Jan. 1993, doi: 10.1016/0169-4332(93)90092-P.

[231] J. Carstensen, G. Popkirov, J. Bahr, and H. Föll, "CELLO: an advanced LBIC measurement technique for solar cell local characterization."

[232] A. Kaminski, O. Breitenstein, J. P. Boyeaux, P. Rakotoniaina, and A. Laugier, "Light beam induced current and infrared thermography studies of multicrystalline silicon solar cells," in *Journal of Physics Condensed Matter*, IOP Publishing, Jan. 2004, pp. 9–18. doi: 10.1088/0953-8984/16/2/002.

[233] M. A. Green *et al.*, "Solar cell efficiency tables (Version 64)," *Progress in Photovoltaics: Research and Applications*, vol. 32, no. 7, pp. 425–441, Jul. 2024, doi: 10.1002/PIP.3831.

[234] Q. Wei *et al.*, “Fusing Science with Industry: Perovskite Photovoltaics Moving Rapidly into Industrialization,” *Advanced Materials*, vol. 36, no. 39, p. 2406295, Sep. 2024, doi: 10.1002/ADMA.202406295.

[235] M. Nukunudompanich, G. Budiutama, K. Suzuki, K. Hasegawa, and M. Ihara, “Dominant effect of the grain size of the MAPbI3 perovskite controlled by the surface roughness of TiO2 on the performance of perovskite solar cells,” *CrystEngComm*, vol. 22, no. 16, pp. 2718–2727, Apr. 2020, doi: 10.1039/D0CE00169D.

[236] E. M. Tennyson, T. A. S. Doherty, and S. D. Stranks, “Heterogeneity at multiple length scales in halide perovskite semiconductors,” *Nature Reviews Materials 2019 4:9*, vol. 4, no. 9, pp. 573–587, Jul. 2019, doi: 10.1038/s41578-019-0125-0.

[237] S. Mastroianni *et al.*, “Analysing the effect of crystal size and structure in highly efficient CH3NH3PbI3 perovskite solar cells by spatially resolved photo- and electroluminescence imaging,” *Nanoscale*, vol. 7, no. 46, pp. 19653–19662, Dec. 2015, doi: 10.1039/c5nr05308k.

[238] G. E. Eperon, D. Moerman, and D. S. Ginger, “Anticorrelation between Local Photoluminescence and Photocurrent Suggests Variability in Contact to Active Layer in Perovskite Solar Cells,” *ACS Nano*, vol. 10, no. 11, pp. 10258–10266, Nov. 2016, doi: 10.1021/acsnano.6b05825.

[239] Z. Song *et al.*, “Perovskite Solar Cell Stability in Humid Air: Partially Reversible Phase Transitions in the PbI2-CH3NH3I-H2O System,” *Adv Energy Mater*, vol. 6, no. 19, p. 1600846, Oct. 2016, doi: 10.1002/aenm.201600846.

[240] Blu-ray Disc Association, “White Paper Blu-ray Disc™ Format.” [Online]. Available: http://www.blu-raydisc.com/Assets/Downloadablefile/BD-ROMwhitepaper20070308-15270.pdf

[241] E. E. Te Hwu and A. Boisen, “Hacking CD/DVD/Blu-ray for Biosensing,” Jul. 27, 2018, *American Chemical Society*. doi: 10.1021/acssensors.8b00340.

[242] F. S. Russell-Pavier, L. Picco, J. C. C. Day, N. R. Shatil, A. Yacoot, and O. D. Payton, “‘Hi-Fi AFM’: High-speed contact mode atomic force microscopy with optical pickups,” *Meas Sci Technol*, vol. 29, no. 10, p. 105902, Sep. 2018, doi: 10.1088/1361-6501/aad771.

[243] B. Hallam *et al.*, “Efficiency enhancement of i-PERC solar cells by implementation of a laser doped selective emitter,” *Solar Energy Materials and Solar Cells*, vol. 134, pp. 89–98, Mar. 2015, doi: 10.1016/J.SOLMAT.2014.11.028.

[244] G. Poulain *et al.*, “Laser process for selective emitter silicon solar cells,” *Wiley Online LibraryG Poulain, D Blanc, A Focsa, B Bazer-Bachi, M Gauthier, B Semmache, Y PellegrinInternational Journal of Photoenergy, 2012•Wiley Online Library*, vol. 2012, 2012, doi: 10.1155/2012/413863.

[245] M. Yu *et al.*, “Imaging and quantifying carrier collection in silicon solar cells: A submicron study using electron beam induced current,” *Solar Energy*, vol. 211, pp. 1214–1222, Nov. 2020, doi: 10.1016/j.solener.2020.10.038.

[246] J. Weber, S. Gutscher, S. Lohmüller, E. Lohmüller, and A. A. Brand, “Laser-doped selective emitter—Process development and speed-up,” in *Proc. 35th Eur. Photovolt. Sol. Energy Conf. Exhib.*, 2018, pp. 379–384.

[247] M. A. Green, “Self-consistent optical parameters of intrinsic silicon at 300 K including temperature coefficients,” *Solar Energy Materials and Solar Cells*, vol. 92, no. 11, pp. 1305–1310, Nov. 2008, doi: 10.1016/j.solmat.2008.06.009.

[248] E. Edri, S. Kirmayer, S. Mukhopadhyay, K. Gartsman, G. Hodes, and D. Cahen, “Elucidating the charge carrier separation and working mechanism of CH 3 NH 3 PbI 3-x Cl x perovskite solar cells,” *Nat Commun*, vol. 5, no. 1, pp. 1–8, Mar. 2014, doi: 10.1038/NCOMMS4461;TECHMETA=120,128;SUBJMETA=1075,299,301,524,624,639,946;KWRD=SOLAR+CELLS,SOLAR+ENERGY+AND+PHOTOVOLTAIC+TECHNOLOGY.

[249] N. Klein-Kedem, D. Cahen, and G. Hodes, “Effects of Light and Electron Beam Irradiation on Halide Perovskites and Their Solar Cells,” *Acc Chem Res*, vol. 49, no. 2, pp. 347–354, Feb. 2016, doi: 10.1021/ACS.ACCOUNTS.5B00469/ASSET/IMAGES/LARGE/AR-2015-00469H_0006.JPEG.

[250] M. H. Miah, M. U. Khandaker, M. B. Rahman, M. Nur-E-Alam, and M. A. Islam, “Band gap tuning of perovskite solar cells for enhancing the efficiency and stability: issues and prospects,” *RSC Adv*, vol. 14, no. 23, pp. 15876–15906, May 2024, doi: 10.1039/D4RA01640H.

[251] K. Datta *et al.*, “Effect of Light-Induced Halide Segregation on the Performance of Mixed-Halide Perovskite Solar Cells,” *ACS Appl Energy Mater*, vol. 4, no. 7, pp. 6650–6658, Jul. 2021, doi: 10.1021/ACSAEM.1C00707.

[252] Y. Guo *et al.*, “Unveiling the impact of photoinduced halide segregation on performance degradation in wide-bandgap perovskite solar cells,” *Energy Environ Sci*, vol. 18, no. 5, pp. 2308–2317, Mar. 2025, doi: 10.1039/D4EE05604C.

[253] B. Ehrler, E. Alarcón-Lladó, S. W. Tabernig, T. Veeken, E. C. Garnett, and A. Polman, “Photovoltaics reaching for the shockley-queisser limit,” *ACS Energy Lett*, vol. 5, no. 9, pp. 3029–3033, Sep. 2020, doi: 10.1021/ACSENERGYLETT.0C01790.

[254] M. C. Schubert, L. E. Mundt, D. Walter, A. Fell, and S. W. Glunz, “Spatially Resolved Performance Analysis for Perovskite Solar Cells,” Jul. 01, 2020, *Wiley-VCH Verlag*. doi: 10.1002/aenm.201904001.

[255] L. Meng, F. J. Ma, J. Wong, B. Hoex, and C. S. Bhatia, “Extraction of surface recombination velocity at highly doped silicon surfaces using electron-beam-induced current,” *IEEE J Photovolt*, vol. 5, no. 1, pp. 263–268, Jan. 2015, doi: 10.1109/JPHOTOV.2014.2361025.

[256] R. Zhou *et al.*, “Understanding and optimizing EBIC pn-junction characterization from modeling insights,” *J Appl Phys*, vol. 127, no. 2, Jan. 2020, doi: 10.1063/1.5139894/566557.

[257] L. Krückemeier, B. Krogmeier, Z. Liu, U. Rau, and T. Kirchartz, “Understanding Transient Photoluminescence in Halide Perovskite Layer Stacks and Solar Cells,” *Adv Energy Mater*, vol. 11, no. 19, p. 2003489, May 2021, doi: 10.1002/AENM.202003489.

[258] P. Würfel, S. Finkbeiner, and E. Daub, “Generalized Planck’s radiation law for luminescence via indirect transitions,” *Appl Phys A Mater Sci Process*, vol. 60, no. 1, pp. 67–70, Jan. 1995, doi: 10.1007/BF01577615/METRICS.

[259] P. Wurfel, “The chemical potential of radiation,” *Journal of Physics C: Solid State Physics*, vol. 15, no. 18, p. 3967, Jun. 1982, doi: 10.1088/0022-3719/15/18/012.

[260] K. Schick, E. Daub, S. Finkbeiner, and P. Würfel, “Verification of a generalized Planck law for luminescence radiation from silicon solar cells,” *Applied Physics A Solids and Surfaces*, vol. 54, no. 2, pp. 109–114, Feb. 1992, doi: 10.1007/BF00323895/METRICS.

[261] J. Haunschild *et al.*, "Quality control of as-cut multicrystalline silicon wafers using photoluminescence imaging for solar cell production," *Solar Energy Materials and Solar Cells*, vol. 94, no. 12, pp. 2007–2012, Dec. 2010, doi: 10.1016/J.SOLMAT.2010.06.003.

[262] J. A. Giesecke, B. Michl, F. Schindler, M. C. Schubert, and W. Warta, "Minority carrier lifetime of silicon solar cells from quasi-steady-state photoluminescence," *Solar Energy Materials and Solar Cells*, vol. 95, no. 7, pp. 1979–1982, Jul. 2011, doi: 10.1016/J.SOLMAT.2011.02.023.

[263] H. C. Sio, S. P. Phang, T. Trupke, and D. Macdonald, "An accurate method for calibrating photoluminescence-based lifetime images on multi-crystalline silicon wafers," *Solar Energy Materials and Solar Cells*, vol. 131, pp. 77–84, Dec. 2014, doi: 10.1016/J.SOLMAT.2014.06.004.

[264] S. Ostapenko, S. Ostapenko, I. Tarasov, J. P. Kalejs, C. Haessler, and E.-U. Reisner, "Defect monitoring using scanning photoluminescence spectroscopy in multicrystalline silicon wafers," *Semicond. Sci. Technol*, vol. 15, pp. 840–848, 2000, doi: 10.1088/0268-1242/15/8/310.

[265] H. Sugimoto *et al.*, "Photoluminescence analysis of intragrain defects in multicrystalline silicon wafers for solar cells," *J Appl Phys*, vol. 102, no. 5, p. 54506, Sep. 2007, doi: 10.1063/1.2776003/906588.

[266] D. Herrmann, S. Lohmuller, H. Hoffler, A. Fell, A. A. Brand, and A. Wolf, "Numerical Simulations of Photoluminescence for the Precise Determination of Emitter Contact Recombination Parameters," *IEEE J Photovolt*, vol. 9, no. 6, pp. 1759–1767, Nov. 2019, doi: 10.1109/JPHOTOV.2019.2938400.

[267] A. Wolf *et al.*, "Uniformity Analysis of Metallization-Induced Recombination Losses by Photoluminescence Imaging," *AIP Conf Proc*, vol. 2487, no. 1, Aug. 2022, doi: 10.1063/5.0089268/2826703.

[268] A. Fell, K. R. McIntosh, and K. C. Fong, "Simplified device simulation of silicon solar cells using a lumped parameter optical model," *IEEE J Photovolt*, vol. 6, no. 3, pp. 611–616, May 2016, doi: 10.1109/JPHOTOV.2016.2528407.

[269] A. Brown, J. A. van den Berg, and J. C. Vickerman, "The application of secondary Ion mass spectrometry to surface analysis of semiconductor substrates and devices," *Surface*

*and Interface Analysis*, vol. 9, no. 5, pp. 309–317, Jul. 1986, doi: 10.1002/SIA.740090508.

[270] M. G. Dowsett and R. D. Barlow, "Characterization of sharp interfaces and delta doped layers in semiconductors using secondary ion mass spectrometry," *Anal Chim Acta*, vol. 297, no. 1–2, pp. 253–275, Oct. 1994, doi: 10.1016/0003-2670(93)E0568-R.

[271] A. Delcorte *et al.*, "Large cluster ions: soft local probes and tools for organic and bio surfaces," *Physical Chemistry Chemical Physics*, vol. 22, no. 31, pp. 17427–17447, Aug. 2020, doi: 10.1039/D0CP02398A.

[272] T. Kelly, M. M.-R. of scientific instruments, and undefined 2007, "Atom probe tomography," *pubs.aip.org*, Accessed: Feb. 12, 2025. [Online]. Available: https://pubs.aip.org/aip/rsi/article/78/3/031101/687953

[273] R. G. Forbes, "Field evaporation theory: a review of basic ideas," *Appl Surf Sci*, vol. 87–88, no. C, pp. 1–11, Mar. 1995, doi: 10.1016/0169-4332(94)00526-5.

[274] B. Ravelo, F. V.-P. I. E. R. Letters, and undefined 2014, "Analysis of excitation pulsed signal propagation for atom probe tomography system," *jpier.orgB Ravelo, F VurpillotProgress In Electromagnetics Research Letters, 2014•jpier.org*, Accessed: Feb. 12, 2025. [Online]. Available: https://www.jpier.org/PIERL/pier.php?paper=14042403

[275] R. Schlesiger *et al.*, "Design of a laser-assisted tomographic atom probe at Münster University," *Review of Scientific Instruments*, vol. 81, no. 4, Apr. 2010, doi: 10.1063/1.3378674/355602.

[276] J. Bunton, J. Olson, … D. L.-M. and, and undefined 2007, "Advances in pulsed-laser atom probe: Instrument and specimen design for optimum performance," *cambridge.orgJH Bunton, JD Olson, DR Lenz, TF KellyMicroscopy and Microanalysis, 2007•cambridge.org*, Accessed: Feb. 12, 2025. [Online]. Available: https://www.cambridge.org/core/journals/microscopy-and-microanalysis/article/advances-in-pulsedlaser-atom-probe-instrument-and-specimen-design-for-optimum-performance/1748AAF071F944317F4C3F63D5CFE6E0

[277] B. Gault *et al.*, "Design of a femtosecond laser assisted tomographic atom probe," *Review of Scientific Instruments*, vol. 77, no. 4, Apr. 2006, doi: 10.1063/1.2194089/913485.

[278] E. Bémont *et al.*, "Effects of incidence angles of ions on the mass resolution of an energy compensated 3D atom probe," *Ultramicroscopy*, vol. 95, no. SUPPL., pp. 231–238, May 2003, doi: 10.1016/S0304-3991(02)00321-2.

[279] B. Gault *et al.*, "Spatial Resolution in Atom Probe Tomography," *Microscopy and Microanalysis*, vol. 16, no. 1, pp. 99–110, Feb. 2010, doi: 10.1017/S1431927609991267.

[280] B. Gault *et al.*, "Advances in the reconstruction of atom probe tomography data," *Ultramicroscopy*, vol. 111, no. 6, pp. 448–457, May 2011, doi: 10.1016/J.ULTRAMIC.2010.11.016.

[281] I. Blum, F. Cuvilly, and W. Lefebvre-Ulrikson, "Atom Probe Sample Preparation," *Atom Probe Tomography: Put Theory Into Practice*, pp. 97–121, Jan. 2016, doi: 10.1016/B978-0-12-804647-0.00004-8.

[282] A. J. Kubis, G. J. Shiflet, D. N. Dunn, and R. Hull, "Focused ion-beam tomography," *Metall Mater Trans A Phys Metall Mater Sci*, vol. 35 A, no. 7, pp. 1935–1943, 2004, doi: 10.1007/S11661-004-0142-4/METRICS.

[283] C. A. Volkert and A. M. Minor, "Focused Ion Beam Microscopy and Micromachining," *MRS Bull*, vol. 32, no. 5, pp. 389–399, 2007, doi: 10.1557/MRS2007.62.

[284] P. R. Munroe, "The application of focused ion beam microscopy in the material sciences," *Mater Charact*, vol. 60, no. 1, pp. 2–13, Jan. 2009, doi: 10.1016/J.MATCHAR.2008.11.014.

[285] W. Zhou, R. Apkarian, Z. L. Wang, and D. Joy, "Fundamentals of Scanning Electron Microscopy (SEM)," *Scanning Microscopy for Nanotechnology: Techniques and Applications*, pp. 1–40, 2006, doi: 10.1007/978-0-387-39620-0_1.

[286] L. Reimer, "Scanning Electron Microscopy: Physics of Image Formation and Microanalysis, Second Edition," *Meas Sci Technol*, vol. 11, no. 12, p. 1826, Dec. 2000, doi: 10.1088/0957-0233/11/12/703.

[287] C. Lotharukpong, "Defect characterisation in multi-crystalline silicon," 2015, Accessed: Feb. 15, 2025. [Online]. Available: https://ora.ox.ac.uk/objects/uuid:a803fada-2296-41c3-9d96-864c186957a2

[288] D. Tweddle, "Atom Probe Analysis of Crystallographic Defects in Silicon," PhD Thesis, University of Oxford, 2019.

[289] M. S. Meier, “All things hydrogen: hydrogen imaging in atom probe tomography and its application to tungsten,” p. 2023, 2023, Accessed: Feb. 15, 2025. [Online]. Available: https://ora.ox.ac.uk/objects/uuid:ce6897e7-c92a-453f-bde2-dc4d1bba69db

[290] W. Vandervorst *et al.*, “Dopant, composition and carrier profiling for 3D structures,” *Mater Sci Semicond Process*, vol. 62, pp. 31–48, May 2017, doi: 10.1016/J.MSSP.2016.10.029.

[291] C. Lotharukpong *et al.*, “Specimen preparation methods for elemental characterisation of grain boundaries and isolated dislocations in multicrystalline silicon using atom probe tomography,” *Mater Charact*, vol. 131, pp. 472–479, Sep. 2017, doi: 10.1016/J.MATCHAR.2017.07.038.

[292] D. Tweddle *et al.*, “Atom Probe Tomography Study of Gettering in High-Performance Multicrystalline Silicon,” *IEEE J Photovolt*, vol. 10, no. 3, pp. 863–871, May 2020, doi: 10.1109/JPHOTOV.2020.2974795.

[293] Y. Ohno, K. Kutsukake, M. Deura, … I. Y.-A. P., and undefined 2016, “Recombination activity of nickel, copper, and oxygen atoms segregating at grain boundaries in mono-like silicon crystals,” *pubs.aip.org*, Accessed: Feb. 16, 2025. [Online]. Available: https://pubs.aip.org/aip/apl/article/109/14/142105/32600

[294] A. Stoffers, J. Barthel, … C. L.-M. and, and undefined 2017, “Correlating atom probe tomography with atomic-resolved scanning transmission electron microscopy: Example of segregation at silicon grain boundaries,” *academic.oup.comA Stoffers, J Barthel, CH Liebscher, B Gault, O Cojocaru-Mirédin, C Scheu, D RaabeMicroscopy and microanalysis, 2017•academic.oup.com*, Accessed: Feb. 16, 2025. [Online]. Available: https://academic.oup.com/mam/article-abstract/23/2/291/6899506

[295] Y. Ohno *et al.*, “Three-dimensional evaluation of gettering ability of Σ 3 { 111 } grain boundaries in silicon by atom probe tomography combined with transmission electron microscopy,” *Appl Phys Lett*, vol. 103, no. 10, doi: 10.1063/1.4820140.

[296] A. Stoffers, O. Cojocaru-Mirédin, W. Seifert, S. Zaefferer, S. Riepe, and D. Raabe, “Grain boundary segregation in multicrystalline silicon: correlative characterization by EBSD, EBIC, and atom probe tomography,” *Progress in Photovoltaics: Research and Applications*, vol. 23, no. 12, pp. 1742–1753, Dec. 2015, doi: 10.1002/PIP.2614.

[297] B. W. Krakauer and D. N. Seidman, “Absolute atomic-scale measurements of the Gibbsian interfacial excess of solute at internal interfaces,” *Phys Rev B*, vol. 48, no. 9, p. 6724, Sep. 1993, doi: 10.1103/PhysRevB.48.6724.

[298] F. De Geuser, W. Lefebvre, F. Danoix, F. Vurpillot, B. Forbord, and D. Blavette, “An improved reconstruction procedure for the correction of local magnification effects in three-dimensional atom-probe,” *Surface and Interface Analysis*, vol. 39, no. 2–3, pp. 268–272, Feb. 2007, doi: 10.1002/SIA.2489.

[299] B. Gault, F. Danoix, K. Hoummada, D. Mangelinck, and H. Leitner, “Impact of directional walk on atom probe microanalysis,” *Ultramicroscopy*, vol. 113, pp. 182–191, Feb. 2012, doi: 10.1016/J.ULTRAMIC.2011.06.005.

[300] E. A. Marquis, B. P. Geiser, T. J. Prosa, and D. J. Larson, “Evolution of tip shape during field evaporation of complex multilayer structures,” *J Microsc*, vol. 241, no. 3, pp. 225–233, Mar. 2011, doi: 10.1111/J.1365-2818.2010.03421.X.

[301] T. F. Kelly and D. J. Larson, “Atom probe tomography 2012,” *Annu Rev Mater Res*, vol. 42, no. Volume 42, 2012, pp. 1–31, Aug. 2012, doi: 10.1146/ANNUREV-MATSCI-070511-155007/CITE/REFWORKS.

[302] A. Bik and P. M. Habraken, “Elastic recoil detection ,” *Rep. Prog. Phys*, vol. 56, pp. 859–902, 1993.

[303] M. Kivekäs *et al.*, “Elastic recoil and scattering yields measured in low energy heavy ion ERD,” *Nucl Instrum Methods Phys Res B*, vol. 557, p. 165542, Dec. 2024, doi: 10.1016/J.NIMB.2024.165542.

[304] Z. Siketić, I. Bogdanović Radović, I. Sudić, and M. Jakšić, “Surface analysis and depth profiling using time-of-flight elastic recoil detection analysis with argon sputtering,” *Scientific Reports 2018 8:1*, vol. 8, no. 1, pp. 1–6, Jul. 2018, doi: 10.1038/s41598-018-28726-x.

[305] F. Adams and C. Barbante, “Particle-Based Imaging Techniques,” *Comprehensive Analytical Chemistry*, vol. 69, pp. 315–337, Jan. 2015, doi: 10.1016/B978-0-444-63439-9.00008-6.

[306] Z. Siketić, I. B. Radović, and M. Jakšić, “Quantitative analysis of hydrogen in thin films using Time-of-Flight Elastic Recoil Detection Analysis,” *Thin Solid Films*, vol. 518, no. 10, pp. 2617–2622, Mar. 2010, doi: 10.1016/J.TSF.2009.07.196.

[307] S. Guo, G. Gregory, A. M. Gabor, W. V. Schoenfeld, and K. O. Davis, “Detailed investigation of TLM contact resistance measurements on crystalline silicon solar cells,” *Solar Energy*, vol. 151, pp. 163–172, Jul. 2017, doi: 10.1016/J.SOLENER.2017.05.015.

[308] D. K. Schroder, “Semiconductor Material and Device Characterization,” Wiley. Accessed: Apr. 25, 2025. [Online]. Available: https://ieeexplore.ieee.org/book/5237928

[309] B. Grübel *et al.*, “Progress of plated metallization for industrial bifacial TOPCon silicon solar cells,” *Progress in Photovoltaics: Research and Applications*, vol. 30, no. 6, pp. 615–621, Jun. 2022, doi: 10.1002/PIP.3528.

[310] “TLM measurement | PVEducation.” Accessed: Apr. 28, 2025. [Online]. Available: https://www.pveducation.org/pvcdrom/tlm-measurement

[311] Y. Seo and W. Jhe, “Atomic force microscopy and spectroscopy,” *Reports on Progress in Physics*, vol. 71, no. 1, p. 016101, Dec. 2007, doi: 10.1088/0034-4885/71/1/016101.

[312] F. J. Giessibl, “Advances in atomic force microscopy,” *Rev Mod Phys*, vol. 75, no. 3, p. 949, Jul. 2003, doi: 10.1103/RevModPhys.75.949.

[313] J. Martín, C. Fernández-Lorenzo, J. A. Poce-Fatou, and R. Alcántara, “A versatile computer-controlled high-resolution LBIC system,” *Progress in Photovoltaics: Research and Applications*, vol. 12, no. 4, pp. 283–295, Jun. 2004, doi: 10.1002/pip.528.

[314] V. Neumann, “Focusing and optical imaging in applied laser technologies,” *Laser Technik Journal*, vol. 9, no. 1, pp. 41–44, Jan. 2012, doi: 10.1002/latj.201290007.

# 9. Appendices

## Appendix A. Photoluminescence Imaging

Photoluminescence (PL) imaging is a versatile, fast and non-destructive technique for characterising semiconductor and solar devices. Photoluminescence is initiated by illuminating the silicon sample with typically a red or near-infrared light source, during which charge carriers are generated within the wafer. These carriers go through radiative recombination (see 1.3.2) to emit photons with representative energies of the material's band structure. This photoluminescence response can be utilised in a time-resolved transient excitation mode [257] or steady state excitation mode [25]. The photoluminescence imaging technique used in this study operates under the steady-state condition.

PL imaging tools capture the spatial distribution of the emitted photons to create a photoluminescence image, using an infrared-sensitive CCD camera for the silicon bandgap. The PL image detected contains information about the spatial distribution of the emission as well as other optical factors. An example PL model interpretation by Fell et.al. gives the detected luminescence map by integrating elements over sample depths of the wafer as follows [140]:

$$PL(x,y) = \int_0^W \int_{\lambda_1}^{\lambda_2} r_{sp}(x,y,z,\lambda)\, f_{esc}(x,y,z,\alpha) f_{dec}(\lambda,\alpha) d\lambda dz \qquad 9\text{-}1$$

Where the PL map at location $x, y$ is related to the integral of a product between three functions over the wavelength and depth range: the emission rate $r_{sp}$, an optical escape function $f_{esc}$ and the detector sensitivity $f_{dec}$. The escape function $f_{esc}$ describes the probability of an emitted photon leaving the sample. The detector sensitivity $f_{dec}$ describes the wavelength dependent photon collection efficiency by the imaging sensor. Since wavelength selective filtering is typically used before the camera, eq. 9-1 only account for photon luminance between a $\lambda_1$ to $\lambda_2$ wavelength range. Such windowed wavelength filtering is implemented to zoom into silicon emission and reduce optical blurring effects across wide wavelength ranges.

The most important factor, the rate of emission $r_{sp}$ from band-to-band transition can be futher given by a generalized form of Planck's law of radiation [258], [259], [260] :

$$dr_{sp} = \alpha(\lambda)P(\lambda)exp\left(\frac{\phi_n - \phi_p}{kT}\right)d\lambda \qquad 9\text{-}2$$

Where $dr_{sp}$ is the emission rate per wavelength interval $d\lambda$, and $\alpha(\lambda)$ is absorption coefficient of silicon. Function $P(\lambda)$ is the plank photon spectrum density at wavelength $\lambda$, described in an extension of Plank's law [259]. The last exponential term describes the separation of local carrier quasi-Fermi energies $\phi_n - \phi_p$. This term is also proportional to the local product of excess carriers, which gives PL a link to the carrier dynamics.

As described in the above eq. 9-2, the detected photon luminance in PL maps can be used after calibration to indicate the spatial excess carrier densities. This enables PL to be used both as a qualitative diagnostic method and a quantitative tool for solar cell characterisation. Fast PL images can be conveniently used to mark high recombination locations, which appear as lower luminescence zones [261]. Local variations in PL signal can reveal differences in spatial minority lifetimes [262], [263]. enabling researchers to map electrically active defects or impurity distributions within silicon wafers[264], [265].

It is also noteworthy from the equation 9-2 that the spatial luminance reflects the integration of spatial carrier recombination over the depth. The excess carrier depth profile is assumed to be uniform in most studies in PL analysis, allowing carrier diffusion to happen only laterally. While this assumption is reasonable for symmetrical, high lifetime samples where excess carrier densities are homogenised over the depth, it can introduce inaccuracies in PL analysis of depth-sensitive recombination processes, including metal contact recombination [131], [132], [266], [267]. Numerical device simulation [140], [266], [268] can be used to evaluate the effect of vertical carrier distribution on PL outputs, thereby facilitating quantitative precision in parameter extraction using PL.

## Appendix B. Secondary Ion Mass Spectrometry

Secondary ion mass spectrometry (SIMS) is a versatile chemical analysis technique widely used in electronics and semiconductor materials [269], [270]. Its operation relies on bombarding the sample surface under high vacuum with a primary ion beam at energies in keV range [181], [183], [184]. Figure 9-1 from [182] shows the surface bombardment by the primary beam, which causes a short-lived collision cascade locally in the materials matrix. This causes the ejection of atoms and molecules from the top layers in a process known as sputtering. A fraction of sputtered species becomes ionised and is detected as secondary ions in SIMS.

These secondary ions from the top few atomic surface layers convey chemical information of the surface composition. By dynamically removing surface material, SIMS provides chemical depth profiles. Some SIMS setups enable further areal surface scanning with the focused primary beam, facilitating 3D sample analysis. The secondary ions are differentiated by mass and counted using a mass spectrometer. Multiple mass analyser setups exist, offering choices between detection precision and speed. These include the quadruple mass filter at high acquisition rate end and time-of-flight detector for high mass solution [181].

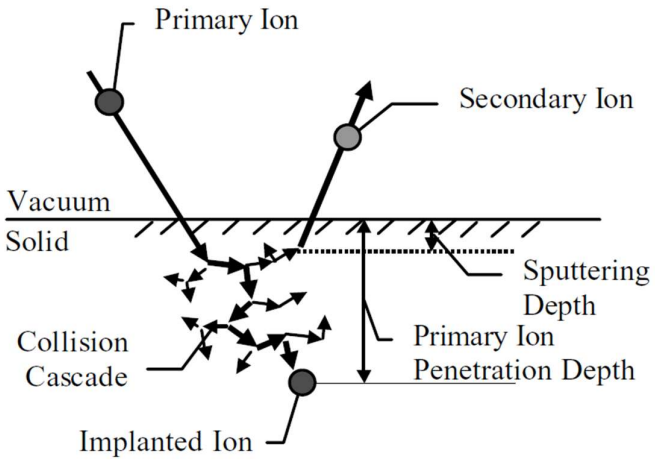


*Figure 9-1 Surface bombardment process in SIMS. The energetic primary ion causes a collision cascade in the matrix before implantation. Secondary ion signals are generated for analysis. Figure from [182]*

SIMS measurement results are influenced by the choices of the primary ion source and energy. A $Cs^+$ ion source is commonly equipped in SIMS as the standard because of known enhancements of secondary ion yields for electronegative elements, while an oxygen ion source is used for electropositive elements. The energy dissipation during the implantation of the primary ion source causes atomic mixing in the matrix, the scale of which is the limiting factor of SIMS depth resolution. Physical models have been developed to study the process of local rearrangement of atoms and energy deposition in the material matrix [271].

An ultra-high vacuum ($<10^{-8}$ mbar) is necessary in the SIMS analysis chamber to reduce the surface condensation of atmospheric contamination. Trace amounts of residuals such as water or hydrocarbons, can remain under SIMS conditions. These gases can adsorb and ionise, leading to 'false' signals, e.g. $OH^-$ or $CN^-$ peaks. Contaminants can also form complex ions with sample species, e.g. $SiH^+$. This effectively obfuscates the detection of C, O, H from sample

at lower levels. Among them the most impacted is the detection limit of hydrogen because of the high hydrogen remanence level [188], [189].

# Appendix C. Atom probe tomography

## I. Working principles

Atom probe tomography (APT) is a high-resolution analytical technique used to determine the three-dimensional elemental composition of materials at the near-atomic scale [206]. Figure 9-2 describes the key components of an APT microscope. It combines the field evaporation process, time-of-flight mass spectrometry, and position-sensitive detection to identify and map individual atoms within a tiny specimen needle. The name atom probe tomography perhaps covers less of its mechanism than the name of its predecessor field ion microscopy (FIM). In APT (as well as FIM) a high electrostatic field is applied to a needle-shaped specimen, initiating two processes: (a) field ionisation, where the surface atoms lose electrons to become ions, and (b) field evaporation, where atoms and ions desorb from the surface. The evaporated species go through flights following the defined electrostatic field lines until they reach an imaging detector. The time between the evaporation and detection is recorded by a time-of-flight spectrometer, which provides information about the mass-to-charge of the ion in flight. The final position-sensitive detector is commonly a microchannel plate with a delay-line system for reading out the two coordinates of detection events (also known as hits). This further allows 3D sample tomographic information to be obtained.

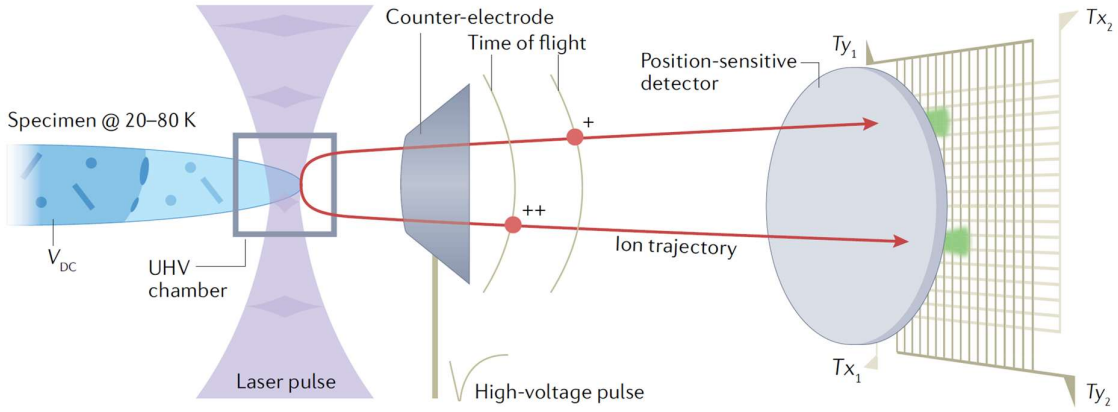


*Figure 9-2 Schematic of components of an APT instrument, showing the sample under field evaporation, the time-of-flight spectrometer, and the position-sensitive detector.*

A high surface field is required for the field evaporation process. This is aided by using a sharp needle-shaped specimen geometry with a tip radius below 100 nm. The electric field at the tip is inversely proportional to the tip radius following [207]:

$$E = \frac{V}{k_F R} \qquad 9\text{-}3$$

Where $E$ is the electric field at the tip. V is the electrostatic potential voltage of the needle. $R$ is the radius of curvature at the tip and $k_F$ is an additional field factor.

Field evaporation kinetics can be treated as a thermally activated process with an energy barrier. The surface electric field applied is linked to the lowering of the energy barrier, and thus enhancement of the evaporation rate [207], [272], [273]. The evaporation rate is described by the following equation:

$$R(E,T) = R_0 \exp\left(-\frac{E_b(E)}{kT}\right) \qquad 9\text{-}4$$

Where the evaporation rate per area $R$ is related to an energy barrier $E_b$, a function of surface electric field $E$, as well as temperature $T$. In addition to those, $R_0$ is an Arrhenius factor. $k$ is the Boltzmann constant.

Evaporation in pauses is used in APT operations to allow sequential signal measurements in short time windows. The evaporation pulses can either be triggered by a high voltage (related to field $E$) or triggered by laser thermal energy (related to tip temperature $T$), meaning APT can operate under either voltage mode of laser mode. Figure 9-3 explains the two schemes to of increasing evaporation rates. The blue region blue correspond to enhanced evaporation scenarios compared to the grey region $\phi_2 > \phi_1$, on a field-temperature plot. During experiments, specimens are held at a base temperature $T_{base}$ and a DC voltage $F_{DC}$ represented by the green dot. To get to the desired high evaporation rates where ions can be adequately detected, either one of the voltage or laser pulsing can be used, which is represented by moving up or right on this plot. The choice between voltage or laser pulsing largely depends on material properties, meaning metallic specimen can benefit from field-assisted evaporation in voltage mode, while semicondutor are more sensitive to thermal pulses in laser mode. A 10-25% overhead voltage lasting nanoseconds [274] is typically used in voltage mode. Laser mode relies on a typically UV picosecond laser source, focused on the specimen tip, to cause temperature pulses [275], [276], [277].

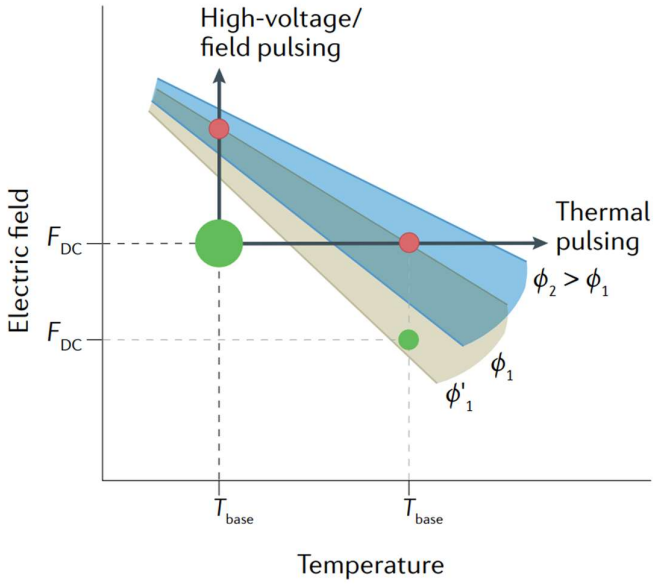


*Figure 9-3 An electric field – temperature plot showing field pulsing and thermal pulsing conditions of APT field evaporation [206]*

Following pulsed field evaporation, ionic species from the specimen enter the flight region of the time-of-flight spectrometer in short bursts at a selected frequency. An additional ion reflectron [278], which is an electrostatic mirror, can be used in some devices to extend ion trajectories, allowing longer flight times. The time between the beginning and end of the flight is recorded for chemical identification since they are related to the ion mass-to-charge ratio following the simple field acceleration relation:

$$\frac{m}{q} = 2U\left(\frac{T_{tof}}{L}\right)^2 \qquad 9\text{-}5$$

Where $m/q$ is mass divided by charge, $U$ is the electrostatic potential drop between the end and the beginning of the flight. $T_{tof}$ is the time of flight and $L$ is the length of the flight.

The recorded time-of-flights can hence be converted to a spectrum of detected mass-to-charges. This mass spectrum is the initial representation of APT data. It enables a ranging process to assign mass signals to specific monoatomic or polyatomic chemical species. Further discussion on mass-spectrum analysis is found in IV.

As a high spatial resolution microscopy technique, APT is also capable of recording sample structural information aided by a combination of the position-sensitive detection and 3D reconstruction protocols. Charged ions are projected nearly radially following the initial electric field lines to provide magnification in the range of $10^6$. Their trajectories are then

confined to go through the counter-electrode to be finally projected onto a position-sensitive detector. An ion hit causes electron pulse signals along two orthogonal dimensions on the microchannel plate, where along each dimension the arrival time of the electron pulse on both ends is recorded and the difference calculated to locate the impact position. A 3D sub-nanometre scale image of the origin evaporated specimen can thus be reconstructed using a backwards projection protocol. Figure 9-4 shows one example algorithm of this backwards projection process. Assumptions here include a hemispherical tip with a constant evolution of radius $R$ along the needle shank.

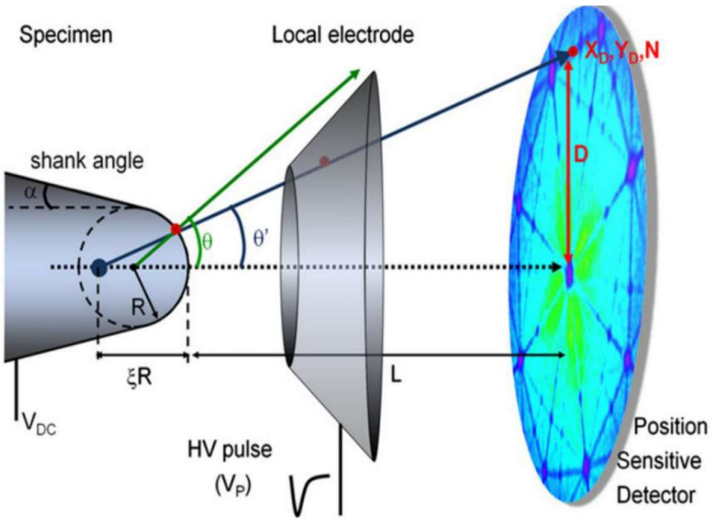


*Figure 9-4 Schematic of the back-projection process to trace a detected event back to its origin in the specimen, figure from [279]*

Following this geometry, the x-y original position of an ion on the spherical surface is given by:

$$x = \frac{\xi R}{L} X_D \qquad 9\text{-}6$$

$$y = \frac{\xi R}{L} Y_D \qquad 9\text{-}7$$

Where $x, y$ are the coordinates of origin and $X_D, Y_D$ are the hit coordinates, $L$ is the distance between needle and doctor, $R$ is the radius of curvature of the tip and $\xi$ is a compression factor for projection.

After the $x, y$ position, the depth coordinate $z_i$ of the ion detected with pulse sequence number $i$ can be obtained by:

$$z_i = \Sigma\delta z + R_i\left(1 - \sqrt{\frac{x^2 + y^2}{R_i^2}}\right) \qquad 9\text{-}8$$

Where $\Sigma\delta z$ is the cumulative depth increase over time, and the $R_i$ is the instantaneous radius. Such a depth calculation method accounts for the sequences in time of ion arrival, meaning that later hits relate to higher depths. The above equations present a simplistic and fit-to-all tomographic reconstruction protocol, while commercial APT instrumentation offers a variety of reconstruction algorithms to reduce spatial distortions, aided by specimen-specific calibration [280].

As such, 3D maps of individual atoms can be reconstructed by the information registered in APT measurements, allowing visualisation of both specimen structure and composition.

## II. Sample preparation procedure

APT sample preparation typically involves either (a) electropolishing, suitable for metals, or (b) focused ion beam (FIB) milling, which accommodates a broader range of materials, including silicon-based solar structures investigated in this thesis [281]. FIB can both remove and deposit small volumes of material, providing key functionality in the fabrication of APT samples. This section describes the APT sample preparation route using Zeiss Nvision 40 FIB/SEM instrument at David Cockayne Centre for Electron Microscopy. The operating principles of FIB [282], [283], [284] are widely of SEM [285], [286] known and hence not included in this thesis. The FIB milling sample preparation route includes extracting a small volume of interest, moving it onto an ex-situ APT sample holder, and fabricating a sharp needle tip. The conditions used in such a procedure, however, is highly material and specimen-specific, which requires precise adjustment of parameters during operation. The following process is practised and refined by the author, while following the development and optimisation works of C. Lotharukpong [287], D, Tweddle [288], and MS Meier [289]. This route is specifically designed for preparing a Si-based buried interface specimen. It can also be a reference to a wider range of semiconductor material preparations.

### Protective Cap Deposition

Once the sample was loaded into the SEM-FIB dual-beam system, a working site with a clear surface was first selected, ensuring that the volume of interest lay just beneath that surface. This site was positioned at the coincident point of the two beams for alignment of views. A dense tungsten capping layer >200 nm was deposited then to protect the sample surface from

ion beam damage. This was accomplished by concurrently scanning the ion beam and introducing a tungsten precursor gas through a nearby injection nozzle. The gallium FIB beam was operated at 30 kV, 150 pA with a pixel fill factor of 70% for the W deposition. The capping layer covered a 40 µm *5 µm rectangular region, aligning with the ROI of the lift-out bar in the following steps.

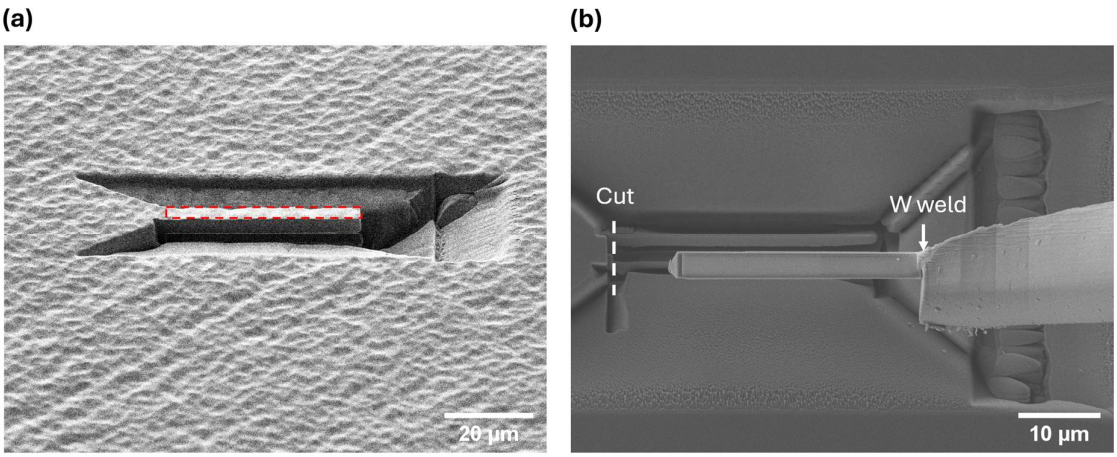


*Figure 9-5 (a) SEM side view of the working site for trenching and undercutting. The cantilever to be lift-out is hanging in the middle. The red rectangle indicates the protected surface by a capping W layer. (b) The cut-out bar (was then the cantilever) attached to a micro-manipulator. The left end of the bar is cut free. The bar is being extracted by pulling the micro-manipulator out.*

### Cantilever Production

After the deposition of the capping layer, deep trenches were milled along both long sides and one short side of the rectangular region via the FIB sputtering removal of the substrate. These trenches exceeded 10 µm in depth and spanned a width of at least 20 µm from the capped region. With the sample tilted, further undercuts were made to free the bottom side of the resulting cantilever. A 30 kV FIB beam at 6.5 nA was employed for large-volume material removal during trenching, while a lower current of 1.5 nA was used for the finer undercutting to minimise damage at the cantilever's bottom edge. Figure 9-5 (a) illustrates the outcome after this step, showing a cantilever connected to the substrate at only one end and free on all other sides. Sufficient clearance (>5 µm) was maintained between the cantilever and its sidewalls, which is an essential consideration for the subsequent lift-out process.

### Lift-out and mounting

In this lift-out step, the cantilever was cut free and transferred onto designated posts for holding further fabricated APT needles. A micro-manipulator was first brought in to contact the free end of the cantilever. The free end was welded to the manipulator tip with W deposition, after

which the fixed end of the cantilever was then cut free with a FIB current of 30 kV 1.5 nA. Figure 9-5 (b) shows a freed cantilever (now called a lift-out bar) end-on attached to the micro-manipulator while it was being evacuated.

After the extraction, small sections of the lift-out bar were transferred onto individual APT posts. Figure 9-6 (a) gives a top view of the lift-out bar with the first ~3 µm section cut off and mounted. This cutting was done with a FIB current of 30 kV 700 nA. Figure 9-6 (b) shows the side view of a mounted section attached to a cone-shaped post at the bottom. W weld was applied from both the left and right sides of the post in Figure 9-6 (b) for enforcement using consistent deposition conditions.

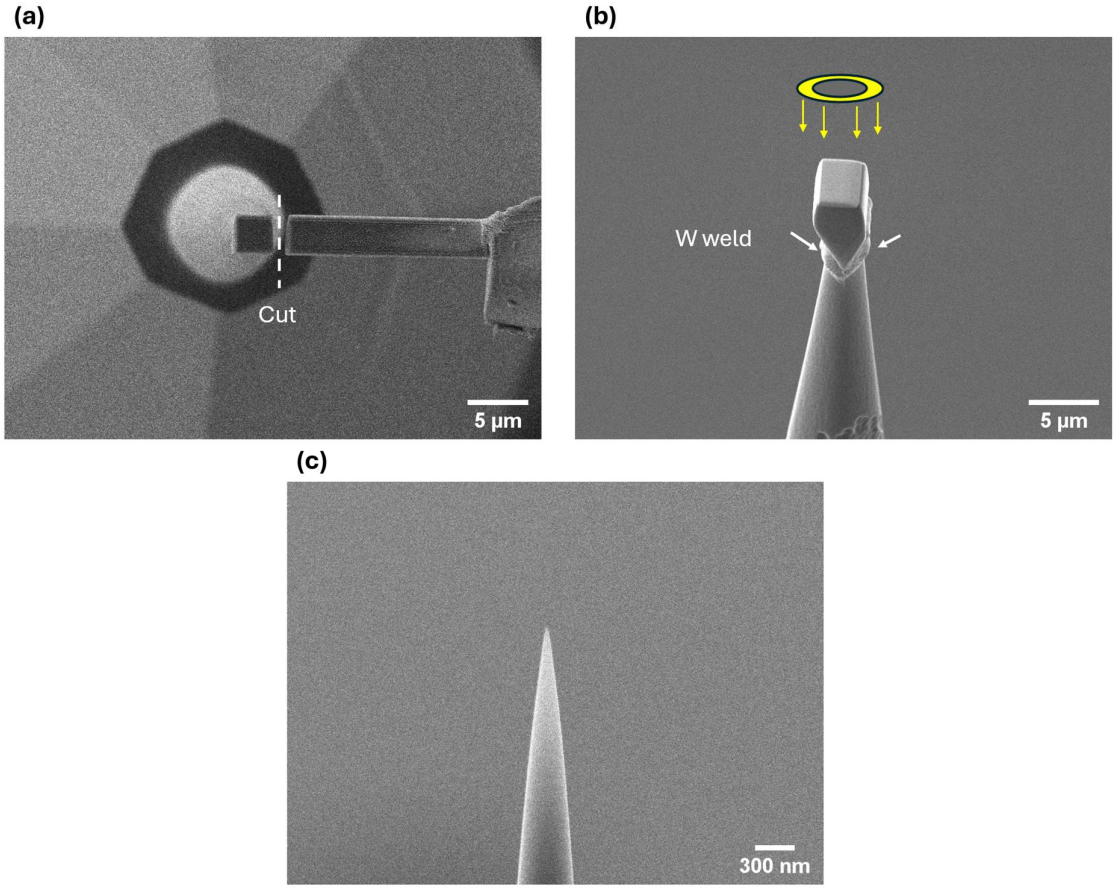


*Figure 9-6 (a) Top view of a small section of the lift-out bar mounted on the APT needle post. (b) side view of a section of the lift-out bar welded to the post with W. The circular marks indicate the direction and pattern of the annular milling. (c) Milled and polished needle ready for ATP tests.*

### Annular Milling and needle polishing

After all sections were mounted, each of them was shaped into one APT needle on one post. The needle shape formation was achieved by vertical FIB milling following an annular (doughnut) pattern. Initial shaping employed a milling condition at 30 kV 700 pA. Gradually

decreasing beam currents from at 300 pA, 150 pA, to 80 pA were used with a smaller ring diameter as the needle got sharper. This was done iteratively until the tip radius reached below 100 nm. A subsequent low-energy FIB etching step at 2 kV, 300 pA helped to remove gallium implantation from earlier milling steps, while slightly sharpening the tip in this final polishing step. The last figure, Figure 9-6 (c) shows a completed needle ready for APT experiments.

It is to be stressed again that special care was taken in this route to preserve the feature (e.g. interface, segregation sites) of interest within the first ~300 nm from the tip of the APT needle specimen. At the final stages of needle milling, the needle tip becomes electron transparent, meaning any features are effectively no longer visible. Hence, precise control and real-time adjustment as it goes are needed to limit milling damage.

## III. APT applications in silicon solar structures

Atom probe tomography has been applied to chemical characterisation of silicon solar structures, topics including dopant distribution [290]Impurity segregation at grain boundaries [291], [292], [293], dislocations [292], and interfaces [204], [210]. Researchers often combine APT with structural characterisation techniques, such as TEM, to link crystallographic interface characters to the corresponding local chemical segregation [294], [295]. Additionally, electrical methods, including PL and EBIC, can be combined with APT to gain insights into how compositional variations affect defect electrical activity [293], [296]. Studies on GB in multi-Si have found that excess impurity decorations can either degrade or enhance local recombination behaviour, depending on the type and extent of segregation [293]. Such findings deepen our understanding of the interaction between defect structures and their chemistry, which informs strategies for defect engineering and interface designs.

The 3D compositional APT data facilitate a quantitative comparison of an element's accumulation (or deficit) at an interface, using the Gibbsian excess parameter [297]. Conceptually, the Gibbsian excess is a valuate of how much of an element is enriched (or depleted) at an interface relative to the bulk. Since it originates from charactering interface behaviours, the result is normalised by the interface area. A general form of the Gibbsian excess $\Gamma$ follows:

$$\Gamma = \frac{N(c_i - c_{i(\mathrm{bulk})})}{\eta A} \qquad 9\text{-}9$$

Where $N$ is the total number of atoms in the 3D interface ROI. $c_i$ and $c_{i(bulk)}$ are percentage concentrations of elements at interface and bulk, respectively. $\eta$ is APT detection efficiency, and $A$ is the cross-sectional area of the interface ROI. This expression assumes constant atomic density in the bulk and interface ROI. Parameter $\Gamma$ hence quantifies atomic decoration of interfaces. An example of the ROIs and the interface from this work is showing in the following Figure 9-7.

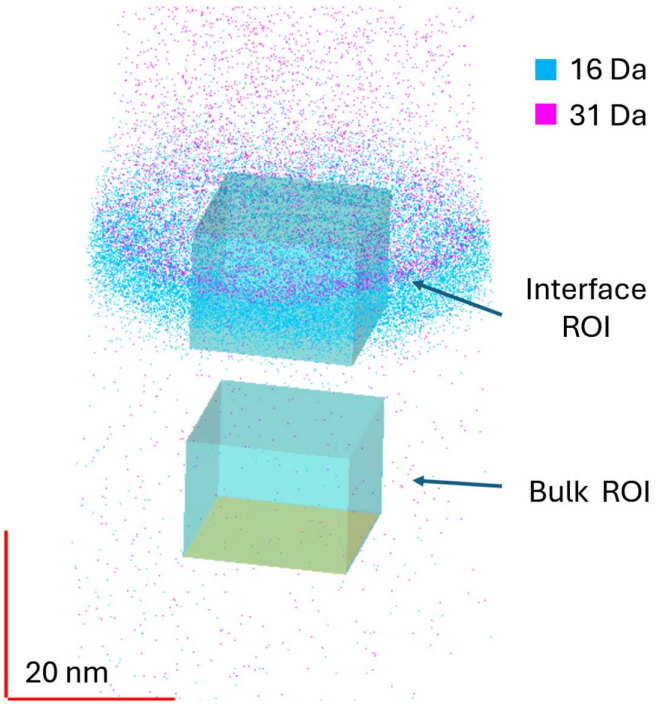


*Figure 9-7 Two regions of interest for Gibbsian interface excess calculation on an APT reconstruction map. The interface ROI contains the flat part of the interfacial oxide. Bulk ROI is of the same size and further into wafer depth. The yellow surface indicates the surface for determining the 2D interface area A.*

## IV. Limitations

Because APT combines processes including field evaporation, mass spectrometry, and 3D spatial reconstruction, several inherent limitations [206] are associated to APT including the following:

**Mass spectrum overlaps**

Overlaps on the APT mass spectra can cause ambiguity in quantitative chemical analysis. identification of chemical species in APT relies on matching peaks in the ionic mass-to-charge spectrum to known element or molecule masses. Figure 9-8 presents an example of an APT mass spectrum, where detected counts are allocated according to their mass-to-charge into a

histogram. Each peak corresponds to a particular concentration of sample-derived ions. However, due to multiple isotopic masses and possible molecular ion formation, different ion species, either monoatomic or molecular, can share the same mass-to-charge ratio, making their signals overlap. This effect is illustrated by the 29-30 Da group of peaks on Figure 9-8, which are each attributed to a collection of possible ions containing isotopic silicon and additional elements. Such overlays prevent the clear assignment of individual contributions, introducing uncertainty in chemical analysis. While statistical peak-deconvolution approaches [214], [215] help estimate contributions within these overlapping peaks, taking known isotopic abundances into account, their applicability can be limited by the number of potential ion components in the overlap.

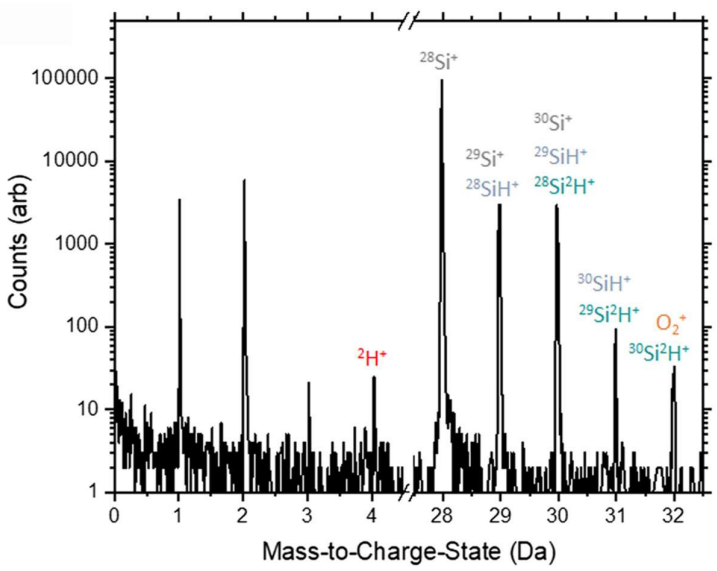


*Figure 9-8 Example mass spectrum from a hydrogenated Si grain boundary ROI in a multicrystalline Si wafer. figure from [213]*

### Reconstruction Errors

APT reconstruction is subject to aberrations from using simplified field and sample geometry assumptions for the complex field evaporation process. In multi-phase materials, different media evaporate at different rates or under different field conditions. Preferential evaporations of a phase component can cause local magnification effects, resulting in distortion of the reconstructed images [298]. Additional aberrations can be caused by surface movement of atoms prior to evaporation. These atoms with higher evaporation field requirements are reported to undergo a directional walk following field gradients over the surface [299], which also causes inaccurate position tracking of the final 3D reconstruction and artefacts in the interfacial composition. In addition, typical APT reconstruction protocols assume simplified

cone geometry for specimen shape evolution over time, which incurs atom position deviations in non-standard specimen shapes [300].

**Low result yield**

APT experiments suffer from low successful result yields. APT needles made from a complex FIB route can suffer from premature fracture under high fields. Electrostatic field-induced fracture happens readily at mechanical weak points (interfaces or GBs) of the specimen. This results in extremely low turnout in imaging of delicate structural systems. Some preventive methods can help to increase sample strength and viability during APT, including switching to laser pulsing mode to reduce the field applied, and surface cleaning to remove surface layers with different evaporation conditions to the specimen [301].

Reported APT results are sometimes prone to low reproducibility because each analysis sample covers only a nanometre-scale volume. Low sample numbers reported in APT studies often limit the statistical representation of the complete region under investigation. Careful ROI targeting is usually implemented instead of many samples, which can further complicate data interpretation.

## Appendix D. Elastic recoil detection

Elastic recoil detection (ERD) is an ion beam analysis technique to measure the chemical composition and depth profiles of thin film materials. Its fundamental principles lie in the elastic collision process between a high-energy incident ion and a sample atom [302]. Figure 9-9 (a) depicts the process of the elastic collision that results in knocking out or 'recoiling' of a target atom. Kinetic energy is transferred from the incident ion to the recoiled target atom. Following conservation of momentum and energy, the energy of the recoiled atom right after the collision with reference to the incident ion is given by [194]:

$$E_r = \left(\frac{4M_i m_r cos^2\theta}{(M_i + m_r)^2}\right) E_0 \qquad 9\text{-}10$$

Where $E_r, E_0$ are the respective kinetic energies of the incident and recoiled target atom, and $M_i, m_r$ are the respective masses. The angle $\theta$ is the scattering angle relative to the incident direction as indicated in Figure 9-9 (a).

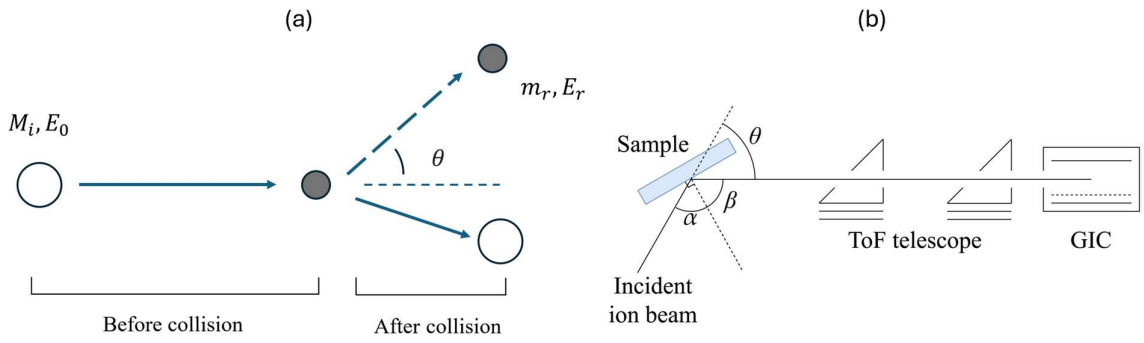


*Figure 9-9 (a) Schematic of the kinematics of the elastic collision process. (b)Schematic of the ToF-ERD setup, $\alpha, \beta$ are incident and exit beam angles to the sample normal. $\theta$ is the scattering angle, figure courtesy of [303]*

The recoiled atoms from the sample are detected and analysed in ERD measurements. Conventional ERD uses solid-state energy detectors, while modern Time-of-flight ERD (ToF-ERD) measures both ToF and energy for improved mass separation [195], [304]. The detection setup in a ToF-ERD is given in Figure 9-9. Recoiled atoms are analysed in two stages: (a) their velocity is determined by measuring the time-of-flight (ToF) between two timing foils, and (b) their energy is measured in a gas ionisation chamber (GIC) after passing through a silicon nitride window. As such, different elements can be separated along their distinct energy-ToF relations [305]. The depth information of sample atoms is interpreted by the energy loss during the incident and recoiling paths within the sample [193]. This means surface atoms exhibit the highest energy and lowest ToF. Quantification of the energy-depth relationship accounts for the 'stopping force' of the sample material, which describes the level of energy attenuation in the thin-film layers.

In comparison to SIMS, which uses an ion source at keV energy ranges, ToF-ERD employs a primary beam in the MeV range for effectively recoiling and operates at a near-glancing detection angle. On the other hand, the SIMS sputtering processing relies on high beam fluence, while ToF-ERD uses a low total incident fluence ($<10^{12}$ ions/cm$^2$). This minimises the sample damage and avoids SIMS artefacts, such as ion beam mixing and continuous arrival of environmental contamination during sputtering. Because the collision process in ToF-ERD excels at detecting light elements, ToF-ERD is particularly suitable for profiling hydrogen [304], [306]. ToF-ERD can thus provide complementary information to SIMS in the distribution of light elements. A few reported studies have demonstrated ERD's capability to measure sample H or D contents with either a He ion [197] or a N ion source [199].

# Appendix E. Contact-related resistance measurements

The contact-related resistances play a part in the total series resistance of a silicon solar cell. Figure 9-10 shows the components in the total cell series resistance, including three contact elements in a broader sense: resistance of the doped surface layer, resistance at the metal contact interface, and resistance within metal fingers. These resistances lead to a loss of current collection under cell operation and a reduction in fill factor, as introduced in the discussion of device characteristics in section 1.3.4.

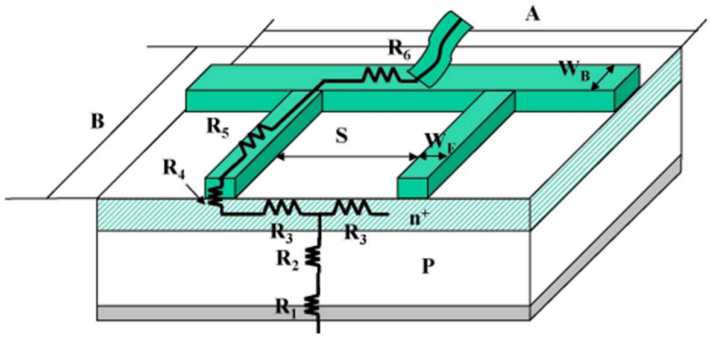


*Figure 9-10 Components of the total solar cell series resistance, contact-related components include: sheet resistance $R_3$ influencing lateral collection, contact interface resistance $R_4$, and resistance on metal lines $R_5$, figure from [61]*

## I. TLM Measurements

A key metric in the characterisation of metal-semiconductor contacts is the contact resistivity, commonly measured using the transfer length method (TLM) [307], [308], [309]. As a resistance testing approach, TLM relies on voltage-current measurements across a defined current path. Figure 9-11 (a) illustrates the current path in a TLM measurement, where two main components of the total path resistance are shown: (a) contact resistance $R_c$, and (b) semiconductor surface layer resistance $R_{semi}$. The metal silicon contact in such measurements is assumed to be ohmic with quasi-linear IV characteristics and a defined $R_c$ value. This assumption is valid on the basis that (a) a low Schottky barrier height is present at the M-S junction and (b) a small voltage drop is present across the interface under testing conditions. The $R_{semi}$ component accounts for the resistance of the conduction path in the semiconductor surface layer, which in the case of n-TOPCon test structure is the heavily doped n-type polysilicon layer. TLM measurements employ remote voltage sensing to minimise any voltage drops in electrical wires and connections. Multiple contact points are placed on the silver fingers, allowing the voltage drops on the fingers to be negligible in total $R_{tot}$.

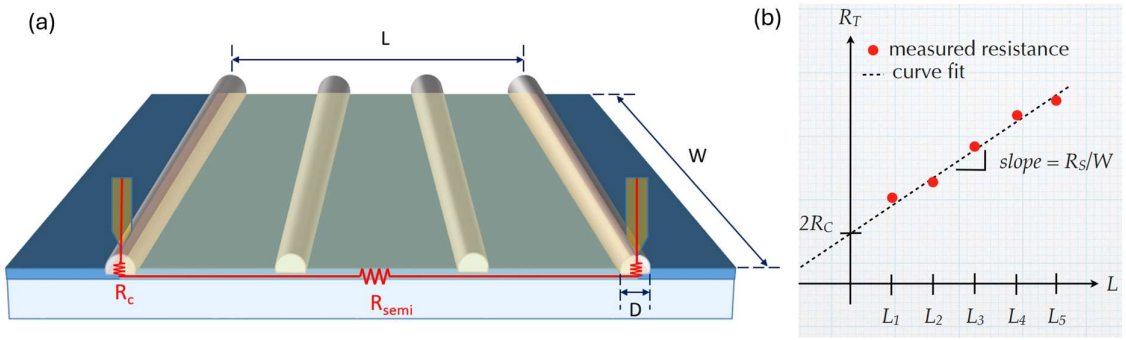


*Figure 9-11 (a) The current path and resistance components in TLM measurement (b) Linear fitting of TLM data, figure from [310]*

TLM measures the total resistance $R_{tot}$ between two separate metal fingers with a parallel distance $L$, as expressed by the following equation:

$$R_{tot} = R_{semi} + 2R_C = \frac{R_S}{W}L + 2R_C \qquad 9\text{-}11$$

Where the surface layer resistance $R_{semi}$ is further expressed with a sheet resistance $R_s$ and the surface layer width $W$ and length $L$ (also the finger distance). By varying the finger distance $L$, the $R_{tot}$ vs $L$ linear relationship can be fitted as illustrated in Figure 9-11 (b). The linear fitting yields the contact resistance as $2R_c$ from the y-intercept and the $Rs/W$ from the slope.

The contact resistivity $\rho_c$, representing the contact resistance per unit area resistance is then determined from $R_C$ as:

$$\rho_c = \frac{R_C}{A} \qquad 9\text{-}12$$

Where $A$ is the effective contact area, which can be smaller than the physical contact coverage due to the current crowding effect. The current crowding is a result of the difference in metal and semiconductor conductivity, which causes the diminishing of the horizontal current flow under the contacted surface. The characteristic length over which current laterally spreads in the semiconductor before entering the metal is known as the current transfer length, given by:

$$L_T = \sqrt{\frac{\rho_c}{R_{sh}}} \qquad 9\text{-}13$$

Where the transfer length $L_T$ is related to the ratio of contact resistivity $\rho_c$ and surface sheet resistance $R_{sh}$. The TLM measurement, as the name indicates, takes into account the value $L_T$ in the determination of the effective contact area $A$. Depending on the estimated current transfer length, the contact area is either (a) the physical coverage when the current transfer length is longer than the contact width, or (b) a reduced area by substituting the contact width with $2L_T$ when the current transfer length is shorter than the contact width. This process of revising the contact area is essential in accurate calculation of the contact resistivity $\rho_c$.

In practice, TLM measurements in this thesis are conducted with an in-house designed test station with four-point probes. The full wafer is cut into 25 mm × 35mm units with metal fingers running parallel to the 25 mm edge. This configuration enables a surface layer width W=25mm and finger distance L up to 35 mm. Example TLM data is shown in Figure 9-12. The assumptions in TLM measurements are satisfied by the measured industrial TOPCon samples, including a uniformly conductive semiconductor surface layer and ohmic metal-semiconductor (M-S) contacts. This is reflected by high linear correlation coefficients (mostly r> 0.9999) in linear fitting.

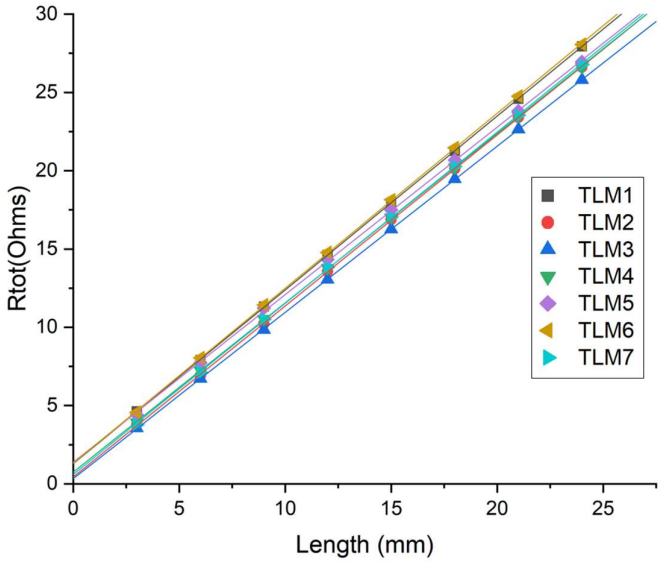


| Equation | y = a + b*x | | | | | | |
|---|---|---|---|---|---|---|---|
| Plot | TLM1 | TLM2 | TLM3 | TLM4 | TLM5 | TLM6 | TLM7 |
| Intercept | 1.2890 ± 0.0199 | 0.4401 ± 0.0474 | 0.3406 ± 0.0221 | 0.7536 ± 0.0456 | 1.3835 ± 0.1079 | 1.3246 ± 0.0520 | 0.5987 ± 0.0627 |
| Slope | 1.1103 ± 0.0013 | 1.0926 ± 0.0031 | 1.0615 ± 0.0014 | 1.0814 ± 0.0030 | 1.0703 ± 0.0071 | 1.1172 ± 0.0034 | 1.0935 ± 0.0041 |
| Pearson's r | 1 | 0.99998 | 0.99999 | 0.99998 | 0.99987 | 0.99997 | 0.99996 |
| R-Square (COD) | 0.99999 | 0.99995 | 0.99999 | 0.99995 | 0.99973 | 0.99994 | 0.99991 |

*Figure 9-12 Example results of TLM line fitting for 7 test units from same wafer. The associated table shows line fitting parameters.*

## II. Metal Finger Line resistivity measurements

The resistance of metal fingers is characterised by the finger line resistivity as follows:

$$r_{line} = \frac{R_{line}}{L} \qquad 9\text{-}14$$

Where the line resistivity $r_{line}$ is the finger resistance $R_{line}$ per unit length $L$. The measurement scheme is illustrated in Figure 9-13, which shows the total resistance between two points along a finger is given by:

$$R_{tot} = R_{lead} + R_{line} = R_{leads} + r_{line}\, L \qquad 9\text{-}15$$

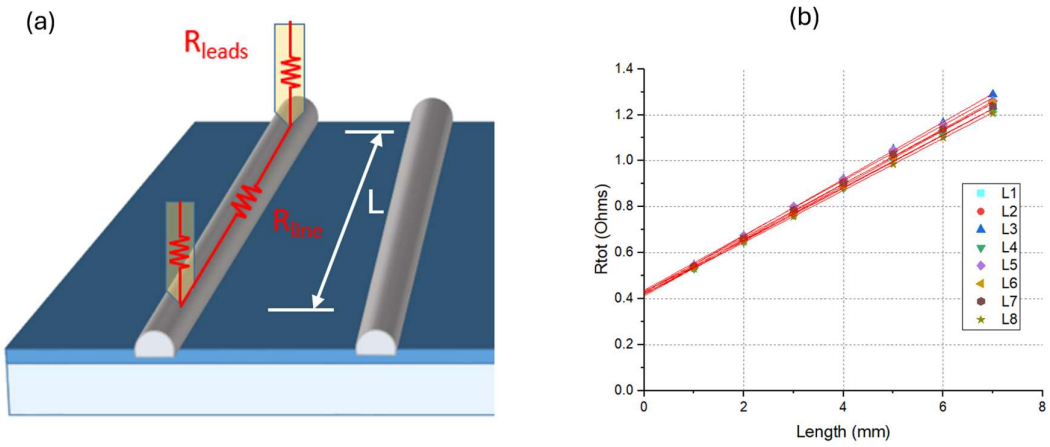


*Figure 9-13 (a) The current path and resistance component in metal finger resistance (b) Linear fitting of metal line resistance*

Here, $R_{leads}$ represents the extra resistance in electrical connections and wires, which must be considered in this case because its value is comparable to the metal finger resistance $R_{line}$.

By taking measurements between points with varying distance $L$ along a finger, the relationship between $R_{tot}$ and $L$ can be established and linearly fitted as illustrated in Figure 9-13. The y-intercept of the fit yields $R_{leads}$ and the slope provides the finger line resistivity $r_{line}$.

In practice, an experimental setup with 8 measurement points spaced at 1 mm intervals was used. Figure 9-13 shows example results using the setup. It is further demonstrated in this figure that metal fingers from L1 to L8 exhibit differences in slopes, reflecting slight variations in their line resistivity $r_{line}$.

## Appendix F. Atomic Force Microscope results

The Atomic Force Microscope is a type of scanning probe microscopy for characterising surface morphology. AFT operates by raster-scanning a sharp tip mounted at the free end of a flexible cantilever beam. The tip, when brought to close proximity to the surface, interacts with surface atoms through short-range forces including van der Waals force, electrostatic force and chemical force. The cantilever deflects in the process, with the deflection measured with nanometre-scale precision using methods such as piezoresistive sensing or optical deflection measurements [311].

The AFM operation modes have been developed to meet material and measurement needs. The cantilever operates in either a static mode, or in oscillation in both dynamic and tapping mode. The oscillation near the resonance frequency is sensitive to surface cyclic forces, allowing for surface examination. In tapping mode, the cantilever undergoes large-amplitude oscillations with intermittent contact with the surface, which is proven to be less damaging to the sample. Modern AFMs also incorporate frequency modulation or amplitude modulation techniques, providing enhanced surface sensitivity and material discrimination capabilities [312]. The output of an AFM scan is a high-resolution surface topography map with additional material contrasts.

AFM is implemented in this study to measure the surface roughness at nanometre scale of a TOPCon wafer surface capped with silicon nitride. Figure 9-14 displays the AFM surface height map over a 40 µm × 40 µm area, revealing a 15.0 nm calculated root mean square roughness. Tapping mode was used due to its relaxation of surface conditions.

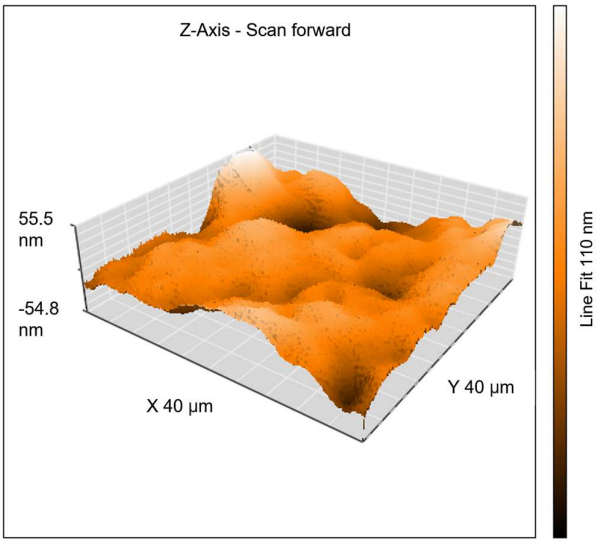

*Figure 9-14 AFM surface tomography map of sample z-axis height over a 40 µm × 40 µm area. Measurement was performed on a CoreAFM (Nanosurf) with 500 scanning points per line. A Tap190Al-G cantilever tip was used.*

## Appendix G. Photoconductance decay measurement

Photoconductance decay (PCD) is a contactless electrical measurement to determine the wafer effective lifetime. The PCD method uses pulsed illumination for carrier generation and measures the decay of photoconductance as the carriers recombine. The wafer conductance is typically measured via inductive coupling in a PCD lifetime tester [169].

The excess wafer conductance can be related to the excess carrier densities by:

$$\Delta\sigma = q(\mu_n \Delta n + \mu_p \Delta p)W \qquad 9\text{-}16$$

Where $\Delta n \; and \; \Delta p$ are excess carrier densities, and $\mu_n \; and \; \mu_p$ are carrier mobilities. $W$ is the wafer thickness and $q$ is the elementary charge. This relation makes wafer conductance suited for tracking carrier densities during recombination.

The effective lifetime of a wafer sample is related to the excess carrier density evolution over time, as given by [74]:

$$\tau_{eff} = \frac{\Delta n(t)}{G(t) - \frac{d\Delta n(t)}{dt}} \qquad 9\text{-}17$$

Where $G$ is the generation rate if non-zero.

Depending on the sample lifetime condition, PCD can operate in either transient mode or quasi-steady state (QSS) mode. The transient mode measures the conductance change after illumination is switch off with zero generation. In QSS mode, a longer illumination pulse is used, allowing the system to reach an assumed steady state with generation and recombination balanced at each point over time. Lifetime determination under QSS mode requires, as shown in eq. 9-17. requires additional wafer-specific optical calibration for the $G$ term. All PCD measurements reported in this thesis were performed in QSS mode with an optical constant of 1.0. Lifetime values are referenced at a $\Delta n$ =1×10$^{15}$ cm$^{-3}$ injection level.

As discussed in section 1.3.2, the sample lifetime is injection dependent. This dependency can be explored to evaluate surface recombination contributions to the overall lifetime [36]. Sample surface recombination parameter $J_{0s}$ were obtained from the lifetime curves following the approach described in [171] [172]. Figure 9-15 shows an example of the lifetime fitting process

for the $J_{0s}$ extraction. It is noted that the extraction of surface $J_{0s}$ is based on symmetrical sample configuration with identical front and rear surface finish.

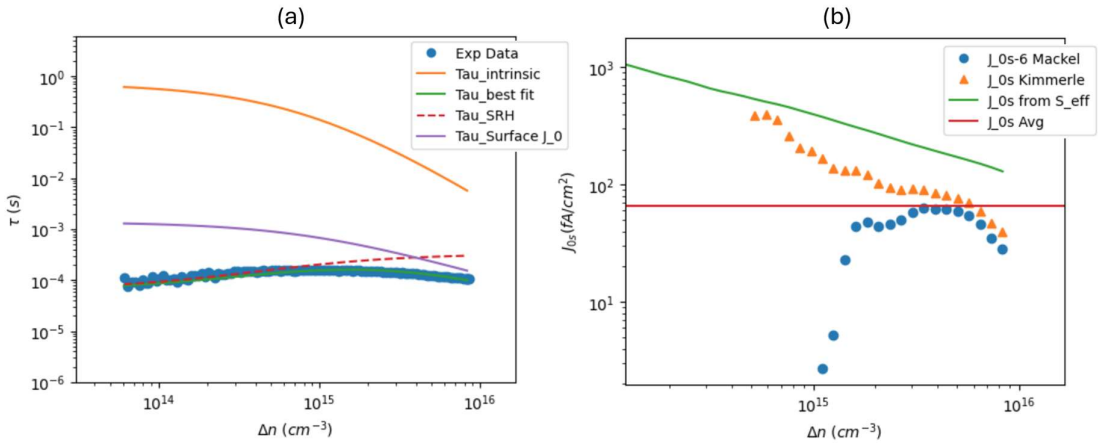


*Figure 9-15 PCD data and extraction of surface $J_0$: (a) curve fitting of the PCD lifetime data with different lifetime components. (b) $J_{0s}$ extraction following different methods, the final $J_0$ result at 65.4 fA/cm$^2$ is obtained from the average number in the high carrier concentration region following Kimmerle's fit approach [171].*

## Appendix H. FIB sequential slicing

This section contains a sequence of SEM images capturing during five consecutive steps of FIB milling. The milling was performed at a fixed angle of 64°, as constrained by the stage rotation limits. Slices are spaced by approximately 1 µm, resulting a total depth coverage of a ~5 µm.

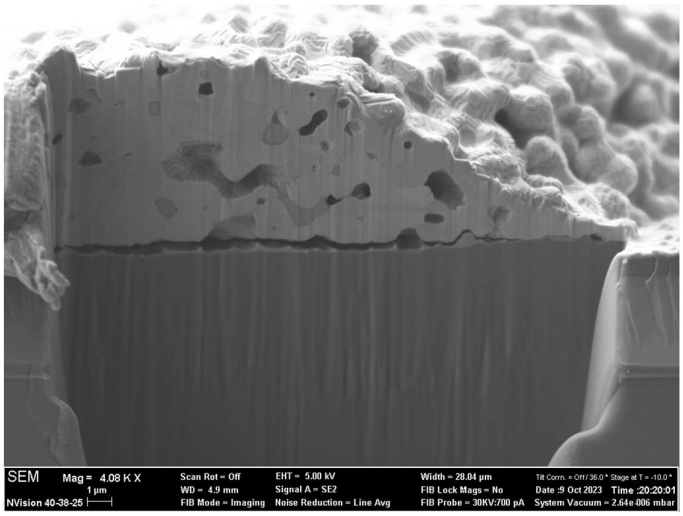


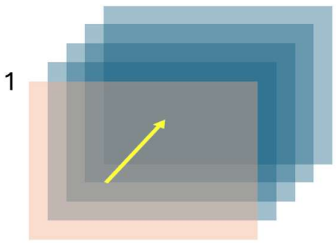

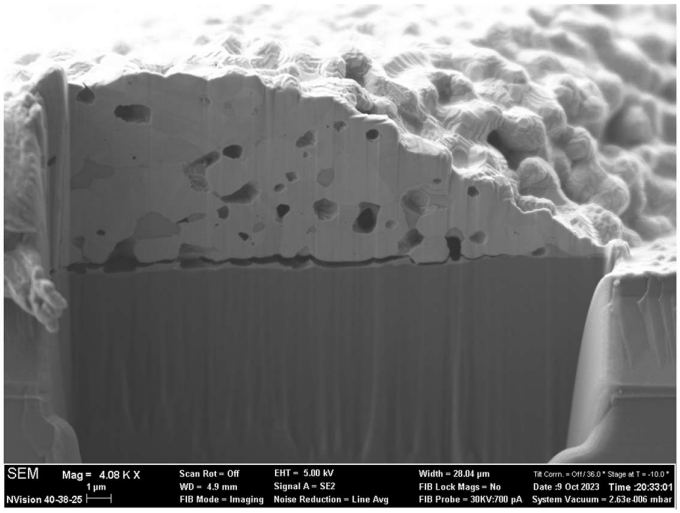
SEM
Mag = 4.08 K X
1 µm
NVision 40-38-25
Scan Rot = Off
WD = 4.9 mm
FIB Mode = Imaging
EHT = 5.00 kV
Signal A = SE2
Noise Reduction = Line Avg
Width = 28.04 µm
FIB Lock Mags = No
FIB Probe = 30KV;700 pA
Tilt Corrn. = Off / 36.0 ° Stage at T = -10.0 °
Date :9 Oct 2023
Time :20:33:01
System Vacuum = 2.63e-006 mbar

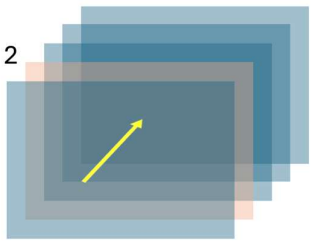
2

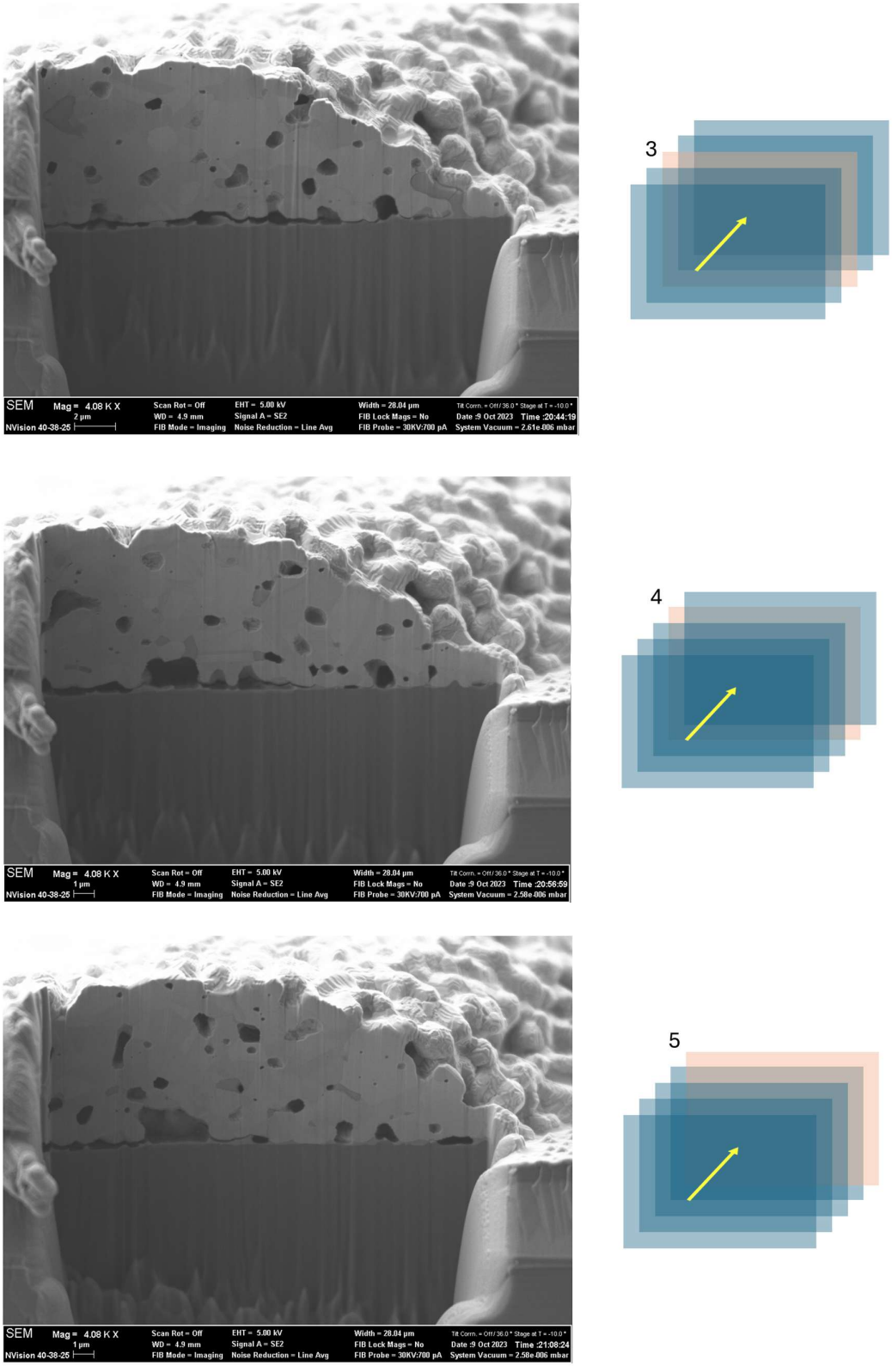


*Figure 9-16 Low magnification SEM images of 5 sequential steps of FIB slicing*

# Appendix I. SEM data for contact microstructure

This section contains additional SEM data for the contact microstructure examination.

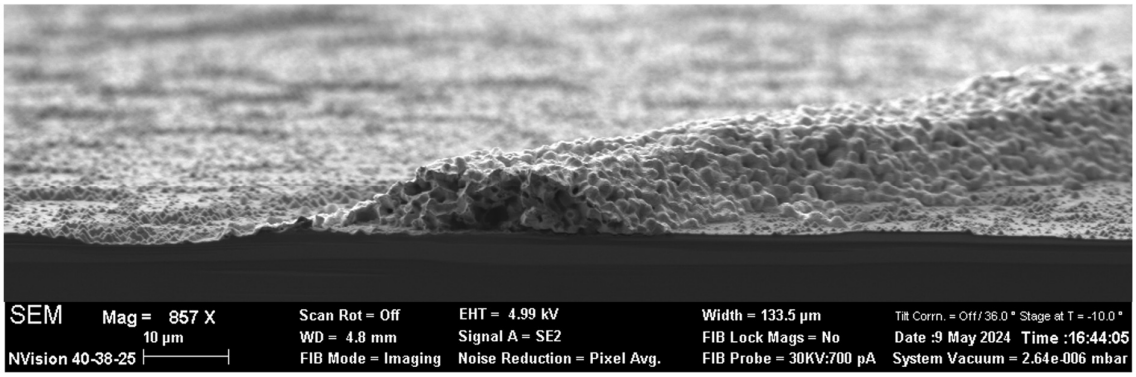


*Figure 9-17 A low magnification SEM image of a metal finger on silicon cell surface (TOPCon side). Both the cleaved cross-section and etched surface are visible.*

A150AlOx

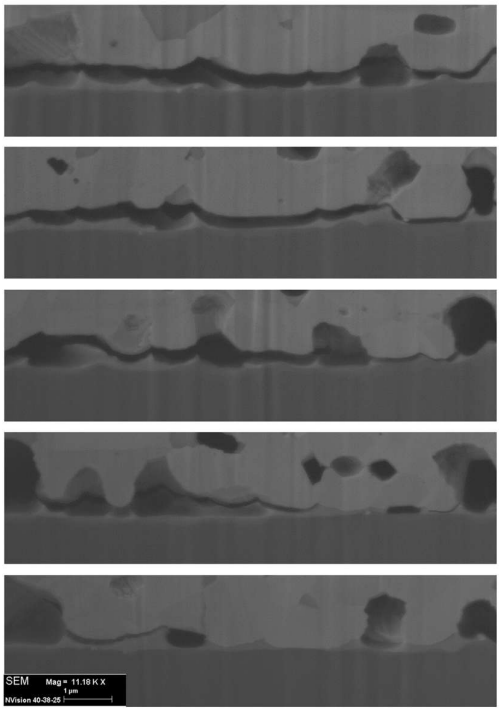


A150

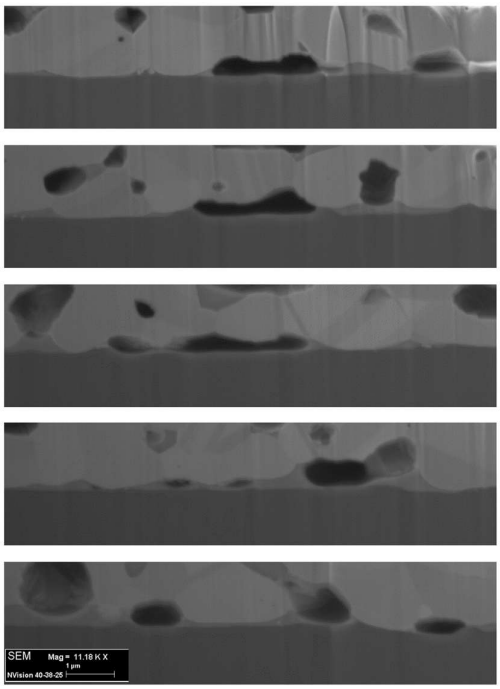


B150AlOx

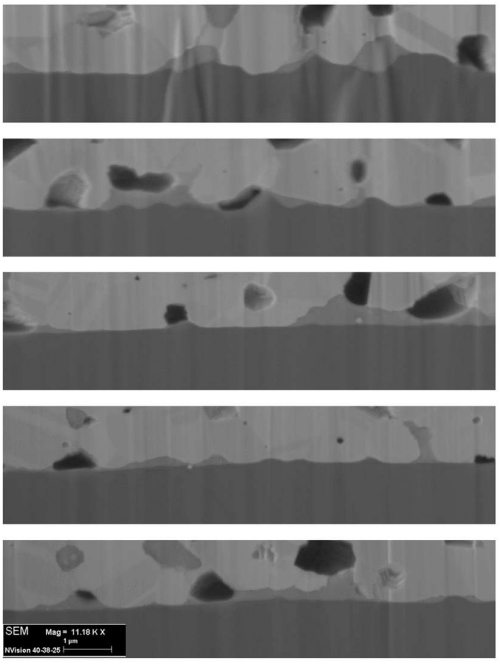


B150

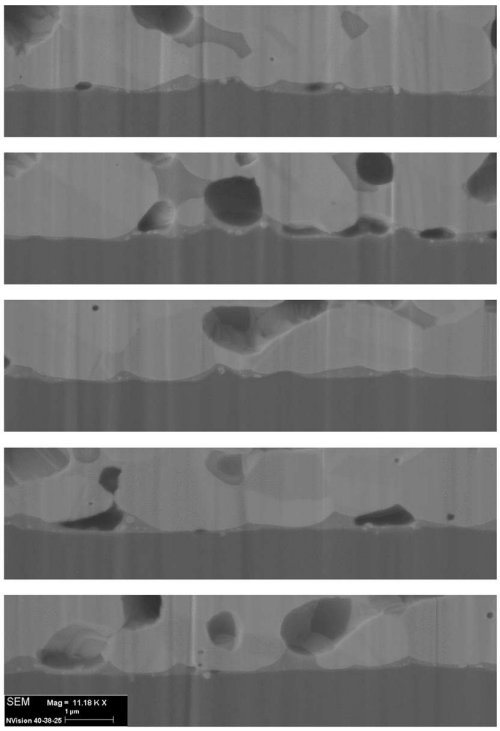

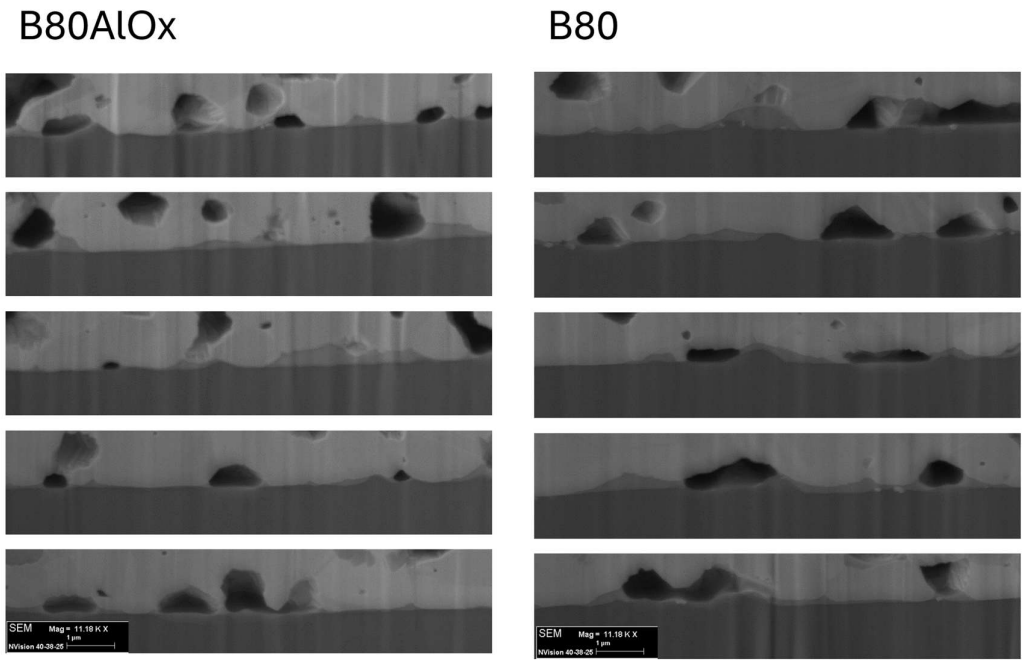


*Figure 9-18 low magnification SEM images of 5 sequential steps of FIB slicing, taken from all sample groups*

## Appendix J. Focusing optics for LBIC systems

This section outlines the fundamental optics that determine the spatial resolution in an LBIC system, with further discussions in [313][314]. For a monochromatic laser beam with a Gaussian cross-sectional irradiance profile, the beam radius (half-width) can be defined as the radial distance at which the irradiance falls to $1/e^2$ of the peak irradiance at the central axis. When a parallel laser beam passes through a converging lens, it is reshaped into a conical beam, with reducing radius until a minimum is found at the beam waist. Figure 9-19 describes the beam shape through a converging lens.

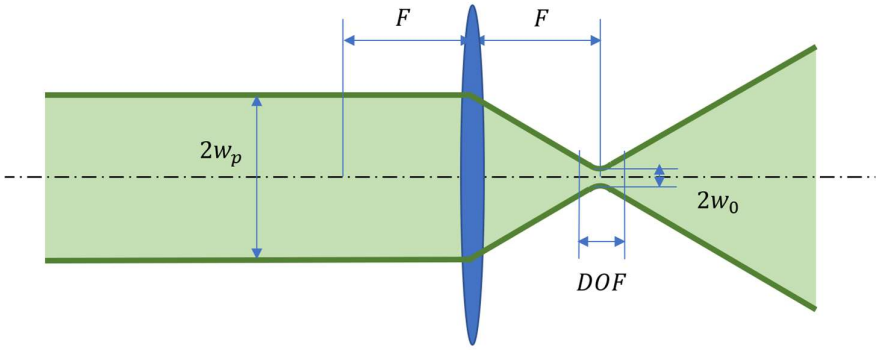


*Figure 9-19 Schematic of a laser beam through a converging lens*

The minimum beam width at its waist $w_0$ can be defined by:

$$w_0 = \frac{\lambda F}{\pi w_p} \qquad 9\text{-}18$$

Where λ is the wavelength of the monochromatic laser. $F$ is the focal length depending on the lens optics. $w_p$ is the parallel beam radius prior to focusing. This expression of $w_0$ establishes that the minimum waist size is dictated by both diffraction (dependent on wavelength λ) and the system parameters (focal power $F$ and parallel beam size $w_p$).

For an LBIC system, the waist spot size determines the mapping resolution. The focal length can be related to the working distance, i.e. the clearance between the objective lens and the sample surface. Thus, it follows that the spatial resolution in an LBIC system is directly proportional to both the laser wavelength and the working distance. Hence, high resolution is achievable with a combination of short wavelength and short working distance.

An additional parameter is the depth of focus (DOF) or the confocal parameter. It is the distance along the propagation axis of a beam from the waist $w_0$ to reach a beam width of $\sqrt{2}\, w_0$. The DOF is determined by:

$$DOF = \frac{2\lambda F^2}{\pi {w_p}^2} = \frac{2\pi w_0^2}{\lambda} \qquad 9\text{-}19$$

The expression corelates DOF to focal length $F$ and beam waist size $w_0$. In the context of the LBIC system, the DOF can hence be calculated, which can be as low as a few micrometres for a a high-resolution, small working distance system.